Atmospheric carbon dioxide retrieved from the Greenhouse gases Observing SATellite; Method, comparisons and algorithm development

Thesis submitted for the degree of

Doctor of Philosophy

at the University of Leicester

by

Austin James Cogan

Earth Observation Science Group

Department of Physics and Astronomy

University of Leicester

November 2012

Declaration

I hearby declare that no part of this thesis has been previously submitted to this or any other University as part of the requirement for a higher degree. The work described herein was conducted by the undersigned except for contributions from colleagues as acknowledged in the text.

Austin J. Cogan
November 27, 2012

I would like to dedicate this thesis to my wife, Katya, and my parents, Christopher and Valerie, for all their support.

Atmospheric carbon dioxide retrieved from the Greenhouse gases Observing SATellite; Method, comparisons and algorithm development

Austin J. Cogan

ABSTRACT

Carbon dioxide is the largest anthropogenic contributor to global warming and atmospheric concentrations have rapidly increased since the start of the industrial revolution. Networks of surface in-situ carbon dioxide sensors provide precise and accurate measurements of the global carbon dioxide concentration, including large scale temporal, seasonal and latitudinal variations. However, these observations are too sparse to allow the establishment of sub-continental carbon budgets, limiting the accuracy of climate change projections and the ability to mitigate future levels of atmospheric carbon dioxide.

Satellite observations can provide data with dense spatial and temporal coverage over regions poorly sampled by surface networks. Specifically, observations in the shortwave infrared region are well suited for constraining carbon fluxes as they can provide total column carbon dioxide with high sensitivity to the source and sink locations at the surface. The first dedicated greenhouse gases sensor, the Greenhouse gases Observing SATellite (GOSAT), was launched in January 2009 by the Japanese Aerospace eXploration Agency (JAXA) and has successfully started to acquire global observations of greenhouse gases, including carbon dioxide.

The Univerisity of Leicester Full Physics (UOL-FP) retrieval algorithm has been designed to estimate total column carbon dioxide from GOSAT shortwave infrared observations. The initial results were compared to coincident ground based measurements for a number of locations and compared on a global scale to a model. This showed an accuracy and precison that should provide improved surface flux estimates. Additionally, a bias correction scheme was developed that reduced observed geographical biases, allowing surface flux uncertainties to be potentially reduced further. To further develop the UOL-FP retrieval algorithm, a simulator capable of creating realistic GOSAT observations was built, allowing the investigation of different retrieval algorithm modifications, which may lead to reduced source and sink flux uncertainties and therefore aid future climate change forecasts.

PUBLICATIONS

Journal Articles

Cogan, A. J., Boesch, H., Parker, R. J., Feng, L., Palmer, P. I., Blavier, J.-F., Deutscher, N., Macatangay, R., Notholt, J., Roehl, C. M., Warneke, T., & Wunch, D. (2012), Atmospheric carbon dioxide retrieved from the Greenhouse gases Observing SATellite (GOSAT): Comparison with ground-based TCCON observations and GEOS-Chem model calculations, *Journal of Geophysical Research*, 117, D21301, doi:10-.1029/2012JD018087.

Fraser, A., Palmer, P.I., Feng, L., Boesch, H., Cogan, A., Parker, R., Dlugokencky, E.J., Fraser, P.J., Krummel, P.B., Langenfelds, R.L., O'Doherty, S., Prinn, R.G., Steele, L.P., van der Schoot, M., & Weiss, R.F. (2012), Estimating regional methane surface fluxes: the relative importance of surface and GOSAT mole fraction measurements, *Journal of Atmospheric Chemistry and Physics*, accepted.

Boesch, H., Deutscher, N. M., Warneke, T., Byckling, K., Cogan, A. J., Griffith, D. W. T., Notholt, J., Parker, R. J., & Wang, Z. (2012), HDO/H_2O ratio retrievals from GOSAT, *Journal of Atmospheric Measurement Techniques Discussions*, 5, 6643-6677, doi:10.5194/amtd-5-6643-2012.

Oshchepkov, S., Bril, A., Yokota, T., Wennberg, P., Deutscher, N. M., Wunch, D., Toon, G., Yoshida, Y., O'Dell, C. W., Crisp, D., Miller, C. E., Frankenberg, C., Butz, A., Aben, I., Guerlet, S., Hasekamp, O., Boesch, H., Cogan, A., Parker, R., Griffith, D., Macatangay, R., Notholt, J., Sussmann, R., Rettinger, M., Sherlock, V., Robinson, J., Kyrö, E., Heikkinen, P., Feist, D. G., Morino, I., Kadygrov, N., Belikov, D., Maksyutov, S., Matsunaga, T., Uchino, O., & Watanabe, H. (2012), Effects of atmospheric light scattering on spectroscopic observations of greenhouse gases from space. Part 2: Algorithm intercomparison in the GOSAT data processing for CO_2 retrievals over TCCON sites, *Journal of Geophysical Research*, in submission.

Oshchepkov, S., Bril, A., Yokota, T., Morino, I., Yoshida, Y., Matsunaga, T., Belikov, D., Wunch, D., Wennberg, P., Toon, G., O'Dell, C., Butz, A., Guerlet, S., Cogan, A., Boesch, H., Eguchi, N., Deutscher, N., Griffith, D., Macatangay, R., Notholt, J., Sussmann, R., Rettinger, M., Sherlock, V., Robinson, J., Kyrö, E.,

Heikkinen, P., Feist, D. G., Nagahama, T., Kadygrov, N., Maksyutov, S., Uchino, O., & Watanabe, H. (2012), Effects of atmospheric light scattering on spectroscopic observations of greenhouse gases from space. Validation of PPDF-based CO_2 retrievals from GOSAT, *Journal of Geophysical Research*, 117, D12305, doi:10.1029/2012JD017505.

Reuter, M., Buchwitz, M., Schneising, O., Hase, F., Heymann, J., Guerlet, S., Cogan, A. J., Bovensmann, H., & Burrows, J. P. (2012), A simple empirical model estimating atmospheric CO_2 background concentrations, *Journal of Atmospheric Measurement Techniques*, 5, 1349-1357, doi:10.5194/amt-5-1349-2012.

Parker, R., Boesch, H., Cogan, A., Fraser, A., Feng, L., Palmer, P., Messerschmidt, J., Deutscher, N., Griffith, D., Notholt, J., Wennberg, P. & Wunch, D. (2011), Methane Observations from the Greenhouse gases Observing SATellite: Comparison to Ground-based TCCON data and Model Calculations, *Geophysical Research Letters*, 38, L15807, doi:10.1029/2011GL047871.

Conference Proceedings

Cogan, A., H. Boesch, R. Parker & P. Monks (2010), Validation of atmospheric CO_2 and CH_4 retrieved from GOSAT, *Proceedings of the ESA Living Planet Symposium*.

Parker, R., H. Boesch, A. Cogan, P. Monks, D. Knappett, P. Palmer, L. Feng, A. Fraser & A. Bloom (2009), Comparison of GOSAT CO_2 and CH_4 to modelled data, *Proceedings of the ESA Atmospheric Science Conference*.

Boesch, H., Parker, R. J., Knappett, K. S., Cogan, A. J. Palmer, P. I., Feng, L., Yokota, T., Maksyutov, S., Crisp, D. & Miller, C. E. (2009), CO_2 and CH_4 Retrievals from GOSAT and SCIAMACHY, *Proceedings of the 8th International Carbon Dioxide Conference*.

Cogan, A. J., Boesch, H., Monks, P. S., Parker, R. J., Knappett, D. S. & Hewitt, A. J. (2009), Observing Atmospheric CO_2 from Space, *Proceedings of Remote Sensing and Photogrammetry Society Annual Conference 2009*.

Boesch, H., Parker, R. J., Knappett, K. S., Cogan, A. J. Palmer, P. I., Feng, L., Yokota, T., Maksyutov, S., Crisp, D. & Miller, C. E. (2009), CO_2 and CH_4 Retrievals from GOSAT and SCIAMACHY, *Proceedings of the 8th International Carbon Dioxide Conference*.

Other Documents

Cogan, A. (2012) National Centre for Earth Observation Research Highlights 2012: Measuring Global Carbon Dioxide Concentrations with Satellites, NCEO highlights Brochure, 31.

Boesch, H., A. Cogan & R. Parker (2011), University of Leicester Level 2 Retrieval Algorithm Theoretical Basis Document, Version 1.0 Revision 1.

Palmer, P., M. Barkley, P. Bernath, H. Boesch, M. Chipperfield, A. Cogan, L. Feng, M. Gloor, P. Monks, M. Scholze, P. Suntharalingam & M. Wooster (2009), Interim Report on GOSAT/TANSO Project, The UK Universities contribution to the analysis of GOSAT L1 and L2 data: towards a better quantitative understanding of surface carbon fluxes.

ACKNOWLEDGEMENTS

I thank JAXA, NIES, and MOE for the GOSAT data and their continuous support as part of the Joint Research Agreement. I gratefully appreciate the support by the NERC and the British Council. I also thank the OCO team at JPL for supplying the retrieval algorithm. I thank the BADC for providing ECMWF Operational Analyses data. TCCON is supported by NASAs Terrestrial Ecology Program through a grant to the California Institute of Technology. Operations support for Lamont and Darwin is provided by NASAs OCO. For the TCCON sites at Bialystok and Orleans, I thank AeroMeteo Service and the RAMCES team at LSCE for station maintenance and acknowledge the funding by the GOSAT team and within the EU-projects IMECC and GEOmon. Finally, I thank Hartmut Boesch and Robert Parker for their support and guidance.

Contents

List of Figures

List of Tables

LIST OF ABBREVIATIONS

4D-VAR	Four-dimensional variational assimilation
ACOS	Atmospheric CO_2 Observations from Space
AERONET	AErosol RObotic NETwork
AIRS	Aqua-advanced Infrared Radiation Sounder
AMSU	Advanced Microwave Sounding Unit
AOD	Aerosol Optical Depth
ARM	Atmospheric Radiation Measurement
ASCENDS	Active Sensing of CO_2 Emissions over Nights, Days and Seasons
ASTER	Advanced Spaceborne Thermal Emission and Reflection radiometer
AVIRIS	Airborne Visible InfraRed Imaging Spectrometer
BTD	Brightness Temperature Difference
CAI	Cloud and Aerosol Imager
CALIOP	Cloud-Aerosol Lidar with Orthogonal Polarization
CALIPSO	Cloud-Aerosol Lidar and Infrared Pathfinder Satellite Observations
CAM	Monitor camera system
CARBONSAT	CARBON monitoring SATellite
CASA	Carnegie-Ames-Stanford Approach
CDIAC	Carbon Dioxide Information Analysis Center
CH_4	Methane
CLAUDIA	CLoud and Aerosol Unbiased Decision Intellectual Algorithm
CMS	Carbon Monoxide and Methane Spectrometer
CNES	Centre National dEtudes Spatiales
CO	Carbon Monoxide
CO_2	Carbon Dioxide
DEM	Digital Elevation Model
DOAS	Differential Optical Absorption Spectroscopy
ECMWF	European Centre for Medium Range Weather Forecasts
EE	Earth Explorer opportunity missions
ENVISAT	ENVironment SATellite
ESA	European Space Agency
ESRL	Earth System Research Laboratory
ESSP	Earth System Science Partnership
FTS	Fourier Transform Spectrometer

FSI	Full Spectral Initiation
FAR	First Assessment Report
FFT	Fast Fourier Transform
GEMS	Global and regional Earth-system (Atmosphere) Monitoring using Satellite and in-situ data
GEOS	Goddard Earth Observing System
GFED	Global Fire Emissions Database
GOSAT	Greenhouse gases Observing SATellite
GWP	Global Warming Potential
H_2O	Dihydrogen monoxide (Water)
HIRS	High resolution Infrared Radiation Sounder
HITRAN	HIgh-resolution TRANsmission molecular absorption database
IASI	Infrared Atmospheric Sounding Interferometer
IFOV	Instantaneous Field of View
IIR	Imaging Infrared Radiometer
ILS	Instrument Line Shape
IPCC	Intergovernmental Panel on Climate Change
IWC	Ice Water Content
JAXA	Japan Aerospace eXploration Agency
L1B	Level 1B
LIDORT	Linearized Discrete Ordinate Radiative Transfer
LWC	Liquid Water Content
MCT	Mercury Cadmium Telluride (HgCdTe)
MEC	Mass Extinction Coefficient
MET	Surface Meteorological Instrumentation
MMR	Mass Mixing Ratio
MOE	Ministry Of Environment
MODIS	MODderate REsolution Imaging Spectroradiometer
MSU	Microwave Sounding Unit
N_2	Dinitrogen
NASA	National Aeronautics and Space Administration
NDVI	Normalized Difference Vegetation Index
NIES	National Institute for Environmental Studies
NIR	Near Infra-Red

NOAA	National Oceanic and Atmospheric Administration
O_2	Dioxygen
OCO	Orbiting Carbon Observatory
OPD	Optical Path Difference
P	Parallel polarisation
PC	Photo-Conductive
PDF	Probability Density Function
PPDF	Path length Probability Density Function
RF	Radiative Forcing
RH	Relative Humidity
RI	Refractive Index
RT	Radiative Transfer
S	Perpendicular Polarisation
SAR	Second Assessment Report
SCIAMACHY	SCanning Imaging Absorption SpectroMeter for Atmospheric CartograpHY
SH	Specific Humidity
SGP	Southern Great Plains
SNR	Signal to Noise Ratio
SPRINTARS	Spectral Radiation-Transport Model for Aerosol Species
SSU	Stratospheric Sounding Unit
SWIR	Short Wave Infra-Red
SZA	Solar Zenith Angle
TANSO	Thermal And Near infrared Sensor for carbon Observations
TAR	Third Assessment Report
TCCON	Total Carbon Column Observing Network
TCM	Tropical Carbon Mission
THWAPS	Temperature, Humidity, Wind and Pressure Sensors
TIR	Thermal Infra-Red
TIROS	Television Infrared Observation Satellite
TOA	Top of Atmosphere
TOVS	TIROS Operational Vertical Sounder
UNFCCC	United Nations Framework Convention on Climate Change
UoL-FP	University of Leicester Full Physics

USA	United States of America
USGS	United States Geological Survey
UV	Ultra Violet
VFM	Vertical Feature Mask
VIS	Visible
VMR	Volume Mixing Ratio
WFC	Wide Field Camera
X_{CO2}	Column averaged dry air mole fraction of CO_2

Chapter 1

Introduction

1.1 Climate Change

The Intergovernmental Panel on Climate Change (IPCC) defines climate change as any change in the mean state of a climate system over an extended period of time, such as decades or longer, whether it be caused by natural variability or due to human activity (IPCC 2001). The Earth's mean climate is a consequence of incoming radiation from the Sun and outgoing radiation from the Earth, known as the radiation budget. Variations in solar radiation can also cause the climate to differ, which for instance can be caused by fluctuations in the radiation emitted from the Sun or due to variations in the Earth's orbit. Also, various properties within the Earth's atmosphere and surface can change the amount of incoming and outgoing radiation, such as reflection, absorption, emission and scattering of radiation.

Human activities have resulted in numerous changes of the atmosphere and surface that can alter the radiation budget of the Earth, see Section 1.2.1. For instance, anthropogenic emissions of greenhouse gases, such as carbon dioxide (CO_2), have increased rapidly over the last couple of centuries, leading to an enhancement of atmospheric absorption of outgoing radiation causing the Earth to become warmer (IPCC 2001). It is important to be able to project future climate changes so that humans can mitigate and adapt to the changing environments. The current knowledge of the Earth's climate system is largely due to historical measurements, such as ice cores, and recent direct instrument observations (Houghton 2004). To this extent, recent climate variations have been observed and an overview of this is shown in Figure 1.1.

The recent anthropogenic emissions of greenhouse gases are considered geologically significant due to a rapid increase in temperature over a very short time frame ($\sim$100

years), see Section 1.2. The present global warming trend is predicted to cause the temperature of the Earth to rise by 2-3 degrees to be similar to that of the mid-Pliocene where temperatures were higher (particularly in higher latitudes), polar ice cover was reduced and precipitation patterns were different (Robinson et al. 2008). Although the potential temperature increase over North America, Europe and Asia would increase agricultural productivity, this would unlikely compensate for substantial productivity losses in mid and low latitudes due to limitations of the terrain and soil (Haywood et al. 2008). As a consequence of higher temperatures, higher evapotranspiration would occur further reducing the productivity of agriculture (Haywood et al. 2008). In addition to changes in agriculture and precipitation, there may be many other consequences of global warming that would require adaptation, such as human migration (McLeman & Smit 2006). Thus, it is important to mitigate the temperature increase and one way to achieve this would be to reduce anthropogenic greenhouse gas emissions, which are the main drivers of global warming.

To attempt to achieve reduced emissions the Kyoto Protocol was adopted in 1997, which commits numerous countries to not exceed their assigned anthropogenic emission quantities and to reduce emissions by 5% below 1990 levels between 2008-2012 (NATIONS 1998). Since 1997 there have been many advances in the understanding of the climate, with the insight that it is more appropriate to limit CO_2 emissions based on a threshold of global temperature increase (Weaver 2011). The Copenhagen Accord (2009), proposed by the United Nations Framework Convention on Climate Change (UNFCCC), defined that an increase of 2 K above the preindustrial level would be the limit (NATIONS 2009). The second commitment of the Kyoto Protocol is proposed to include this and determine emission limits upon this (Weaver 2011). However, for countries to know how to reduce emissions it is important to understand what the sources and sinks are of each driver (e.g. gas, aerosol, land change) of climate change.

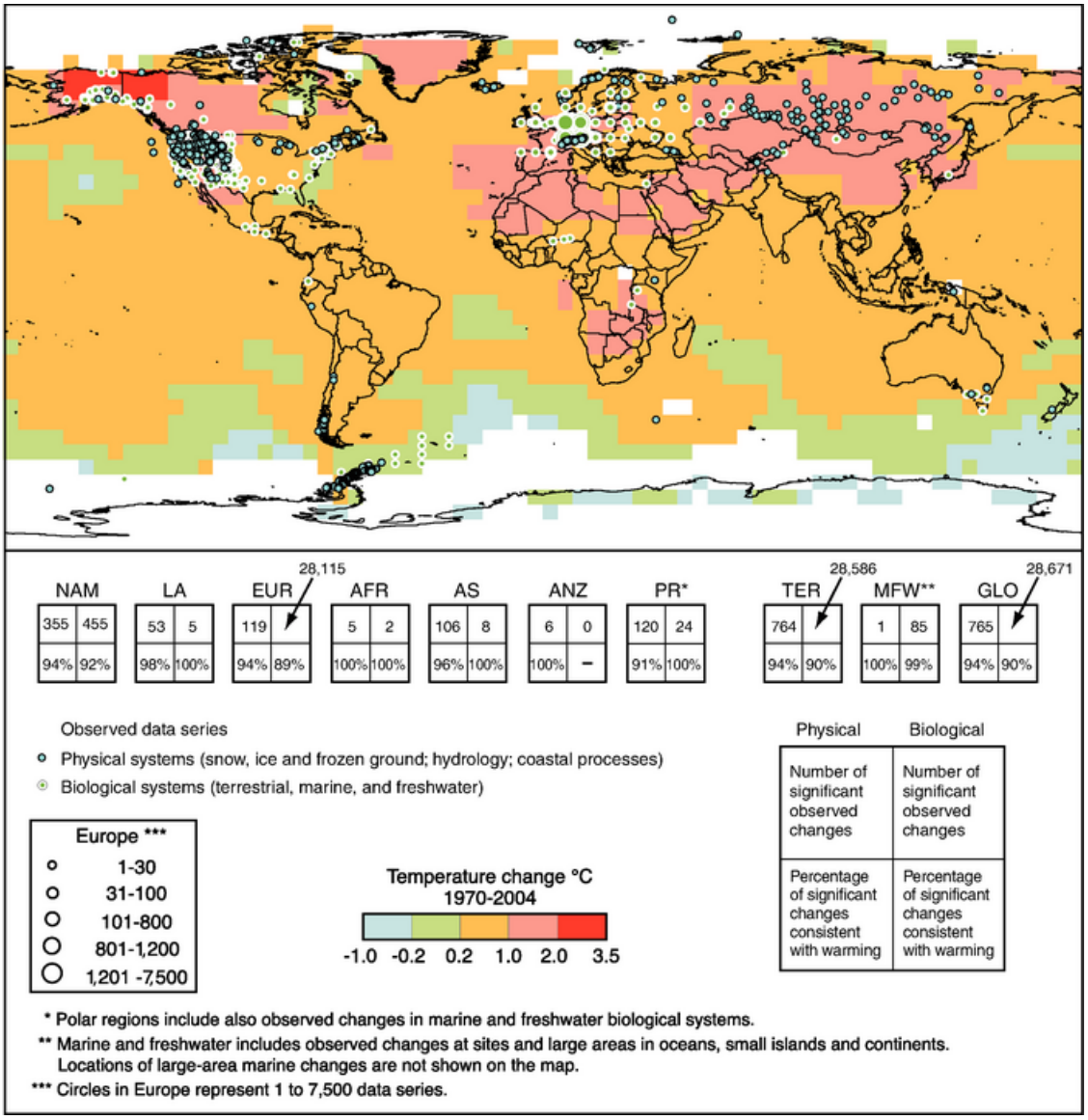

FIGURE 1.1. An overview of recorded climate variations between 1970 and 2004, showing temperature changes and locations of significant changes of physical systems (snow, ice, hydrology, and coastal processes) and biological systems (terrestrial, marine, and freshwater). For each continental region the number of significant changes and those correlating with temperature are given in the 2 x 2 boxes. These regions include; North America (NAM), Latin America (LA), Europe (EUR), Africa (AFR), Asia (AS), Australia and New Zealand (ANZ), and Polar Regions (PR). This is also shown for a global-scale, Global (GLO), with it separated into Terrestrial (TER), Marine and Freshwater (MFW). Figure taken from IPCC (2001).

1.2 Global Warming

Global warming refers to the increases in mean global surface temperature, which provides one way to monitor climate change. Global surface temperatures have increased rapidly since a pre-industrial age, as shown in Figure 1.2, indicative of a changing climate.

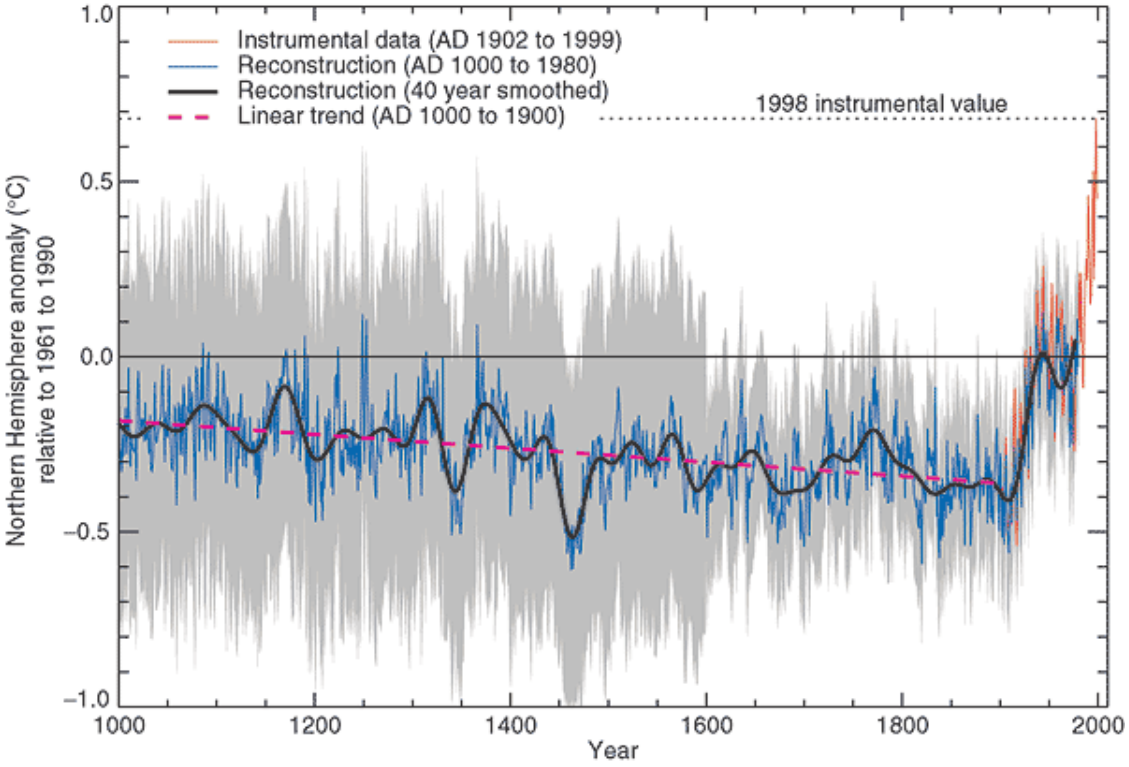

FIGURE 1.2. Northern Hemisphere temperatures over the last two millenia. Shows temperature reconstructed from tree rings, corals, ice cores and historical records (blue) and recent instrumental data (red), with the data smoothed (black) and two standard error limits given (grey). Figure taken from IPCC (2001).

Whilst many different aspects could affect the surface temparature, measurements taken from ice cores have shown a strong correlation between temperature increases and atmospheric concentrations of CO_2 and CH_4 (IPCC 2001), see Figure 1.3 for example. This is likely due to the greenhouse effect, whereby atmospheric greenhouse gases, such as CO_2 and CH_4, cause the temperature of the atmosphere to increase (a more detailed explanation of this is given in Section 1.2.2).

Human activities such as fossil fuel combustion and land use change have led to dramatic increases in atmospheric greenhouse gas concentrations. Model simulations using

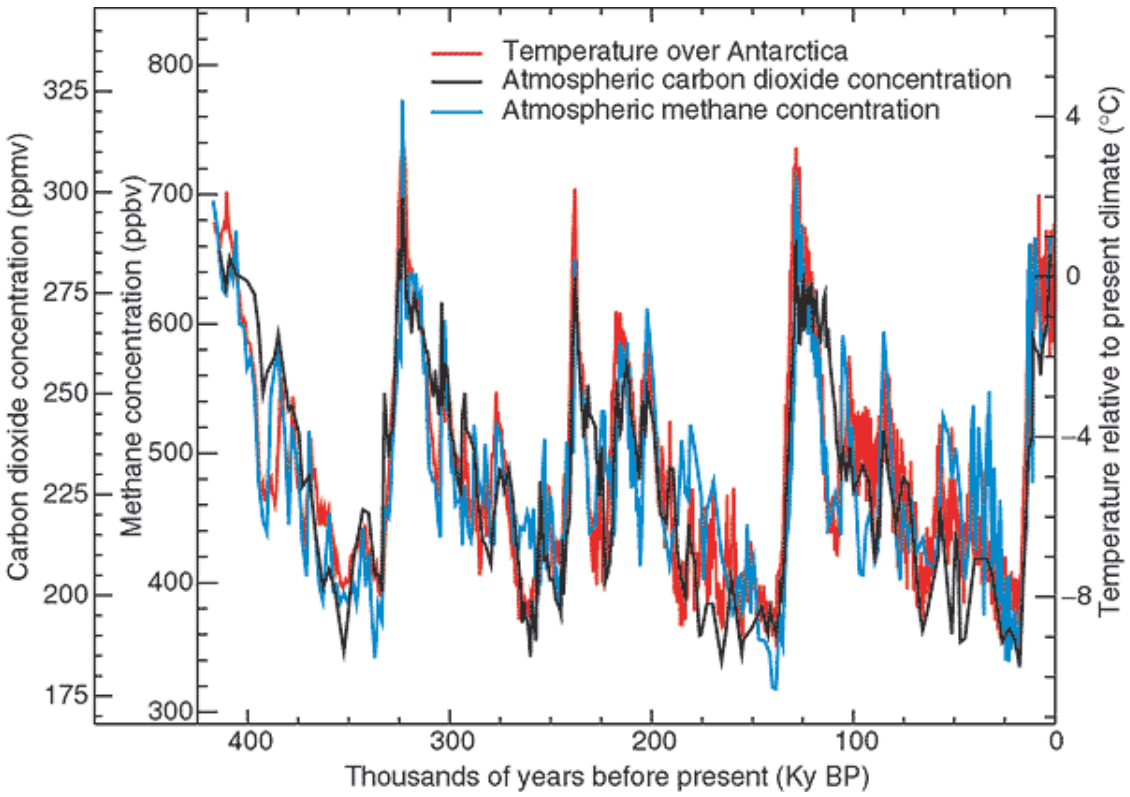

FIGURE 1.3. Antarctic ice core measurements of temperature, methane and carbon dioxide concentrations. Figure taken from IPCC (2001).

knowledge of the climate system predict that this will lead to increased global warming and future climate change. Model projections from the IPCC First Assessment Report (FAR) (IPCC 1990) and the Second Assessment Report (SAR) (IPCC 1996) estimated global mean temperature increases of $\sim$0.3 K and $\sim$0.15 K per decade respectively, with SAR including cooling effects from aerosols. The Third Assessment Report (TAR) (IPCC 2001) suggested a similar projection as SAR. These projections have been compared to recent observations that show an increase of $\sim$0.2 K per decade, see Figure 1.4, showing the projections to be generally reasonable (IPCC 2007).

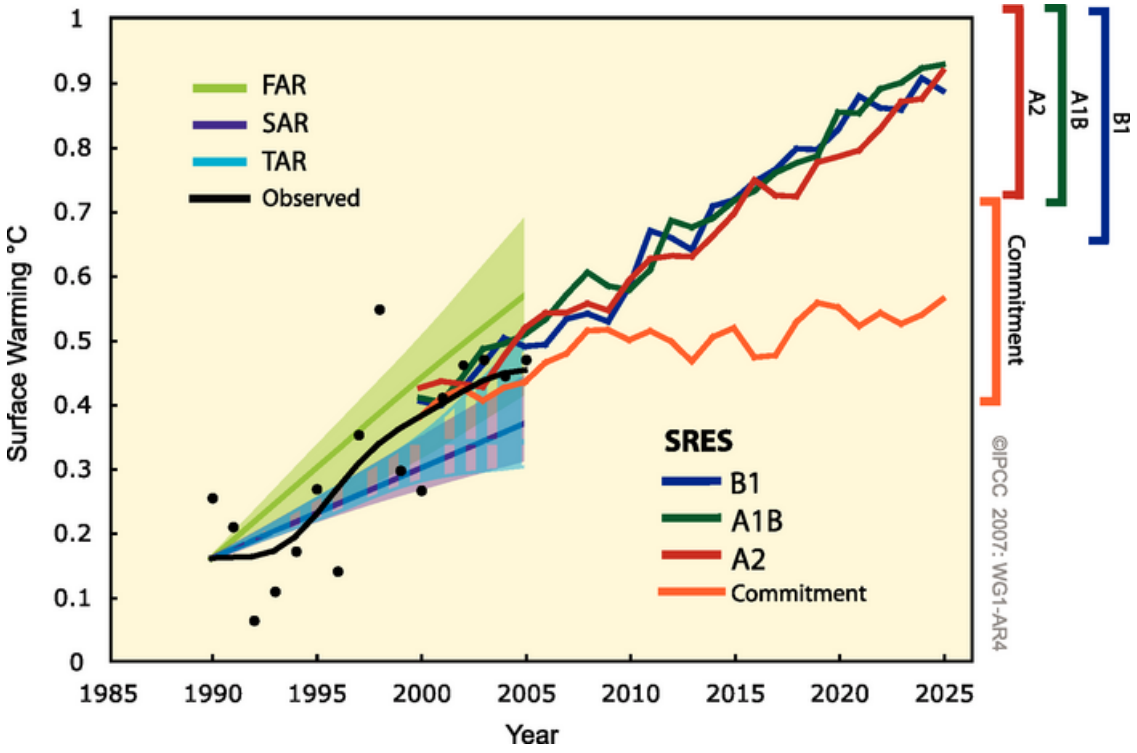

FIGURE 1.4. Observed global mean surface warming compared to model projected trends and ranges from the IPCC First (FAR), Second (SAR) and Third (TAR) Assessment Reports. B1 (blue) , A1B (green), and A2 (red) represent the mean projected trends and ranges from multiple model scenarios and the commitment (orange) shows the mean predicted trend and range if greenhouse gas and aerosol concentrations were held constant from the year 2000. Figure taken from IPCC (2007).

1.2.1 Radiative Budget

The Earth absorbs and reflects radiation from the Sun and emits infra-red radiation towards space. For the Earth to be in dynamic equilibrium the incoming and outgoing radiation must be of equal energy, which would result in a constant planetary temperature. The incoming solar flux energy intercepted by the day-side of the Earth's surface, F_i, per second can be written as

$$F_i = F_s\,(1 - A)\,\pi R_e^2 \tag{1.1}$$

where F_s is the solar flux constant (1368 $Js^{-1}m^{-2}$), R_e is the radius of the Earth (6.38x10^6 m), and A is the Earth's albedo, representing the fraction of solar flux that is reflected from the Earth's surface. The outgoing infra-red radiation F_o per second from the entire Earth's surface is

$$F_o = 4\pi R_e^2 \epsilon S T_e^4 \tag{1.2}$$

where ϵ is the surface emissivity, S is Stefan's constant (5.67x10^{-8} $Js^{-1}m^{-2}K^{-4}$) and T_e is the temperature of the Earth. Balancing the incoming and outgoing radiation, using the Stefan-Boltzmann law, gives the temperature of the Earth as

$$T_e = \left[\frac{F_s\,(1 - A)}{4\epsilon S}\right]^{1/4} \tag{1.3}$$

If the Earth is assumed to be a black body, whose emissivity equals 1, with an albedo of 30$\%$, then the temperature of the Earth would be about 256 K. However, observations have shown that the temperature of the Earth is closer to a value of 290 K. This elevation in temperature is caused by the greenhouse effect.

1.2.2 Greenhouse Effect

Excluding anthropogenic contributions, the greenhouse effect raises the temperature of the Earth to a level that is vital for many habitats. Essentially, the emitted infra-red radiation from the Earth's surface becomes absorbed by atmospheric molecules and is re-emitted in all directions, such that some will be re-absorbed by the Earth's surface causing the surface temperature to increase. These atmospheric molecules correspond to

gases with absorption bands in the infra-red wavelength range and are known as greenhouse gases, as described in Table 1.1. Water vapour is by far the most abundant greenhouse gas but has a very short lifetime of ∼8 days in the atmosphere (Trenberth 1998). However, all other greenhouse gases exist for many years in the atmosphere so can contribute to the greenhouse effect for prolonged periods (IPCC 2001).

Table 1.1. The main greenhouse gases and their quantities during a pre-industrial time (1700-1800) compared to 1998 (IPCC 2007).

Gas	Chemical Formula	Pre-Industrial Level	2005 Level
Water Vapour	H_2O	∼0.03	∼0.03
Carbon Dioxide	CO_2	280 ppm	379 ppm
Methane	CH_4	715 ppb	1774 ppb
Nitrous Oxide	N_2O	270 ppb	314 ppb
Ozone	O_3	24 ppb	34 ppb
Chlorofluorocarbons,	CFC-11	0 ppt	251 ppt
	CFC-12	0 ppt	538 ppt
	CFC-113	0 ppt	79 ppt
Hydrochlorofluorocarbons	HCFC-22	0 ppt	169 ppt
	HCFC-141b	0 ppt	18 ppt
	HCFC-142b	0 ppt	15 ppt
Methyl Chloroform	CH_3CCl_3	0 ppt	19 ppt
Carbon Tetrachloride	CCl_4	0 ppt	93 ppt
Hydroflurocarbons	HFC-125	0 ppt	3.7 ppt
	HFC-134a	0 ppt	35 ppt
	HFC-152a	0 ppt	3.9 ppt
	HFC-23	0 ppt	18 ppt
Perflurorocarbons	CF_4 (PFC-14)	0 ppt	74 ppt
	C_2F_6 (PFC-116)	0 ppt	2.9 ppt
Sulphur Hexafluoride	SF_6	0 ppt	5.6 ppt

Since the start of the industrial revolution the atmospheric concentrations for some of these gases have rapidly increased leading to an enhanced greenhouse effect, hence higher planetary temperature. To demonstrate this, consider a single gas layer consisting of only greenhouse gases that is above a surface, as shown in Figure 1.5. Greenhouse gases are transparent to the incoming radiation that consists of ultra violet (UV) and visible (VIS) wavelengths, but absorb the outgoing infrared radiation. Consider the surface to be a black body that absorbs the incoming solar flux and emits infrared radiation.

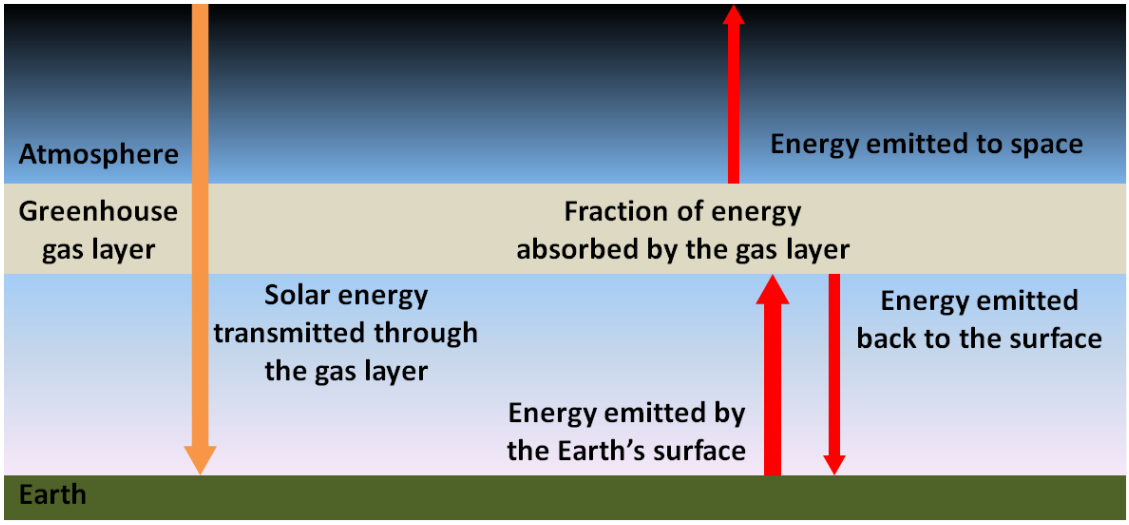

FIGURE 1.5. Illustration of a single gas layer.

The energy received by the surface is the sum of the solar energy and the energy directed back to the surface from the gas layer, it can be expressed as

$$ST_g^4 = ST_s^4 + fST_a^4 \tag{1.4}$$

where f is the fraction of outgoing infra-red radiation absorbed by the gas layer and T_g, T_s and T_a are the temperatures of the surface, solar flux and atmosphere respectively. The radiative balance of the atmosphere can be simplified to be

$$fST_g^4 = 2fST_a^4 \tag{1.5}$$

where the energy emitted from the surface is expressed by the left term of Equation 1.5 and the right term represents the sum of the energy that is absorbed by the gas layer and then re-emitted partly to space and partly to back towards the surface. By substitution the surface temperature is given as

$$T_g = \left[\frac{T_s^4}{\left(1 - \frac{f}{2}\right)}\right]^{1/4} \tag{1.6}$$

If we assume f to be 0.75 then the surface temperature would be 30 K larger than without any gas layer. Additionally, if there was a higher concentration of greenhouse gases, then the fraction of outgoing radiation absorbed would be higher. For example, if

we assume f to rise from 0.75 to 0.8 then the corresponding surface temperature would increase by 2 K.

1.2.3 Radiative Forcing

One way to assess and compare anthropogenic and natural drivers of climate change is through radiative forcing. The radiative forcing value is defined as the change in the average net irradiance at the tropopause (IPCC 2001) that occurs solely due to a driver of climate change. Radiative forcing, RF, can be related linearly to the global mean surface temperature change, $\Delta \mathrm{T}_g$, by

$$\Delta T_g = \lambda \mathrm{RF} \tag{1.7}$$

where λ is the climate sensitivity parameter (IPCC 2007). Thus, a positive radiative forcing value would indicate the surface warms on average and a negative value would indicate a cooling effect on the surface. The radiative forcing for human influenced drivers are shown in Figure 1.6, with greenhouse gases all being positive because they absorb part of the outgoing radiation from Earth to space. Notably, CO_2 gives the largest radiative forcing and its production is largely due to human activities.

However, radiative forcing does not take into account the temporal, spatial and vertical variations nor the lifetime of each driver of climate change. Therefore, to be able to evaluate the potential climate change caused by anthropogenic emissions an alternative method is required. Global Warming Potentials (GWPs) are one technique for assessing these.

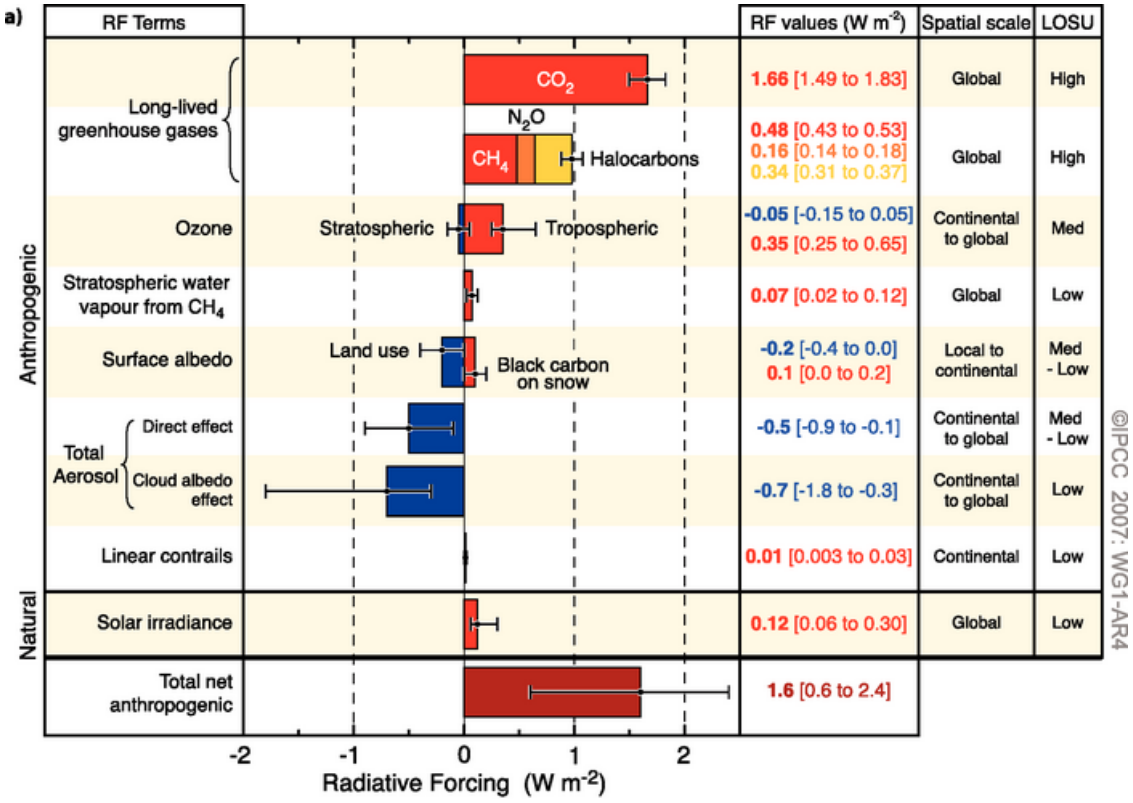

FIGURE 1.6. Overview of the main components of radiative forcing with values representing the forcings in 2005 with respect to a pre-industrial age of about 1750. The black error bars give the range of uncertainty of the radiative forcing value. Figure taken from IPCC (2007).

1.2.4 Global Warming Potential

Strategies to limit anthropogenic climate change require a structure and comparative quantification of the emissions of climate drivers. Global Warming Potentials are the currently accepted method used to implement policies (NATIONS 1998) to allow multiple anthrogenic emitters (e.g. industrial companies or countries) to impose reductions of those emissions by the substitution of climate drivers, according to the specified emission constraints (IPCC 2007). Although alternative methods have been designed (Kandlikar 1996, Hammitt & Adams 1996, Tol 2002, den Elzen & Lucas 2005) these include some problematic issues so the simpler GWP method was developed and adopted for use in the Kyoto Protocol (IPCC 2007). This compares the time-integrated global mean radiative forcing of a 1 kg emission of the driver relative to that of CO_2, which can be defined by

$$\mathrm{GWP}_i = \frac{\int_0^{TH} \mathrm{RF}_i\,(t)\,dt}{\int_0^{TH} \mathrm{RF}_r\,(t)\,dt} - \frac{\int_0^{TH} a_i\,[C_i\,(t)]\,dt}{\int_0^{TH} a_r\,[C_r\,(t)]\,dt} \tag{1.8}$$

where RF is the radiative forcing, a is the radiative efficiency that is defined as the RF per unit mass increase in atmospheric abundance, C(t) is the time-dependent abundance, TH is the time horizon (i.e. 100 years in Kyoto Protocol), i represents the climate driver considered, and r is the reference (i.e. CO_2). This method clearly gives a GWP of 1 for CO_2, whilst for other gases such as CH_4 and N_2O have GWPs of 21 and 310 respectively. The GWP of Halocarbons varies from 90 to 11700 and the GWP of Sulphur hexafluoride is even higher with a value of 23900 (IPCC 2007). Although other substances have higher GWPs than CO_2 their abundances and emissions are far lower.

1.3 Role of CO_2

Other than water vapour, CO_2 is by far the most abundant greenhouse gas in the atmosphere contributing largely to global warming (IPCC 2007). In the absence of anthropogenic CO_2 emissions, the carbon cycle had periods of millennia where large carbon exchanges were in near balance, implying nearly constant reservoir contents (IPCC 2007). The addition of fossil fuels as anthropogenic CO_2 into the atmosphere has caused some carbon exchanges to become unbalanced. To this extent, atmospheric CO_2 concentrations have risen from a pre-industrial level of 280 ppm to a current level of about 385 ppm (IPCC 2007), as shown in Figure 1.7. Temperature has also increased over this period, as shown in Figure 1.2, correlating with increased anthropogenic emissions of greenhouse gases (IPCC 2007).

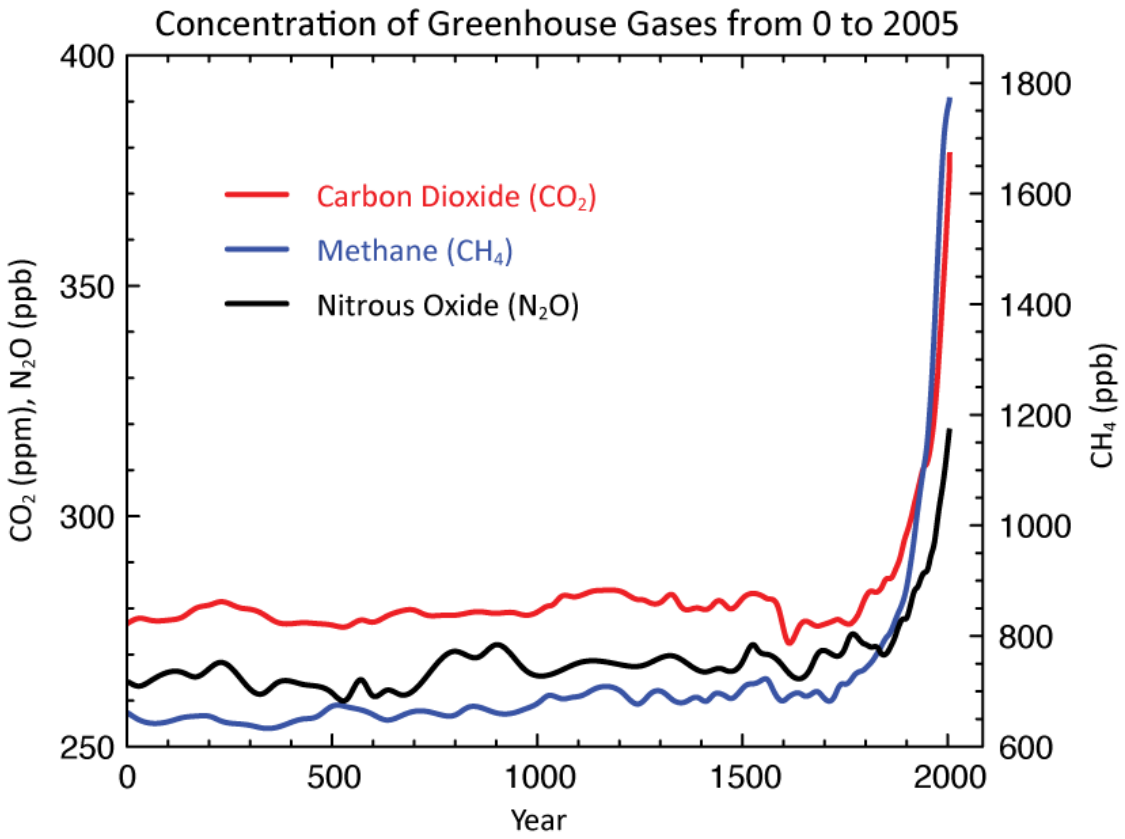

FIGURE 1.7. Atmospheric concentrations of CO_2, CH_4 and N_2O over the last 2 miilenia, showing rapid increases since about 1750 that are attributed to human activities during the industrial revolution. Figure taken from IPCC (2007).

To improve global warming projection models, accurate knowledge of greenhouse gases is required, especially that of CO_2 which is the largest anthropogenic contributor. An overview of the current understanding of the carbon dioxide cycle is given in Figure 1.8.

The combustion of fossil fuels has increased rapidly since the start of the industrial revolution, emitting large amounts of anthropogenic CO_2. Fossil fuels are the remains of dead organisms that have undergone anaerobic decomposition. Coal is typically formed on land where waterlogged soil inhibits aerobic decomposition or where organisms are buried deep in soil quickly. Oil and natural gas are normally formed at the bottom of the ocean where the water transport is very slow. Over millions of years the pressure and heat created by the weight of the sediment above causes the remains to become compacted and takes the form of the fossil fuels. When fossil fuels are combusted they produce CO_2

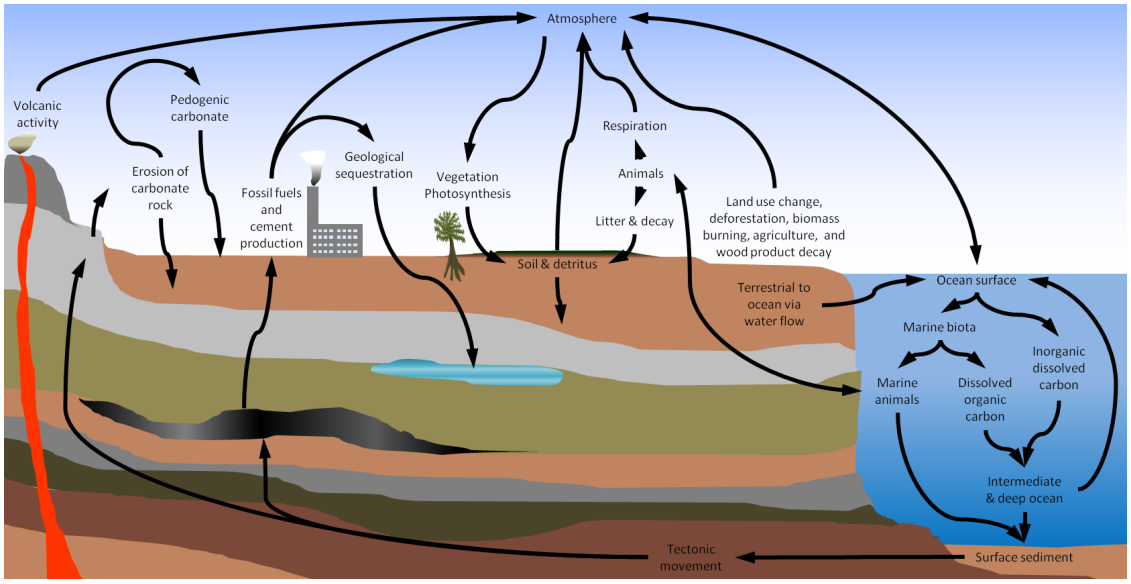

FIGURE 1.8. Diagram showing an overview of the main carbon dioxide cycle features.

and the simplest example of this is for pure coal where the chemical reaction is

$$C + O_2 \rightarrow CO_2 + hv \tag{1.9}$$

and hv represents the energy released. Another example is that of natural gas which has the reaction

$$CH_4 + 2O_2 \rightarrow CO_2 + 2H_2O + hv \tag{1.10}$$

Cement production is also a large source of anthropogenic CO_2, accounting for about 5% of global emissions (Pade & Guimaraes 2007). The production process requires fossil fuel combustion and the conversion of limestone to Calcium Oxide (CaO) and CO_2 (Pade & Guimaraes 2007), called calcination. However, if cement products are exposed to the atmosphere then CO_2 will diffuse back into the cement, forming Calcium Carbonate ($CaCO_3$) (Pade & Guimaraes 2007). This process is known as carbonation and over 100 years carbonation CO_2 uptake can account for most of the CO_2 released from calcination, acting as a sink of atmospheric CO_2 (Pade & Guimaraes 2007).

Animals produce CO_2 through respiration when the oxygen breathed in reacts with carbohydrates in the presence of enzymes in cells to produce CO_2, H_2O and energy (hv), as shown by

$$C_6H_{12}O_6 + 6O_2 \rightarrow 6CO_2 + 6H_2O + hv \tag{1.11}$$

Photosynthesis of vegetation is essentially the reverse of this chemical reaction and cap-

tures CO_2. However, photosynthesis only occurs for a lot of vegetation in the spring/ summer when they are growing, whilst in autumn/winter time they form litter on the ground which undergoes biological decomposition that returns most of CO_2 to the atmosphere. Also, some vegetation is eaten by animals, transferring the carbon to the animals which eventually will decay and contribute CO_2 to the soil and atmosphere.

The top layer of soil is composed of litter or detritus, in which carbon only has a lifetime of about 1 year due to microbial decay and erosion. The soil underneath comprises of $\sim 5\%$ living microbial biomass and $\sim 95\%$ humic material, which is a metabolic by-product of microbial activity. This has been found to be hundreds of thousands of years old, whilst the soil near the surface typically has a cycle of 30 years (Wigley & Schimel 2000). Soil carbon is released with increasing temperature and so acts as an additional global warming feedback (Fang & Moncrieff 2001). Thus, storage of carbon in soils generally increases from low to high absolute latitudes due to slower decomposition of dead plant material in colder environments. Additionally, the carbon stored in frozen soils and permafrost can be released as CO_2 by microbial aerobic respiration under warming temperature conditions (Lee et al. 2010). Flooded soils, where oxygen becomes depleted, have extremely low rates of decomposition and may accumulate large amounts of organic matter as peat (Wigley & Schimel 2000). Also, some soil is found as charcoals, especially where fires are frequent, although it is currently unknown how much carbon exists there (Ohlson et al. 2009).

The change in land use can cause CO_2 to be released into the atmosphere. Deforestation often includes the burning of vegetation and soil which produces CO_2, and removes the capture of CO_2 by photosynthesis. Carbon is released during logging from the decay of trees damaged in the harvest, decay of logging debris, and oxidation of wood products (Hoscilo et al. 2011). If the forest is allowed to regrow then the long term net carbon loss would be zero, providing no biomass burning takes place. However, sometimes when logging occurs artificial rivers are created to transport the logged trees, thus lowering the existing water table causing the top soil/vegetation to become dry. This in turn increases the probability of biomass burning events occurring, that produce even more CO_2 (Hoscilo et al. 2011). Agriculture both requires the land to be changed initially via deforestation, releasing CO_2, and then the soil repetitively undergoes tillage which causes additional CO_2 to be released from the soil (e.g. Paustian et al. 2000, Jr. et al. 2005).

Biomass burning can occur naturally and artificially, across large areas of the world. This has been observed by the National Aeronautics and Space Administration (NASA) Moderate Resolution Imaging Spectroradiometer (MODIS) which showed that biomass burning happened over $\gtrsim 2\%$ of land globally between July 2001 to June 2002 (Roy

et al. 2008). The amount of global fires remained reasonably constant between 2002 and 2007, and declined during 2008 and 2009 by about 30% (van der Werf et al. 2010). The main compound emitted from biomass fires is CO_2. For efficient fires CO_2 can account for $\sim$99% of emissions, whilst smoldering fires could emit slightly less ($\sim$90%) CO_2 (Wooster et al. 2011). Carbon monoxide (CO) is the next dominant compound released from fire emissions which can further react to produce more CO_2 by

$$CO + OH \rightarrow CO_2 + H \tag{1.12}$$

The oceans contain $\sim$50 times that of atmospheric CO_2 and $\sim$95% of it is in the form of inorganic dissolved carbon; bicarbonate ($HCO_3{}^-$) and carbonate ions ($CO_3{}^{2-}$) (Wigley & Schimel 2000). The rest is composed of organic carbon, consisting of living organic matter, particulate and dissolved organic carbon (Wigley & Schimel 2000). Terrestrial CO_2 can be transported to the oceans via the water flow in rivers. Additionally, CO_2 is transferred between the atmosphere and ocean via the air-sea interface, where it changes between atmospheric and dissolved CO_2 as

$$CO_{2(\text{Atmospheric})} \rightleftharpoons CO_{2(\text{Dissolved})} \tag{1.13}$$

The dissolved CO_2 converts to carbonic acid and vice versa by the reaction

$$CO_{2(\text{Dissolved})} + H_2O \rightleftharpoons H_2CO_3 \tag{1.14}$$

The carbonic acid can convert to bicarbonate and carbonate ions by the ionizations

$$H_2CO_3 \rightleftharpoons H^+ + HCO_3^- \tag{1.15}$$

and

$$HCO_3^- \rightleftharpoons H^+ + CO_3^{2-} \tag{1.16}$$

CO_2 is transported into the intermediate and deep ocean by water mass transport where it can be stored for long durations. However, due to ocean circulations there is also a source created from upwelling water (Wigley & Schimel 2000). Phytoplankton exists near the ocean surface where it absorbs CO_2 via photosynthesis (Follows et al. 2007). Zooplankton feed on phytoplankton and in turn get eaten by larger marine organisms (Stige et al. 2011). These organisms will normally die and sink to the bottom of the ocean, but with a growing human population increasing numbers of these are fished and eaten by terrestrial animals, so the carbon can contribute to both the soil and atmosphere

subsequently. Bicarbonate can be converted to marine shell material that eventually sinks to the ocean floor, fossilizing to become carbonaceous rock.

In some regions, such as arid and semi-arid climates, the underlying geology often consists of carbonate rock. All surfaces undergo erosion, whether it be from precipitation, wind blown particle impacts, contraction/expansion due to temperature, ice formation, geological factors, biological factors, or land use change. When carbonate rock is broken down it releases inorganic carbon ($CaCO_3$) into the atmosphere, this process is known as pedogenic carbonate which becomes precipitated back to the surface (Wigley & Schimel 2000). However, the pedogenic carbonate can be transported in the atmosphere with the prevailing winds to an area of non-carbonate terrain, providing a net sink of carbon from the atmosphere (Wigley & Schimel 2000).

CO_2 has been previously measured from volcanoes (Ryan 2001) and is known to be emitted in volcanic gas (Shinohara et al. 2011) as a consequence of decarbonation of underlying carbonate rocks (Frondini et al. 2004). There are a number of difficulties in measuring CO_2 from volcanoes. For ground based observations this mainly includes the inaccessibility and risk of taking measurements at the summits and the high level of background CO_2 concentrations (Spinetti et al. 2008). Whilst airborne observations overcome most of these problems, both techniques have trouble measuring CO_2 within a volcanic plume (Burton et al. 2000).

One method to reduce the current levels of CO_2 is the enhancement of natural sinks. Forests and soils could be increased to sequester CO_2 , however this requires a large land mass (Chadwick et al. 2000) which would cause competition with agriculture. Also, the CO_2 captured by trees would only last for $\sim$100 years and that is provided that the area does not undergo deforestation, logging, biomass burning or that it becomes unsuitable for forestry due to increasing temperatures from climate change (Baines & Worden 2004). Agricultural techniques could be modified to enhance soil CO_2 sequestration but this would not be a permanent sink (IPCC 2007). Although these natural sinks could be increased, it is not a feasible method to use for large scale reductions in CO_2.

Geological sequestration is another way that is currently being used to reduce CO_2 concentrations. This method is capable of lowering fossil fuel emissions by over 80% (Freund 2003) but has two disadvantages; it requires energy (so fossil fuels are depleted quicker) and the CO_2 has the potential to leak back into the atmosphere, possibly leading to future climate change events (Keller et al. 2008). The rate of CO_2 leaking depends on where it is geologically stored (Freund 2003). Deep oceans will take centuries to leak. Whilst geological reservoirs have a much longer timescale of millennia and sequestration in thermodynamically stable minerals will take even longer to leak (Freund 2003,

Lackner 2003).

1.4 Observations of CO_2

Observations of CO_2 can be made on a local scale and the scaled up to estimate regional carbon fluxes, which are useful for land management and emission policies (Wofsy & Harriss 2002). This bottom-up method can be limited by the distribution of observations, and regional scaling can be difficult where multiple ecosystem types, heterogeneous terrain or urban areas exist (Desai et al. 2008, Dolman et al. 2009, Riley et al. 2009). Alternatively, regional estimates can be made using a top-down approach, by scaling down global surface flux estimates which are based on atmospheric observations of CO_2 (Ahmadav et al. 2009, Gurney et al. 2002a). Top-down observations have previously been limited to continental scales due to the complexity of regional carbon fluxes (Desai et al. 2010). However, with improvements in remote sensing technologies, top-down observations are approaching the point where they may be useful for the estimation carbon fluxes on a sub-continental scale, which this thesis focases on.

CO_2 has been measured in the atmosphere directly since 1957 (Wigley & Schimel 2000). The concentration and isotope records before then consist from evidence of ice cores, moss cores, packrat middens, tree rings, and isotopic measurements of plantonic and benthic foraminifera (Wigley & Schimel 2000). The longest record of atmospheric CO_2 concentrations is at Mauna Loa, which was started at the Institute of Oceanography in 1958. The National Oceanic and Atmospheric Administration (NOAA) has continued to measure in parallel here since 1974 until present (Tans & Keeling 2012). This is shown in Figure 1.9 which clearly shows the annual increase and seasonal cycle of CO_2.

In recent years there have been many in-situ measurements made from instruments such as ground based, tower, and aircraft observations. These have been collected into the GLOBALVIEW-CO2 product, as a Cooperative Atmospheric Data Integration Project (Maserie & Tans 1995). This project includes the work of many organisations and is coordinated by the Carbon Cycle Greenhouse Gases Group of the NOAA, Earth System Research Laboratory (ESRL). The measurement locations of this project are shown in Figure 1.10.

Airborne measurements have previously been obtained from commercial airliners typically, which normally provide data over short distances and mostly at a single altitude (Wofsy et al. 2010). However, the HIAPER Pole-to-Pole Observations (HIPPO) programme has taken a sequence of measurements, going from North to South with vertical information (Wofsy et al. 2010). These flights were made in 2009 and 2010, and have shown both the latitudinal and vertical gradients of a number of trace gases, specifically illustrating that CO_2 has a low variability in the Southern hemisphere (Wofsy et al.

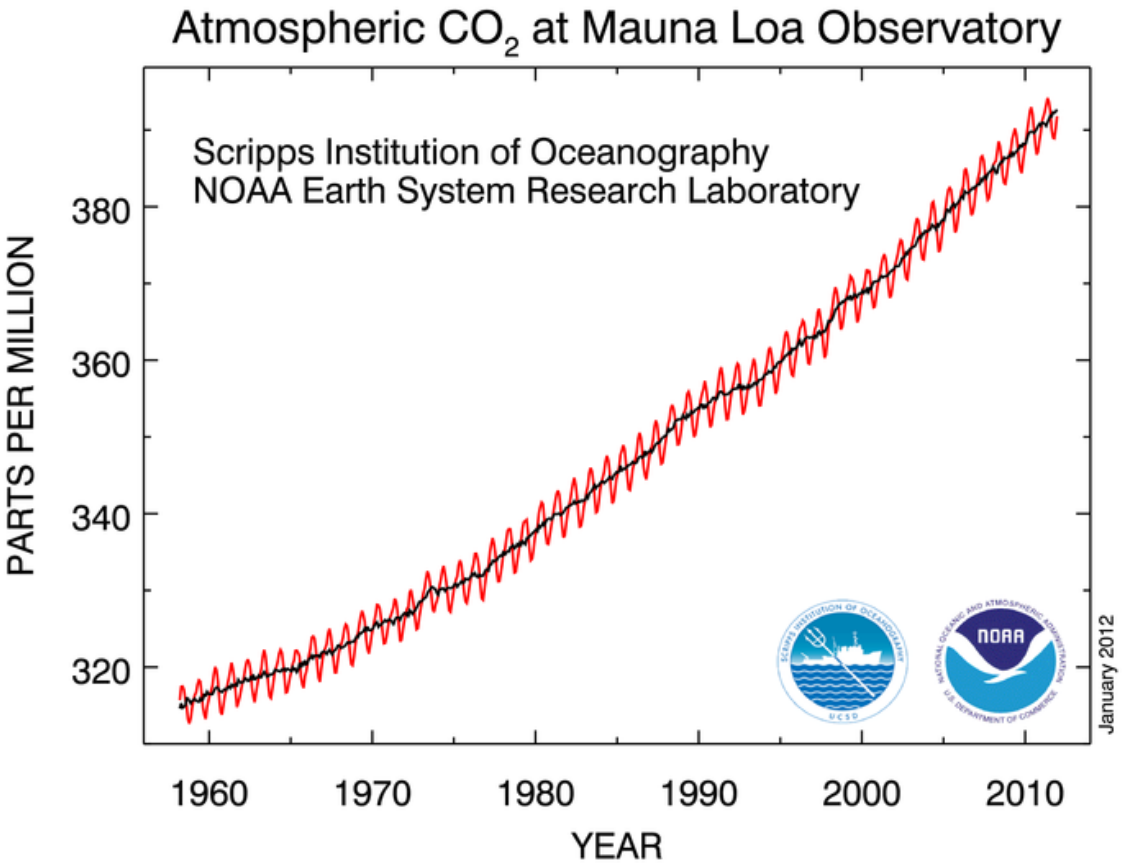

FIGURE 1.9. Atmospheric carbon dioxide concentrations measured at Mauna Loa between 1958 and 2012. The red line shows monthly data and the black line gives the monthly data corrected for a smoothed seasonal cycle (Tans & Keeling 2012).

2010).

However, due to the variability of CO_2 and lack of a comprehensive network of measurement locations, in-situ observations only allow inferred carbon fluxes on a sub-continental scale. Furthermore, their sparse and uneven distribution results in large uncertainties in the natural carbon cycle for key regions such as tropical and boreal regions (Hungershoefer et al. 2010, Gurney et al. 2002a). As shown by numerous synthetic studies, densely sampled satellite observations of CO_2 concentrations can help to reduce uncertainties in estimated regional carbon fluxes if the observations have a precision of 1-2 ppm on a regional scale with no regional to continental scale geographical biases (Rayner & O'Brien 2001, Houweling et al. 2004, Chevallier 2007b, Miller et al. 2007, Feng et al. 2009, Baker et al. 2010, Hungershoefer et al. 2010, Palmer et al. 2011). Additionally,Hungershoefer et al. (2010) investigated the concept of using a larger network of ground based measurement sites, costing $\sim$200 Million Euros (roughly the same as

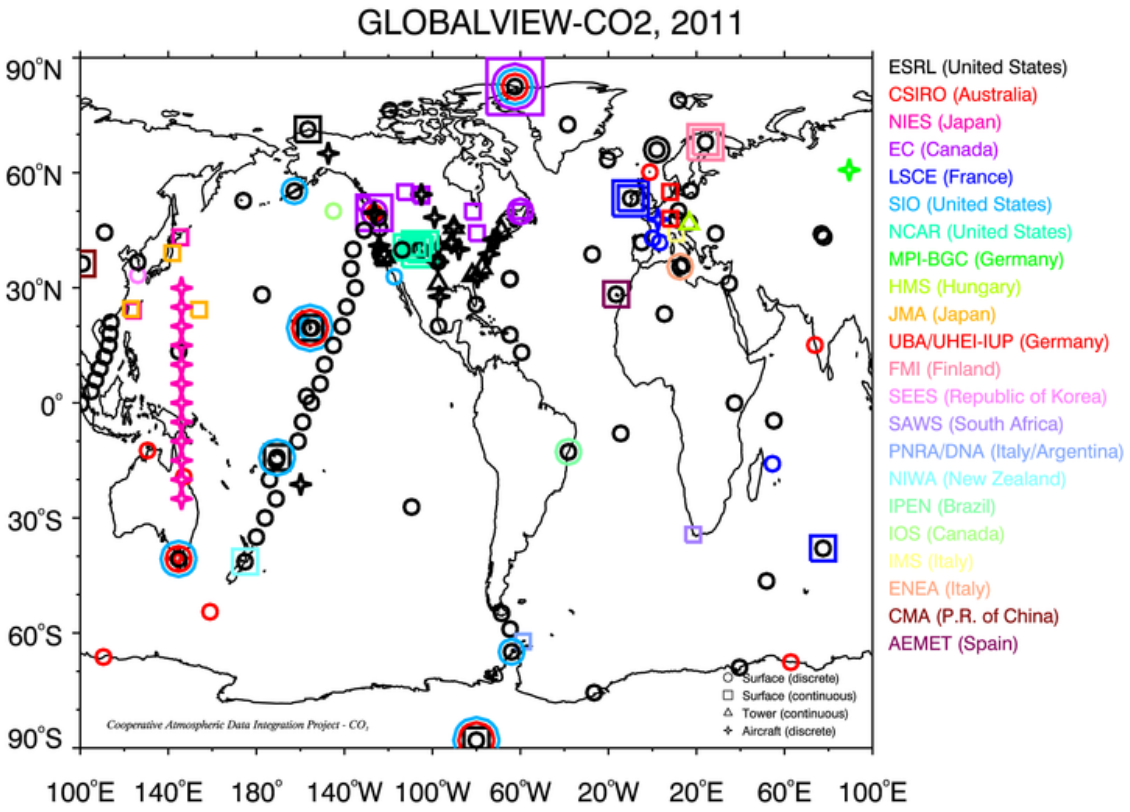

FIGURE 1.10. Current GLOBALVIEW sampling locations of instruments measuring CO_2 (GLOBALVIEW-CO_2 2011).

a satellite mission) and found that the model error reduction was far higher if satellites are used, mainly due to the fact that remote sensing by satellite observations can provide a high density of measurements globally (Hungershoefer et al. 2010). However, Palmer et al. (2011) found that the benefit of the increased number of soundings of satellite observations is reduced with more correlated data. An example of the number of satellite observations globally can been seen in Figure 1.12.

Unlike most in-situ measurements, satellites observe throughout the atmosphere rather than at a single location and altitude, giving total column average concentrations. To validate these remotely sensed observations, the Total Carbon Column Observing Network (TCCON) of ground based Fourier Transform Spectrometers (FTS) was setup to retrieve accurate and precise column averaged abundances of greenhouse gases (Wunch et al. 2011a). The locations of TCCON stations are given in Figure 1.13.

Observations of CO_2 have been made from previous satellites. One notable example is the SCanning Imaging Absorption spectroMeter for Atmospheric CHartographY (SCIAMACHY) instrument. This was launched onboard the ENVISAT satellite in

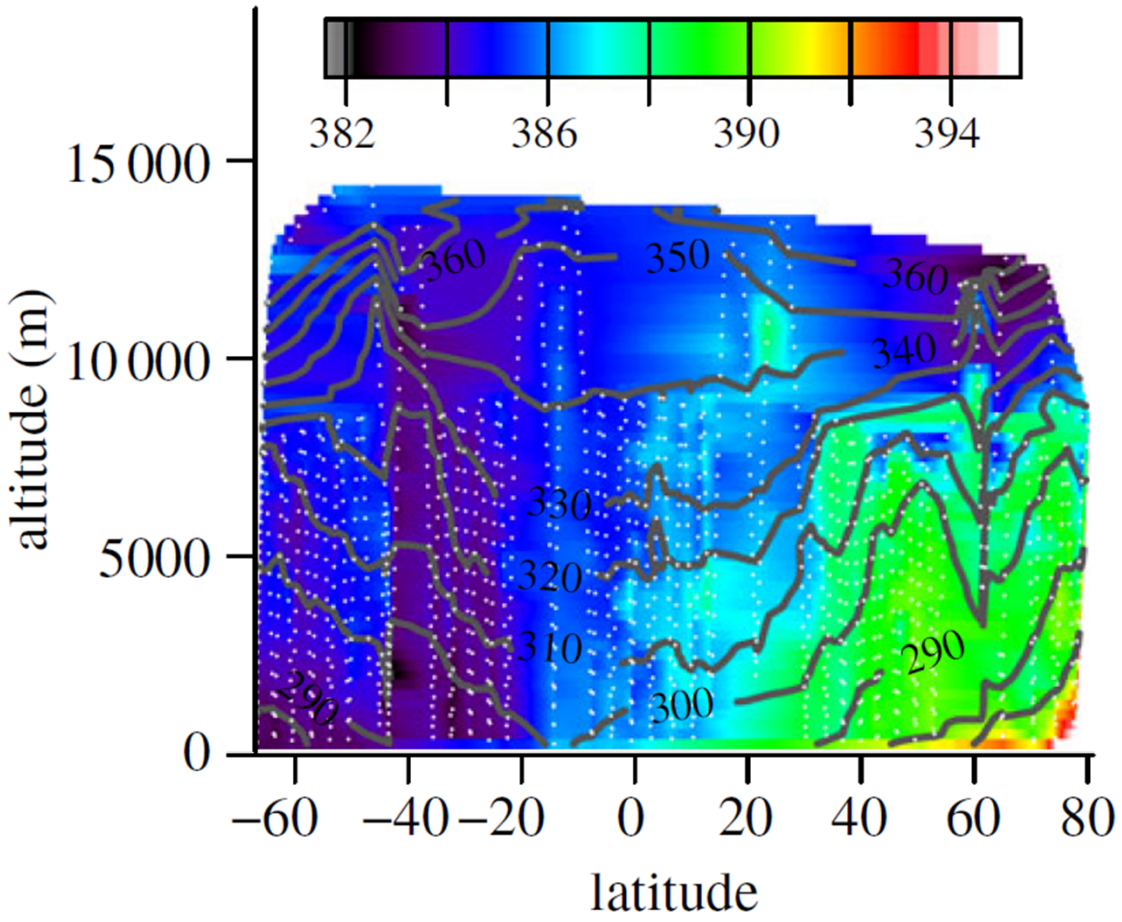

FIGURE 1.11. HIPPO 2009 CO_2 measured concentrations (ppm) for different latitudes and altitudes. The grey contour lines indicate the potential temperature. Figure taken from Wofsy et al. (2010).

March 2002 and has allowed continental and seasonal variations in CO_2 to be observed (Barkley et al. 2006a, Buchwitz et al. 2005, Scheising 2009, Schneising et al. 2008), as shown in Figure 1.14 which compares SCIAMACHY CO_2 with model CO_2 from the NOAA ESRL CarbonTracker model (Peters et al. 2007). Also, the Atmospheric Infrared Sounder (AIRS) instrument onboard the NASA Aqua satellite, launched in May 2002, has provided information about CO_2 in the upper troposphere globally, see Figure 1.15 for example. The main findings include a variability in the distribution of CO_2 with larger values observed over the northern hemispheric land masses and also a belt across the southern hemisphere, both of which were not previously incorporated in models (Chahine et al. 2008, Pagano 2011). Further details of previous satellite observations of CO_2 are given in Chapter 2.

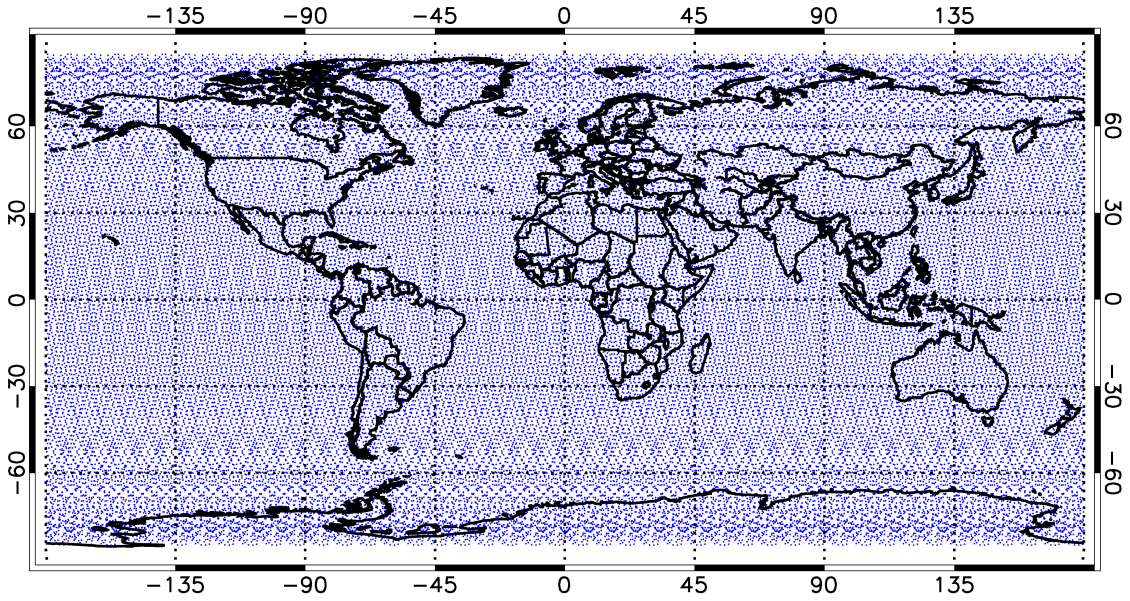

FIGURE 1.12. Nominal ground track measurement locations of the Greenhouse gases Observing SATellite (GOSAT) for a 3-day orbital repeat cycle, with each measurement location is shown by a blue circle.

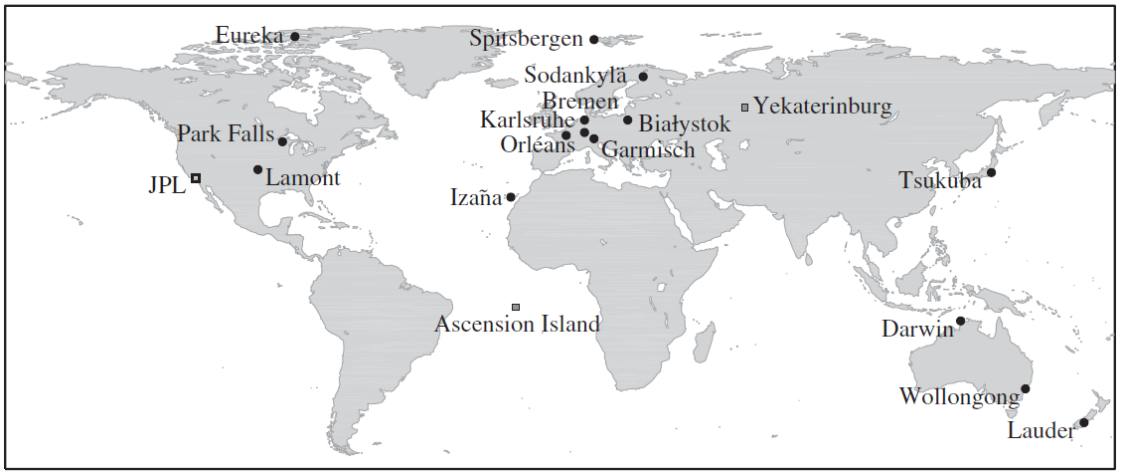

FIGURE 1.13. Current Total Carbon Column Observing Network (TCCON) sites located around the world. Figure taken from Wunch et al. (2011a).

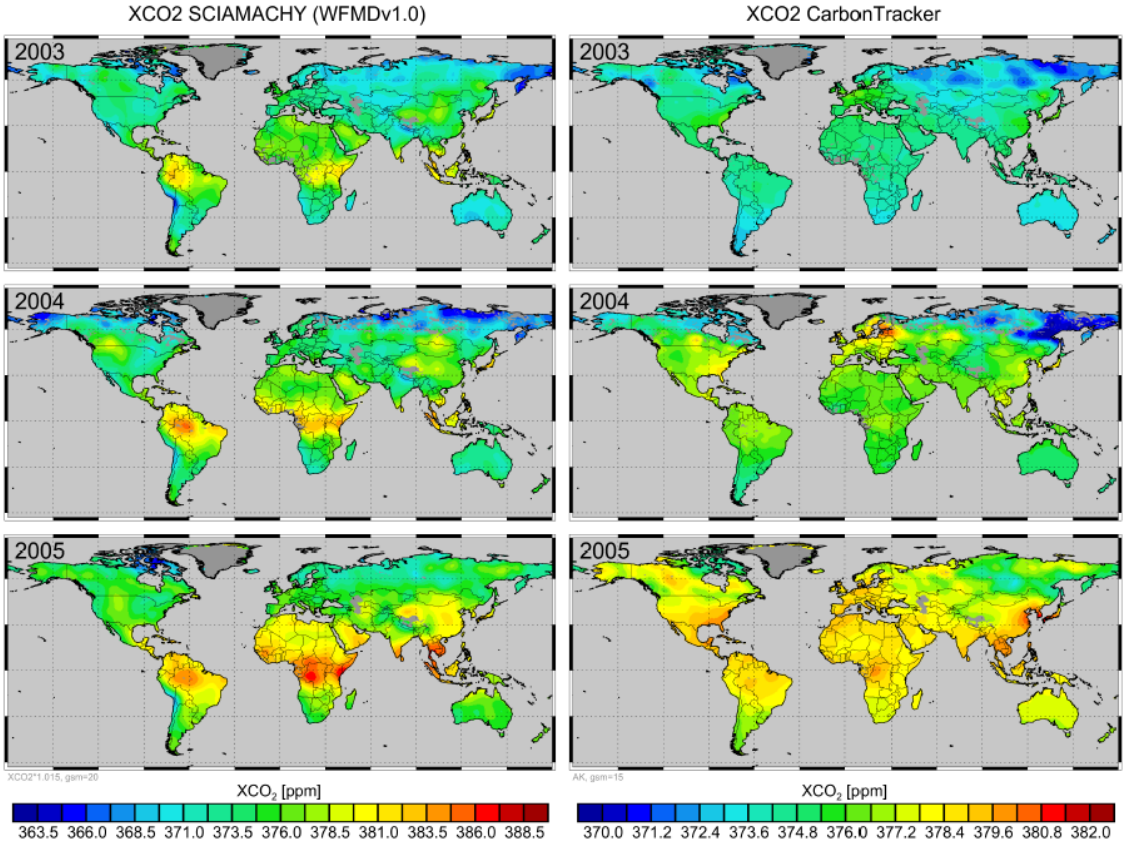

FIGURE 1.14. A comparison of column-averaged dry air mole fractions of CO_2 retrieved from SCIAMACHY using the WFM-DOAS version 1.0 (WFMDv1.0) retrieval algorithm with CarbonTracker model calculations for three years. Figure taken from Scheising (2009).

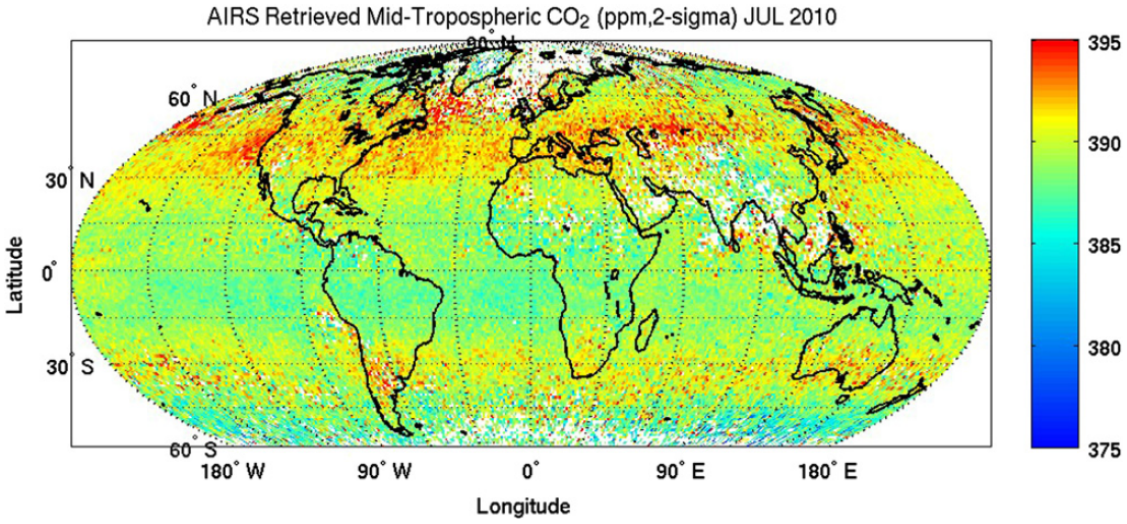

FIGURE 1.15. Monthly average mid-tropospheric CO_2 retrieved from AIRS for July 2010. Figure taken from Pagano (2011).

1.5 Current understanding of the carbon cycle

It has been established in recent decades that over half the anthropogenic CO_2 emitted into the atmosphere has been sequestered into the oceans and terrestrial biosphere, leaving the remainder in the atmosphere to accumulate (see Figure 1.16). This has lead to a rise in atmospheric CO_2 which has been observed since the start of the industrial revolution and reflects the inability of the natural carbon sinks to uptake the increased volume of atmospheric CO_2.

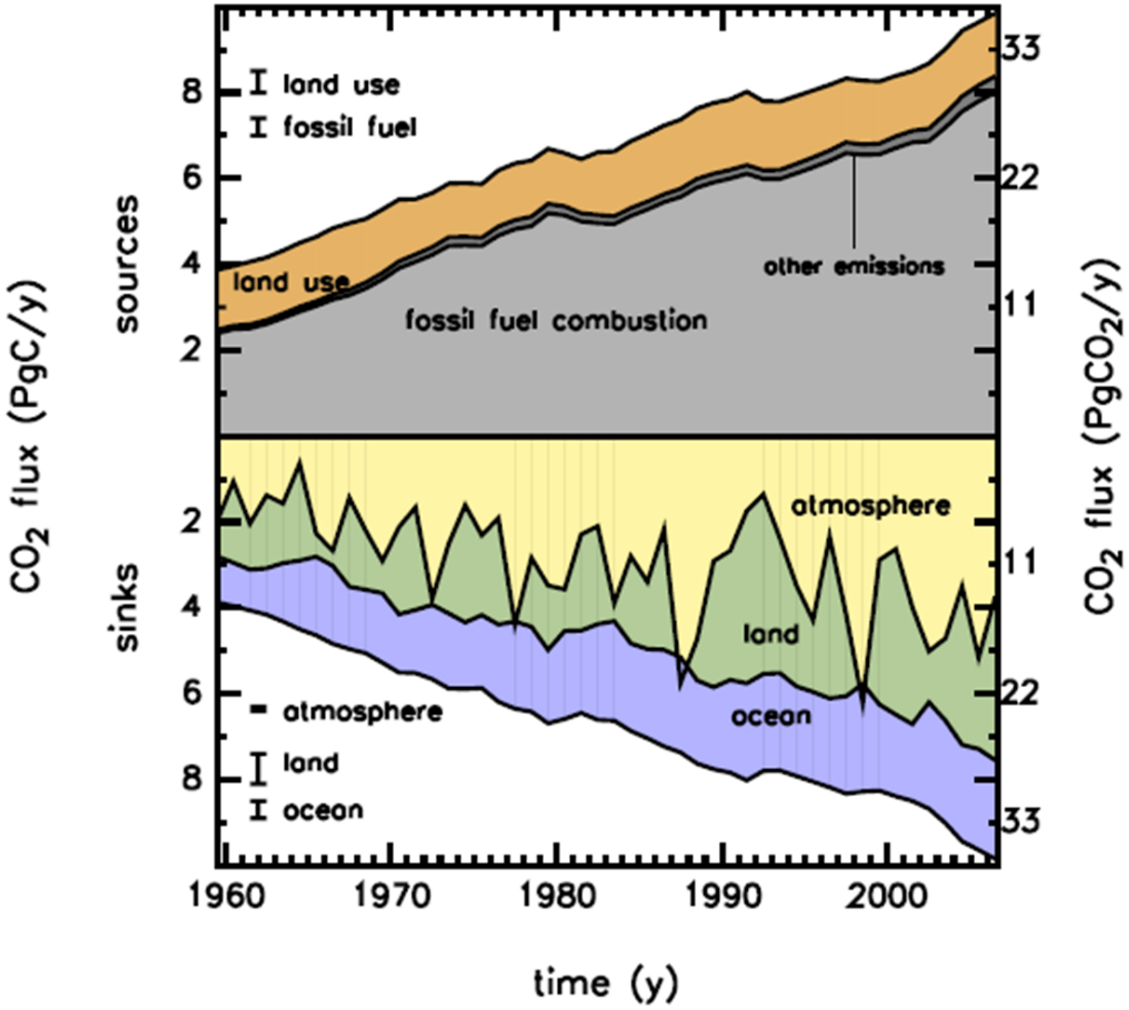

FIGURE 1.16. The budget of CO_2 between 1959 and 2006. The upper panel shows CO_2 emissions to the atmosphere as combination of fossil fuel combustion, land-use change and other emissions (primarily from cement production). The lower panel shows the resulting atmospheric, ocean and land accumulations of CO_2, where interannual variations are driven by the land sink. Figure taken from Canadell et al. (2007).

Although anthropogenic CO_2 emissions are consistently increasing, interannual CO_2 variations are observed (Figure 1.16), which are primarily controlled by changes of CO_2 flux between the atmosphere and terrestrial biophere (IPCC 2007). There is a lack of accurate quantitative knowledge of the carbon sinks, specifically their identity, strength and geographical distribution, as well as how they might change in the future and their potential feedback on the carbon-climate system (Houghton 2002, Fung et al. 2005, IPCC 2007). Also, the fraction of atmospheric CO_2 absorbed between the ocean and terrestrial sinks is highly uncertain (see Figure 1.17), with some studies suggesting the ocean sink to be dominant (e.g. Bopp et al. 2002) while others point to terrestrial reservoirs being dominant (e.g. Fan et al. 1998, Bousquet et al. 1999, Pacala et al. 2001). The uptake of carbon by the southern hemisphere oceans remains largely uncertain (Takahashi et al. 2002, McNeil et al. 2003), as does coastal ocean regions (Tsunogai et al. 1999, Muller-Karger et al. 2005). The geographical distribution of the northern hemisphere terrestrial sink has been suggested to be dominant in various regions, ranging from North America (Fan et al. 1998) to Asia (Bousquet et al. 1999).

Numerous chemistry transport models have been previously used to estimate surface-atmosphere CO_2 fluxes using inversion techniques, which assimilated in-situ CO_2 measurements from flasks, continuous sensors, tall towers and aircraft flights. The Atmospheric Tracer Transport Model Intercomparison Project (Transcom) provided an intercomparison of such models, giving estimates of the uncertainties in the net carbon fluxes from oceans and terrestrial reservoirs (Gurney et al. 2002b). The regional flux uncertainty estimates of the TRANSCOM experiment are summarised in Figure 1.18, showing that the uncertainties are large enough that most ocean and terrestrial regions could be net sources or net sinks (Gurney et al. 2002a). Furthermore, the experiment highlighted that the existing network of CO_2 measurements were too sparse and unevenly distributed, leading to an under sampled system and hence the requirement for more measurements.

Presently, large uncertainties exist for climate-carbon cycle feedback mechanisms (see Figure 1.19). It is expected that anthropogenic emissions will increase throughout the 21st century, leading to a reduced CO_2 uptake efficiency of oceans due to the carbonate buffering mechanism, and of land due to the saturation of terrestrial sinks (Friedlingstein et al. 2006). Additionally, the predicted change in future climate is estimated to suppress carbon sinks, therefore increasing the fraction of atmospheric CO_2 (e.g. Gurney et al. 2002a, Friedlingstein et al. 2006). This creates a positive climate change feedback that is highly uncertain, with current models estimating a rise in the rate of increase of CO_2 ranging between 4% and 44% (IPCC 2007).

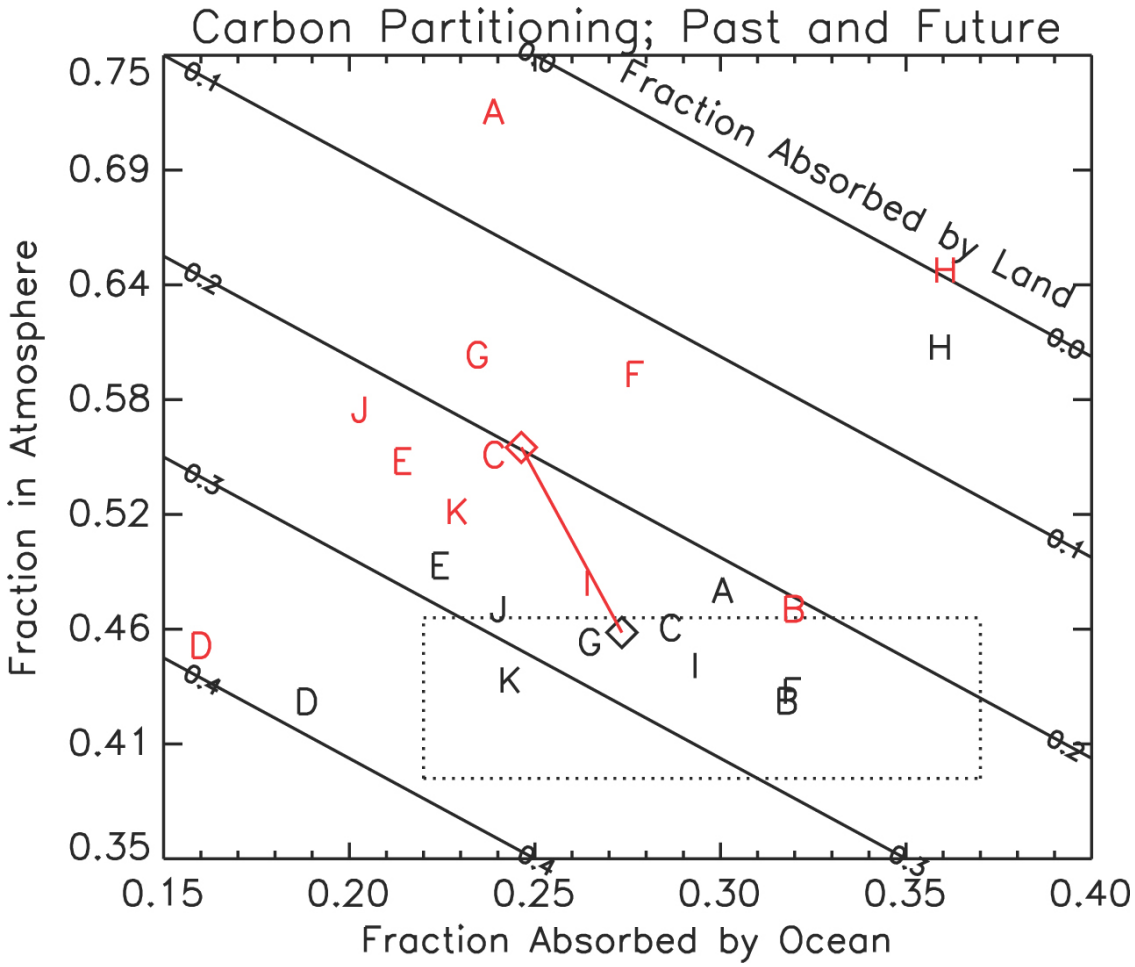

FIGURE 1.17. Fractional partitioning of the predicted increase in total emissions that contribute to atmospheric CO_2. Variations of the emissions partitioning as simulated by the C^4MIP models up to 2000 are given by black letters and for the entire simulation period to 2100 are given in red letters, where each letter represents a different model. The dotted box shows a constraint on the historical carbon balance based which was based on records of atmospheric CO_2 increase, estimates of total emissions from fossil fuel combustion and land use change, and oceanic uptake of anthropogenic CO_2 (Sabine et al. 2004). The black and red diamond symbols give the mean carbon partitioning of all the models for the historical and entire simulation periods, respectively. The red line between these diamond symbols shows the mean model tendency towards an increasing atmospheric fraction through the 21st century, which is common to all models. Figure taken from IPCC (2007).

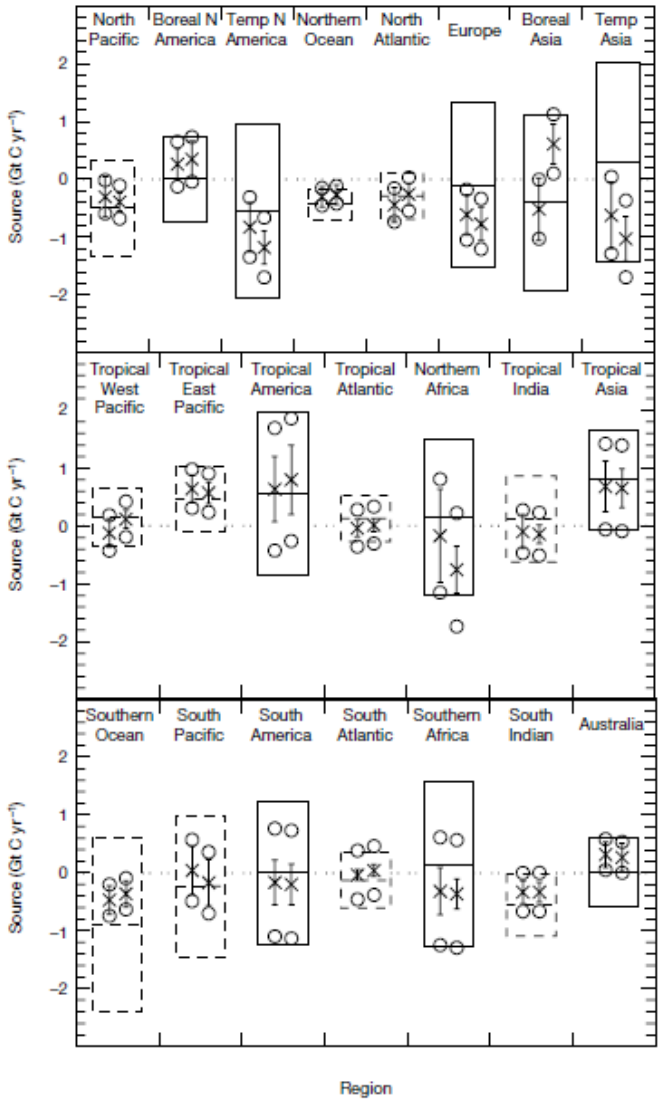

FIGURE 1.18. The mean estimated CO_2 sources and uncertainties for two different inversion models for various ocean and land regions. For each region the left-hand symbols are for a control inversion and the right-hand symbols are for an inversion without any background seasonal biosphere flux. The mean estimated flux is shown by a cross symbol, which includes all background fluxes expect fossil fuels. The circle symbols represent the mean estimated uncertainty across all models. The error bars give the standard deviation of the models' estimated fluxes. The priori flux estimates and their uncertainties are indicated by the boxes (solid for land, dashed for ocean), where the central horizontal bar gives the prior flux estimate, and the top and bottom of the box shows the prior flux uncertainty range. Figure taken from Gurney et al. (2002a).

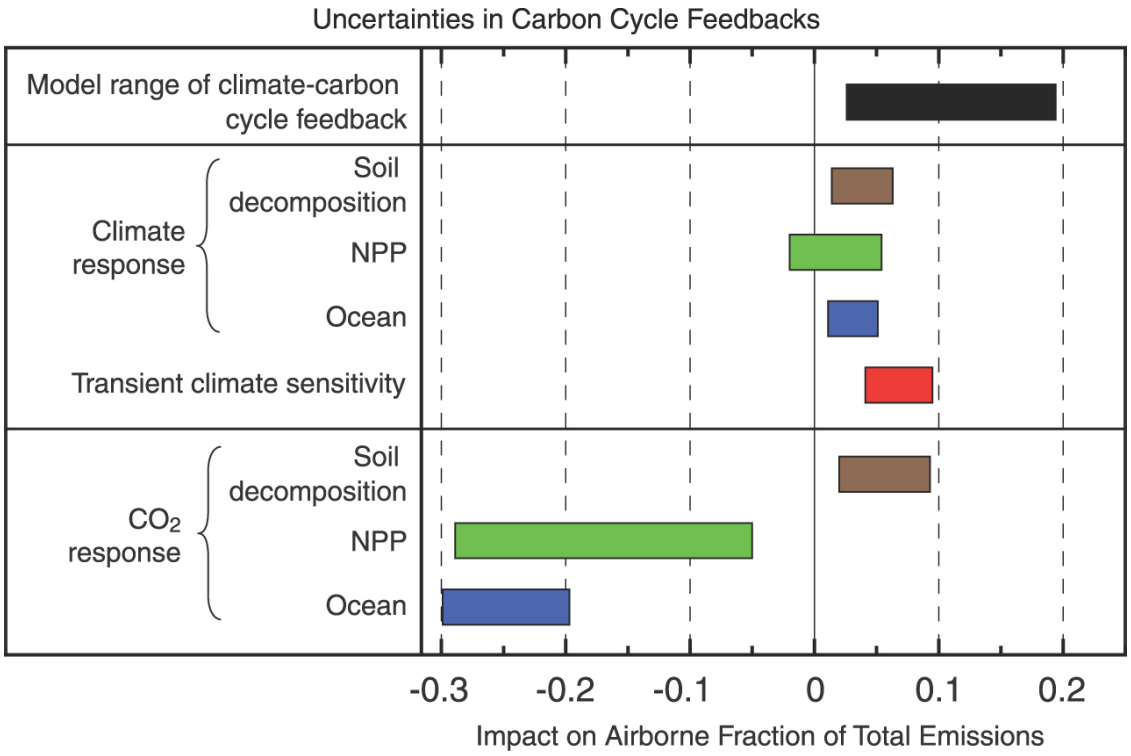

FIGURE 1.19. The uncertainties in carbon cycle feedbacks estimated from C^{4}MIP models for the simulated period of typically 1860 to 2100. The top bar shows the range that the climate-carbon cycle feedback is estimated to have on the airbourne fraction of total emissions. Similarly, the middle 4 bars show the impact of climate change on the carbon cycle, and the lower 3 bars give the direct response to increasing atmospheric CO_2 concentrations. Figure taken from IPCC (2007).

1.6 Precision Requirements

CO_2 inferred from global satellite measurements has been shown through numerous sensitivity studies to improve carbon flux inversions provided the observations are precise (Baker et al. 2006b, Dufour & Breon 2003, Houweling et al. 2004, Moa & Kawa 2004, O'Brien & Rayner 2002, Rayner et al. 2002, Rayner & O'Brien 2001). These investigations conclude that precisions between 1 - 10 ppm will reduce uncertainties of CO_2 sources and sinks due to the dense global sampling of satellites. The spatial and temporal resolution of the satellite measurements and the surface flux inversion spatiotemporal scale effects the requirement for precision (Houweling et al. 2004). The greater the precision the more beneficial the data will be for determining sources and sinks, but this must also be balanced against what our current level of satellite technology, retrieval method and validation system can reproduce (Miller et al. 2007). The most realistic study (Rayner et al. 2002) has shown that satellites with a 8° x 10° monthly mean column CO_2 precision of 2.5 ppm or less would surpass the capability of existing surface networks in determining sources and sinks on a continental scale (Rayner & O'Brien 2001) (see Figure 1.20). The ESA Climate Change Initiative (CCI) for the Essential Climate Variable (ECV) Greenhouse Gases (GHG) provides the latest accuracy and precision requirements for CO_2 satellite observations that are based on studies of synthetic data (e.g. Chevallier et al. 2005a, 2007a, 2009, Miller et al. 2007). It states a breakthrough requirement for satellite observations would be a $<$0.3 ppm accuracy (systematic error) and a precision (random error) of $<$3 ppm for a single observation and $<$1 ppm for monthly mean 1000 km^2 observations. Additionally, it gives the ideal satellite requirement of $<$0.2 ppm accuracy (systematic error) and a precision (random error) of $<$1 ppm for a single observation and $<$0.3 ppm for monthly mean 1000 km^2 observations (Buchwitz et al. 2011).

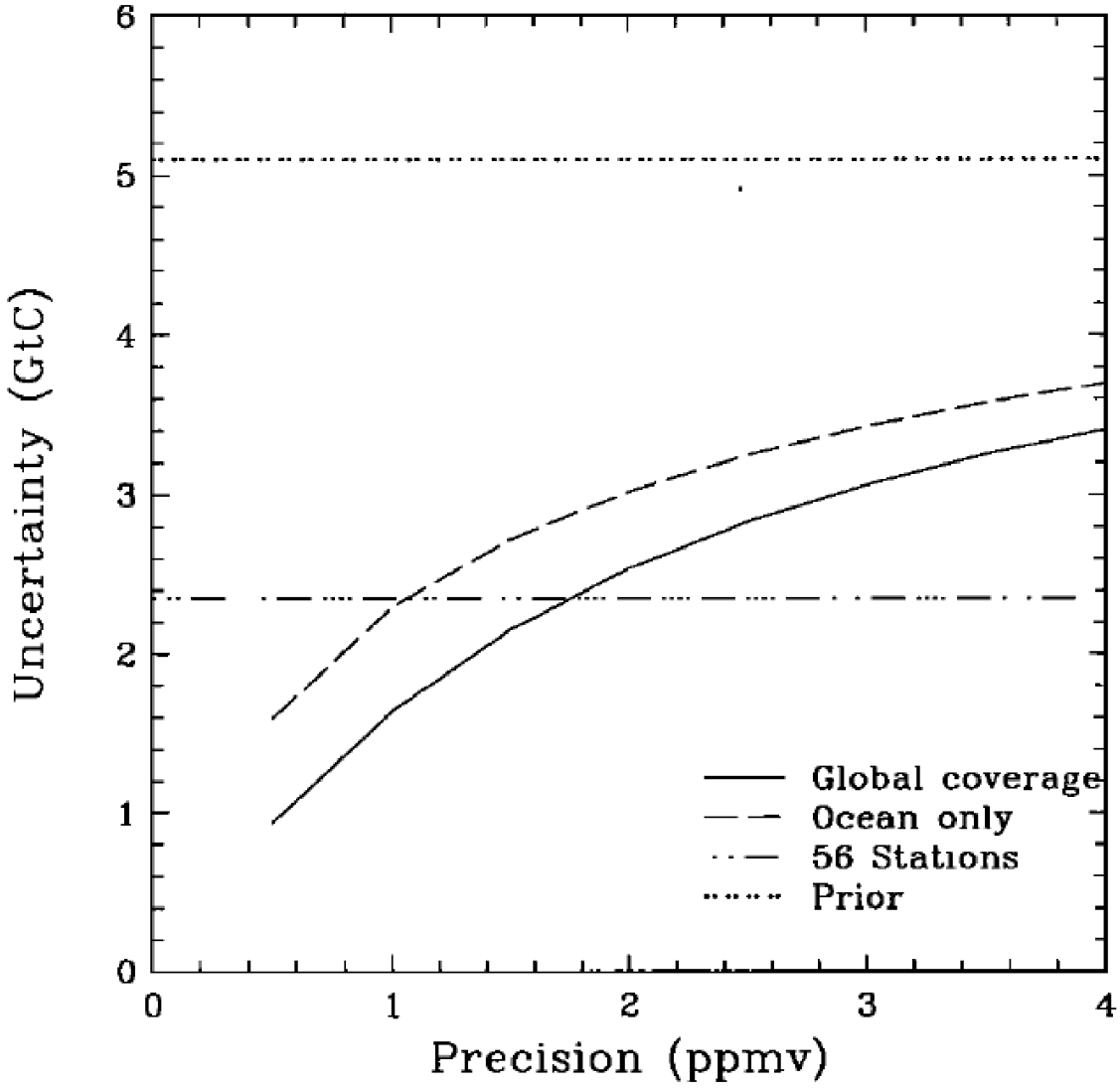

FIGURE 1.20. Comparison of global CO_2 uncertainty and precision when no observations are assimilated (dotted line), observations from 56 ground based measurement stations are assimilated (dashdotted line), simulated global coverage from satellite observations are assimilated (solid line), and simulated global coverage of oceans only from satellite observations are assimilated (dashed line). Figure taken from Rayner & O'Brien (2001).

1.7 Thesis Overview

The aim of this thesis is to develop an algorithm to estimate atmospheric CO_2 from space based observations and to assess the accuracy of these estimations by validating them with independent in-situ observations. Satellites measurements, if acquired with a high accuracy and precision, have the potential to reduce model flux uncertainties and improve our knowledge of the carbon cycle, allowing the identification of surface sources and sinks of CO_2.

This thesis describes the development of a new retrieval algorithm capable of retrieving CO_2 from space borne measurements, called the University of Leicester Full Physics (UoL-FP) retrieval algorithm. The second chapter provides the fundamental theories for remote sensing and how these have been used by previous satellite instruments to infer CO_2. The first satellite that is proposed to meet this requirement, called GOSAT, is then described. Chapter three explains the UoL-FP retrieval algorithm that was developed for use with GOSAT observations. The retrieved CO_2 estimates are validated against ground based remote sensing measurements in the fourth chapter to assess the accuracy of the algorithm. Chapter four also includes global comparisons to a global chemistry transport model providing the first steps towards source/sink flux inversions and compares to alternative retrieval algorithms to evaluate any obvious retrieval dependent biases. The framework of the algorithm is developed in the fifth chapter by the creation of a simulator that can be used to investigate multiple retrieval algorithm modifications, which may lead to the development of a new retrieval algorithm method with improved CO_2 precision. Chapter six summarises the thesis and provides an outlook for future expansion.

Chapter 2

Remote Sensing of Atmospheric CO_2

2.1 Introduction to Remote Sensing of Atmospheric CO_2

Satellite instruments can measure light at the top of the atmosphere that has come from the Earth. These measurements can be made using active or passive remote sensing techniques. Active sensing is where monochromatic light is sent from the satellite to the Earth's surface and then the reflected light is measured. The difference between the original and measured light can then provide information about the content of the atmosphere. However, this method requires high levels of power and only measures light at specifc wavelengths. Passive sensing measures Sun light reflected off the Earth's surface, and the difference between the measured light and estimated light from the Sun can provide information about the Earth's atmosphere. This method requires much less power, can measure multiple wavelength ranges and has a high accuracy.

The Sun emits light strongly in the visible and shortwave infrared (SWIR) range, but any radiation absorbed by the Earth will be re-radiated at wavelengths in the thermal infrared (TIR) range (the same range as the Earth's surface naturally radiates at). Space based TIR measurements therefore provide information where absorption occurs throughout the atmosphere, especially in the upper troposphere where clouds are present. Satellite SWIR measurements also provide information throughout the atmosphere, but are more sensitive to reflection. Hence, SWIR observations are obstructed by thick clouds. However, for cloud free scenes, SWIR measurements are most sensitive to the lower troposphere, where there are more gas molecules, and can provide information about the atmosphere just above surface CO_2 sources and sinks.

As light travels through the atmosphere some of it gets absorbed by gas molecules and some light will be absorbed or scattered by aerosols and clouds. Each of the different

gases that make up the atmosphere will cause light to be absorbed at certain wavelengths specific to the structure of that gas. Hence, remote sensing of specific wavelengths can provide information about a particular type of gas, allowing its atmospheric concentration to be inferred.

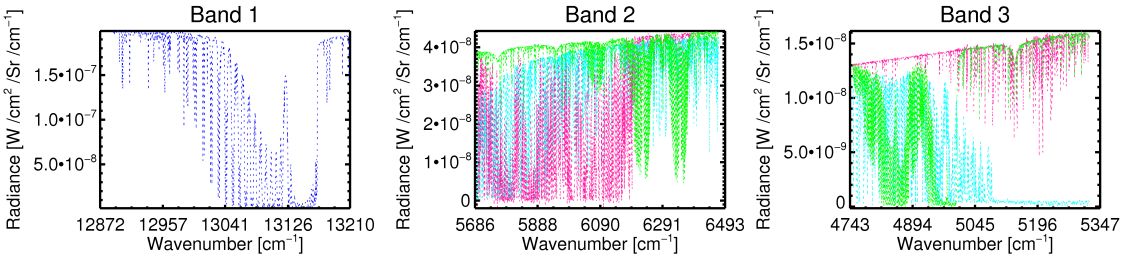

FIGURE 2.1. Example radiances for each of the TANSO-FTS SWIR bands showing absorption of different gases, where blue represents O_2, green represents CO_2, pink represents CH_4, and cyan represents H_2O.

Figure 2.1 illustrates absorption by different atmospheric gases for some example wavelength ranges, where lower radiance values typically mean absorption has occurred. The amount of absorption that has occurred (i.e. how much the radiance is decreased by compared to the continuum level) can be compared to tabulated information of a single molecule to estimate how much of that gas exists.

2.2 Fundamentals of Radiation in the Atmosphere

2.2.1 Light Absorption

The absorption spectral lines observed in measurements of atmospheric light are created when light of a certain wavelength becomes absorbed by a molecule within the beam. If a photon with energy δE=hv is absorbed then a molecule goes through a transition from its ground energy state to an excited energy state, where h is Planck's constant (6.626076 x 10^{-34} Js) and v is the frequency of the electromagnetic radiation. The total energy of a molecule is given by the sum of the potential energy and kinetic energy, which can be represented by the Hamiltonian operator $\hat{H}$. The energy level, E, of a molecule must obey the time independent Schrödinger equation

$$E\Psi = \hat{H}\Psi \tag{2.1}$$

where Ψ is the eigenvalue of the operator. During the absorption of light by a molecule, there are additionally four contributing aspects that must be considered; the electronic, vibrational, rotational and nuclear energies of the molecule. Assuming these to be independent (Born-Oppenheimer approximation), the Schrödinger equation can be solved for each energy seperately and the total energy of a molecule can then be given as

$$E = E_{\text{Electronic}} + E_{\text{Vibrational}} + E_{\text{Rotational}} + E_{\text{Nuclear}} \tag{2.2}$$

where the eigenvalue is the product of each aspect:

$$\Psi = \Psi_{\text{Electronic}}\Psi_{\text{Vibrational}}\Psi_{\text{Rotational}}\Psi_{\text{Nuclear}} \tag{2.3}$$

In the SWIR wavelength range the nuclear energies are small, whilst the electronic, vibrational and rotational energies are larger, with the vibrational energy being comparable in energy to that of infrared radiation.

2.2.1.1 Rotational Transitions

Molecules can be considered as rigid structures that may rotate. This rotation can be described about three orthoganal axes that pass through the molecules centre of gravity. The axes A, B and C are defined such that the corresponding inertia, I, of the molecule rotating around each axis is given as $\text{I}_A \leq \text{I}_B \leq \text{I}_C$. The rotational energy can be given

by

$$E_{\text{Rotational}} = \frac{1}{2} I_A \omega_A^2 + \frac{1}{2} I_B \omega_B^2 + \frac{1}{2} I_C \omega_C^2 \tag{2.4}$$

where ω represents the corresponding angular velocity around each axis. The energy is proportional to both inertia and angular velocity about each axis, which both depend on the structure of the molecule. Thus, molecules are categorized by their structure, as shown in Table 2.1.

Table 2.1. Molecule structure classification.

Classification	Moment of inertia I	Example molecules
Linear	I_A=0, I_B=I_C	CO_2, N_2O
Symmetric top	$I_A \leq I_B = I_C$† or $I_A = I_B \leq I_C$‡	$CFCl_3$, NH_3
Spherical top	$I_A = I_B = I_C$	CH_4, SF_6, CCl_4
Asymmetric top	$I_A \neq I_B \neq I_C$	H_2O

Symmetric top molecules can be sub-catagorised as prolate† or oblate‡ symmetric top molecules.

However, the assumption of rigid structures rotating is only an approximation and in reality there are clear deviations from this model.

2.2.1.2 Vibrational Transitions

Molecules may vibrate with a given number of modes. This is determined by the number of degrees of freedom, where a molecule of x atoms has 3x degrees of freedom. However, three of the degrees of freedom represent the translational motion of the molecule in each axis direction and another three represent the rotational motion about each axis. Therefore, 3x$-$6 degrees of freedom is the number of vibrational modes for a non-linear molecule. For a linear molecule the rotational motion can be described by two degrees of freedom, so the number of modes becomes 3x$-$5. Taking CO_2 as an example, it is linear and comprises of 3 atoms so has 4 vibrational modes, which are shown in Figure 2.2.

The energy associated with each vibrational mode, i, can be approximately described by the harmonic displacements of each atom in the molecule which vibrate at a certain characteristic frequency, ν_i. This is given by the equation

$$E_{i,v} = h\nu_i \left(v_i + \frac{1}{2} \right) \tag{2.5}$$

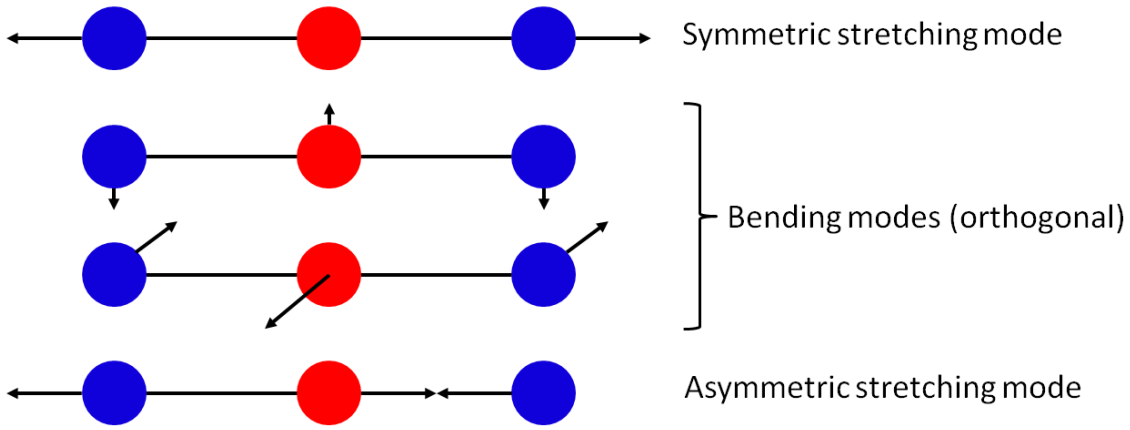

FIGURE 2.2. Illustration of CO_2 vibrational motions, where the carbon atom is shown in red and oxygen in blue. The black lines give the bonds between atoms, with the arrows representing the vibrational movement direction.

where υ is the vibrational quantum number. However, in reality only harmonic displacements for low vibrational modes are valid. Higher vibrational modes are better characterised by anharmonic displacement, with the energy given by

$$E_{i,\upsilon} = h\nu_i \left(\upsilon_i + \frac{1}{2}\right) + h\nu_i x_i \left(\upsilon_i + \frac{1}{2}\right)^2 \tag{2.6}$$

where x represents the anharmonicity constant.

2.2.1.3 Vibrational-Rotational Bands

The energy needed for a molecule to rotate is much smaller than that for vibration. Therefore, when a vibrational transition occurs a simultaneous rotational transition will accompany it. There may be multiple rotational transitions occuring simulataneously from different energy levels. But because the rotational transitions are too close together to be resolved they are grouped together as a vibration-rotation band (Griffiths & de Haseth 2007). The vibration-rotation band is generally defined by three branches; P, Q and R branches. The P and R branches correspond to wavelengths higher and lower than the band centre, respectively. Whilst the Q branch occurs during a vibration bending mode. In the SWIR range, CO_2 contains mostly strong P and R branches (Toth et al. 2008).

2.2.1.4 Line Shape

The spectral line intensity depends on the absorption by the interfering molecule, which can be related as

$$S = \int_{-\infty}^{\infty} C_v dv \tag{2.7}$$

where S is the line intensity and C is the absorption cross section. The energy levels during transitions change slightly due to external influences on the molecule and the loss of energy in emission. Repeated energy transitions cause non-monochromatic radiances, therefore spectral lines have a finite width. This can be expressed in terms of the shape of the spectral line:

$$k_v = S\Phi\left(v - v_0\right) \tag{2.8}$$

where $\Phi(\mathrm{v}-\mathrm{v}_0)$ represents the line shape factor of absorption at specific spectral distances from the line centre, v_0. The broadening of lines depends on the damping of molecular vibrations; a doppler effect resulting from differences in thermal velocities, and any collisions between molecules.

Natural broadening of lines is caused by the loss of energy in emission. This can be explained by the Heisenberg uncertainty principle, whereby the line width is inversely proportional to the lifetime of an excited state (Δt), which in turn is related to the energy of that quantum state ($\Delta \mathrm{E}=\mathrm{h}\Delta \mathrm{v}$):

$$\Delta t \approx \frac{1}{2\pi\Delta v} \tag{2.9}$$

The line shape of natural broadening, Φ_N, can be given as a Lorentz profile (Lorentz

1906):

$$\Phi_N\left(v - v_0\right) = \frac{\alpha_L/\pi}{\left(v - v_0\right)^2 + \alpha_L^2} \tag{2.10}$$

where α_L represents the natural Lorentz shape at half-width-half-maximum (HWHM).

Pressure broadening occurs due to the collisions of molecules and therefore is more dominant in the lower atmosphere where more molecules exist. The line shape of pressure broadening is also described by a Lorentz profile:

$$\Phi_P\left(v - v_0\right) = \frac{\alpha_L/\pi}{\left(v - v_0\right)^2 + \alpha_L^2} \tag{2.11}$$

At higher altitudes there are less molecules that can collide so the doppler effect becomes important. If a molecule has a velocity in the line of sight and v<<c then the doppler effect occurs:

$$v = v_0\left(1 \pm \frac{v}{c}\right) \tag{2.12}$$

In Kinetic theory, translational states are in thermodynamic equilibrium and the probability that the velocity is between v and v+dv is p(v)dv. The maxwell distribution gives p(v) such that

$$p\left(v\right)dv = \left(\frac{m}{2\pi kT}\right)^{\frac{1}{2}} e^{\left(-\frac{mv^2}{2kT}\right)}dv \tag{2.13}$$

where k is Boltzmann's constant, T is temperature and m is the mass. Combining Equations 2.12 and 2.13, the line shape of doppler broadening can be given as

$$\Phi_D\left(v - v_0\right) = \frac{1}{\alpha_D\sqrt{\pi}}\exp\left[-\left(\frac{v - v_0}{\alpha_D^2}\right)^2\right] \tag{2.14}$$

where the HWHM is $\alpha_D\sqrt{ln2}$ and

$$\alpha_D = v_0\left(\frac{2KT}{mc^2}\right)^{\frac{1}{2}} \tag{2.15}$$

In the upper atmosphere both pressure and doppler broadening are important to consider. Therefore, the line shapes of both are convolved to create a Voigt profile shape:

$$\Phi_V\left(v - v_0\right) = \frac{1}{\pi^{\frac{3}{2}}}\frac{\alpha_L}{\alpha_D}\int_{-\infty}^{\infty}\frac{1}{\left(v' - v_0\right)^2 + \alpha_L^2}\exp\left[\frac{-\left(v - v'\right)^2}{\alpha_D^2}\right]dv' \tag{2.16}$$

where the doppler shift is added to the pressure broadened line at wavenumbers v'$-$v$_0$.

It is also possible for line-mixing to occur, where multiple absorption lines overlap.

Recent studies have shown this must be taken into account for highly accurate retrievals of X_{CO2} to be achieved (e.g. Hartmann et al. 2009, Lamouroux et al. 2010, Vangwichith et al. 2009).

2.2.2 Radiative Transfer

2.2.2.1 The Radiative Transfer Equation

Passive space borne SWIR remote sensing instruments measure the intensity of electromagnetic radiation that has travelled from the Sun and been reflected off the Earth's surface towards the instrument optics, which is the focus of this study. This beam of radiation travels through the Earth's atmosphere where a number of different physical processes can alter the intensity of the radiation. Figure 2.3 illustrates these processes which include; absorption of radiation, radiation scattered out of the beam, single scattering of direct solar radiation into the beam, emitted radiation into the beam, and multiple scattering of indirect diffuse radiation into the beam (both solar and emitted radiances). The radiative transfer equation describes the change in the radiance of the beam for a specified wavelength, dI_λ, over the distance travelled, ds, and can be given for simplicity as

$$dI_\lambda = -dI_{SO,\lambda} - dI_{AO,\lambda} + dI_{SI,\lambda} + dI_{MI,\lambda} + dI_{EI,\lambda} \tag{2.17}$$

where the first term on the right hand side is the intensity of radiation scattered out of the beam and is expressed as

$$dI_{SO,\lambda} = I_\lambda \sigma_{s,\lambda} ds \tag{2.18}$$

where I is the intensity and σ_s is the scattering extinction coefficient. The second term of Equation 2.17 gives the intensity of radiation absorbed throughout the beam and can be written as

$$dI_{AO,\lambda} = I_\lambda \sigma_{a,\lambda} ds \tag{2.19}$$

where σ_a is the absorption extinction coefficient. The intensity of solar radiation directly scattered into the beam by a single particle is represented in Equation 2.17 as the third term and is given as

$$dI_{SI,\lambda} = \left[\sum_k \left(\frac{\sigma_{s,k,\lambda}}{4\pi} P_{s,k,\lambda,\mu,-\mu_s,\phi,\phi_s} \right) \right] F_{s,\lambda} e^{-\frac{\tau_\lambda}{\mu_s}} ds \tag{2.20}$$

where k represents different particles, P is the scattering phase function that describes the angular distribution of scattering with directions, F is the total irradiance (solar ra-

diation) at the top of the atmosphere, and Beer's law is included with the exponential term showing that the absorption of radiation increases exponentially with the optical depth, τ. The fourth term of Equation 2.17 represents the multiple scattering of diffuse radiation into the beam and is given by

$$dI_{MI,\lambda} = \left[\sum_{k}\left(\frac{\sigma_{s,k,\lambda}}{4\pi}\int_{0}^{2\pi}\int_{-1}^{1} I_{\lambda,\mu',\phi'} P_{s,k,\lambda,\mu,\mu',\phi,\phi'} d\mu' d\phi'\right)\right] ds \tag{2.21}$$

The final term of Equation 2.17 represents the emitted radiation into the beam. The emission occurs in the infrared wavelength range whereby particles that have previously absorbed radiation re-emit infrared radiation. This can be expressed as

$$dI_{EI,\lambda} = \sigma_{a,\lambda} B_{\lambda,T} ds \tag{2.22}$$

where $B_{\lambda,T}$ represents Planck's law, which gives the intensity emitted from a particle as a function of wavelength and temperature. Planck's law is given by

$$B_{\lambda,T} = \frac{2hc^2}{\lambda^5\left[e^{\left(\frac{hc}{\lambda k_b T}\right)} - 1\right]} \tag{2.23}$$

where h is Planck's constant (6.6256 x 10^{-34} Js), c is the speed of light (2.9979 x 10^8 ms^{-1} in a vacuum), k_b is Boltzmann's constant (1.38 x 10^{-23} JK^{-1}), and T is temperature. Thus, substituting Equations 2.18 to 2.22 into Equation 2.17 the radiative transfer equation can be given as

$$\begin{aligned}\frac{dI_{\lambda,\mu,\phi}}{ds} = &-I_{\lambda,\mu,\phi}\left(\sigma_{s,\lambda} + \sigma_{a,\lambda}\right) + F_{s,\lambda} e^{-\frac{\tau_\lambda}{\mu_s}} \sum_{k}\left(\frac{\sigma_{s,k,\lambda}}{4\pi} P_{s,k,\lambda,\mu,-\mu_s,\phi,\phi_s}\right) \\ &+ \sum_{k}\left(\frac{\sigma_{s,k,\lambda}}{4\pi}\int_{0}^{2\pi}\int_{-1}^{1} I_{\lambda,\mu',\phi'} P_{s,k,\lambda,\mu,\mu',\phi,\phi'} d\mu' d\phi'\right) + \sigma_{a,\lambda} B_{\lambda,T}\end{aligned} \tag{2.24}$$

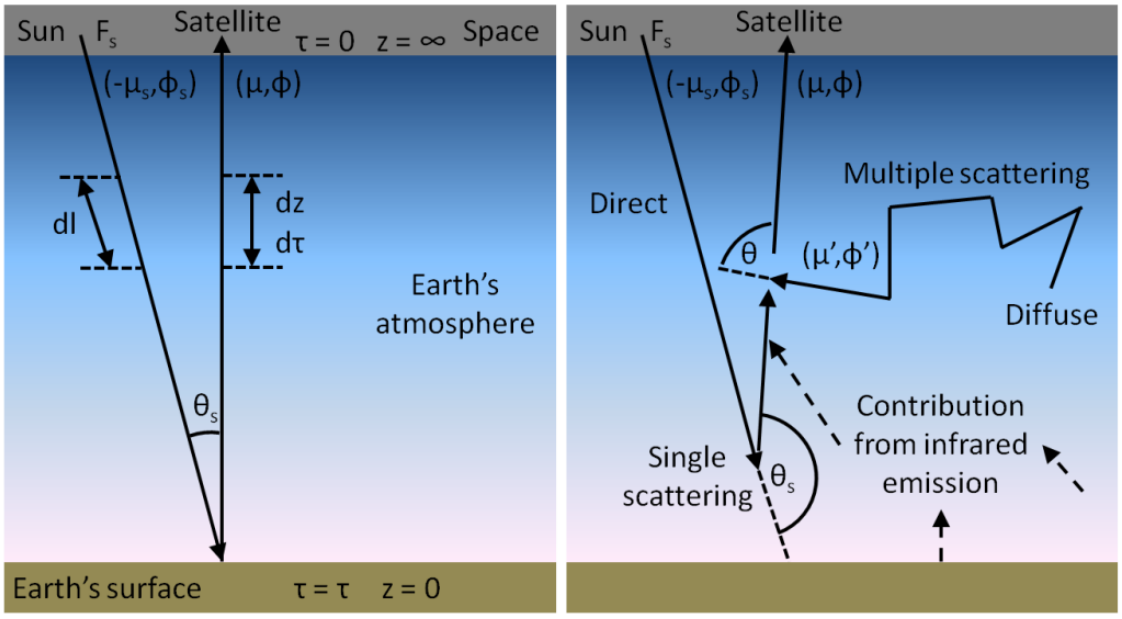

FIGURE 2.3. Radiative transfer diagram, illustrating the unattenuated beam (left) and the beam with multiple processes interacting with it (right), where the beam orientation is μ, ϕ. The solar zenith angles of the beam and diffuse radiation is given by θ and θ', respectively. ϕ is the azimuth angle, ϕ' is the azimuth angle of the diffuse radiation, $\mu = \cos\theta$, and $\mu' = \cos\theta'$. For downward radiances μ is negetively assigned and for upward radiances μ is positively assigned. Adapted from Jacobson (2005) and Liou (2002).

2.3 Types of Scattering

Electromagnetic radiation becomes scattered when a particle is within the path of a light wave, causing light to become reflected, refracted or diffracted, changing the direction of the light path. The effect that the size of the particle has on scattering is defined by a term called the size parameter, which for a spherical particle is given as

$$x = \frac{2\pi a}{\lambda} \tag{2.25}$$

where x is the size parameter, a is the particle radius and λ is the wavelength of light. Scattering can be defined with two types; Rayleigh scattering where x$\ll$1 and Lorenz-Mie scattering where x$\gtrsim$1.

The polarisation state of an electromagnetic wave can be described using four linearly independent values referred to as the Stokes parameters:

$$I = E_P E_P^* + E_S E_S^* \tag{2.26}$$

$$Q = E_P E_P^* - E_S E_S^* \tag{2.27}$$

$$U = E_P E_S^* + E_S E_P^* \tag{2.28}$$

$$V = -i\left(E_P E_S^* - E_S E_P^*\right) \tag{2.29}$$

where I is the total intensity of the wave, Q and U give the linear polarisations, V gives the state of the circular polarisation of the wave, $*$ denotes the complex conjugate, and i equals $\sqrt{-1}$. These parameters are based on the wave being characterised by the electric field, E, being parallel (P) and perpendicular (S) to the incident plane. These stokes parameters can be summarised by the Stokes vector

$$\mathbf{I} = \begin{bmatrix} I \\ Q \\ U \\ V \end{bmatrix} \tag{2.30}$$

The intensity of scattered light can be given in terms of the incident light ($\mathbf{I}_0$) by

$$\mathbf{I} = \mathbf{P}\left(\Omega\right)\mathbf{I}_0 \tag{2.31}$$

where P represents the phase matrix as a function of scattering angle, Ω. The phase

matrix gives the phase function with polarisation, and can be defined as

$$\mathbf{P}(\Omega) = \begin{bmatrix} P_{11}(\Omega) & P_{12}(\Omega) & 0 & 0 \\ P_{12}(\Omega) & P_{22}(\Omega) & 0 & 0 \\ 0 & 0 & P_{33}(\Omega) & P_{34}(\Omega) \\ 0 & 0 & -P_{34}(\Omega) & P_{44}(\Omega) \end{bmatrix} \tag{2.32}$$

The phase matrix is defined by the phase function, P, which gives the intensity as a function of scattering angle. For spheres, P_{22}=P_{11} and P_{44}=P_{33}.

When light is scattered by particles that are small compared to the wavelength of light or the photons are elastically scattered, Rayleigh scattering occurs. The scattering cross section for Rayleigh scattering, $C_{Rayleigh}$, is given as:

$$C_{\text{Rayleigh}} = \frac{8\pi r^6}{3}\left(\frac{2\pi n}{\lambda}\right)^4\left(\frac{m^2-1}{m^2+2}\right)^2 \tag{2.33}$$

where n is the refractive index of the surrounding medium (air), r is the radius of the particle and m is the ratio of the particle refractive index to n. Note that the Rayleigh scattering cross section is proportional to r^6, so all air molecules will scatter and more scattering will occur for longer light paths through the atmosphere (hence at higher SZAs). Additionally, this means that larger particles have a larger scattering cross section, but are inversely proportional to wavelength, giving larger scattering cross sections at smaller wavelengths. Thus, Rayleigh scattering is small in the SWIR range. The phase function for Rayleigh scattering can be defined as

$$P(\Omega) = \frac{3}{4}\left(1 + cos^2\Omega\right) \tag{2.34}$$

Figure 2.4 shows the phase function for Rayleigh scattering, which scatters light equally in the forward and backward directions.

In the SWIR, Lorenz-Mie scattering dominates, where larger particles scatter light ($x \gtrsim 1$). The direction of the scattered light becomes more towards the forward direction (see Figure 2.4). For Lorenz-Mie scattering, the off diagonal terms of the phase matrix are typically small, so polarisation will not affect intensity much. Thus, intensity can be approximated by P_{11}, which can be defined as

$$P_{11}(\Omega) = \frac{4\pi}{k^2 C_{Lorenz-Mie}}\frac{|S_1|^2 + |S_2|^2}{2} \tag{2.35}$$

where $C_{Lorenz-Mie}$ is the scattering cross-section, k = $2\pi n/\lambda$, and S_1 and S_2 represent scattering amplitudes which are given as

$$S_1(\Omega) = \sum_{n=1}^{\infty} \frac{2n+1}{n(n+1)} \left[a_n \pi_n(cos\Omega) + b_n \tau_n(cos\Omega)\right] \tag{2.36}$$

$$S_2(\Omega) = \sum_{n=1}^{\infty} \frac{2n+1}{n(n+1)} \left[b_n \pi_n(cos\Omega) + a_n \tau_n(cos\Omega)\right] \tag{2.37}$$

where a and b are complex Mie coefficients that are expressed in terms of the spherical Bessel functions, and the Mie angular functions are defined as

$$\pi_n(cos\Omega) = \frac{1}{sin\Omega} P_n^1(cos\Omega) \tag{2.38}$$

$$\tau_n(cos\Omega) = \frac{d}{d\Omega} P_n^1(cos\Omega) \tag{2.39}$$

where P_n^1 represent Legendre polynomials, where the number of terms is proportional to the size parameter. Additionally, the strength of forward scattering can be indicated by the asymmetry parameter which is given as

$$Q = \frac{4}{x^2}\left[\sum_n \frac{n(n+2)}{n+1} Re\left(a_n a_{n+1}^* + b_n b_{n+1}^*\right) + \frac{2n+1}{n(n+1)} Re\left(a_n b_n^*\right)\right] \tag{2.40}$$

where Re represents the effective radius.

Normally, the scattered light has the same wavelength as the incident light, this is known as elastic scattering and both Rayleigh and Lorenz-Mie scattering are examples of this. However, inelastic scattering can occur where a different wavelength is emitted. This is often referred to as Raman scattering, although fluorescence can also be considered an example of this.

The amount of radiation removed from a certain length of the light path by scattering and absorption is known as the optical depth. The total column optical depth is the total amount of light removed as it passes through the atmosphere towards the Earth's surface and as it travels throughout the atmosphere after being reflected towards the satellite. The total optical depth is also the sum of the optical depth due to Rayleigh molecules, R, aerosols, A, and atmospheric gases, G. As shown for Rayleigh and Lorenz-Mie scattering, the amount of scattering varies with wavelength, therefore the optical depth is wavelength dependent and can be expressed as

$$\tau(\lambda) = \tau_R(\lambda) + \tau_A(\lambda) + \tau_G(\lambda) \tag{2.41}$$

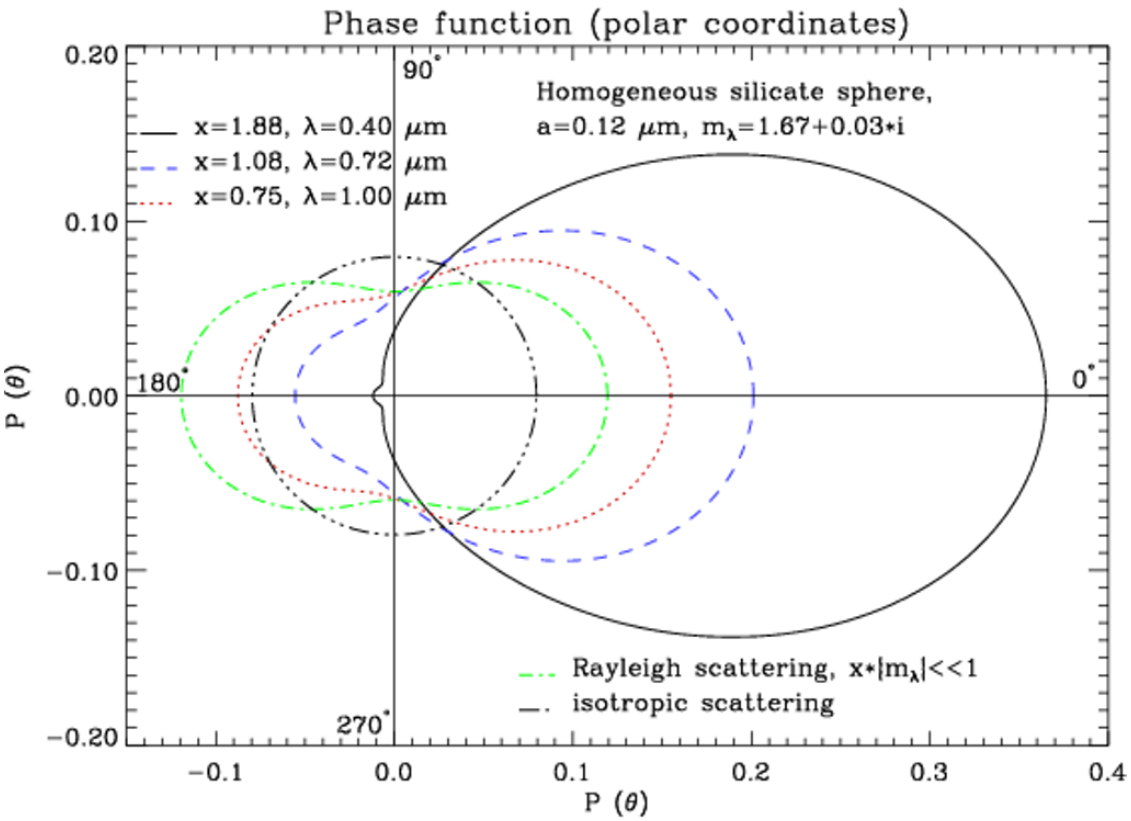

FIGURE 2.4. Example scattering phase function in polar coordinates for a homogenous spherical particle of different sizes and wavelengths. An example of Rayleigh scattering is shown in green. Whilst an example of Lorenz-Mie scattering is shown by the solid black line. Figure taken from (Steinacker et al. 2003).

The optical depths at different wavelengths (1 and 2) can be related by the angstrom coefficient:

$$\alpha = -\frac{log\left(\frac{\tau_1}{\tau_2}\right)}{log\left(\frac{\lambda_1}{\lambda_2}\right)} \tag{2.42}$$

2.4 Atmospheric Scattering Particles

Although the type of scattering depends on the size of the particle, the direction and strength of scattering also depends on the shape of the particle and its refractive index as a function of wavelength in the Lorenz-Mie regime. In the atmosphere there is a large variety of particles, both natural and anthropogenic.

Cloud particles form when the temperature is low enough for water vapour to condense. However, condensation can only occur if there is a surface to condense onto.

In the atmosphere minute particles (aerosols) act as condensation nuclei allowing water vapour to condense to form clouds. Under normal conditions, water vapour will condense into water droplets, unless below 0°C when ice crystals form. However, under certain conditions water droplets can exist below 0°C and these are known as supercooled droplets. Since the type of cloud particle formed depends on temperature, water droplets are found at low altitudes (e.g. Stratus and Cumulus clouds), ice crystals at high altitudes (e.g. Cirrus, Cirrustratus and Cirrocumulus clouds) and a mixture of water and ice at middle altitudes (e.g. Altostratus and Altocumulus clouds). Water droplets are spherical in shape whilst ice crystals are uniaxial with a high variability (see Figure 2.6), and both may grow due to coalescence (collison of droplets as they fall through the atmosphere) (Lawson et al. 2001). Additionally, the Bergeron process may create larger cloud particles, whereby water molecules transfer from supercooled water droplets to nearby ice crystals due to the vapour pressure difference between them (Liou 1992). The refractive index of water and ice particles vary with wavelength as shown in Figure 2.5. Water droplets typically have a radius between 1 and 40 μm and and due to their spherical shape, scatter mostly in the forward direction with a smaller backwards peak (see Figure 2.7). Ice crystals are larger in size, ranging between roughly 10 and 2000 μm, and scatter slightly less in the forward direction. There is also a large range in size for mixed phase (part water and ice) particles and these have similar scattering properties (Jourdan et al. 2003).

The other type of particles that scatter light are aerosols. Some aerosols are created naturally and these are generally well distributed around the world with sources covering large areas. Examples of this include; dust blown into the atmosphere from desert regions, sea salt spraying/blowing into the atmosphere from oceans, organic compounds from plant particles, and soot from biomass burning. These aerosols typically exist in the troposphere and have a lifetime of a couple of weeks due to water vapour condensing onto them and also due to coagulation of aerosols forming larger particles, both of which will cause the aerosol to fall to the surface (Williams et al. 2002). Another source of aerosols comes from volcanic eruptions which may throw up particles into the troposphere but also into the stratosphere where there is less water vapour for condensation to occur so aerosol lifetimes of 1-3 years are possible (Robuck et al. 2002). Urban aerosols tend to be anthropogenic and concentrated over small polluting regions in the lowest kilometer of the atmosphere. Urban aerosols are complex due to the mixtures of aerosols from various anthropogenic emission sources. Aerosols are highly variable in shape, size and refractive index (Williams et al. 2002), see Figures 2.8 and 2.9 for examples. Additionally, some aerosol types are hydrophobic whilst others are hydrophilic and may

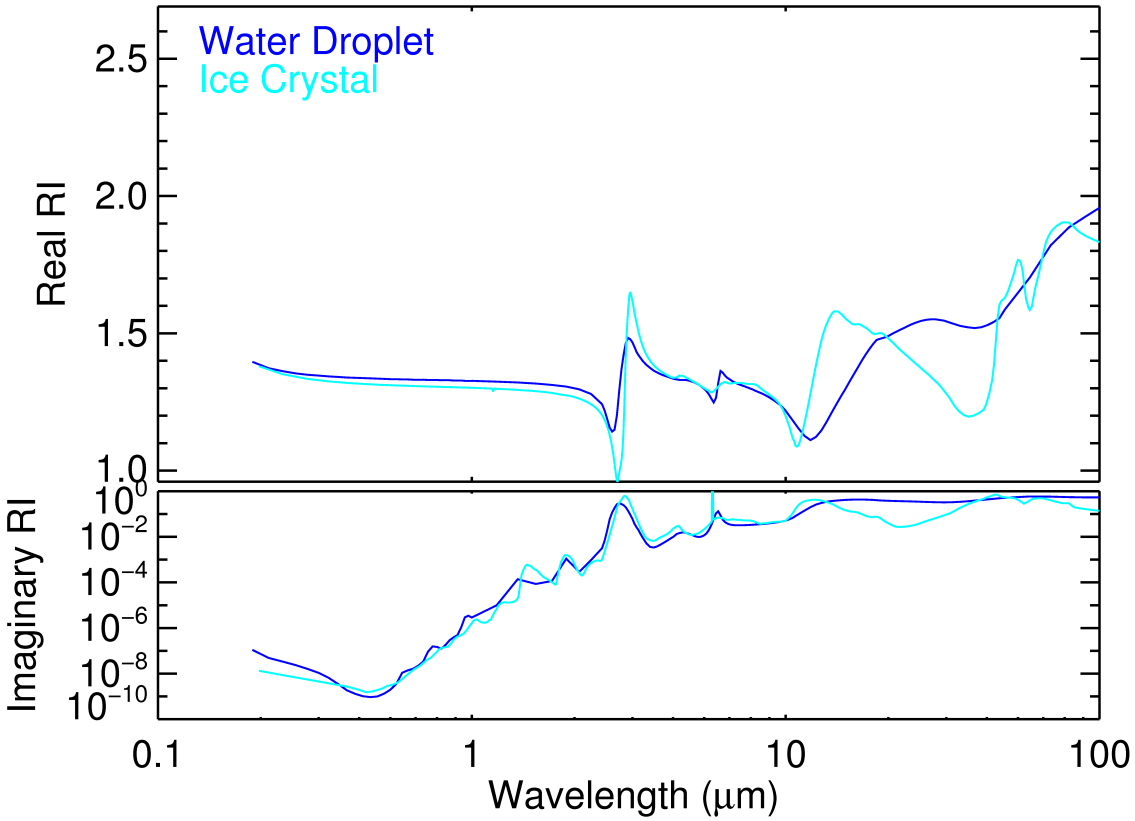

FIGURE 2.5. Example of real and imaginary refractive index of liquid and ice cloud particles. The water refractive index values were obtained from Hale & Querry (1973) and the ice from Warren (1984).

change in size and shape with humidity (Shettle & Fenn 1979).

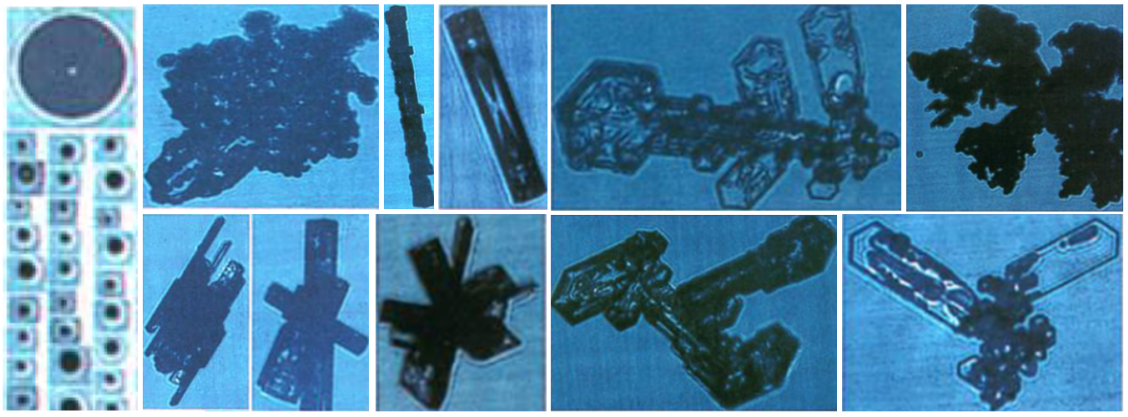

FIGURE 2.6. Example images of spherical water particles (left) and a few ice crystal shape variations (centre and right). Obtained from Lawson et al. (2001).

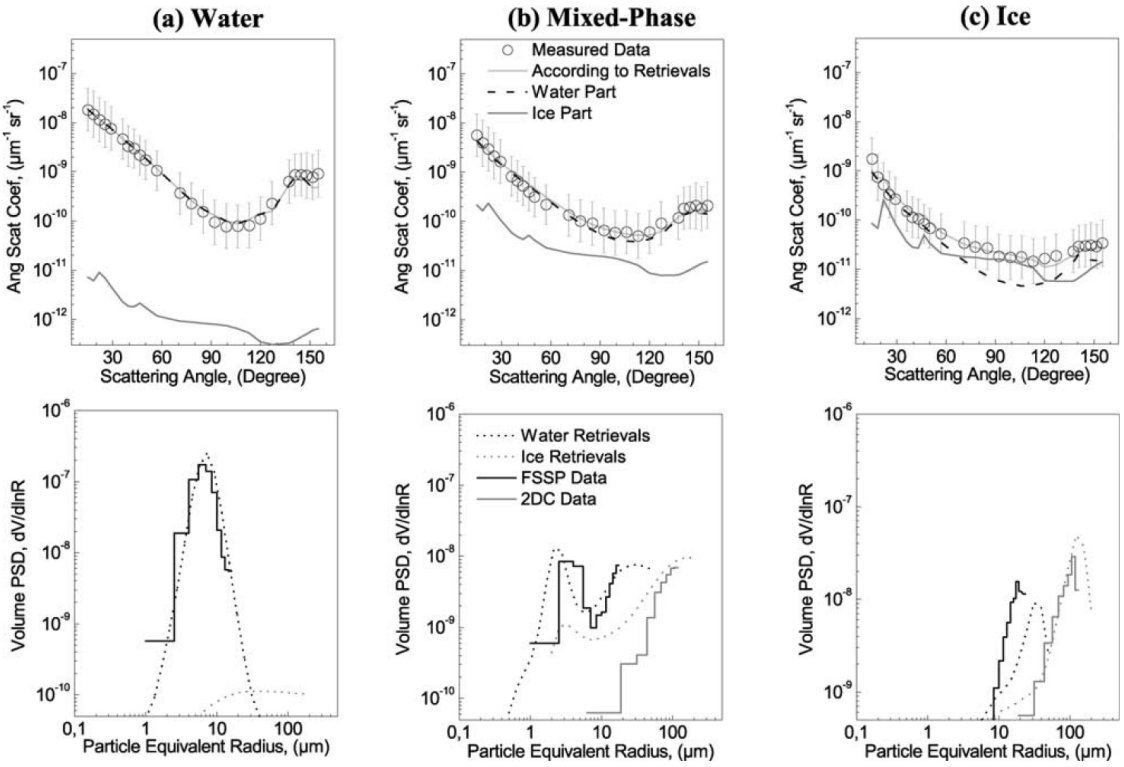

FIGURE 2.7. Measured and retrieved scattering phase functions and particle size distributions for water droplet clouds (a), mixed-phase clouds (b) and ice crystal clouds (c). Figure taken from Jourdan et al. (2003).

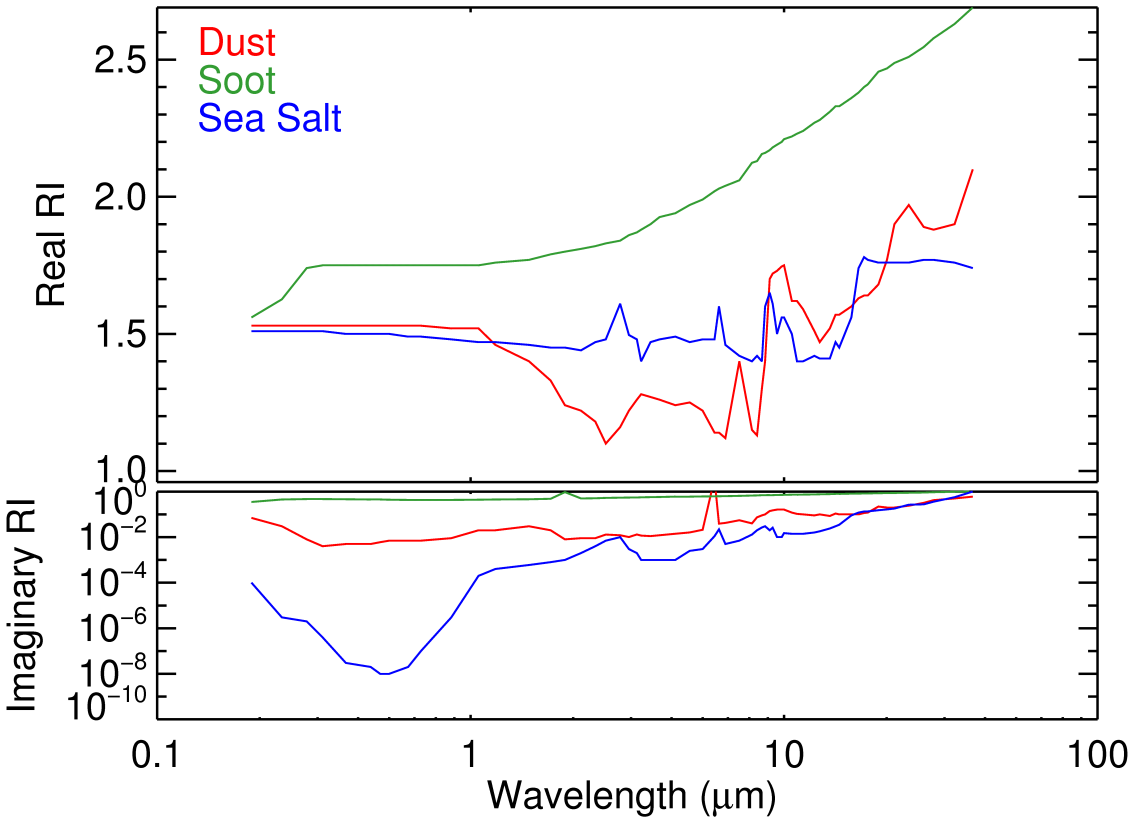

FIGURE 2.8. Example of real and imaginary refractive index of different three different aerosol types; dust, soot and sea salt. The refractive index values were obtained from Shettle & Fenn (1979).

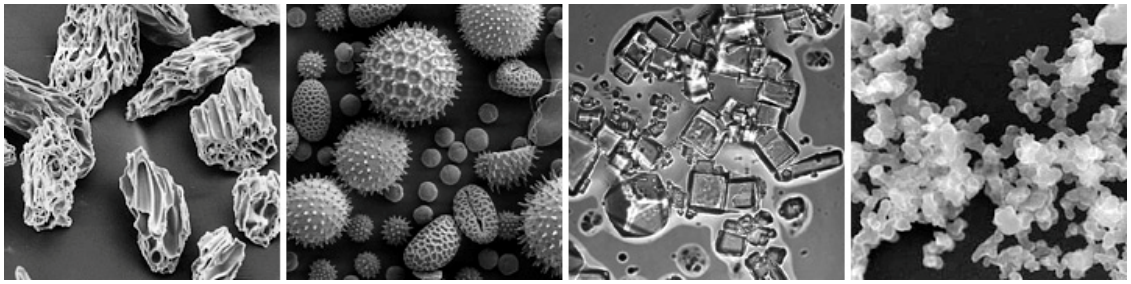

FIGURE 2.9. Example images of aerosols from scanning electron microscopes courtesy of USGS, UMBC (Chere Petty, and Arizona State University (Peter Buseck). This shows a variety of aerosol shapes, including; volcanic ash (far left), pollen (centre left), sea salt (centre right), and soot (far right).

2.5 Previous Satellite Remote Sensing Observations of CO_2

The fundamental theories used for remote sensing described in the previous sections has allowed CO_2 to be inferred from satellite measurements for over three decades. A summary of these observations is given below.

The Television and Infrared Operational Satellite Next Generation (TIROS-N) Operational Vertical Sounder (TOVS) have been included onboard the National Oceanic and Atmospheric Administration (NOAA) polar meteorological satellites since 1978 (Chedin et al. 2003, Smith et al. 1979). This instrument comprises of three sounding units; the High-Resolution Infrared Radiation Sounder (HIRS-2), the Microwave Sounding Unit (MSU) and the Stratospheric Sounding Unit (SSU). Atmospheric and surface emissions can be inferred from HIRS-2 in seven channels; one at 15.0 μm, five channels around 4.3 μm, and one channel at 11.0 μm wavelength. The spectral bands around 15.0 μm and 4.3 μm observe radiances which highly depend on both atmospheric temperature and greenhouse gas concentrations, such as CO_2. Although CO_2 has been retrieved from TOVS it has an accuracy of the same order as the seasonal amplitude of atmospheric CO_2 (approximately 10 ppm) (Engelen & Stephens 2004) and the vertical sensitivity is largest in the mid-troposphere, making surface flux estimations have a large uncertainty. Additionally, regional biases cause the inferred fluxes to be not useful for biogeochemical analysis (Chevallier et al. 2005b).

The next generation of satellites that were capable of measuring CO_2 were launched in 2002. The SCanning Imaging Absoprtion spectroMeter for Atmospheric CHartographY (SCIAMACHY) instrument, launched onboard the ENVISAT satellite in March 2002, is a passive ultraviolet (UV) - visible (VIS) - near infrared (NIR) hyper-spectral spectrometer designed to investigate tropospheric and stratospheric composition and processes with a nadir instantaneuos field of view (IFOV) of 60 x 30 km^2 at the ground (Barkley et al. 2006, Bovensmann et al. 1999). Observations of CO_2 were retrieved from the 1.57 μm radiance channel (Barkley et al. 2006a, Buchwitz et al. 2005) and have been shown to follow the CO_2 seasonal cycle, but with a bias of approximately 4% and standard deviation of about 3% to in-situ observations (Barkley et al. 2006b). The relative accuracy and precision were both determined to be 1-2% for monthly averages for approximately a 7° x 7° footprint (Schneising et al. 2008). CO_2 retrieved from SCIAMACHY observations were unable to meet the 1% precision required for a 8° x 10° footprint to improve upon surface network measurements (Barkley et al. 2006). The differences between SCIAMACHY column average dry air mole fraction of CO_2 (X_{CO2})

with ground based observations and model data were attributed to the low variabilty of global CO_2 distribution, and the inherent difficulties in retrieval algorithms to be able to account correctly for light scattering caused by clouds and aerosols (Houweling et al. 2005).

The SCIAMACHY instrument is most sensitive to CO_2 concentrations near the boundary layer due to it measuring in the near infrared (NIR) wavelength range. This sensitivity can be expressed by an averaging kernel, which indicates how sensitive a retrieval algorithm is to the true atmospheric profile for different altitude ranges. Figure 2.10 illustrates how the averaging kernel for SCIAMACHY peaks close to the boundary layer.

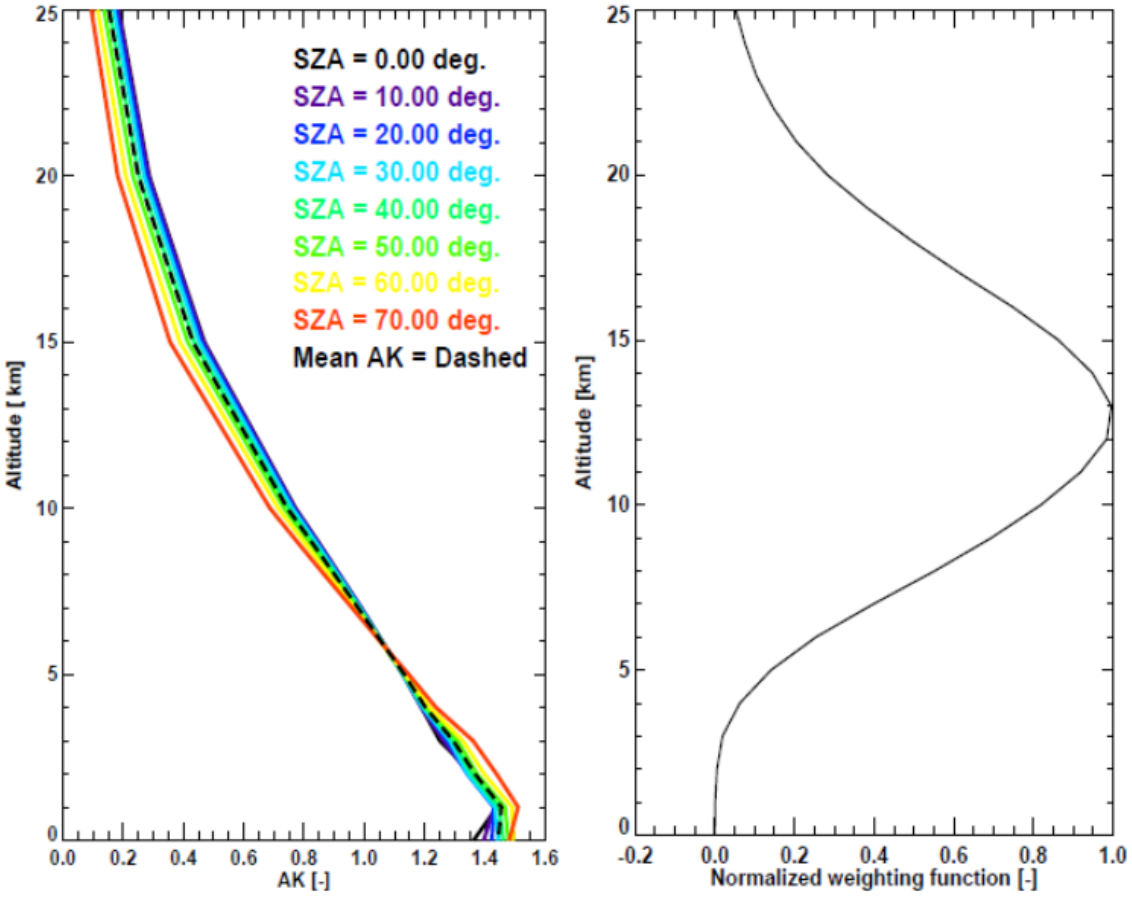

FIGURE 2.10. SCIAMACHY NIR averaging kernels from the Full Spectral Initiation (FSI) CO_2 retrieval algorithm for a range of SZA using a spectral window of 1561.03 to 1585.39 nm and albedo of 0.2 (left), with the mean averaging kernel given by the black dashed line. The normalised mean weighting function of AIRS which observes in the TIR spectral range is given (right) for comparison. Figure taken from Barkley et al. (2006).

Figure 2.10 also gives the averaging kernel of another instrument which is sensitive

broadly thoughout the troposphere, peaking at 12 km in the tropics (Barkley et al. 2006). This instrument, the Atmospheric Infrared Sounder (AIRS) instrument, was launched in May 2002 onboard NASA's AQUA satellite and is a high spectral resolution spectrometer that measures radiances in the TIR wavelength range (3.7-15.4 μm) with an IFOV of roughly 13.5 x 18 km^2 at nadir. AIRS radiances have been assimilated directly into the European Centre for Medium-Range Weather Forecasts (ECMWF) four-dimensional variational (4D-Var) system, allowing tropospheric CO_2 to be estimated (Engelen et al. 2004). However, due to atmospheric mixing in the upper troposphere, the CO_2 concentrations estimated from AIRS are quite zonal and can only provide information about broad features of surface fluxes (Chevallier et al. 2005a).

Similarly, the Infrared Atmospheric Sounding Inteferometer (IASI) and Advanced Microwave Sounding Unit (AMSU), launched together onboard the European MetOp platform in October 2006, can be used to retrieve CO_2 in the upper troposphere using the TIR wavelength range. Although these instruments provide accurate tropospheric CO_2 concentrations (0.5% monthly for a 5° x 5° footprint) they give little information on surface fluxes (Chevallier et al. 2005a, Crevoisier et al. 2009).

Studies have revealed that retrievals of CO_2 in the NIR exceed the performance of those in the TIR and provide more lower tropospheric information, provided the atmospheric scatterers are properley constrained (e.g. Christi & Stephens 2004). Furthermore, using the combination of the 1.61 and 2.06 μm NIR CO_2 bands with the 0.76 μm O_2 A band can provide precisions of 0.3-2.5 ppm when the scattering optical depth is less than 0.3 (Kuang et al. 2002). Encorporating the above, the latest generation of satellite instruments, launched in 2009, enable CO_2 to be estimated from observed radiances in these three bands. The NASA Orbiting Carbon Observatory (OCO) satellite consisted of a grating spectrometer designed to measure these bands (Connor et al. 2008). Unfortunately, during the launch of the OCO satellite, in February 2009, it failed to reach its desired orbit so no observations were possible. However, the Japanese Greenhouse gases Observing SATellite (GOSAT) was successfully launched into orbit in January 2009 to become the first satellite with the potential to allow CO_2 to be inferred within the required precision (JAXA 2009).

2.6 GOSAT

2.6.1 Overview

GOSAT was successfully launched on the 23rd January 2009 by JAXA's H-IIA rocket and was the first dedicated greenhouse gas satellite (JAXA 2009). Onboard GOSAT is the Thermal And Near-infrared Sensor for carbon Observation (TANSO) that is comprised of two instruments; a Fourier Transform Spectrometer (FTS) that is used to measure greenhouse gases, and a Cloud and Aerosol Imager (CAI) that provides information about the scene, such as cloud and aerosol quantities. Both instruments are kept looking towards the Earth's geocentric direction by a three-axis attitude control system. The power required for this as well as the sensor operation is gained from two solar panels that face the Sun. The satellite has a Sun synchronous orbit, optimising the power supply, and is quasi-recurrent with 14 + 2/3 revolutions per day (Kuze et al. 2009). GOSAT provides global measurements of total column CO_2 from its SWIR bands and of mid-tropospheric sub-columns from its TIR band.

The GOSAT project was developed jointly by the Japan Aerospace Exploration Agency (JAXA), the National Institute for Environmental Studies (NIES) and the Ministry of Environment (MOE). Its primary aim was to estimate emissions and absorptions of greenhouse gases with an increased accuracy on a sub-continental scale and to provide the environmental administration with an assessment of forest carbon balances, regional emissions and absorptions (JAXA et al. 2008). Research using GOSAT may provide an increased understanding of the global distribution and temporal variations of greenhouse gases. This could develop our knowledge of the carbon cycle on a global scale and its influence on the climate, which is essential for the prediction of climate change and its possible impacts. Additionally, it aims to lead to new developments in both Earth observation satellite measurement techniques and the approach of greenhouse gas measurements.

Studies have indicated (e.g. Kadygrov et al. 2009) that the assimilation of GOSAT observations into inverse models may provide an uncertainty reduction greater than that of surface networks alone and a larger improvement when both are assimilated (see Figure 2.11). Furthermore, the regional reduction in uncertainty has been assessed (see Figure 2.12 for example) and has shown large improvements over South America, Africa and Asia (Kadygrov et al. 2009).

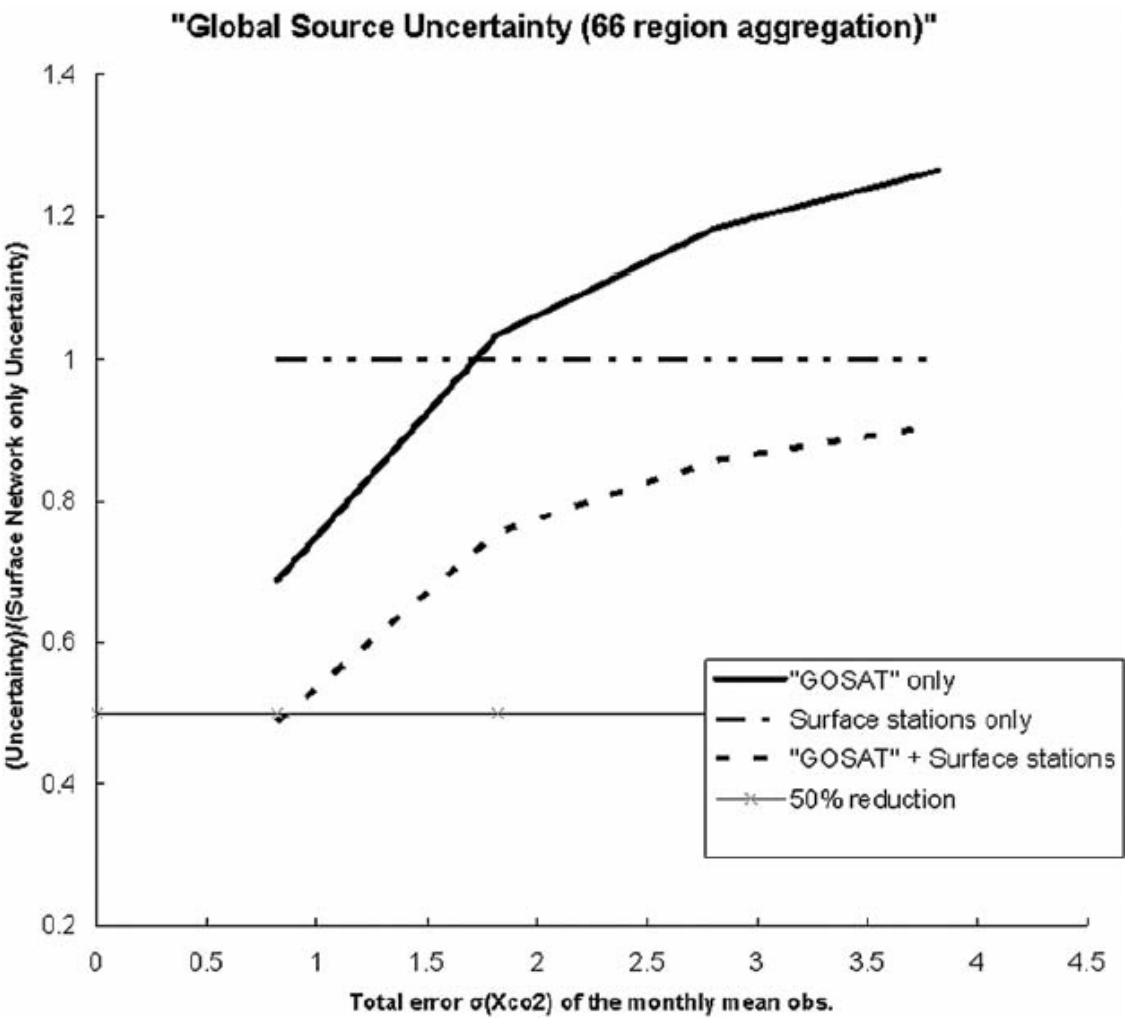

FIGURE 2.11. Comparison of global CO_2 flux uncertainties and standard deviation of monthly mean observations of X_{CO2} estimated for the assimilation of existing ground based measurement stations (dashdotted line), GOSAT (solid line), GOSAT and ground based stations (dashed line), and a 50% reduction level of existing total flux uncertainties. Figure taken from Kadygrov et al. (2009).

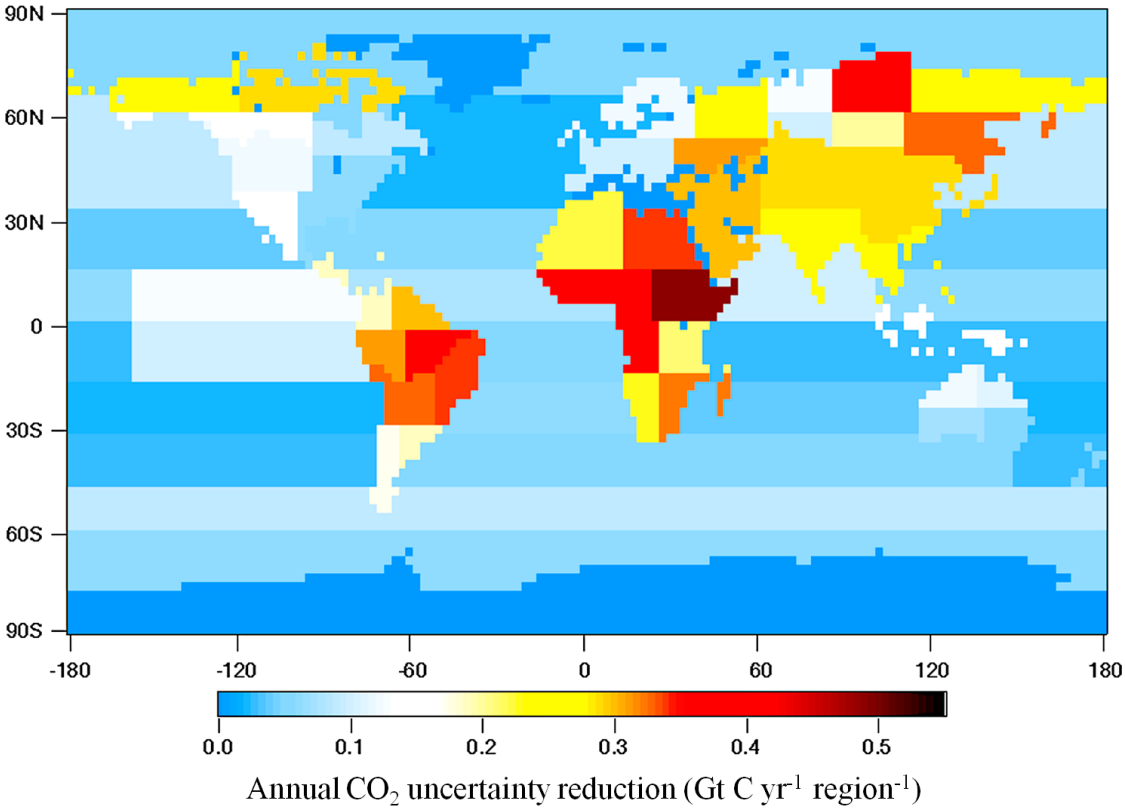

FIGURE 2.12. Annual CO_2 flux uncertainty reduction of GOSAT observations with 1.8 ppm precision for monthly mean and systematic error of 1 ppm. Figure taken from (Kadygrov et al. 2009).

2.6.2 Instruments

2.6.2.1 TANSO-FTS

TANSO-FTS comprises of three units; an electronic circuit unit, a control unit and an optical unit. The electronic unit is composed of a main and a redundant digital processing circuit that functions as a data processor, data-telemetries-commands-transmission interface with the satellite bus system and includes the temperature controller. The control unit acts as a controller for the cooling machine, the electronic cooling machine, the optical path switcher and solar irradiance diffusing board. It also functions as a driver and controller of the interferometer and the pointing mechanism. The optical unit contains the pointing mechanism (with redundancy), the blackbody diffusing board, the solar irradiance diffusing mechanism, the optical path switcher, monitoring camera, Fourier interferometer, relay and band splitting optics, the detector optics, analogue processing circuit and the cooling machine (Kuze et al. 2009).

The interferometer, based on the original Michelson interferometer (Michelson & Morley 1887), is a device that can split a beam of radiation into two separate paths and then recombine these after a path difference has been introduced. This creates a condition whereby interference between the two beams can occur. The intensity variations of the resulting beam is measured as a function of path difference by the detector.

The interferometer used by TANSO-FTS is of double pendulum type as shown in Figure 2.13. It uses corner cube mirrors which are statically aligned with each other and the rotary motor to maximise modulation efficiency with the minimum optical shear (Kuze et al. 2009). These are attached to a swing arm that is moved by the rotary motor with less than 1% speed stability, creating uniform frequency of the output modulated signal (Kuze et al. 2009). A rotary speed of four seconds is required in order to achieve a small enough sampling of the electrical bandwidth and the necessary signal to noise ratio (SNR). This is used as the nominal time for interferogram acquisition, although TANSO-FTS is also capable of faster scanning modes that allow denser observations but at the expense of SNR (Kuze et al. 2009).

Between the mirrors is a beamsplitter, where a beam of radiation from an external source can be partially reflected to one mirror and partially transmitted to the other mirror. Once reflected from the mirrors both beams return to the beam split and are partially reflected, transmitted and interfere. Due to the effect of interference, the intensity of the beam at the detector depends on the optical path difference (OPD) of the two beams. The OPD created are $\pm$ 2.5 cm, four times as long as the mechanical motion, and are

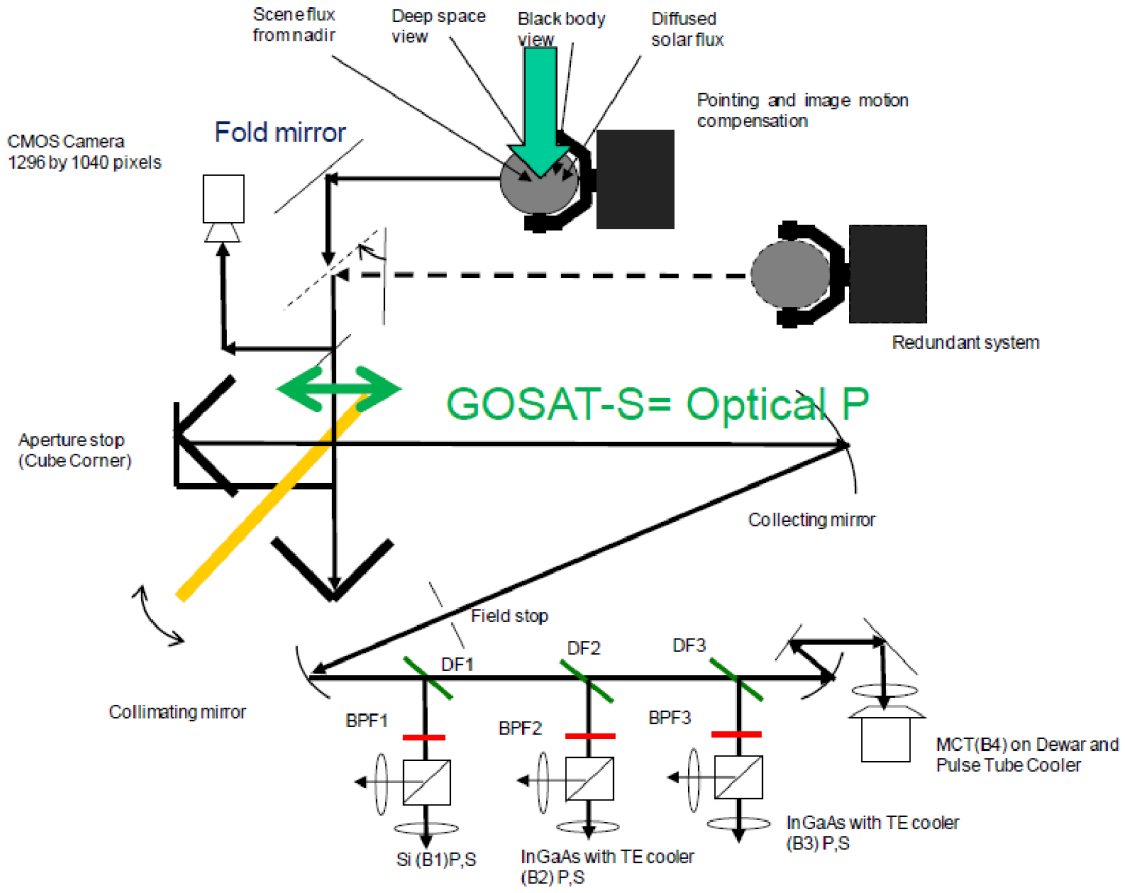

FIGURE 2.13. TANSO-FTS instrument design showing the major optic components and optical path. Figure taken from Kuze et al. (2009).

obtained to make both the real and imaginary spectra for suitable phase correction (Kuze et al. 2009).

The width of the beam splitter was selected to be larger than the maximum OPD to try to reduce the effects of channelling, which is caused by multiple reflections at the band separation optics (Kuze et al. 2009). The resulting light is reflected from a collecting mirror towards a circular slit, which due to its physical geometry forces the different spectral bands to be adequately aligned. The circular slit's geometry was designed to provide the maximum efficiency while maintaining within the maximum IFOV divergence for band 2 for 0.2 cm^{-1} spectral resolution (Kuze et al. 2009). This defines the IFOV to be 15.8 mrad, equivalent to 10.5 km projected onto the surface of the Earth (Kuze et al. 2009). The narrowed light passes to a collimating mirror and is then split through dichroic filters for each band in series. To minimize the background TIR, these filters transmit longer wavelength light and reflect shorter wavelength light. This min-

imises the polarization sensitivity of the shorter wavelengths which then travel though a narrow band-pass filter. These are divided by a beam splitter into two polarizations, parallel (P) and perpendicular (S), that are then measured by two detectors. The band-pass filters are fixed to reduce channelling, to decrease stray light and to discard shorter wavelength light to evade aliasing (indistinguishable signals). While band 1 is measured by two Silicon detectors, both bands 2 and 3 are measured using Indium Gallium Arsenide (InGaAs) detectors that are non-biased and cooled to -40 °C using thermoelectric coolers which minimises dark currents. The TIR light is observed by a Photo-Conductive (PC) Mercury Cadmium Telluride (HgCdTe) (MCT) detector that is cooled to 70 K using a pulse tube cooler with low vibration, which does not influence the interferogram (Kuze et al. 2009).

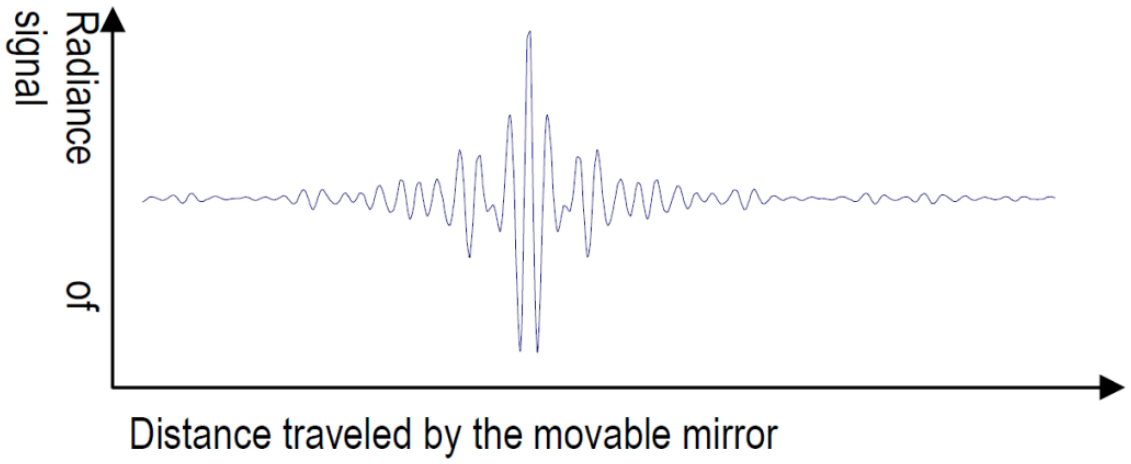

FIGURE 2.14. Example interferogram data. Figure obtained from JAXA et al. (2008).

The interferogram is essentially the interference pattern of the two beams recorded as the OPD changes, and an example of this is shown in Figure 2.14. The measured spectral radiances are obtained by inverse Fourier transforming the interferograms and provide information of absorption in the atmosphere. Figure 2.15 shows example radiances for each of the GOSAT spectral bands.

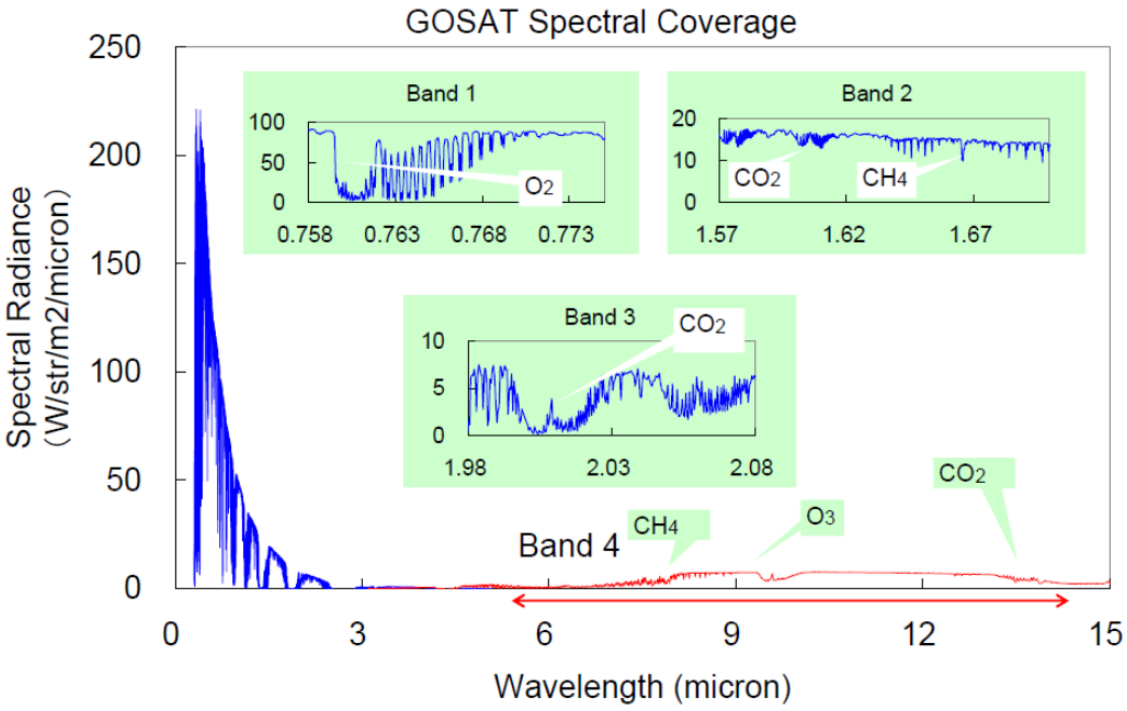

FIGURE 2.15. Example TANSO-FTS radiances for each spectral band with the main atmospheric gases that absorb radiation within those bands shown. Figure taken from JAXA et al. (2008).

2.6.2.2 TANSO-CAI

TANSO-CAI consists of an electronics unit and an optics unit with the aim to observe radiances which could allow different aerosol types and optical thicknesses to be derived. The electronics unit functions as a data processor and command interface with the satellite. The optics unit has three telescopes covering four spectral bands; 0.380 ± 0.005 μm (band 1), 0.674 ± 0.005 μm (band 2), 0.870 ± 0.005 μm (bands 3), and 1.600 ± 0.01 μm (band 4). These bands were chosen specifically to avoid water vapour and oxygen absorption, as well as to provide information on polarisation which can not be obtained by the observing angles due to TANSO-CAI being very close to nadir (Kuze et al. 2009). Additionally, each spectral band was selected to provide useful information; band 1 can observe aerosols over land where the albedo is small, bands 2 and 3 are shorter/longer than the red-edge where reflectance of vegetation changes, and band 4 gives measurements in the same spectral region as the CO_2 in TANSO-FTS band 2. TANSO-CAI has a wide swath of $\pm$ 36.1° with continuous spatial coverage and higher spatial resolution than TANSO-FTS providing sub-pixel information, such that it can detect clouds and aerosols outside of the TANSO-FTS field of view (Kuze et al. 2009).

2.6.3 Observation Modes

GOSAT TANSO-FTS nominally performs a cross-track scanning pattern (see Figure 2.16) where the number of lattice points can be varied from one to nine points per one cross-track scan, with five points being normal (Kuze et al. 2009). Additionally, it can measure in a specific observation mode which provides targeted observations for validation and experimental purposes. It can also measure over the ocean using the sun glint mode, aiming where the Sun light is reflected off of the waves of the ocean causing the radiance to be very high. However, this can only be measured at certain solar zenith angles which vary with latitude depending on the season. This overcomes the difficulty of measuring SWIRs over the ocean that have very low albedo, hence a low radiance and low signal-to-noise ratio (SNR). TANSO-FTS also applies a signal amplification factor (gain) to the SWIR signals to amplify the signal to an appropriate voltage to compensate for high and low intensities. It has the option of three gain levels; low, medium and high. Normally the high gain is used due to most land surfaces having a low albedo, however the medium gain is applied over high albedo regions such as deserts. The fourth instrument channel measures the TIR region that allows vertical profiling over both land and ocean. SWIRs can only be measured in day time since it depends on reflected sun light, but TIR measurements are made throughout both day and night time, as the Earth will ra-

diate TIR from the surface. The instrument uses a solar irradiance (light directly from the Sun) calibration for the SWIR observations and a blackbody calibration for the TIR observations. It also performs deep-space and lunar calibrations for both SWIR and TIR bands (Kuze et al. 2009). Furthermore, the specific observation mode has been utilised for vicarous calibration of both TANSO-FTS and TANSO-CAI by aiming at the Railroad Valley Desert in Nevada, USA (Kuze et al. 2011).

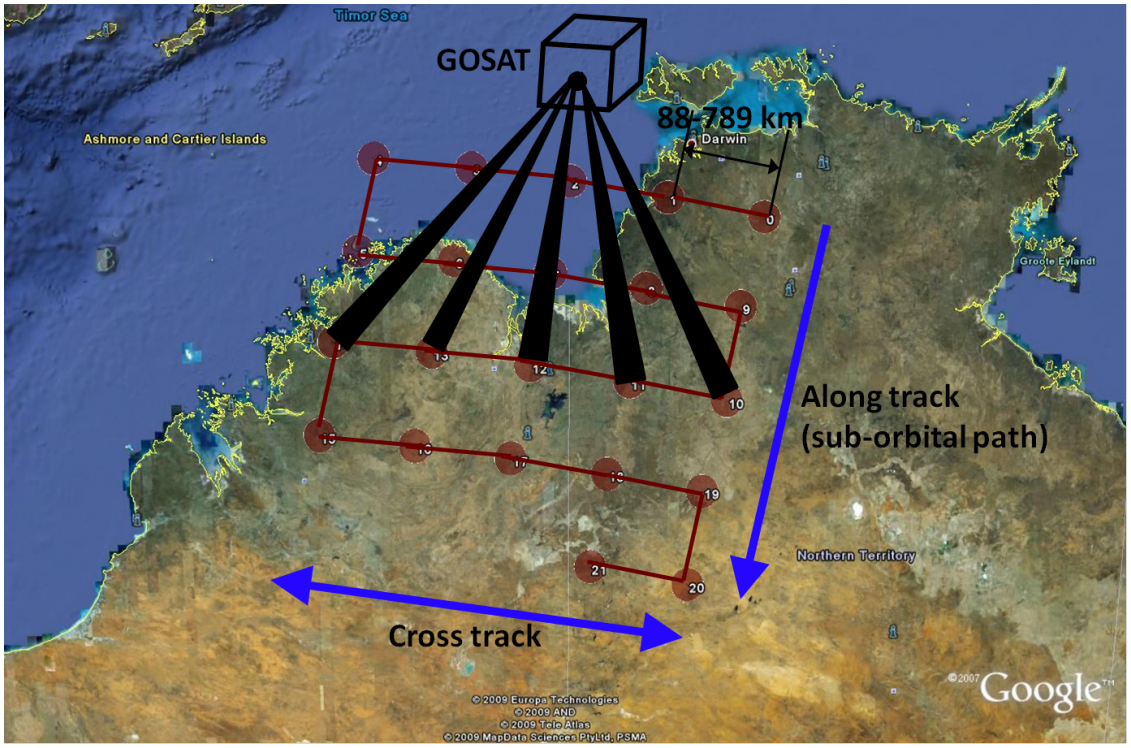

FIGURE 2.16. Diagram illustrating the observation points of TANSO-FTS in 5-point mode for one scene over Australia during April 2009.

2.7 Current Operational Performance

GOSAT has generally performed as expected during its current lifetime, however a couple of issues have arisen. The solar diffuser is used to calibrate the spectral radiances observed by TANSO-FTS with the irradiance from the Sun. Unfortunately, degradation of the solar diffuser has been found, see Figure 2.17. Since all TANSO-FTS spectral radiances rely on the solar diffuser for signal calibration a correction would be required for this. Until recently, a preliminary radiometric factors were provided by NIES to try to compensate for the degradation. However, Yoshida et al. (2012) provides a more accurate method of correction, but this has not been applied to the results shown in Chapter 4.

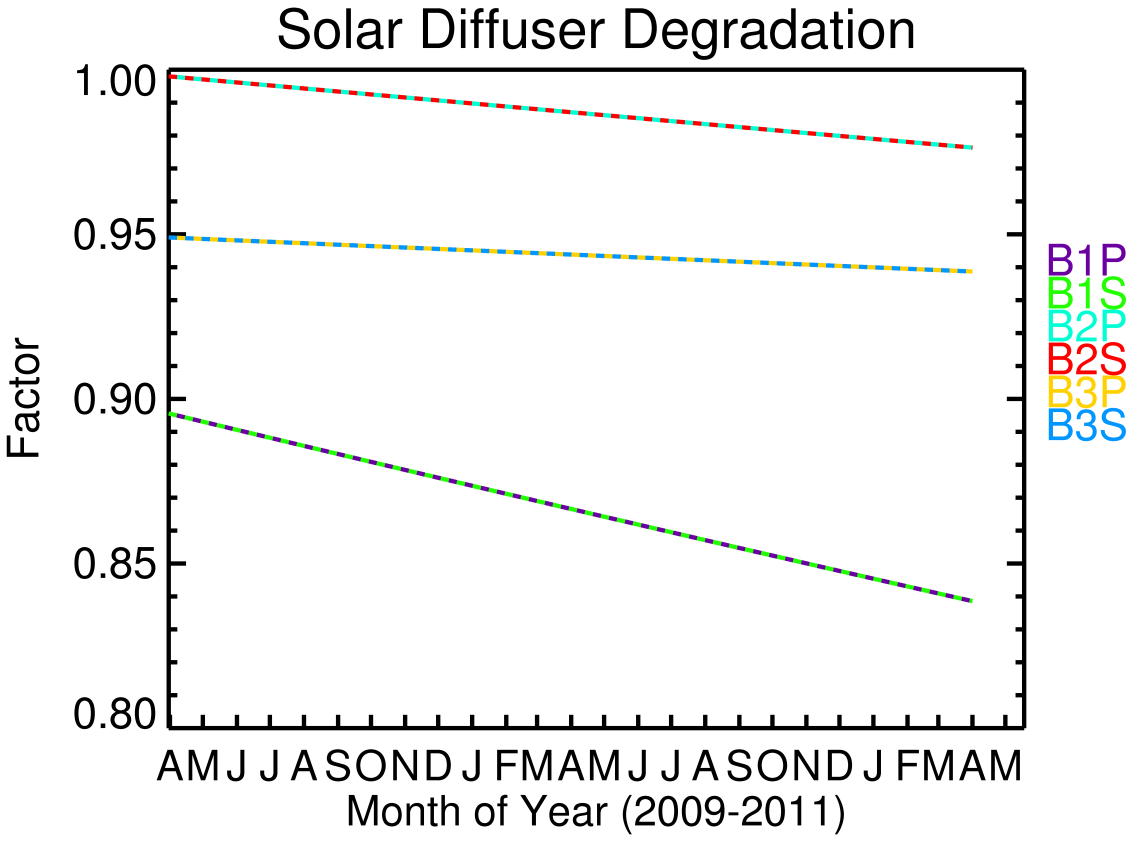

FIGURE 2.17. Solar diffuser degradation factor for each TANSO-FTS spectral band and polarisation.

Secondly, instability has been found in the pointing mirror of TANSO-FTS leading to the location of the observed points being incorrect. Microvibrations in the pointing mirror increase towards larger pointing angles causing the outermost observation points to become most affected with cross-track pointing being up to approximately 1 km incor-

rect in some cases (Kuze et al. 2011). This is further complicated as the pointing mirror also rotates along-track causing the outermost cross-track points to be at a larger angle. Additionally, the pointing mirror reverses in the cross-track direction at the outermost points, causing these points to be increasingly succeptable to unstable movements, with errors in the IFOV location of up to about 10 km (Yoshida 2011). The pointing error was preliminarily analysed by JAXA by comparing onboard camera (CAM) images with TANSO-FTS locations. The amplitude of the offset and the variability was found to be substantially reduced when using three cross-track points, rather than five points, likely due to the pointing mirror being moved by smaller angles. Therefore, after August 2009 the nominal observation mode was changed from five to three points. The pointing error has been investigated by NIES and a separate product (simplified L2 Input Data Sets) has only recently been made available in 2012 which includes corrected geolocation data.

Also, a non-linear response of the band 1 detector to the intensity of incident radiation was found recently (Frankenberg et al. 2011a) and is currently being characterised and calibrated for (Crisp et al. 2012, Suto et al. 2011). Additionally, Frankenberg et al. (2011a) found GOSAT observes fluorescence lines in the O_2 A band. The latest TANSO-FTS Level 1B datasets (130.130C, 141.141C, and 150.150C) released by NIES include corrections for the band 1 detector.

2.8 Summary

Although previous satellites have successfully provided global spatial and temporal trends in CO_2, their designs were not suited to the precision required to allow surface flux inversions to resolve sources and sinks of CO_2 on a sub-continental scale. Both OCO and GOSAT were specifically planned to meet this need, and with the successful launch of GOSAT there is currently a satellite that could potentially allow precise CO_2 measurements to be inferred. The next chapter describes a new retrieval algorithm developed to retrieve CO_2 from GOSAT observations.

Chapter 3

Retrieval of Atmospheric CO_2 from GOSAT

3.1 Algorithm Overview

The University of Leicester Full Physics (UoL-FP) retrieval algorithm was developed to infer column-averaged dry air mole fractions of CO_2 (X_{CO2}) from GOSAT SWIR measurements. UoL-FP retrieval utilises the algorithm developed for the NASA Orbiting Carbon Observation (OCO) mission (Boesch et al. 2006, 2011, Connor et al. 2008, Crisp et al. 2012, Parker et al. 2011), which was lost due to a launch vehicle malfunction (Boesch et al. 2011). The UoL-FP algorithm and the algorithm used for the NASA Atmospheric CO_2 Observations from Space (ACOS) project and the NASA OCO-2 mission (Crisp et al. 2012, O'Dell et al. 2012), are two parallel developments based on the OCO algorithm and thus both algorithms follow a similar retrieval strategy. While the UoL-FP algorithm utilises the OCO algorithm, the ACOS algorithm is a re-development of it such that the implementation of both algorithms are independent of each other. Both retrieval algorithms differ in their definition of the state vector, a priori values, and a priori covariances, especially in the treatment of aerosols and cirrus clouds. There are also differences in spectroscopy, sounding selection methods, and post-screening criteria. All of these aspects can lead to differences in algorithm performance and X_{CO2}.

The UoL-FP retrieval algorithm comprises of a pre-processing algorithm, a cloud-screen, a post-processing algorithm and the OCO Level 2 Full Physics retrieval algorithm which has been modified to be used with GOSAT observations. This chapter provides details of the UoL-FP retrieval algorithm design and how X_{CO2} can be accurately retrieved from GOSAT SWIR radiances.

3.2 Retrieval Algorithm

The key problem of retrieving CO_2 from measured SWIR spectra is that the discrete measurements are a function of many parameters (e.g. CO_2, H_2O, CH_4, albedo, temperature, pressure, and aerosols) that we may or may not accurately know, creating an underconstrained situation with no unique solution. It is therefore necessary to use additional prior information to constrain the solution to be realistic compared to real atmospheric observations. An explanation of the relevant aspects of retrieval theory are given in this section and a detailed description is given in Rodgers (2000). A brief overview of this module, illustrating the main aspects involved, is shown in Figure 3.1.

The UoL-FP algorithm has been designed to accurately retrieve X_{CO2} from SWIR spectra by simulateneously fitting the 0.76 μm O_2 A band, the 1.61 μm and the 2.06 μm CO_2 bands (Boesch et al. 2006, 2011, Connor et al. 2008). The algorithm employs the inverse method, where an iterative retrieval system based on Bayesian optimal estimation (maximum likelihood estimation) fits the simulated spectral radiance to the measured spectral radiance in order to infer X_{CO2} (Rodgers 2000). The OCO algorithm has been modified to perform retrievals of X_{CO2} from each of the GOSAT SWIR bands using the wavelength ranges of 0.7575-0.7722 μm, 1.5880-1.6231 μm, and 2.0399-2.0833 μm.

The simulated spectral radiance is derived using a forward model that uses solar, radiative transfer, and instrument models to simulate the spectral radiance of a scene based on a set of parameters, known as the state vector, with initial a priori values. The low-streams interpolation functionality (O'Dell 2010) is used to accelerate the Linearized Discrete Ordinate Radiative Transfer model (LIDORT) (Spurr et al. 2001) which is combined with a fast 2-orders-of-scattering vector radiative transfer code (Natraj & Spurr 2007).

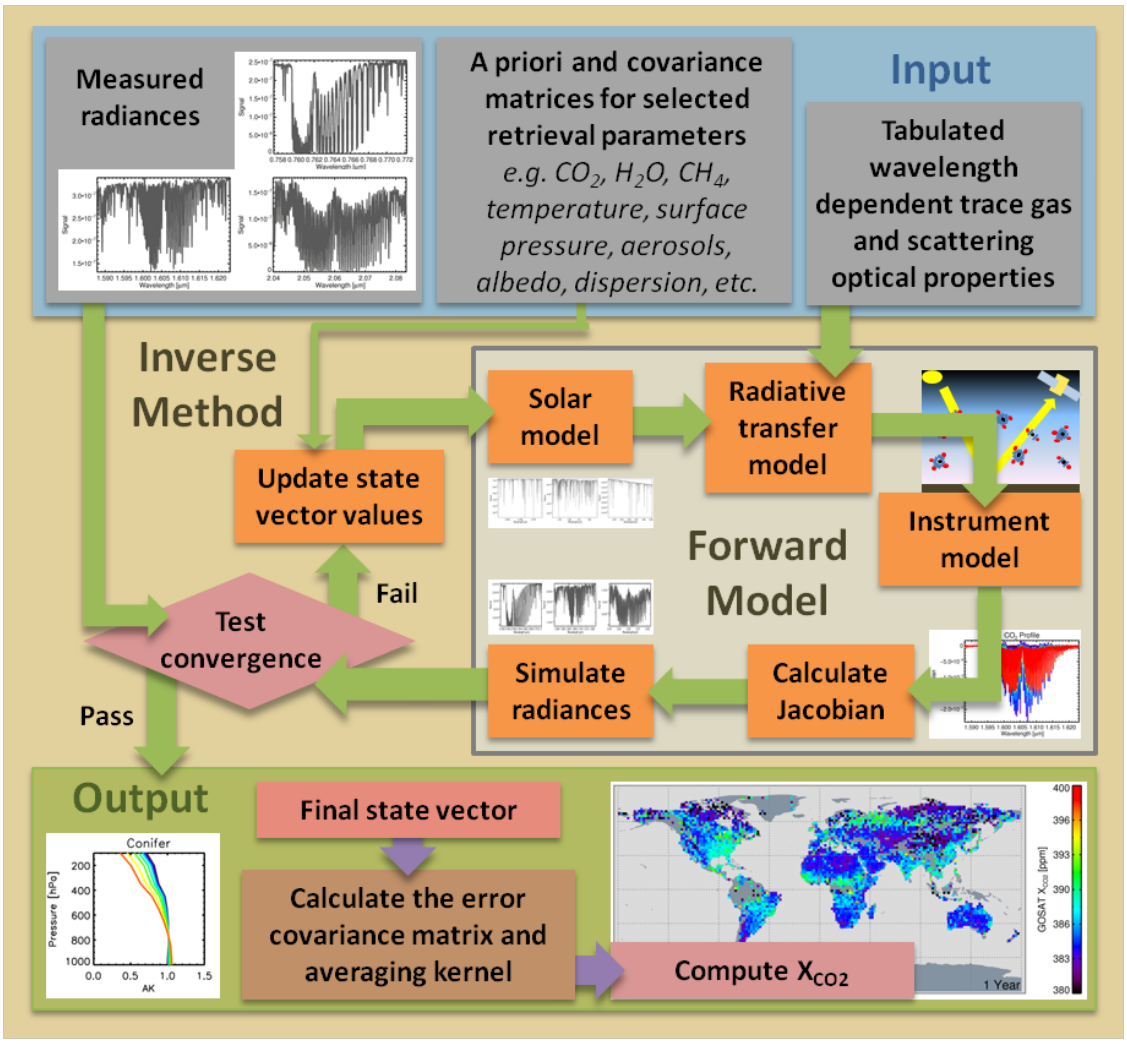

FIGURE 3.1. Overview of the retrieval module used in the UoL-FP retrieval algorithm.

3.3 The State Vector

The state vector gives the retrieved parameters and consists of a 20-level profile of CO_2 volume mixing ratio (VMR) and 20-level logarithmic extinction profiles of cirrus and two aerosol types. The number of profile levels chosen provides a compromise between retrieval accuracy and computational speed. In addition, the state vector includes multiplicative scaling factors for CH_4 VMR and H_2O VMR, an additive offset for a temperature profile, surface pressure, surface albedo, spectral albedo slope, and spectral shift/stretch. An additive O_2 A band intensity offset is also retrieved to mitigate the effects of fluorescence and the GOSAT Band 1 non-linear response to the intensity of incident radiation, that is currently being characterized and calibrated (Crisp et al. 2012, Frankenberg et al. 2011a, Suto et al. 2008). The state vector structure presently consists of 97 state vector elements as shown in Table 3.1.

Table 3.1. State Vector for CO_2 retrievals

Description	Parameters	Number of Elements
Aerosols	3 x 20 levels	60
CO_2	20 levels	20
Albedo	2 x 3 bands	6
Dispersion	2 x 3 bands	6
Zero-Level Offset	Scalar	1
Surface Pressure	Scalar	1
Temperature	Scalar	1
Water Vapour	Scalar	1
CH_4	Scalar	1
Total		97

The UoL-FP retrieval algorithm includes a pre-processing stage that generates all the a priori values needed for retrievals and applies any neccesary calibrations to the GOSAT measurements. These a priori values are used firstly in the cloud screen and then in the CO_2 retrievals. The cloud screen is based on an O_2 A band retrieval of surface pressure and is explained in detail in Section 3.21. The O_2 A Band retrieval has a state structure of 5 elements; surface pressure, albedo scaling, albedo slant, spectral shift and spectral stretch. The retrievals for CO_2 are then performed on only cloud screened exposures and use a state structure that represents the atmosphere, surface and instrument (see Table 3.1). The results from these CO_2 retrievals are gathered together and subjected

to a post-processing stage, which essentially applies a post-screen to the results to only keep retrievals which performed well, see Section 3.22. An overview of the algorithm is given by Figure 3.2, showing the main steps involved to infer X_{CO2} from GOSAT observations.

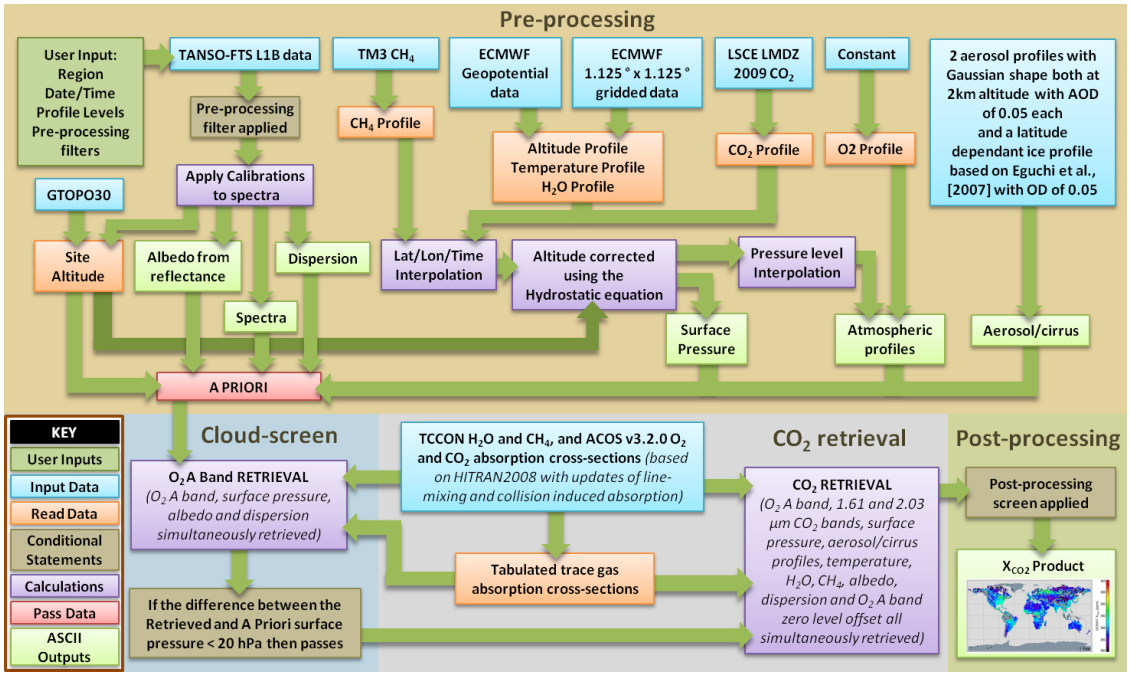

FIGURE 3.2. Overview of the UoL-FP retrieval algorithm, providing the flow of information passing between different steps of the algorithm. These steps are grouped into four main modules; the pre-processing, cloud-screen, CO_2 retieval and post-processing modules.

3.4 Forward Model

The forward model simulates spectra based on the state vector, **x**, that comprises of n parameters, such as temperature, pressure and volume mixing ratios that are retrieved. The measurement vector, **y**, represents a set of m measurements and can be related to the state vector by

$$\mathbf{y} = \mathbf{F}(\mathbf{x}, \mathbf{b}) + \mathbf{e} \tag{3.1}$$

where the vector **y** is the measurement containing GOSAT radiances with measurement error **e**, the foward function **F** represents the relationship between the measurement vector and state vector, and the forward function parameter, **b**, represents all non-retrieved parameters that are used in the forward model but are assumed to already be accurately known.

The forward model consists of three major modules; a radiative transfer (RT) model, a solar model, and an instrument mode. The solar model described in Boesch et al. (2011) was used, which provides a high-resolution empirical list of absorption lines for the full solar disk. It includes over 20,000 absorption lines with their corresponding frequency, strength and doppler width. The solar spectrum is obtained by calculating the Planck function for the Sun and multiplying with the listed solar absorption lines. The continuum radiance of the solar model is based on a polynomial fit to the NIR range of the extra-terrestrial solar spectrum acquired by the SOLSPEC instrument (Thuillier et al. 2003). The solar model is assumed time independent but allows the continuum radiance to be adjusted by the Earth-Sun distance. Figure 3.3 shows the solar continuum with solar absorption lines for each SWIR band retrieved.

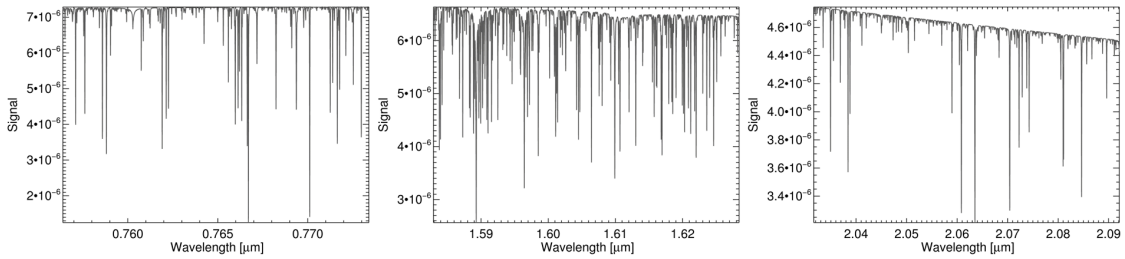

FIGURE 3.3. The solar continuum and solar absorption lines of each SWIR band used in the UoL-FP retrieval algorithm.

The RT model calculates the transfer of radiation throughout the beam path based on a priori information for atmospheric and surface parameters. It uses the LIDORT model which simulataneously derives backscatter intensities for a plane parallel, multi-layered,

multiple-scattering atmosphere at arbitrary elevation angles and a set of atmospheric variations. The computational speed of the RT model was increased by using two orders of scattering and the low-streams interpolation functionality (O'Dell 2010). This computes low accuracy line-by-line RT calculations which are corrected by an error curve derived from the computation of both low and high accuracy RT calculations for a number of wavelengths throughout the bands.

For absorption within the Earth's atmosphere, the RT model utilises tabulated spectroscopic parameters for each trace gas. CO_2 and O_2 include line-mixing and are taken from v3.2 of the OCO linelists (Crisp et al. 2012), whereas CH_4 and H_2O are from the TCCON linelists (Wunch et al. 2011a). These are based on HITRAN08 (Rothman et al. 2009) with updates to CO_2 (Toth 2005), H_2O (Toth et al. 2008, Jenouvrier et al. 2007) and CH_4 (Frankenberg et al. 2011b). The absorption lines and strengths are applied to the solar spectrum using Voigt line shapes.

The instrument model is used to generate noise and intensity and different wavelengths with respect to the instrument line shape (further discussed in Section 3.19), using a priori information of the instrument parameters.

3.5 Jacobian

Measurements are typically non-linear, so linearisation of the forward model about some reference state, $\mathbf{x}_0$, is required to be able to examine the information content within a measurement. Providing that the forward model is linear within the error bounds of the retrieval, Equation 3.1 can be linearlised to get

$$\mathbf{y} - \mathbf{F}(\mathbf{x_0}) = \frac{\partial \mathbf{F}(\mathbf{x})}{\partial \mathbf{x}}(\mathbf{x} - \mathbf{x_0}) + \mathbf{e} \tag{3.2}$$

where the partial derivative d**F**/d**x** denotes the sensitivity of the Forward model to the change in the state vector, **x**. This quantity is known as the Jacobian, **K**, and is a matrix consisting of m forward model elements (number of measurements) with respect to n state vector elements (number of parameters retrieved). Thus if there are more elements in the measurement vector than unknowns in the state vector (m>n) then the retrieval can be described as over-constrained. Similarly if there are less elements in the measurement vector than unknowns in the state vector (m<n) then the retrieval is under-constrained. The state vector is described in detail in Section 3.3.

An example of the partial derivatives of each state vector element is given in Figures 3.4, 3.5 and 3.6, which were calculated during a CO_2 retrieval from GOSAT for the 4th September 2009 over Lamont/USA. Figure 3.4 gives the Jacobians of CO_2, aerosols and cirrus for each atmospheric retrieval level and wavelength retrieved. The Jacobian for CO_2 is large in the 1.61 and 2.06 μm bands, specifically where CO_2 absorption lines occur, and zero in the O_2 A band where no CO_2 absorption occurs. Additionally, the Jacobian for CO_2 remains large throughout the atmospheric profile. The aerosol/cirrus Jacobians show some sensitivity to all absorption lines (O_2, H_2O, CO_2, etc) in all three wavelength bands. The aerosol Jacobian is larger towards lower atmospheric levels, whilst the cirrus Jacobian is only sensitive at about 200 hPa, reflecting the optical depth at each level.

Figure 3.5 shows the Jacobians of surface pressure, temperature, H_2O, CH_4 and O_2 A band zero level intensity offset for the same example retrieval. The Jacobian of surface pressure shows sensitivity to absorption lines, whilst the temperature scalar Jacobian appears inversely proportional to all absorption lines. The Jacobian of the H_2O scale factor relates to water vapour absorption lines, thus there is no sensitivity in the O_2 A band. Similarly, there are no CH_4 absorption lines in the O_2 A band, so the Jacobian of the CH_4 scale factor only corresponds to CH_4 absorption lines in the 1.61 and 2.06 μm bands. The zero level offset Jacobian only relates to the O_2 A band where this intensity

offset is retrieved.

The albedo, albedo slope and dispersion shift/stretch Jacobians for the example retrieval are shown in Figure 3.6. The albedo Jacobian is zero for all bands, showing no sensitivity of the foward model to a change in albedo, since albedo acts to change the overall intensity of each band and is not related to absorption. The albedo slope changes the intensity and absorption across each band, so the Jacobian therefore shows sensitivity to all absorption lines and varies in sensitivity across each band. The dispersion shift represents the wavelength shift needed for the Forward model to match the measured spectra. Since the pre-processing module adjusts the wavenumbers of the GOSAT measured spectra to match a well known Solar absorption line, the dispersion shift will not change much during a retrieval. Thus, the Jacobian of the dispersion shift is zero in all bands. However, the dispersion stretch is also retrieved and the Forward model will be sensitive to any variations of this as it can cause corresponding modelled and measured absorption lines to differ in wavelength, as illustrated by the Jacobian.

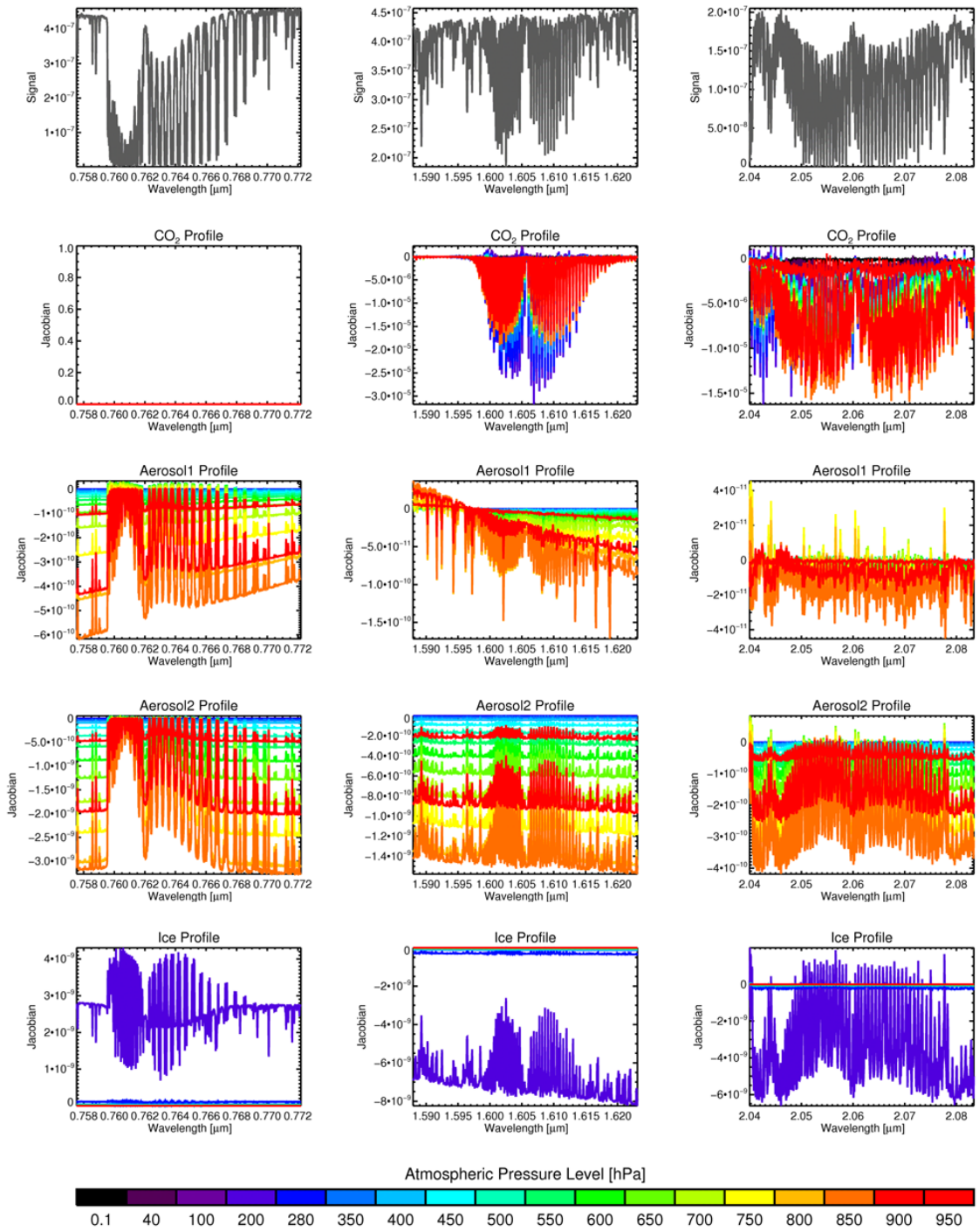

FIGURE 3.4. Example of the Jacobians of CO_2, aerosols and cirrus profiles for each SWIR band retrieved, with the measured signal from GOSAT given in the top panels for reference. The profile levels are shown using different colours, where red represents the boundary layer and black represents the top of the atmosphere. This retrieval was from GOSAT SWIR radiances for the 4th September 2009 over Lamont/USA and passed all screens.

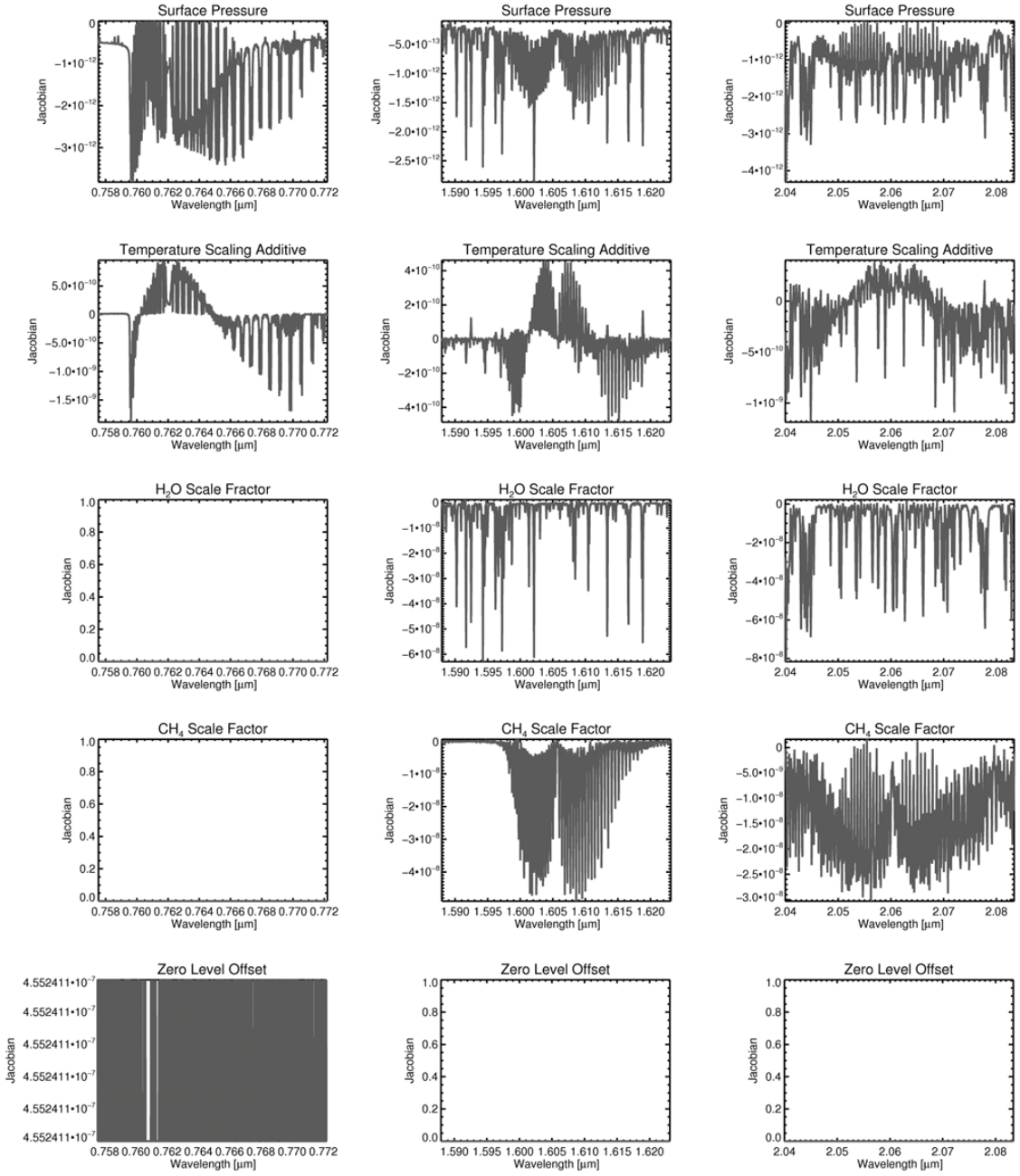

FIGURE 3.5. Example of the Jacobians of surface pressure, temperature, H_2O, CH_4 and O_2 A band zero level intensity offset. This retrieval was from GOSAT SWIR radiances for the 4th September 2009 over Lamont/USA.

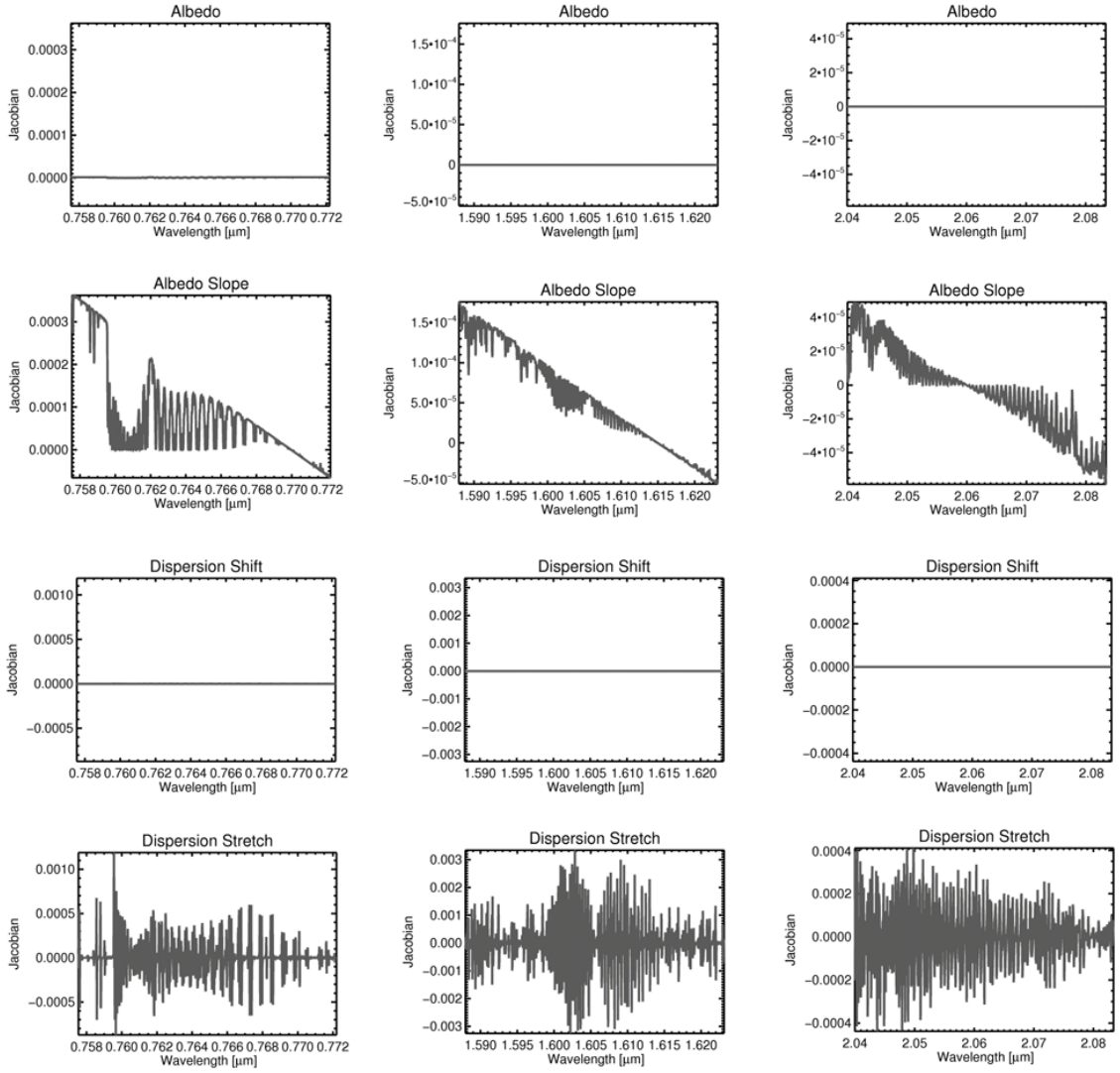

FIGURE 3.6. Example of the Jacobians of albedo, albedo slope and dispersion shift/stretch. This retrieval was from GOSAT SWIR radiances for the 4th September 2009 over Lamont/USA.

3.6 Inverse Method

In an under-constrained retrieval scenario there are less measurements than unknown state vector elements. This can be constrained using a priori information.

In an over-constrained retrieval case there are more measurements than unknown state vector elements, but even in an ideal situation the extra measurement information does not provide any new information to the retrieval. It is more likely in reality that there would be no solution that agrees with all of the measurements, since each will have an error associated with it. Whether under or over-constrained, an optimal estimation approach may be used to find the best solution.

3.7 Optimal Estimation

Optimal estimation uses an a priori estimate of the state vector to constrain the retrieval to find reasonable solutions, which might not be possible from only the measurements. Since this does not obtain a unique solution, the optimal solution can be gained by two possibilities; the most probable state where d$\mathbf{P}(\mathbf{x},\mathbf{y})$/d$\mathbf{x}$=0 or the expected state, $\hat{x}$, which is the mean state averaged over its probability density function (PDF)

$$\hat{\mathbf{x}} = \int \mathbf{x}\mathbf{P}(\mathbf{x} \mid \mathbf{y})\,\mathrm{d}\mathbf{x} \tag{3.3}$$

Assuming the probability fits a Gaussian model, hence the PDF is symmetric about its maximum, the most probable state equals the expected state.

The most probable state is determined by minimising the cost function. The cost function represents the different minimum costs yielded by optimising the difference between the measured and modelled spectra as well as the difference between the state vector and the a priori. The cost function can be written as

$$X^2 = (\mathbf{y} - \mathbf{K}\mathbf{x})^{\mathbf{T}}{\mathbf{S}_\mathbf{y}}^{-\mathbf{1}}(\mathbf{y} - \mathbf{K}\mathbf{x}) + (\mathbf{x} - \mathbf{x_a})^{\mathbf{T}}{\mathbf{S}_\mathbf{a}}^{-\mathbf{1}}(\mathbf{x} - \mathbf{x_a}) \tag{3.4}$$

where $\mathbf{x}_a$ is the a priori estimate of the state vector. The most probable state can then be expressed as

$$\hat{\mathbf{x}} = \mathbf{x_a} + (\mathbf{K}^{\mathbf{T}}{\mathbf{S}_\mathbf{y}}^{-\mathbf{1}}\mathbf{K} + {\mathbf{S}_\mathbf{a}}^{-\mathbf{1}})^{-\mathbf{1}}\mathbf{K}^{\mathbf{T}}{\mathbf{S}_\mathbf{y}}^{-\mathbf{1}}(\mathbf{y} - \mathbf{K}\mathbf{x_a}) \tag{3.5}$$

3.8 Iterative Approach

The most probable state found might be far from the true solution. To reach a state closer to the truth an iterative approach can be used, with each iteration re-running the forward model but with priori information gained from the previous iteration. This priori information is most likely to be closer to the true solution and would result in the forward model producing a state closer to the truth. However, that may not always be the case. Therefore, to attempt to obtain a solution closer to the truth the Gauss-Newton scheme (Rodgers 2000) is used to force the state to significantly change to find a state closer to the truth. This iterative approach minimises the cost function, such that for each iteration step the foward model is used to re-calculate the Jacobians and the modelled spectra. Assuming the retrieval is not too non-linear the Gauss-Newton iteration solution can be given as

$$\mathbf{x_{i+1}} = \mathbf{x_i} + \left[\mathbf{S_a}^{-1} + \mathbf{K_i}^{\mathbf{T}}\mathbf{S_e}^{-1}\mathbf{K_i}\right]^{-1}\left[\mathbf{K_i}^{\mathbf{T}}\mathbf{S_e}^{-1}\left(\mathbf{y} - \mathbf{F}\left(\mathbf{x_i}\right)\right) - \mathbf{S_a}^{-1}\left(\mathbf{x_i} - \mathbf{x_a}\right)\right] \quad (3.6)$$

where the first iteration, $\mathbf{x}_0$, is set to the a priori state vector, $\mathbf{x}_a$. However, if the solution is too far from the true solution or if the retrieval is too non-linear then the Gauss-Newton method becomes inadequate. In this scenario the Levenberg-Marquardt method (Rodgers 2000) is included whereby an adjustable factor, γ, is used to minimise the cost function. The iteration is then

$$\mathbf{x_{i+1}} = \mathbf{x_i} + \left[(\mathbf{1}+\gamma)\,\mathbf{S_a}^{-1} + \mathbf{K_i}^{\mathbf{T}}\mathbf{S_e}^{-1}\mathbf{K_i}\right]^{-1}\left[\mathbf{K_i}^{\mathbf{T}}\mathbf{S_e}^{-1}\left(\mathbf{y} - \mathbf{F}\left(\mathbf{x_i}\right)\right) - \mathbf{S_a}^{-1}\left(\mathbf{x_i} - \mathbf{x_a}\right)\right] \quad (3.7)$$

After each iteration γ is either increased or decreased by an arbitrary factor depending on the cost function. If the cost function increases then γ is increased and the same iteration is re-attempted. Whereas if the cost function decreases then γ is decreased, the state vector is updated, and the next iteration is performed. This process continues until the retrieval converges.

3.9 Convergence

At the end of an iteration three tests are performed. First, the updated cost function plus the previous cost function is compared to the cost function forecast plus the previous cost function to give a ratio, as described in Section 3.8. If this ratio is < 0.25 then the model has diverged away from the measurement and the iteration is repeated with an increased

γ factor. If the ratio is between 0.25 and 0.75 then the model has become closer to the measurement but not close enough so another iteration is performed. If the ratio is $>$ 0.75 then the model and measurement are said to have converged (Rodgers 2000). The second test of convergence compares the error variance derivative (dσ^2) with the dσ^2 of the previous iteration. If the difference is less than or equal to the number of state vector elements then convergence is achieved, otherwise iterations are continued. The error variance derivative is expressed as

$$d\sigma_i^2 = \mathbf{dx_{i+1}}^{\mathbf{T}} \hat{\mathbf{S}}^{-\mathbf{1}} \mathbf{dx_{i+1}} \tag{3.8}$$

where the covariance of the retrieved state is given by $\hat{S}$. Both of these tests must be passed for the retrieval to actually converge. The third test computes the χ^2 of the fit to check quantitively how good the model compares to the measurement. If the normalised χ^2 is less than 1 then it is a good fit, between 1 and 10 is a reasonable fit, and greater than 10 is a poor fit (Rodgers 2000). However, the normalised χ^2 is also dependent on the assumptions of noise.

Upon convergence the retrieved X_{CO2} can be resolved as

$$X_{CO2} = \mathbf{h^T \hat{x}} \tag{3.9}$$

where the pressure weighting operator, **h**, has elements of zero for all non-CO_2 elements.

The averaging kernel expresses the ability of the retrieval to constrain the true state, hence how sensitive the algorithm is to the truth throughout the atmosphere, and is defined as

$$\mathbf{A} = \frac{\mathbf{d\hat{x}}}{\mathbf{dx}} = \mathbf{S K^T S_e K} \tag{3.10}$$

where **S** is the a posteriori error covariance, which provides a measure of the estimated accuracy of the solution and is given by

$$\mathbf{S} = (\mathbf{K^T S_e K} + \mathbf{S_a}^{-\mathbf{1}})^{-\mathbf{1}} \tag{3.11}$$

The column averaging kernel can then be calculated as

$$\mathbf{a^T} = \mathbf{h^T A} \tag{3.12}$$

where an averaging kernel with a value of 1 is good and 0 is bad. Additionally, the X_{CO2} error variance is computed by

$$\sigma^2_{X_{CO2}} = \mathbf{h^T S h} \tag{3.13}$$

3.10 Covariance Matrix

The covariance matrix defines the correlation and constraint of a state vector element within the retrieval scheme. $\mathbf{S}_y$ is the measurement error covariance matrix where the diagonal elements are the variances of the individual elements of **y** and the off-diagonal elements give the covariance between the different elements of **y**. Similarly the covariance of the a priori data can be given by the covariance matrix $\mathbf{S}_a$.

For all retrievals a single a priori covariance matrix has been used, with a column variabiltiy of 12 ppm for CO_2 (based on global estimates of Dufour & Breon (2003)) which decreases with altitude, by $\sim$10% at the boundary layer to $\sim$1% in the stratosphere (see Figure 3.7). For surface pressure a standard deviation of 4 hPa was used to allow for more difficult topographies. To account sufficiently for the expected large variability of aerosols and cirrus clouds, the profiles were given a large flexibility with a covariance of 50 times the 1-σ uncertainty for each atmospheric level (see Figure 3.8).

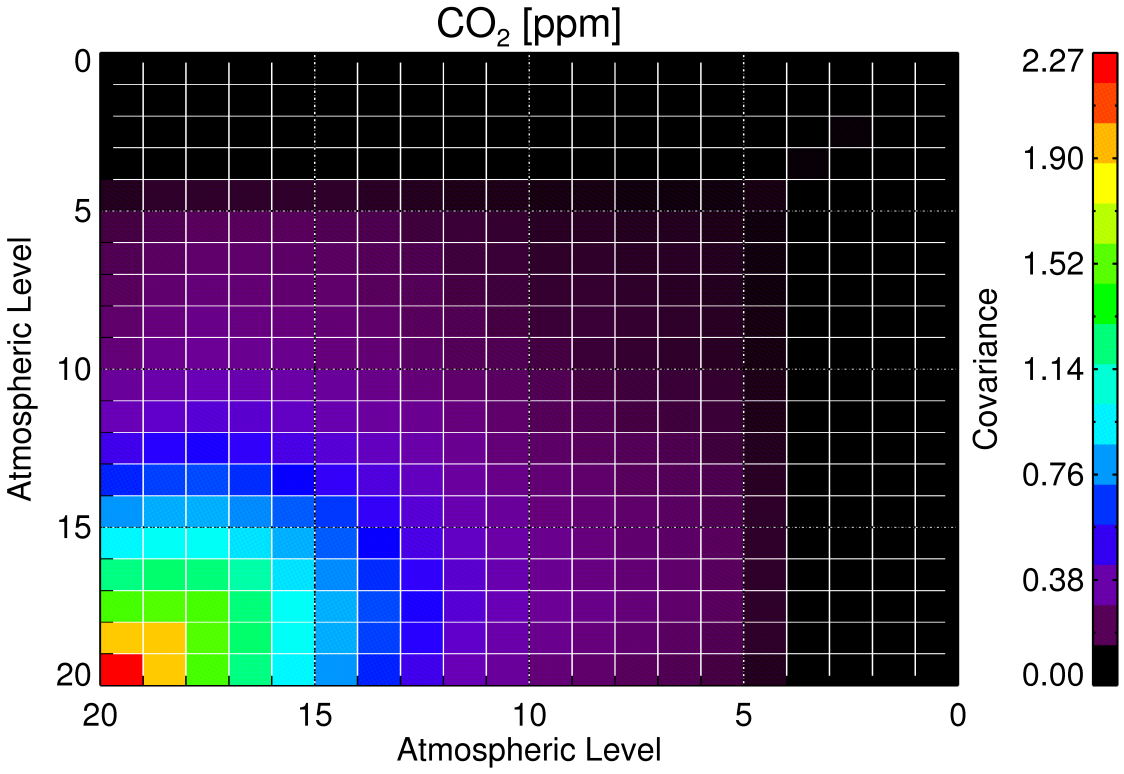

FIGURE 3.7. CO_2 covariance used for all retrievals of X_{CO2}. Zero represents the top of the atmosphere and 20 represents the boundary layer.

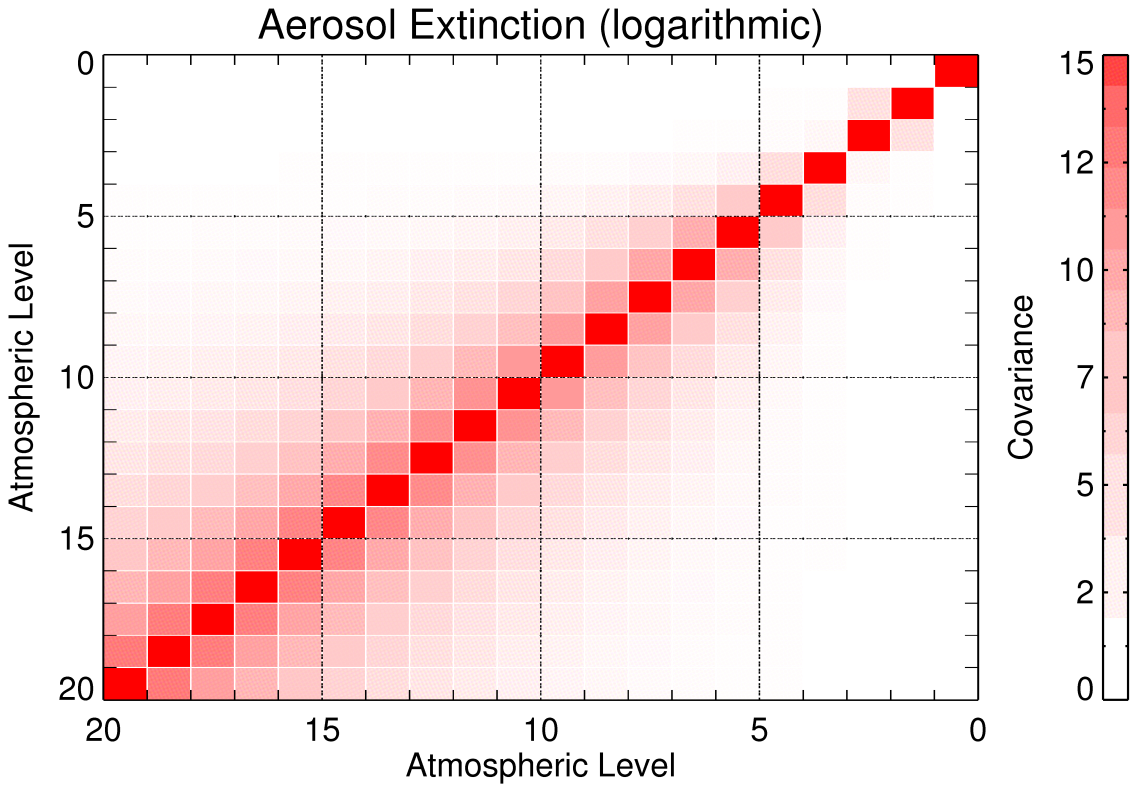

FIGURE 3.8. Aerosol/cirrus covariance of 50 times the 1-σ uncertainty. Zero represents the top of the atmosphere and 20 represents the boundary layer.

3.11 Theoretical retrieval assessment of GOSAT and OCO

To assess the potential of retrieving X_{CO2} from GOSAT SWIR bands, scenes were simulated and retrieved for different surface types and SZAs using the OCO Level 2 retrieval algorithm (Boesch et al. 2006), with the instrument model based on pre-flight information of GOSAT. A non-apodized sinc-function was used to simulate the ILS for an OPD of 2.5 cm and field of view (FOV) of 15.8 mrad. This relates to a full-width-half-maximum (FWHM) of 0.35 cm^{-1} for band 1 and 0.27 cm^{-1} for bands 2 and 3 of TANSO-FTS. The noise has been calculated for each band by using the SNR values given in Suto et al. (2008), for an albedo of 0.3 and SZA of 30°.

Figures 3.9 and 3.10 show the X_{CO2} averaging kernels and retrieval errors, respectively, for different simulated scenarios. X_{CO2} error gives the expected error of X_{CO2} retrievals, which is found to be less than $\sim$1.5 ppm over all surfaces, except over snow and ocean in nadir where the error is in the order of 1-2%. However, GOSAT measures

over the ocean with the Sun-glint mode where the errors are low. Therefore, it is expected that GOSAT will not provide useful measurements of X_{CO2} over areas of inland water where nadir mode is used, and over regions with snow cover (such as mountains, poles, and seasonally high latitudes). The averaging kernels describe the sensitivity of the instrument and retrieval algorithm to retrieve X_{CO2} at different altitudes. The averaging kernels peak near the surface and remain high throughout the troposphere, hence the X_{CO2} near the boundary layer is retrieved which will provide important insight into the source and sinks of CO_2 over land.

Similarly, Figures 3.11 and 3.12 show simulated averaging kernels and expected X_{CO2} error for the OCO instrument for a variety of surface types. The averaging kernels of OCO are very similar to that of GOSAT, however OCO is more sensitive at higher SZAs over snow surfaces than GOSAT. The X_{CO2} error of GOSAT is in general higher than OCO (e.g. $\sim$0.5 ppm larger for conifer/vegetation), although ocean (Sun-glint) and desert surfaces show similar X_{CO2} errors as OCO. Also, GOSAT shows much higher X_{CO2} errors ($\sim$2 ppm larger) over snow and ocean (nadir) surfaces than OCO. Both instruments show that the X_{CO2} error depends on the surface type and increases with SZA and AOD.

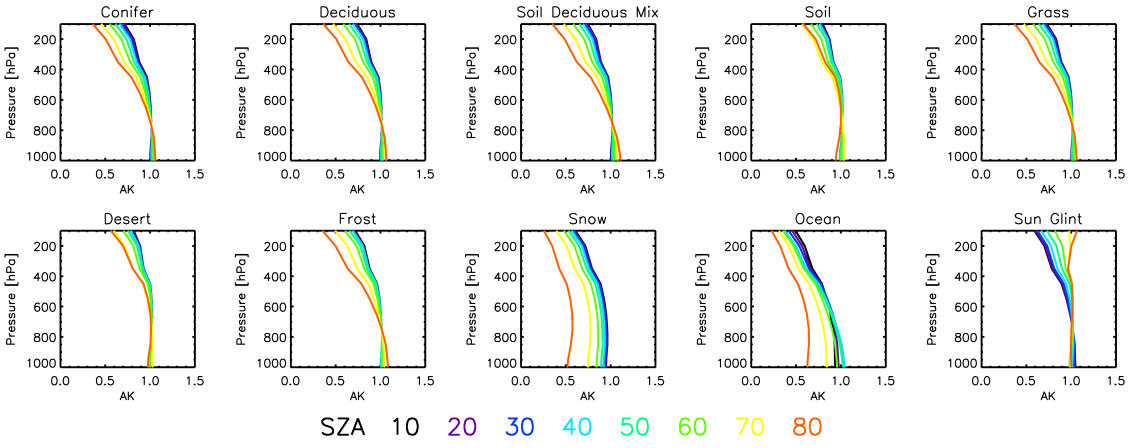

FIGURE 3.9. Calculated averaging kernels (AK) for simuated scenes of different surface types and SZAs, all with a 0.1 total column optical depth and instrument model based on GOSAT pre-flight characteristics.

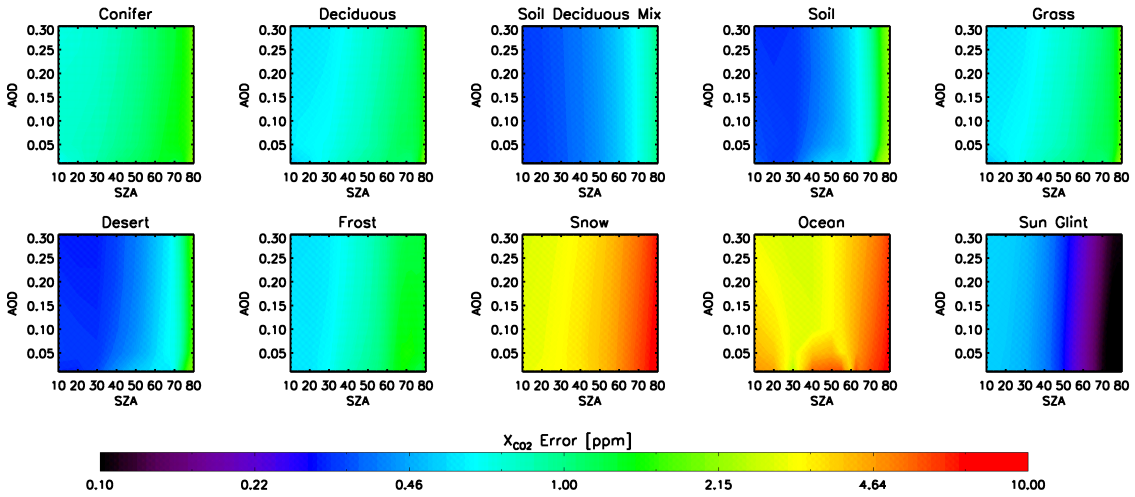

FIGURE 3.10. Calculated X_{CO2} error for simuated scenes of different surface types, SZA, and total column optical depth. All simulations used an instrument model based on GOSAT pre-flight characteristics.

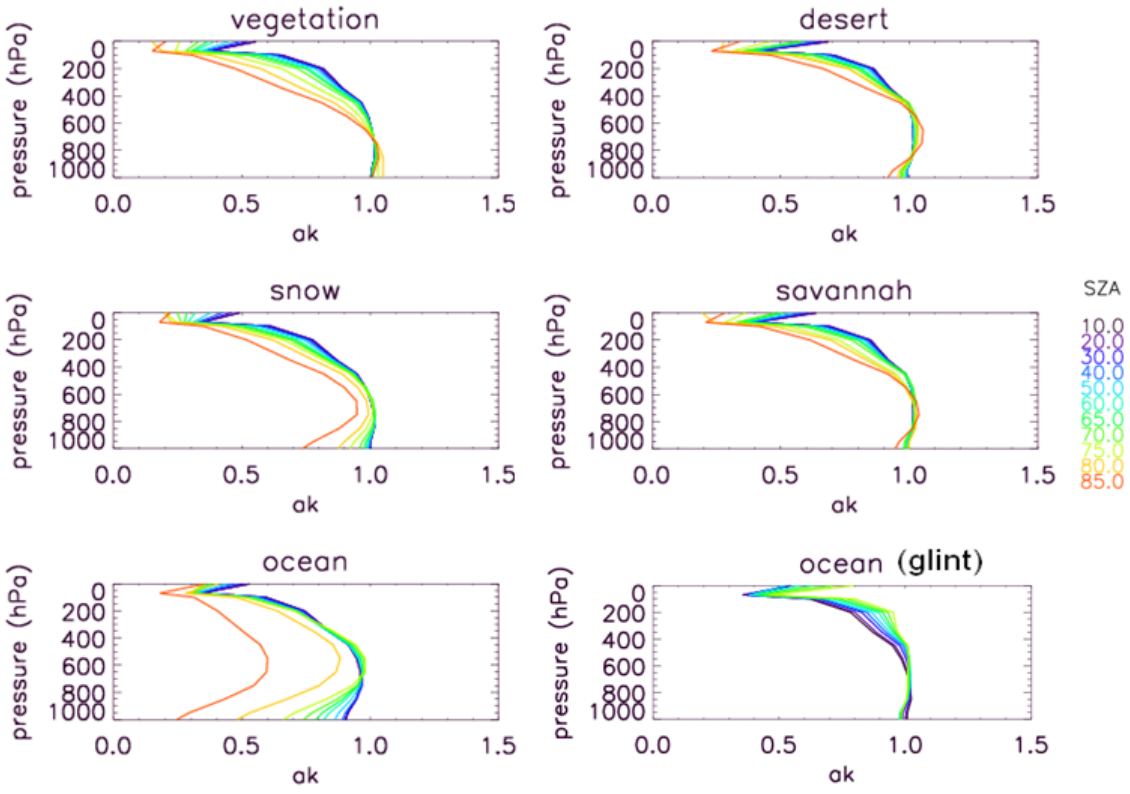

FIGURE 3.11. Calculated averaging kernels (AK) for simuated scenes of different surface types and solar zenith angle, all with a 0.1 total column optical depth and instrument model based on OCO pre-flight characteristics (courtesy of H. Boesch, 2009).

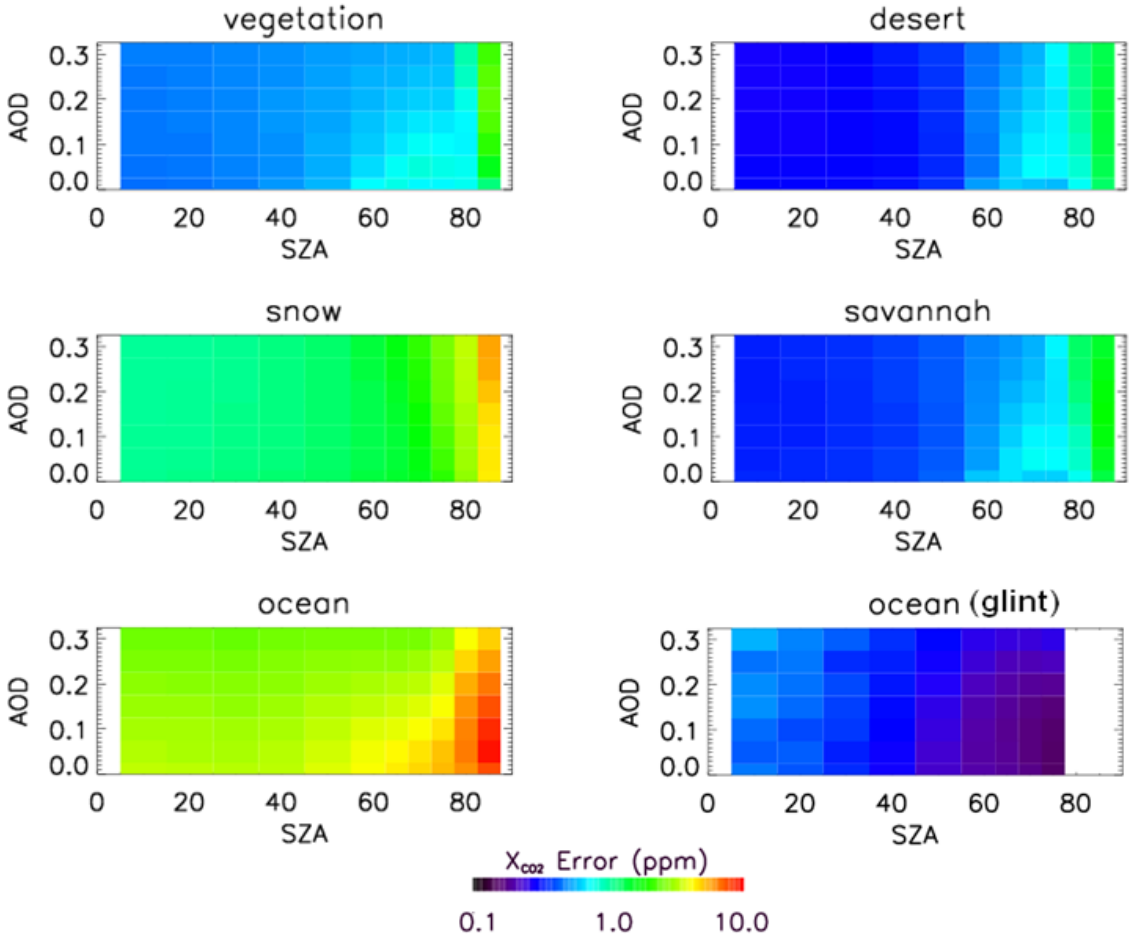

FIGURE 3.12. Calculated X_{CO2} error for simuated scenes of different surface types, solar zenith angle, and total column optical depth. All simulations used an instrument model based on OCO pre-flight characteristics (courtesy of H. Boesch, 2009).

3.12 Testing the spectral window setup

There are four CO_2 absorption bands within the SWIR spectral range of TANSO-FTS (see Figure 3.13); the 1.58 μm CO_2 band (1.558 - 1.592 μm range), the 1.61 μm CO_2 band (1.588 - 1.623 μm range), the 2.01 μm CO_2 band (1.980 - 2.024 μm range), and the 2.06 μm CO_2 band (2.040 - 2.083 μm range). Thus, providing a choice of wavelength ranges to retrieve CO_2 from. Additionally, there are two polarised signals available; parallel (P) and perpendicular (S) to the incident plane. Each of these absorption bands and polarisations may result in a different retrieved X_{CO2} value, due to instrument and spectroscopy variations. To test for any differences and to determine which bands or polarisations are most suitable to use, each of these bands and polarisations were individually used to retrieve X_{CO2}.

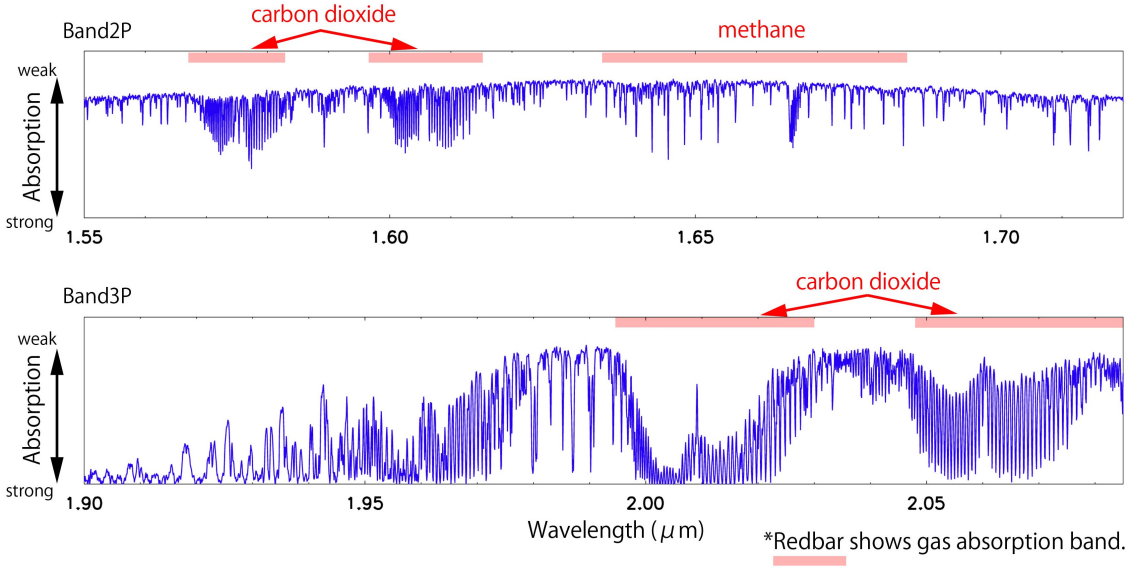

FIGURE 3.13. The first TANSO-FTS band 2 and 3 radiances obtained, illustrating the CO_2 absorption regions within these bands. Figure taken from JAXA (2009).

The measured radiances were calibrated with the initial radiometric conversion coefficients and the retrievals used the official GOSAT ILS from JAXA (version 006) (Kuze et al. 2009) and tabulated absorption cross-sections of HITRAN08 (Rothman et al. 2009). The a priori were obtained from the pre-processing module. A single Gaussian profile of 2 km height and width with an AOD of 0.075 and scattering optical properties of Kahn type 4b (carbonaceous and dusty environments) were used for the a priori aerosol (Kahn et al. 2001). The state vector included a 20 level profile of CO_2, a scale factor for H_2O, albedo, albedo slope, and dispersion shift and stretch.

Figures 3.14 and 3.15 show the retrieved X_{CO2} for each polarisation and CO_2 absorption band for Park Falls/USA and Darwin/Australia, providing northern and southern hemisphere scenes. The X_{CO2} values retrieved range between ~325 ppm and ~410 ppm, with the 2.01 μm X_{CO2} being generally ~20 ppm higher than that of the other CO_2 bands. The 3rd exposure of Park Falls shows a different distribution of X_{CO2} than the other two exposures. Using the official NIES TANSO-CAI L1B false RGB image of this scene, this exposure appears to coincide with a cloud, whereas the other two exposures appear cloud-free. Similarly, the 3rd and 8th exposures of Darwin show a different distribution of X_{CO2} than the other two exposures and also coincide with clouds. This highlights are few issues; some clouds remain even after the NIES cloud-screen has been applied, the retrieved X_{CO2} of a cloudy exposure can be biased high or low, and the amount that the X_{CO2} is biased for a cloudy exposure is different for each CO_2 absorption band and polarisation. Furthermore, the retrieved X_{CO2} is similar (~0.5 to 2 ppm different) for each polarisation, but for cloudy exposures there is a large difference between polarisations (up to ~25 ppm). If the cloudy exposures and 2.01 μm band X_{CO2} retrievals are neglected, then all the other X_{CO2} values retrieved are roughly consistent (within ~10 ppm of each other) and have a mean value of ~389 ppm for Park Falls and ~385 ppm for Darwin, which are very similar to the global levels of CO_2 observed by NOAA at Mauna Loa (Masarie & Tans 1995).

These preliminary results were all retrieved using a single spectral window, such as the 1.61 μm CO_2 band (1.588 - 1.623 μm range). However, Kuang et al. (2002) found that using a combination of the 0.76 μm O_2 A band, 1.58 μm and 2.06 μm CO_2 bands provided improved precisions in simulations.

O'Brien et al. (1998) demonstrated that the 0.76 μm O_2 A band can provide constraints on surface pressure, which can be uncertain due to topographic and local weather variations. Additionally, it can provide constraints on optical path length variations, where uncertainties due to cloud and aerosol scattering can exist. Whilst the 1.58 μm and 1.61 μm CO_2 bands are almost free of other absorbing atmospheric gases, variations in water vapour produce uncertainties in the retrieved X_{CO2} by broadening the CO_2 absorption lines slightly and effecting the dry-air fraction when calculating the X_{CO2} (Kuang et al. 2002). However, the 2.01 μm and 2.06 μm CO_2 bands contain weak water vapour absorption lines that can provide a constraint on the water vapour. The 2.01 μm and 2.06 μm CO_2 bands contain CO_2 absorption lines that are strong enough to be sensitive to scattering, so provide additional constaints on optical path length uncertainties from clouds and aerosols (Kuang et al. 2002). However, the 2.01 μm CO_2 band contains lots of water vapour absorption that may cause intereference. Futhermore, the 1.58 μm

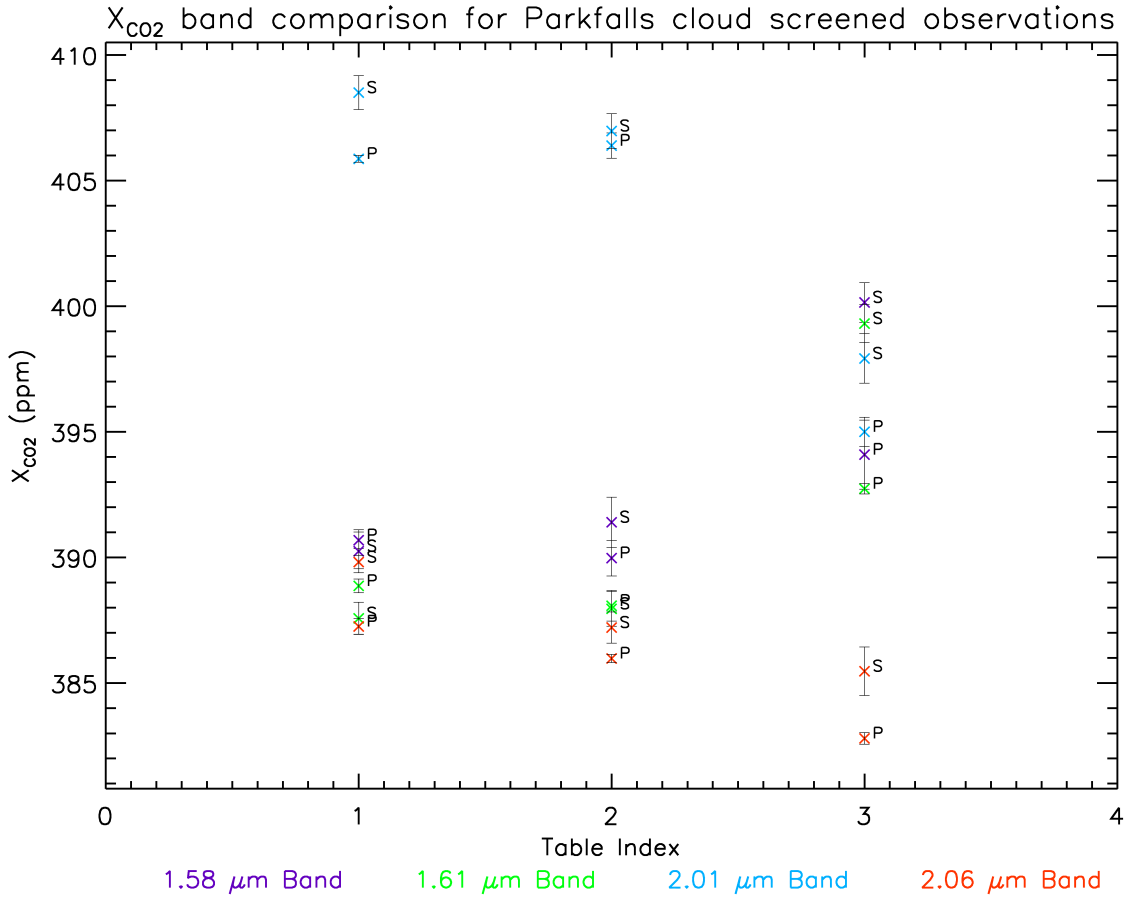

FIGURE 3.14. X_{CO2} retrieved from GOSAT between 23rd - 30th April 2009 within 500 km of the Park Falls/USA TCCON site. Each retrieval was designed to retrieve a single polarisation signal (P or S) and a single CO_2 absorption band (shown by different colours). The index represents different TANSO-FTS exposures.

CO_2 band has O_2 day glow emissions that may potentially perturb measurements in this band (Boesch et al. 2006). O_2 day glow emission is known to occur in the mesosphere and thermosphere due to three mechanisms; the excitation of O_2 from a collision with an $O(^1D)$ atom produced in the photolysis of O_2 or O_3, resonant absorption of oxygen bands (including the O_2 A band), or the chemical reacton between two oxygen atoms and either a N_2 or O_2 molecule (Sheese et al. 2010).

These preliminary results showed the X_{CO2} retrieved from GOSAT to be similar between the different CO_2 bands, with the exception of the 2.01 μm CO_2 band which gave much higher values (due to poor spectroscopy). Thus, to reduce spectroscopic biases the 2.01 μm CO_2 band should not be used. Additionally, the 1.61 μm CO_2 band gave X_{CO2} values closer to the 2.06 μm CO_2 band than that of the 1.58 μm CO_2 band, and

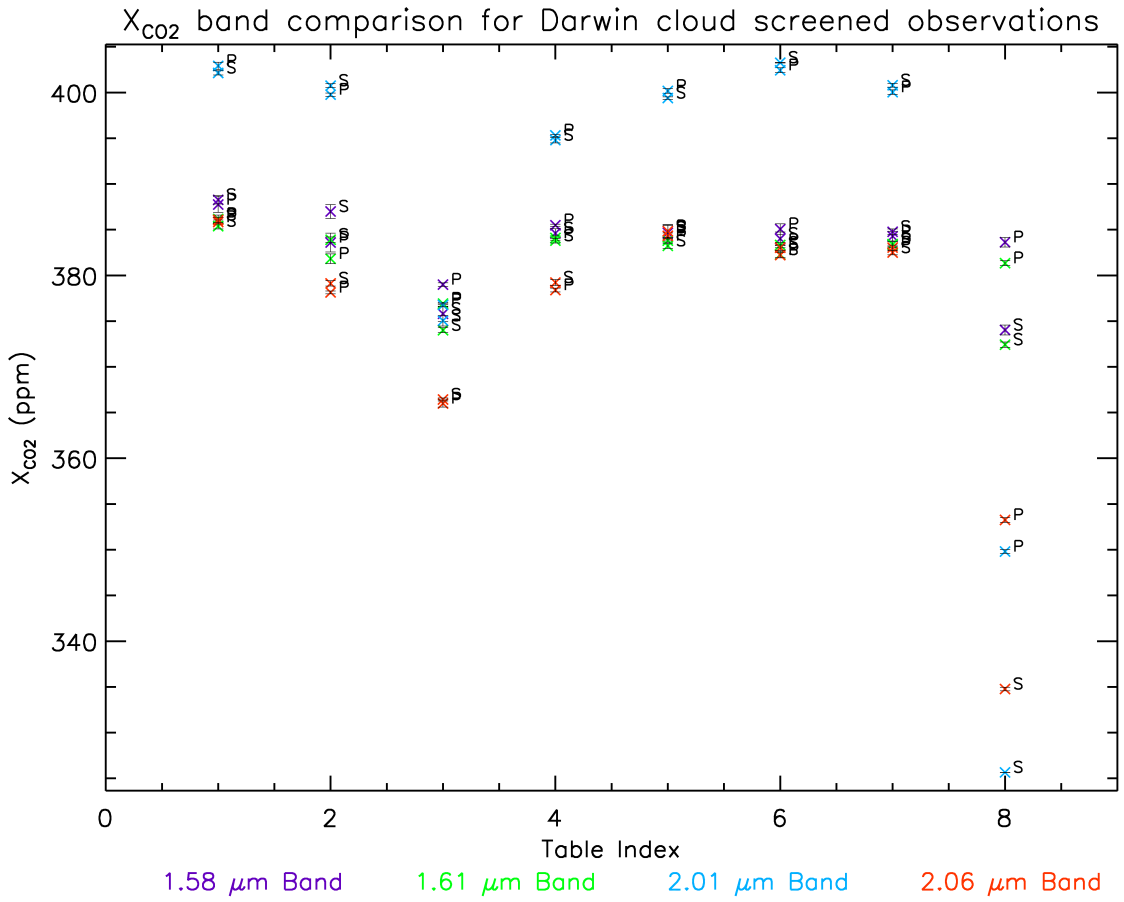

FIGURE 3.15. X_{CO2} retrieved from GOSAT between 23rd - 30th April 2009 within 500 km of the Darwin/Australia TCCON site. Each retrieval was designed to retrieve a single polarisation signal (P or S) and a single CO_2 absorption band (shown by different colours). The index represents different TANSO-FTS exposures.

since the 1.58 μm CO_2 band contains day glow it is not appropriate to use. Therefore, the combination of the 0.76 μm O_2 A band, 1.61 μm and 2.06 μm CO_2 bands was tested in the UoL-FP retrieval algorithm. The O_2 A band provides information on surface pressure and aerosols, which is highly beneficial to help constrain the retrieval of X_{CO2}.

X_{CO2} was retrieved from GOSAT using different spectral bands in the UoL-FP retrieval algorithm for observations within $\pm$5 degrees over the Lamont/USA TCCON site between April and September 2009. The exposures were pre-screened for a SNR $>$ 50 and the NIES cloud-screen was used (Taylor et al. 2012). Figure 3.16 shows the difference in retrieved X_{CO2} from the 1.61 μm CO_2 band with the retrieval setup to use either; the 0.76 μm O_2 A band with the 1.61 μm CO_2 band, the 2.06 μm CO_2 band, or all three bands together. On average, there is little difference in X_{CO2} when including the O_2 A

band, but the scatter in X_{CO2} is of the order of $\sim$5 ppm. However, since the surface pressure was fixed to the a priori assumption any constraints provided by the inclusion of the O_2 A band would not effect the surface pressure. The X_{CO2} retrieved from the 2.06 μm CO_2 band is higher on average but the X_{CO2} values lower than about 370 ppm are much lower than that retrieved using the 1.61 μm CO_2 band. These low values are potentially influenced by aerosols which the 2.06 μm CO_2 band is sensitive to, due to aerosol optical properties have more effect in this wavelength range. When all three bands are retrieved simultaneously, it produces X_{CO2} that appears an amalgam of the effects already found. Although the precision of the data changes little between the different setups, it allows for the possibility of additional constraints and potentialy useful additional parameters to be retrieved such as surface pressure and clouds/aerosols.

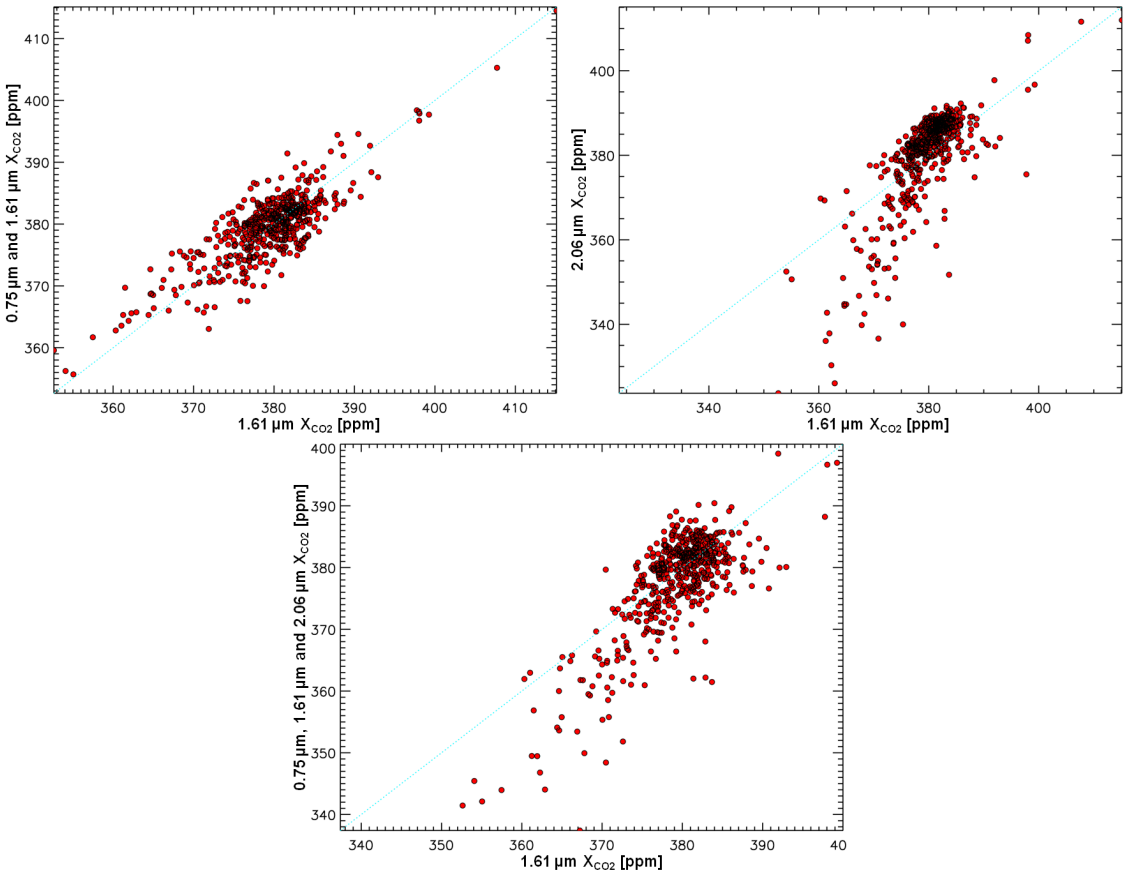

FIGURE 3.16. X_{CO2} retrieved from GOSAT using different spectral bands in the UoL-FP retrieval algorithm for observations within $\pm 5^{\circ}$ of the Lamont/USA TCCON site between April and September 2009. The data was pre-screened and cloud screened but no post-screening was applied. The top left panel shows the X_{CO2} retrieved using the 1.61 μm CO_2 band compared with that retrieved when using the 1.61 μm CO_2 band and the 0.76 μm O_2 A band. The top right panel shows a comparison of the X_{CO2} retrieved from the 1.61 μm and 2.06 μm CO_2 bands seperately. The bottom panel shows the X_{CO2} retrieved using the 1.61 μm CO_2 band compared with that retrieved when using the 0.76 μm O_2 A band, 1.61 μm and 2.06μm CO_2 bands.

3.13 Profile of Carbon Dioxide Concentration

The a priori CO_2 profiles were obtained from 3 hourly model 3.75° longitude by 2.5° latitude gridded 2009 fields of the Laboratory of Climate Sciences and Environment (LCSE) General Circulation Model of Laboratoire de Meteorologie Dynamique (LMDZ) (Pickett-Heaps et al. 2011). A correction of 18.25 ppm was applied to the 2009 CO_2 profiles that was derived from a comparison with National Oceanic and Atmospheric Administration (NOAA) observations over Mauna Loa, see Figure 3.17. Additionally, yearly increments of 1.63 ppm and 2.36 ppm were taken from global NOAA observations (Masarie & Tans 1995) and applied to the CO_2 profiles for 2010 and 2011 respectively, to account for increasing atmospheric CO_2 concentrations (see Figure 3.18).

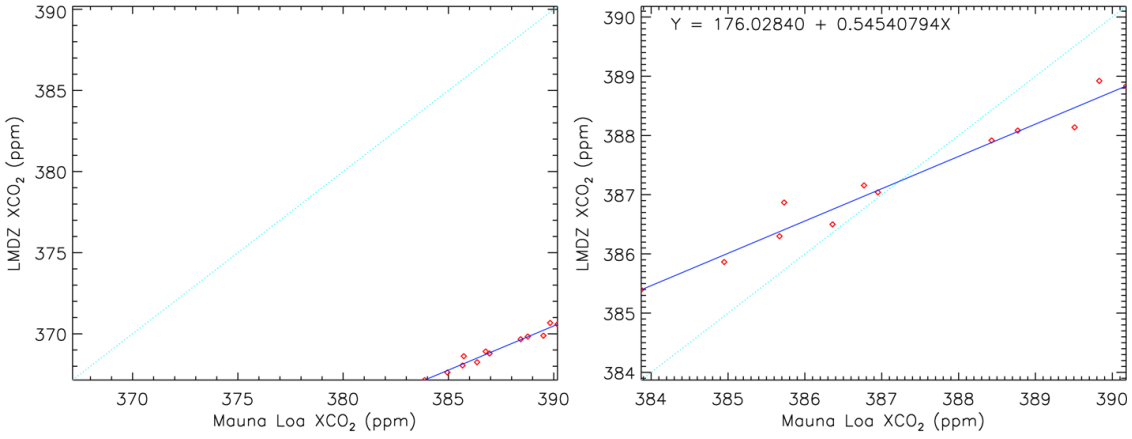

FIGURE 3.17. X_{CO2} calculated for LMDZ 2009 model CO_2 fields interpolated to the time and location of CO_2 observations of Mauna Loa/Hawaii, compared to X_{CO2} calculated for Mauna Loa observations (left). LMDZ X_{CO2} was found to be 18.25 ppm lower than Mauna Loa on average. After applying this offset to the LMDZ X_{CO2} (right) a difference is still observed, with LMDZ estimating a smaller range of X_{CO2} than observed by Mauna Loa.

However, the Mauna Loa comparison is only based on a small sample size, therefore the offset LMDZ X_{CO2} was compared to X_{CO2} retrieved from different TCCON sites (see Figure 3.19), including; Lamont/USA, Park Falls/USA, Orleans/France, Bremen/Germany, Garmisch/Germany, Bialystok/Poland, Tsukuba/Japan, Darwin/Australia, Wollonong/Australia, and Lauder/New Zealand. This analysis provides comparisons of X_{CO2} for both northern and southern hemispheres at various locations, and shows the calculated offset to give LMDZ X_{CO2} of similar value as TCCON for all locations. The LMDZ X_{CO2} estimated for northern hemisphere sites shows a good comparison to TCCON with correlation coefficients ranging from 0.86 to 0.98. However, the LMDZ X_{CO2}

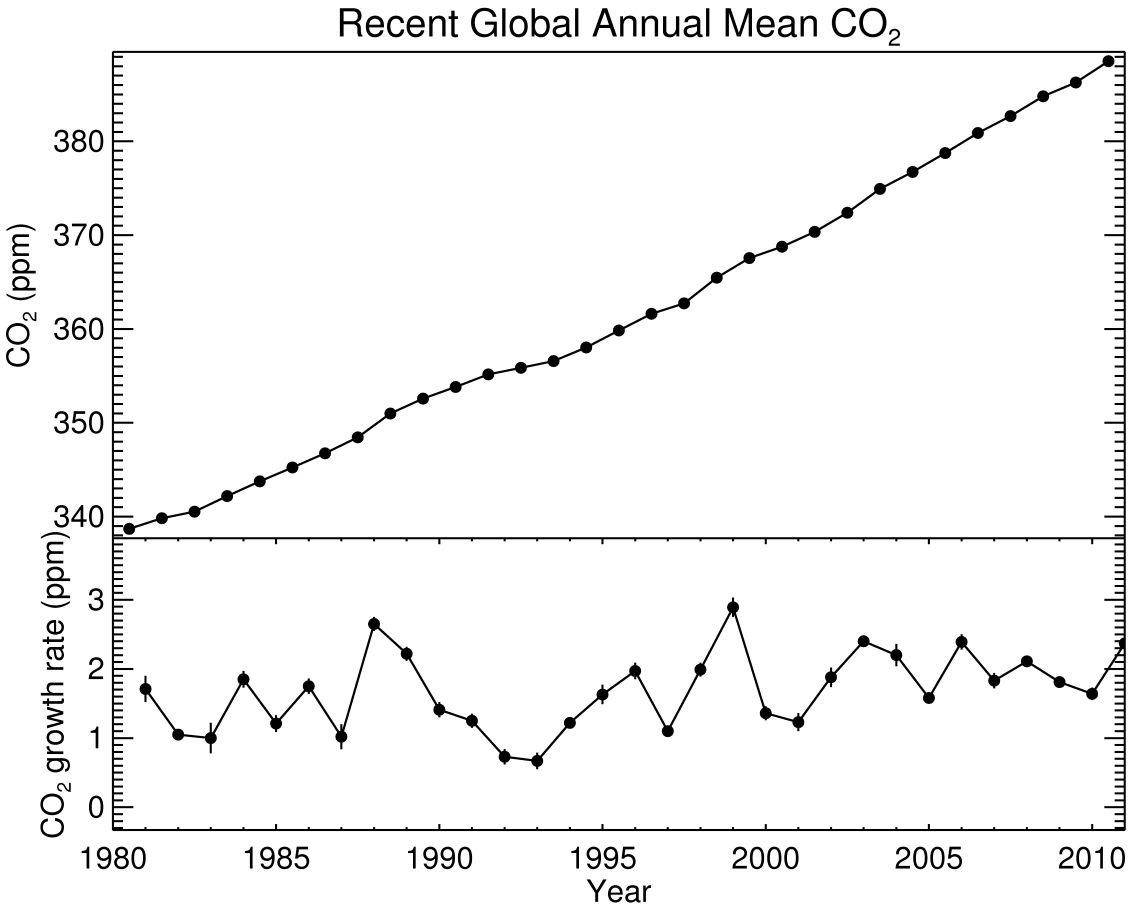

FIGURE 3.18. Mean yearly CO_2 from NOAA in-situ observations (top) and the yearly increment in CO_2 (bottom).

is found to estimate a lower range of X_{CO2} values than observed by TCCON, as previously found with the Mauna Loa comparison. For the southern hemisphere sites, LMDZ poorly reproduces the X_{CO2} retrieved from TCCON with correlation coefficients ranging from 0.48 to 0.64. Again, the offset applied to LMDZ provides X_{CO2} values of a similar mean value as TCCON for southern hemisphere sites. Thus, applying this offset to the model CO_2 allows the retrievals to use a CO_2 a priori profile with values that are on average closer to the truth.

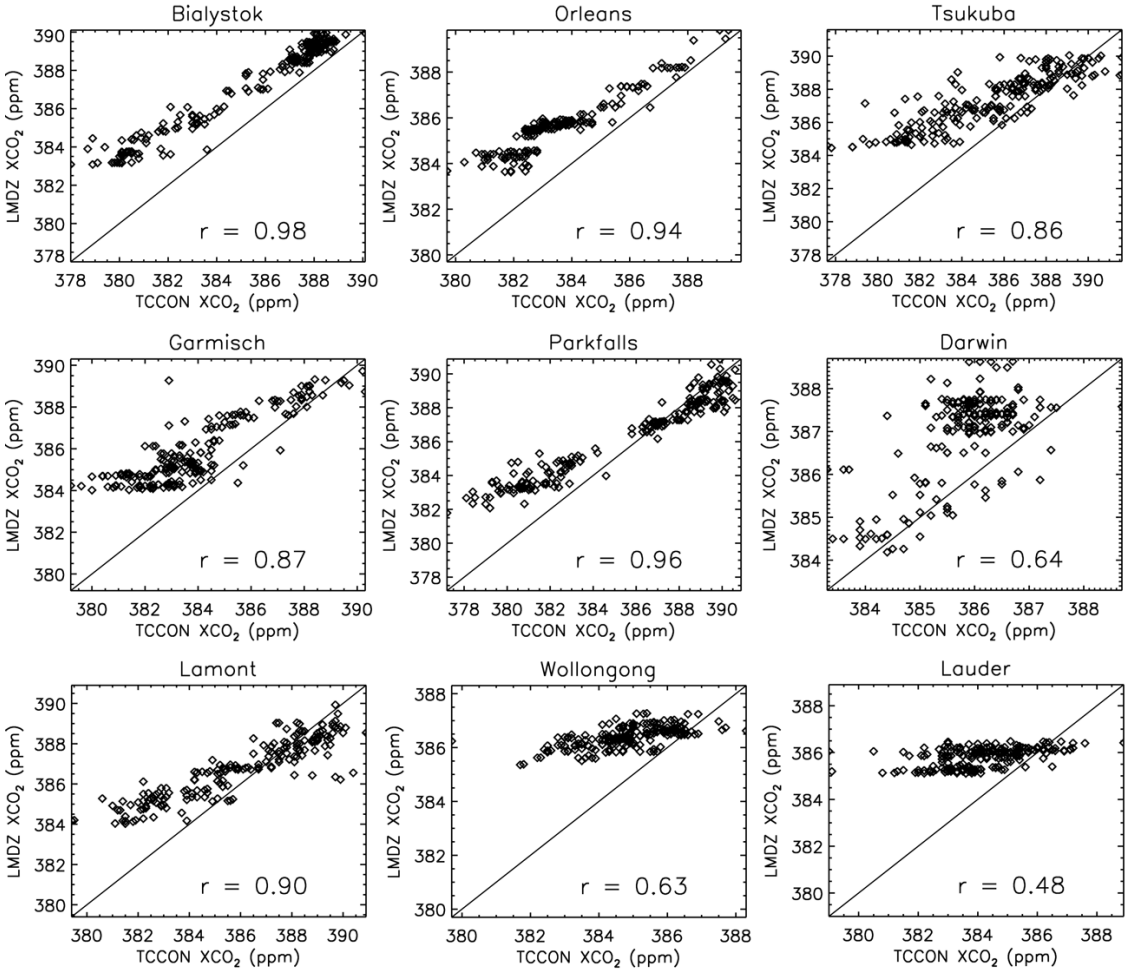

FIGURE 3.19. X_{CO2} calculated for LMDZ 2009 model CO_2 fields interpolated to the time and location of TCCON observations for nine different sites, compared to the retrieved X_{CO2} from TCCON. The one-to-one line is shown in black and each observation is shown by a black diamond. The correlation coefficient per site is given by r.

3.14 Methane Concentration

The a priori profile of CH_4 is acquired from a TM3 model run (Houweling 2009) and is interpolated to the desired latitude, longitude and time. This is only retrieved as a scaling of the profile, assuming the profile shape to be true. The retrieval uses a standard deviation of 0.32 for the CH_4 scale factor.

3.15 Surface Pressure

The European Centre for Medium-Range Weather Forecasts (ECMWF) provides model data that includes assimilated observations from surface buoy and satellite measurements (ECMWF 2008). ECMWF provides atmospheric profiles of pressure, temperature and specific humidity on a 1.125 degree by 1.125 degree global grid with 90 layers every 6 hours. Given the latitude, longitude and altitude of a site of interest the surface pressure can be determined from these profiles. All 90 layer datasets can be converted onto 91 levels using coefficients provided by ECMWF (ECMWF 2007). ECMWF also provides potential data, ϕ, for the lowest level of the same grid, which can be used to find the geopotential height, Z_g, of each grid point level as

$$Z_g = \frac{\phi}{g} \tag{3.14}$$

where gravity, g, is calculated as a function of latitude and approximate altitude. Taking the four surrounding grid points of the site of interest, the pressure, P, at the site altitude can be found for each grid point by using the hydrostatic equation

$$P = P_0 e^{-\frac{Z}{Z_0}} \tag{3.15}$$

where P_0 is the pressure of the grid point level lower than the site altitude, Z is the difference in altitude between the grid point level and the site altitude and Z_0 is the scale height defined as

$$Z_0 = \frac{RT}{Mg} \tag{3.16}$$

where R is the ideal gas constant, T is the average temperature across the differential, M is the Molar mass of wet air and g is the gravitational acceleration as a function of latitude and altitude. The Molar mass of wet air can be calculated by

$$M = \rho_d(1 - SH) + \rho_w SH \tag{3.17}$$

where SH is the ECMWF specific humidity, ρ_d is the dry air mass and ρ_w is the mass of wet air. The site altitude can be obtained from a global digital elevation model with a horizontal grid spacing of 30 arc seconds named GTOPO30 provided by the U.S. Geological Survey (USGS 1996). Note, that in the case that the site altitude is lower than the lowest level of a grid point, the pressure is calculated with respect to the lowest level. Also, the temperature and molar mass are extrapolated downwards based on the lapse rate and gradient of the 5 lowest levels above, respectively. The surface pressure for the site can then be resolved by interpolating the pressures with latitude, longitude and time.

To validate the surface pressure two sites were chosen; Southern Great Plains (SGP) /USA, and Black Forest/Germany. Since pressure changes with altitude, highly variable topographies will also vary in pressure. These sites are flat and mountainous in topography respectively, providing an assessment of the extremes in topography where data from observations are available. The Atmospheric Radiation Measurement (ARM) program (Ackerman & Stokes 2003) has a central facility in SGP which takes in situ ground based measurements of surface pressure using the Temperature, Humidity, Wind and Pressure Sensors (THWAPS) (Peppler et al. 2008), which has a precision of 0.1 hPa and an uncertainty of 0.7 hPa (ARM 2011a). Figure 3.20 shows that the surface pressure is within 1 hPa of THWAPS observations. Surface Pressure observations were also made by the ARM mobile facility that visited Black Forest, Germany, in 2007 with the Surface Meteorological Instrument (MET) (Peppler et al. 2008), which has a precision of 0.1 hPa and an uncertainty of 0.7 hPa (ARM 2011b). Figure 3.20 illustrates that over a mountainous topography the surface pressure can still be resolved to within 1 hPa. Hence, the surface pressure a priori could be constrained to less than 0.1%. In the retrieval a standard deviation of 4 hPa is used to allow for more difficult topographies.

Initially, the a priori surface pressure was calculated for the centre of the TANSO-FTS IFOV location. However, regions of large topographic variations may cause this surface pressure to be unrealistic for the entire IFOV. Therefore, a new method was created that calculates the surface pressure for all known altitudes within the IFOV. The altitude information is obtained from GTOPO30 (USGS 1996) which has a 30-arc second resolution (approximately 1 km), allowing roughly 70 surface pressures to be calculated within the IFOV ($\sim$10.5 km diameter) from which the mean and standard deviation can be computed.

The a priori surface pressure was calculated using each method for GOSAT observations within $\pm 5^{\circ}$ of the Lamont TCCON site between April and December 2009. Figure 3.21 gives a comparison of these surface pressures and shows differences up to $\sim$3.5 hPa, which is within the assumed a priori surface pressure 1-sigma uncertainty used

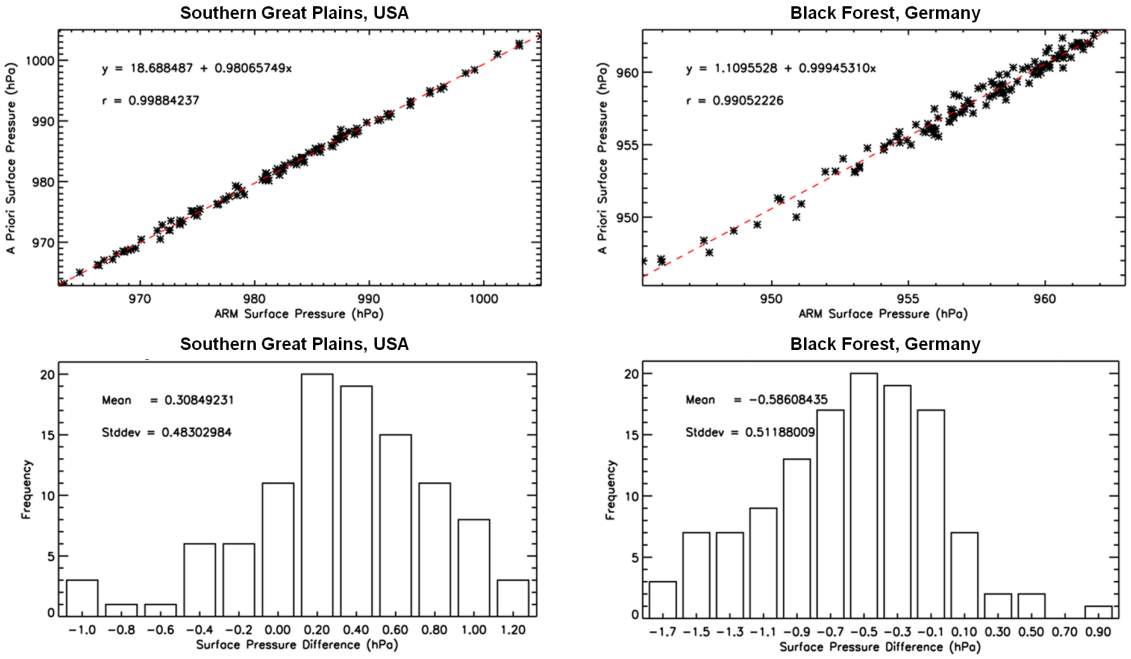

FIGURE 3.20. Comparison of a priori surface pressure with in-situ ground based measurements from ARM instruments in Southern Great Plains/USA and Black Forest/Germany.

in the retrievals.

On average, a bias in retrieved surface pressure of ∼4 hPa is observed (see Figure 3.22), which is lower than reported by Crisp et al. (2012). This bias has been suggested to be due to deficiencies in the O_2 A band spectroscopy and that scaling the line strength of O_2 could reduce it (Butz et al. 2011). For this retrieval, instead of scaling the line strength, the systematic overestimates of surface pressure are corrected by normalizing the retrieved X_{CO_2} with the ratio of retrieved surface pressure and ECMWF surface pressure.

The effect of normalising the retrieved X_{CO2} with the surface pressure ratio was tested for retrievals from GOSAT. Figure 3.23 shows a one year comparison of the retrieved X_{CO2} globally with and without the surface pressure normalisation applied. In general, the X_{CO2} becomes higher in value when the surface pressure normalisation is applied, thus reducing the X_{CO2} bias compared to TCCON.

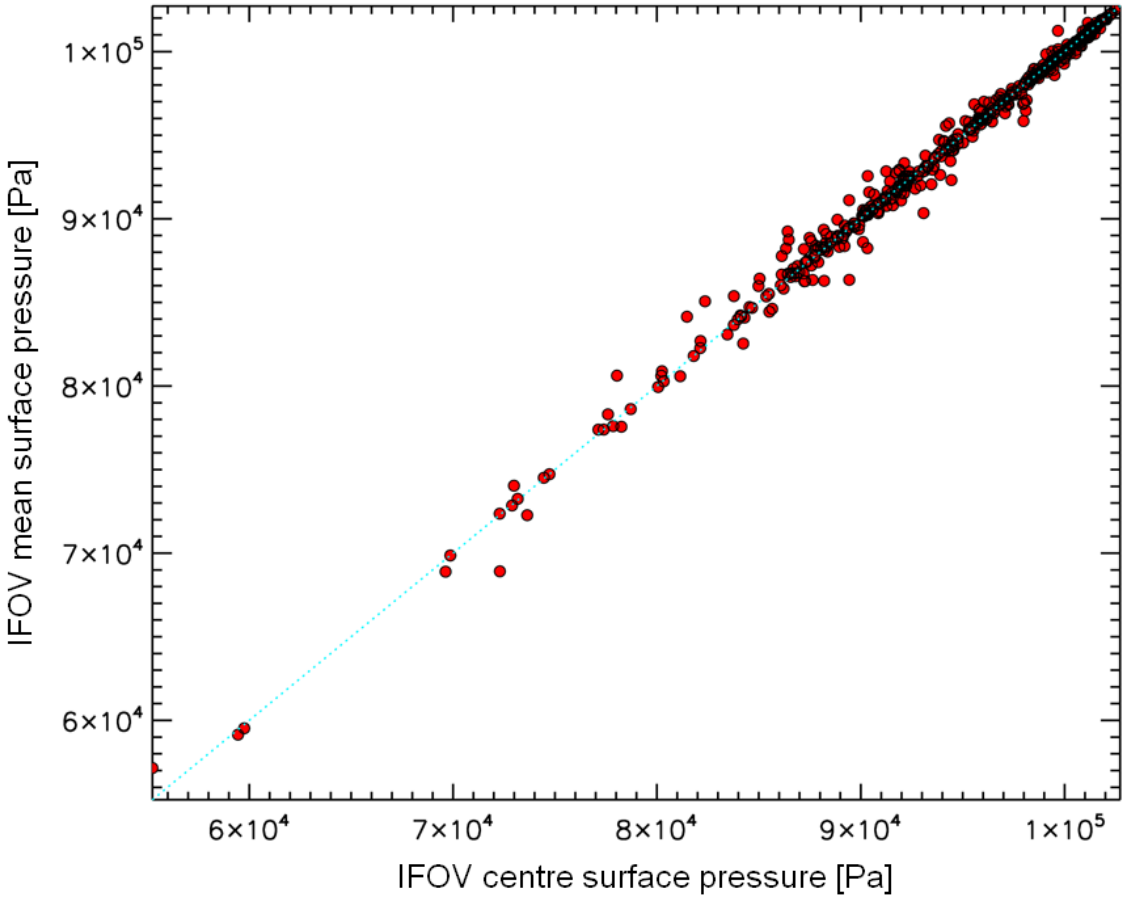

FIGURE 3.21. Comparison of surface pressure calculated for the GOSAT IFOV centre and for the mean across the IFOV, for GOSAT observations within $\pm 5^{\circ}$ of the Lamont TCCON site. All surface pressures were calculated from ECWMF and interpolated to the time and location of the observation.

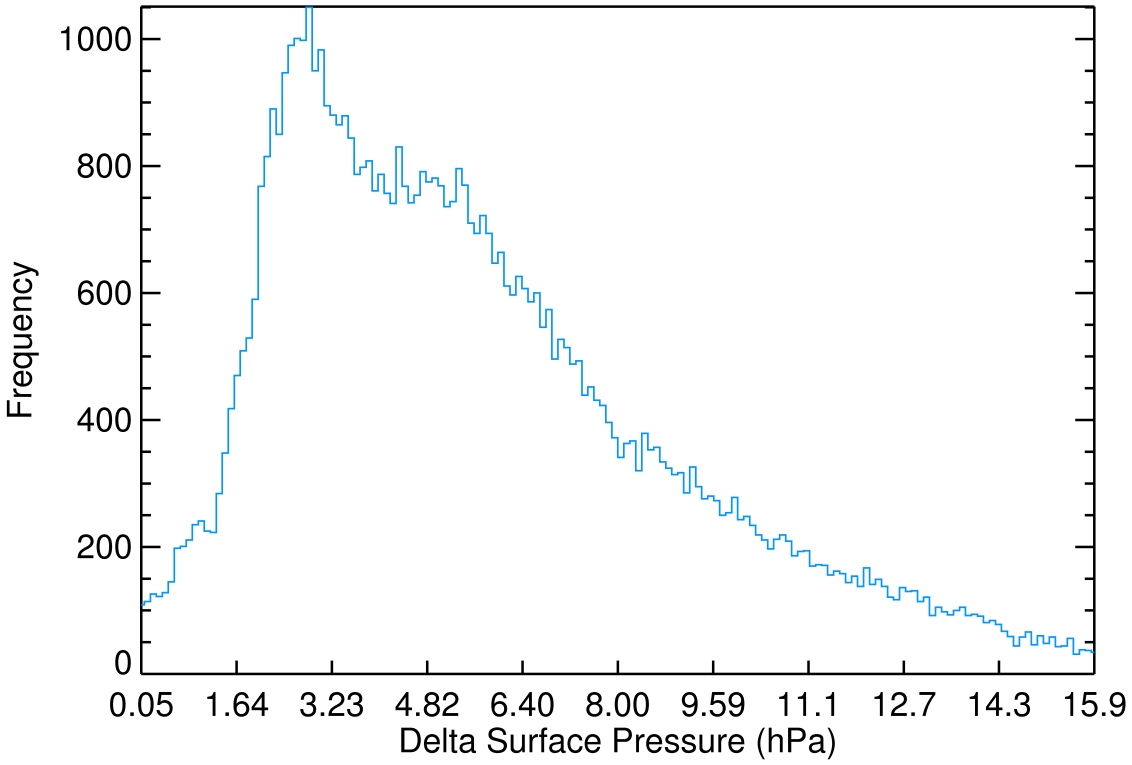

FIGURE 3.22. Histogram of the difference between the retrieved surface pressure from GOSAT observations between July 2009 and June 2010 globally, and ECMWF surface pressure calculated for the times and locations of the GOSAT observations.

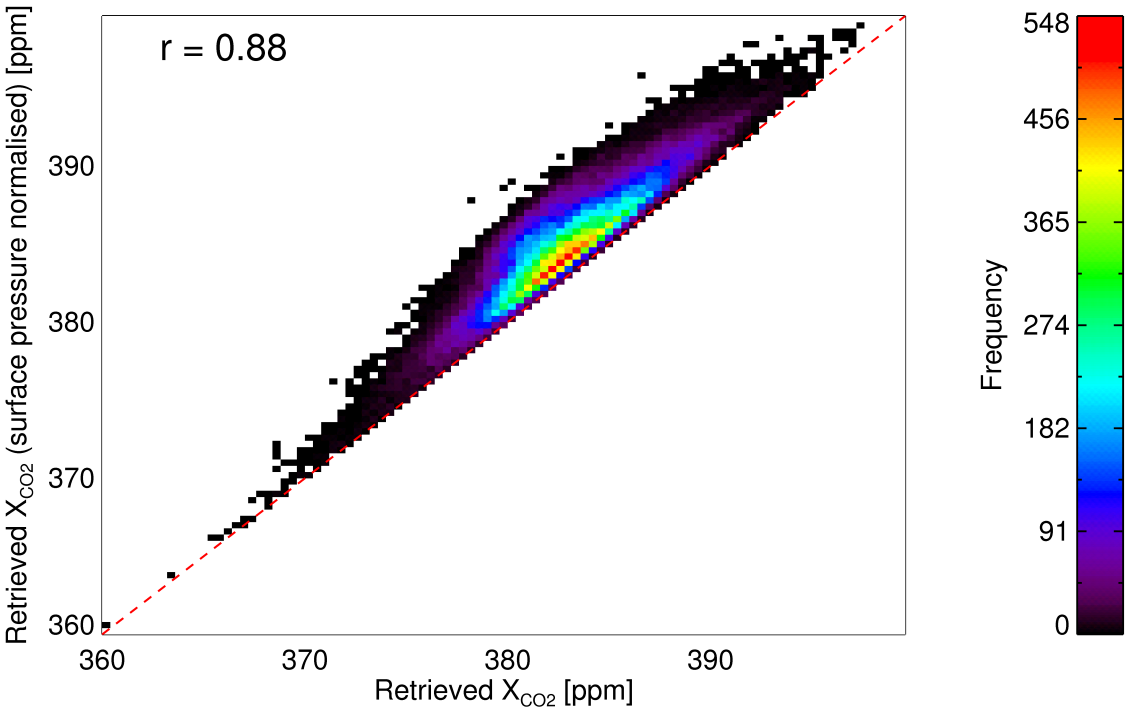

FIGURE 3.23. Comparison of X_{CO2} retrieved from GOSAT with and without surface pressure normalisation applied. Shown are pre-screened, cloud-screened and post-screened GOSAT observations globally between July 2009 and June 2010.

3.16 Temperature and Water Vapour

The ECMWF specific humidity data can be used to generate water vapour VMR profiles using the equation

$$H_2O_{VMR} = 10^6 \left(\frac{SH}{((R_d R_w) - (SH((R_d R_w) - 1))} \right) \tag{3.18}$$

where R_d and R_w are the gas constants in dry and wet air respectively. ECMWF also provides temperature profiles which, along with the H_2O_{VMR}, are interpolated with latitude, longitude and time to the specific observation. A constant O_2 VMR profile of 0.2095 is also used as an a priori. Often the retrieved surface pressure may be larger than the a priori surface pressure such that the atmospheric profiles for temperature and water vapour may be extrapolated below the a priori surface pressure value. In some cases this results in spurious values in the lowest levels of the profiles. To resolve this a static 20 level pressure grid is always used, and the a priori profiles are extrapolated using the lapse rate for temperature and gradient for water vapour of the 5 atmospheric levels above the surface pressure, such that a reasonable extrapolation occurs as shown in Figure 3.24. The temperature and H_2O profiles are assumed correct but the retrieval is allowed to scale them. For the temperature offset a standard deviation of 3.2 K is used and for the H_2O scale factor a standard deviation of 0.32 is used.

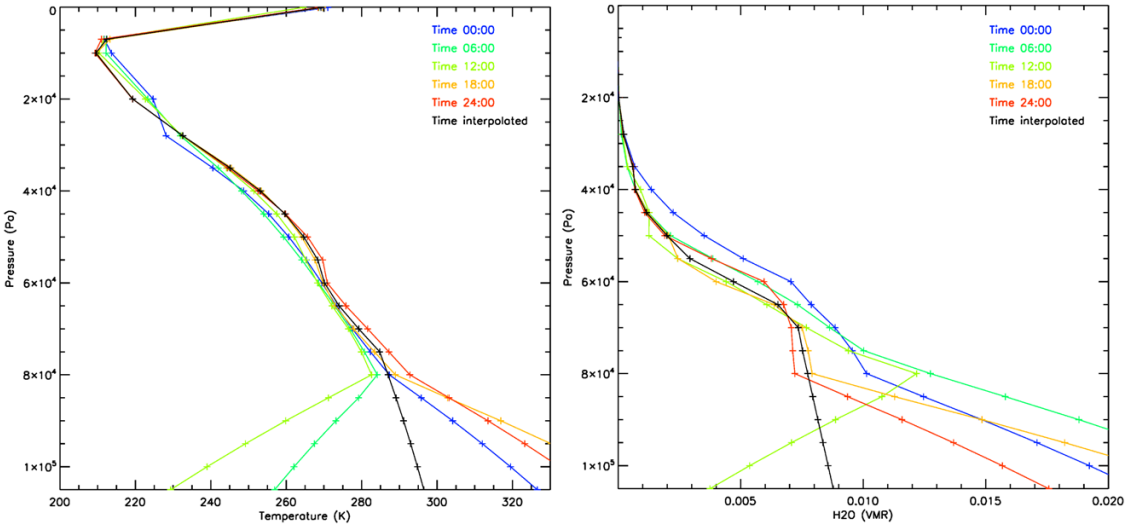

FIGURE 3.24. Example of the extraplolation technique used for temperature and water vapour profiles. The black lines show the time interpolated profile with the lapse rate/gradient applied, whereas the other profiles show the profiles for each time frame which have been simply extrapolated below the surface pressure. These profiles are already interpolated with latitude and longitude from four ECMWF grid points.

3.17 Aerosol Profiles

Atmospheric aerosols can scatter light into or out of the measured light path causing the measured intensity to vary and the optical path length to change. Additionally, some aerosols can absorb some of the light being measured, reducing the signal intensity and effecting the absorption lines of trace gases. Initially, the retrieval algorithm was setup to retrieve a single aerosol profile with an a priori AOD equal to the Moderate Resolution Imaging Spectroradiometer (MODIS) monthly mean AOD inferred for that 1° x 1° grid cell location. MODIS is a remote sensing instrument that is onboard the Terra and Aqua satellites that were launched in 1999 and 2002, respectively. However, aerosols are known to be highly variable and using a monthly mean AOD could potentially be improved.

The ARM Climate Reseach Facility includes a network of ground-based instruments located around the world. The central facility at Lamont/USA and the Darwin facility in Darwin/Australia are both located near to the respective TCCON sites. AOD was obtained from these ARM sites within the observation period of GOSAT using a Cimel sunphotometer (CSPHOT) instrument. The CSPHOT measures direct solar irradiance and sky radiance from the ground at visible and near infrared wavelengths to calculate atmospheric absorption and scattering (Gregory 2011). It derives AOD with a high accuracy (between 0.01 and 0.02 (Gregory 2011)), providing a useful source of in-situ AOD.

X_{CO2} was retrieved from GOSAT using a single aerosol profile with an a priori AOD equal to the ARM CSPHOT AOD closest temporally. The a priori AOD at the O_2 A band was calculated from CSPHOT AOD data at 0.50 μm and 0.87 μm using the angstrom coefficient data by

$$\tau_{0.76\mu m} = \tau_{0.87\mu m} * \left(\frac{\lambda_{0.76}}{\lambda_{0.87}}\right)^{-\alpha_{0.50\mu m - 0.87\mu m}} \tag{3.19}$$

where τ represents the AOD, λ the wavelength and α the angstrom coefficient. Figures 3.25 and 3.26 show the retrieved X_{CO2} from GOSAT over Lamont and Darwin, respectively, when using ARM AOD as a priori. For comparison, the retrieved X_{CO2} from GOSAT when using MODIS AOD as a priori and X_{CO2} inferred from TCCON are shown. The X_{CO2} retrieved from GOSAT using ARM AOD is very similar in value to the X_{CO2} retrieved when using MODIS AOD and follow the same temporal pattern in general. Both sets of GOSAT retrievals show a bias of about -6 ppm on average compared to TCCON, with ARM AOD based retrievals being slightly lower than MODIS AOD based retrievals.

However, the ARM network is sparsely distributed globally, making it unsuitable to

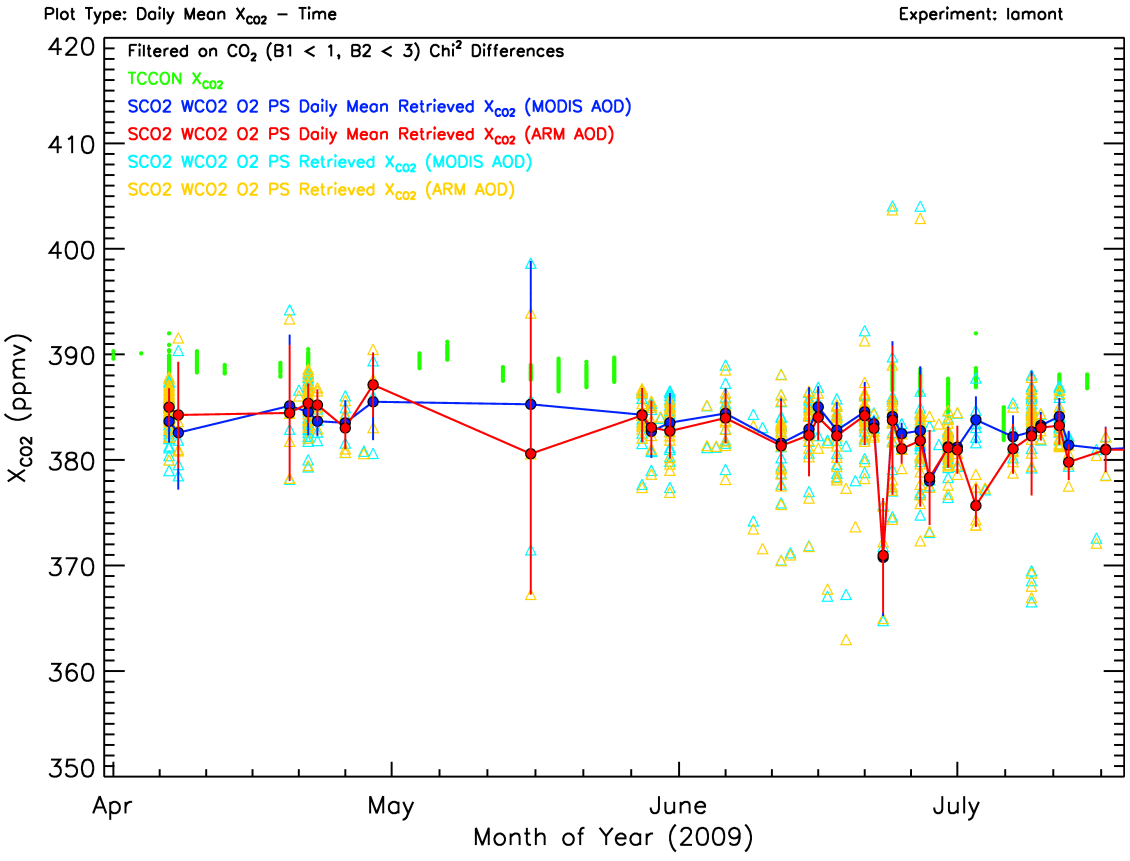

FIGURE 3.25. X_{CO2} inferred from TCCON compared with X_{CO2} retrieved from GOSAT using the UoL-FP retrieval algorithm where the a priori aerosol AOD equals either MODIS monthly mean AOD or ARM temporally closest AOD, calculated for the O_2 A band. All TCCON X_{CO2} data between April and mid-July 2009 from the Lamont site is shown in green and only GOSAT observations within $\pm 5^{\circ}$ of the TCCON site and within 2 hours of an ARM AOD measurement are given. All retrieved GOSAT observations using MODIS AOD are given by cyan triangles and those using ARM AOD by orange triangles. The daily mean of the retrieved X_{CO2} from GOSAT is given in blue and red where MODIS and ARM AOD were used respectively (with error bars representing the X_{CO2} daily scatter). The retrieved observations from GOSAT were post-screened for low χ^2 in bands 1 and 2 to filter out retrievals with poor fits of the simulated spectra to GOSAT spectra.

be used for global retrievals of X_{CO2} from GOSAT. Although satellite measurements of aerosols exist, they are limited to only provide measurements at the locations and times of their orbital paths, not coincident with GOSAT. Although GOSAT includes a cloud and aerosol imager (TANSO-CAI) no aerosol data product has been released yet. Currently, the only way to obtain temporally and spatially coincident aerosol information is to use model estimates.

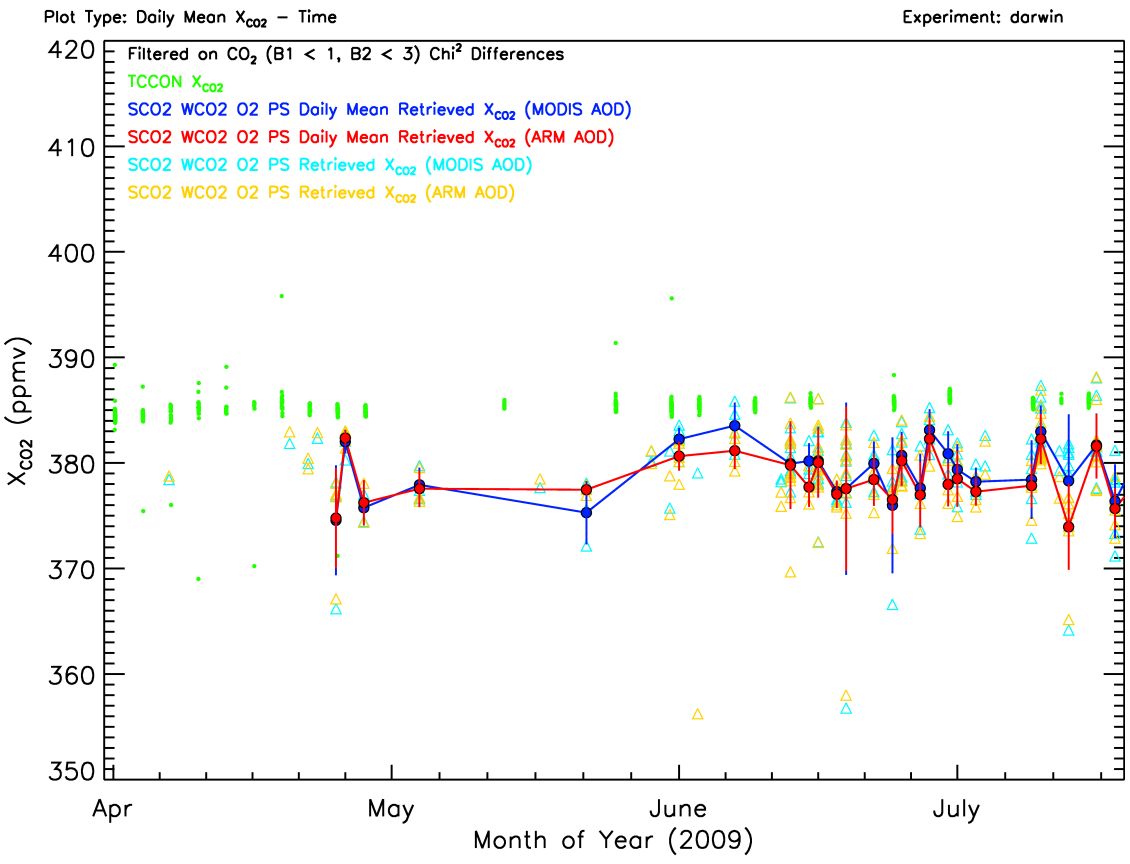

FIGURE 3.26. X_{CO2} inferred from TCCON compared with X_{CO2} retrieved from GOSAT using the UoL-FP retrieval algorithm where the a priori aerosol AOD equals either MODIS monthly mean AOD or ARM temporally closest AOD, calculated for the O_2 A band. All TCCON X_{CO2} data between April and mid-July 2009 from the Darwin site is shown in green and only GOSAT observations within $\pm 5°$ of the TCCON site and within 2 hours of an ARM AOD measurement are given. All retrieved GOSAT observations using MODIS AOD are given by cyan triangles and those using ARM AOD by orange triangles. The daily mean of the retrieved X_{CO2} from GOSAT is given in blue and red where MODIS and ARM AOD were used respectively (with error bars representing the X_{CO2} daily scatter). The retrieved observations from GOSAT were post-screened for low χ^2 in bands 1 and 2 to filter out retrievals with poor fits of the simulated spectra to GOSAT spectra.

The Global and regional Earth-system (Atmosphere) Monitoring using Satellite and in-situ data (GEMS) provides re-analysis model AOD data on 1.125° x 1.125° grid cells globally. GEMS includes two natural aerosol types, sea salt and desert dust, that are surface and weather dependent. These aerosols types both have 3 different sizes; small, medium and large. In addition to the natural aerosols, five anthropogenic aerosols are included. These comprise of sulphate, hydrophilic/hydrophobic organic matter and

hydrophilic/hydrophobic black carbon. The GEMS model obtains information about these aerosols from the Global Fire Emission Database (GFED), the Speciated Particulate Emission Wizard (SPEW), and climatologies of the Emission Database for Global Atmospheric Research (EDGAR) (Simmons 2010). Thus, the GEMS model incorporates emissions of aerosols from fires as well as from domestic, industrial, power generation, transport and shipping activites (Simmons 2010). To complement these aerosol sources, the GEMS model assimilates global measurements of AOD from MODIS. One disadvantage of using the GEMS model is that it does not include any aerosol emissions from volcanic activity. The GEMS model (experiment f1kd) provides the total AOD at multiple wavelengths every twelve hours at 00:00 and 12:00, with a model forecast every three hours proceeding an analysis.

X_{CO2} was retrieved from GOSAT using a single aerosol profile with an a priori AOD equal to the GEMS AOD interpolated to the time and location of the GOSAT observation. The a priori AOD at the O_2 A band was calculated from the GEMS 0.670 μm and 0.865 μm AOD data similar to Equation 3.19, where the angstrom coefficient was calculated as

$$\alpha_{0.670\mu m-0.865\mu m} = -\frac{\ln\left(\frac{\tau_{0.670\mu m}}{\tau_{0.865\mu m}}\right)}{\ln\left(\frac{\lambda_{0.670\mu m}}{\lambda_{0.865\mu m}}\right)} \tag{3.20}$$

Figure 3.27 shows the retrieved X_{CO2} from GOSAT when using GEMS AOD as the a priori AOD, compared to retrieved X_{CO2} when an a priori AOD of 0.15 was always used. The retrieved X_{CO2} is very similar between the two methods, with slightly lower values when GEMS AOD was used. This indicates that the a priori AOD, if not extreme in value, does not affect the retrieval of X_{CO2} significantly.

Instead of retrieving aerosol extinction for each atmospheric level, one option could be to retrieve the height, width and optical depth of a Gaussian shaped aerosol extinction profile. This test provides a different approach to aerosols, allowing the peak of the aerosol distribution to be retrieved, rather than letting the optical depth of each atmospheric layer to vary individually. The retrieval algorithm was modified for this test and X_{CO2} was retrieved from GOSAT between April 2009 and February 2010 for observations within $\pm 5^{\circ}$ of the Lamont TCCON site. Figure 3.28 shows this retrieved X_{CO2} compared to X_{CO2} inferred by TCCON. Between April and July 2009, the retrieved X_{CO2} shows similar values to that previously seen in Figure 3.25. On average, the retrieved X_{CO2} is biased low compared to TCCON by roughly 6 ppm with large daily mean scatters ranging from $\sim$2 ppm to $\sim$20 ppm. Thus, changing the way the aerosol profile shape is retrieved does not improve the retrievals of X_{CO2}.

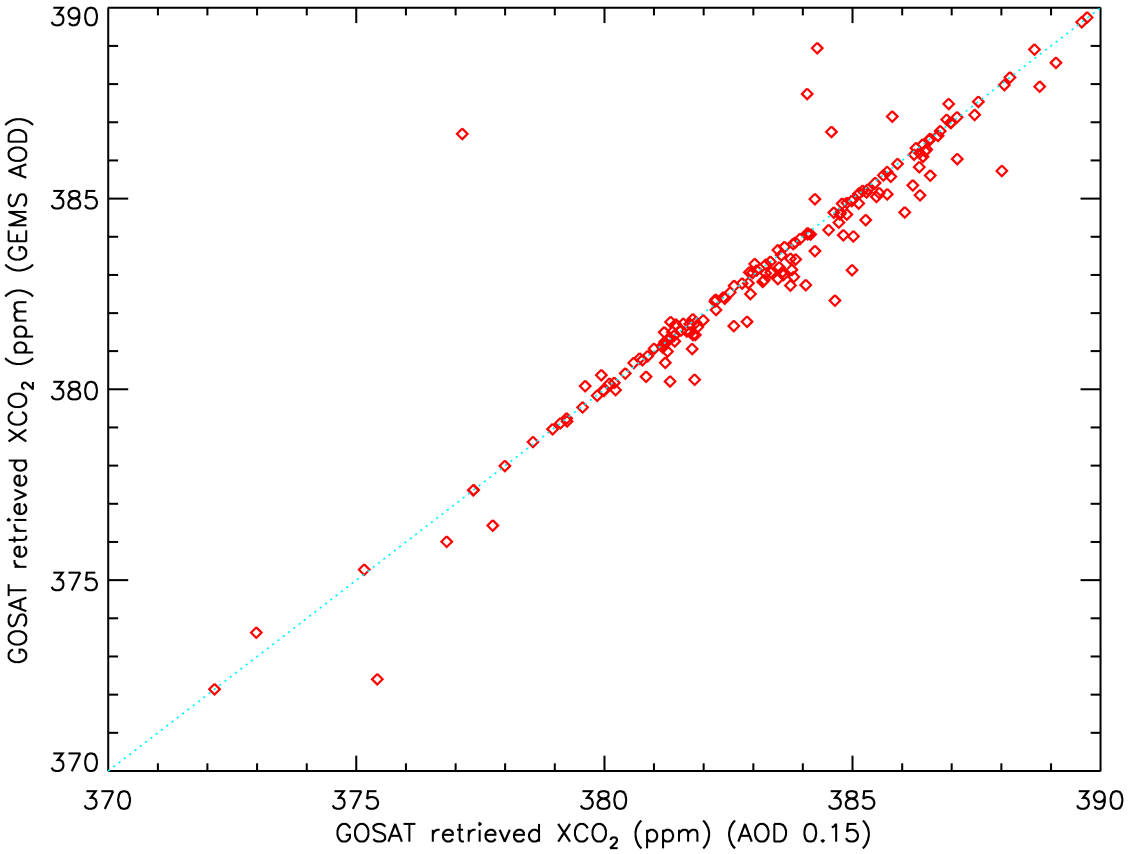

FIGURE 3.27. A comparison of X_{CO2} retrieved from GOSAT between April 2009 and April 2010 using the UoL-FP retrieval algorithm with an a priori optical depth either equal to 0.15 always or equal to GEMS AOD. The retrieved observations were pre-screened, cloud-screened, and then post-screened for low χ^2 values.

In addition to the aerosol profile shape and optical depth, the optical properties assumed could be changed. Instead of using a mixture of carbonaceous and dust aerosols based on Kahn et al. (2001) for a single aerosol, different aerosol types could be given seperate profiles. The retrieval algorithm was modified to retrieve four aerosol logarithmic extinction profiles, each a priori profile having a Gaussian shape with a height and width of 2 km and an optical depth of 0.05. Using a Lorenz-Mie code (Mishchenko et al. 2002) for spherical particles, these aerosols were given optical properties based on GEMS medium sized desert dust, sulphate, hydrophobic organic matter and hydrophobic black carbon properties. Figure 3.29 shows the retrieved X_{CO2} from GOSAT using this setup for observations within $\pm 5^\circ$ of the Lamont TCCON site, compared to TCCON X_{CO2}. The retrieved X_{CO2} shows a reduced bias ($\sim$4 ppm) compared to TCCON than previously found and a much lower daily scatter, between 1 ppm and 8 ppm.

An alternative method could be to use multiple aerosol mixtures rather than seperate aerosol types, this would allow a faster computational time of the retrievals by reducing the number of state vector elements. To test this, aerosol optical properties were computed using a Mie code for carbonaceous/dusty continental and carbonaceous/sooty continental aerosol mixtures described in Kahn et al. (2001). Both these mixtures were given the same a priori extinction profiles that were Gaussian shaped with a height and width of 2km, and an optical depth of 0.05 each. Figure 3.30 shows the retrieved X_{CO2} from GOSAT for this retrieval setup, for observations between April 2009 and February 2010 within $\pm 5^{\circ}$ of the Lamont TCCON site. The retrieved X_{CO2} was found to have a mean bias of $\sim$6 ppm and a daily scatter between 1 ppm and 10 ppm.

Furthermore, it is not just aerosols that can cause absorption and scattering of light in the atmosphere, but clouds too. Although the cloud-screen already removes most observations influenced by clouds, some scenes are falsely flagged as clear. These scenes most likely include thin cirrus clouds that are low absorbing, letting the light still be measured by GOSAT. Therefore, the inclusion of cirrus in the state vector may allow these observations to still be retrieved successfully. A Gaussian shaped profile with a 10 km height, 2 km width and optical depth of 0.05 was used as a priori to test this. Optical properties for an effective radius of 60 μm was assumed for a non-spherical ice particles obtained from the Baum model (Baum et al. 2005a,b). The aerosol was setup the same as the last test, where two aerosol profiles of the same profile shape were used with different aerosol mixtures were used for the optical properties, but this test also includes the cirrus profile described. The retrieved X_{CO2} is shown in Figure 3.31 for GOSAT observations between April 2009 and February 2010 within $\pm 5^{\circ}$ of the Lamont TCCON site. Compared to TCCON, the retrieved X_{CO2} has a daily mean bias of approximately 3 ppm and a daily mean scatter between 1 ppm and 10 ppm. Importantly, less exposures were filtered out by the post-screen, meaning that retrievals of exposures that previously poorly fitted the measured GOSAT spectra are now retrieved. This gives X_{CO2} values within the same range as the exposures whose retrievals previously fitted the measurements well. Furthermore, the retrieved X_{CO2} shows a large increase of 3 ppm compared to exactly the same retrievals but without the cirrus included. Thus, not only does this approach produce a larger X_{CO2} dataset but it provides a lower bias.

Eguchi et al. (2007) found that cirrus clouds vary in height depending on the latitude, with larger values towards the equator (as shown in Figure 3.32). Since the use of a cirrus profile had a large effect on the retrieved X_{CO2}, it was important to follow it up by testing the use of profile shape that varies with latitude. Mean values of cirrus cloud center heights and widths were obtained from Eguchi et al. (2007) for the tropics and

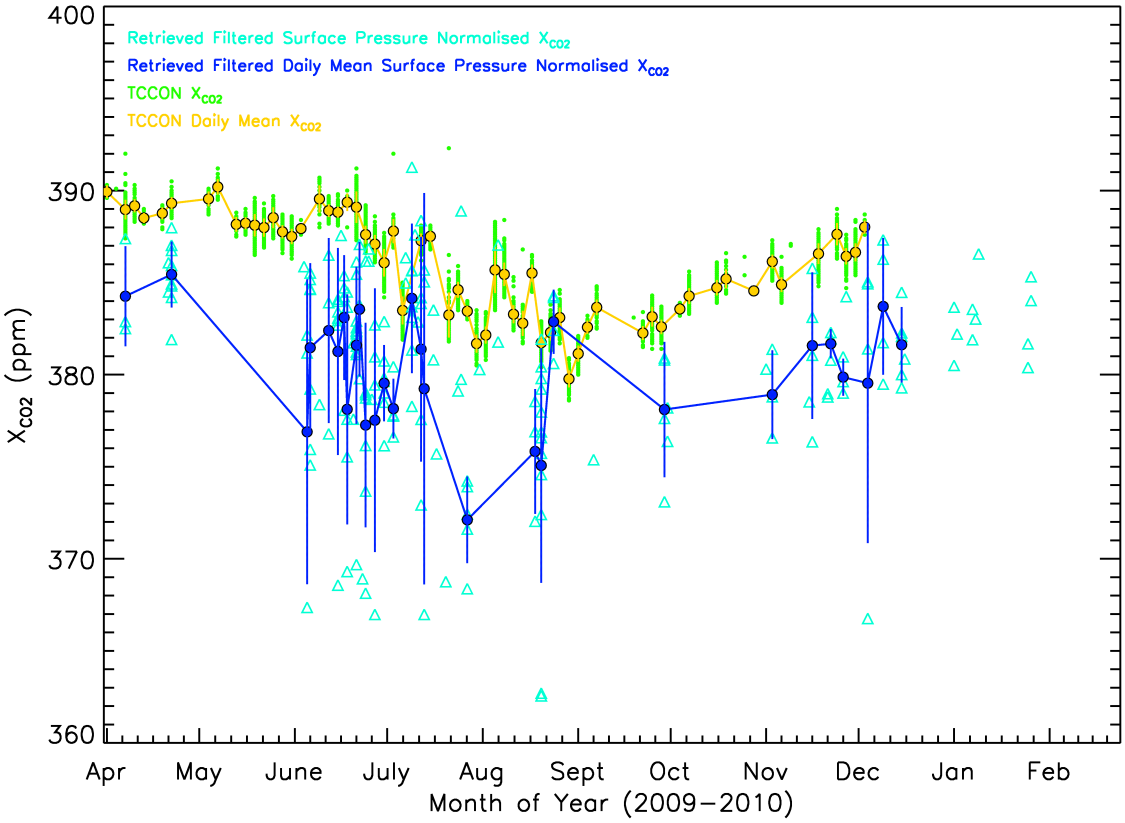

FIGURE 3.28. X_{CO2} retrieved from GOSAT using the UoL-FP retrieval algorithm with the aerosol height, width and optical depth retrieved. All pre-screened and cloud-screened GOSAT observations within $\pm 5^{\circ}$ of the Lamont TCCON site between April 2009 and February 2010 were retrieved and post-screened for low χ^2 values. The X_{CO2} retrieved from TCCON is given in green with the daily mean shown in orange. The retrieved GOSAT X_{CO2} is given by cyan triangles and the daily mean by blue circles, with the daily scatter given as error bars.

subtropics in both hemispheres, mid-latitudes in both hemispheres, and globally (see Table 3.2). These values were interpolated onto a 1° latitudinal grid and for every grid point a Gaussian shaped cirrus profile was created with the corresponding height and width. Thus providing a latitudinal dependent cirrus profile that can be used with retrievals of X_{CO2} from GOSAT.

Figure 3.33 shows a comparison of the retrieved X_{CO2} from GOSAT when using a constant cirrus profile and when using a latitudinally dependent cirrus profile, for observations between April 2009 and February 2010 within $\pm 5^{\circ}$ of the Lamont TCCON site. On average, higher X_{CO2} and a lower retrieved cirrus optical depth is retrieved when a latitude dependent cirrus profile is used. Thus, using a latitudinally dependent cirrus profile reduces the X_{CO2} bias to TCCON, by providing the retrieval with a more realistic

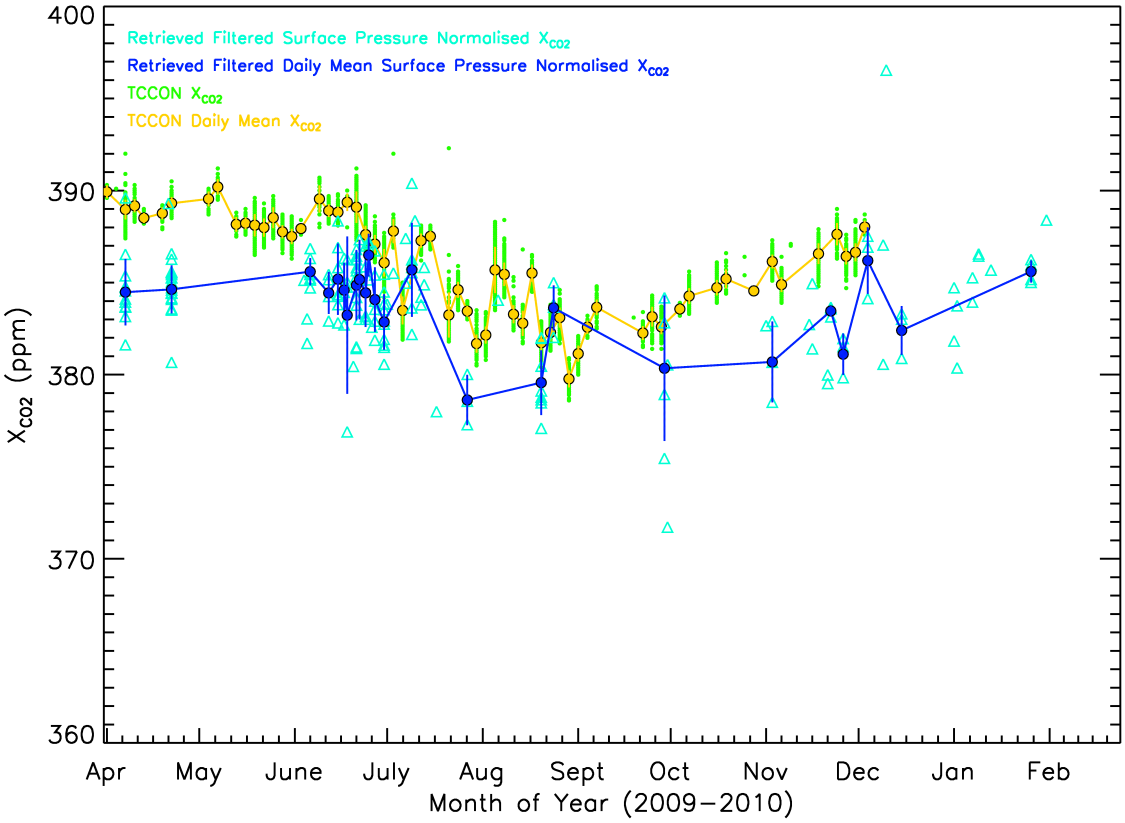

FIGURE 3.29. X_{CO2} retrieved from GOSAT using the UoL-FP retrieval algorithm with four different aerosol profiles retrieved. The a priori of each aerosol was given a Gaussian shaped profile with a height and width of 2 km and optical depth of 0.05, but different optical properties. The optical properties were computed using a Mie code for the GEMS medium sized desert dust, sulphate, hydrophobic organic matter and hydrophobic black carbon. All pre-screened and cloud-screened GOSAT observations within $\pm 5^{\circ}$ of the Lamont TCCON site between April 2009 and February 2010 were retrieved and post-screened for low χ^2 values. The X_{CO2} retrieved from TCCON is given in green with the daily mean shown in orange. The retrieved GOSAT X_{CO2} is given by cyan triangles and the daily mean by blue circles, with the daily scatter given as error bars.

a priori assumption of the atmosphere.

Based on these tests, three atmospheric extinction profiles are used. Two of these profiles are the same shape, Gaussian profile with a 2 km height and width, and have a total column aerosol optical depth of 0.05 each (as shown in Figure 3.34). The only difference between these profiles are the aerosol properties used for each. Based on Kahn et al. (2001) one uses classification 4b and the other uses classification 5b. Therefore providing one profile designed for carbonaceous and dusty environments and the other profile for carbonaceous and sooty environments. The third profile allows for the pos-

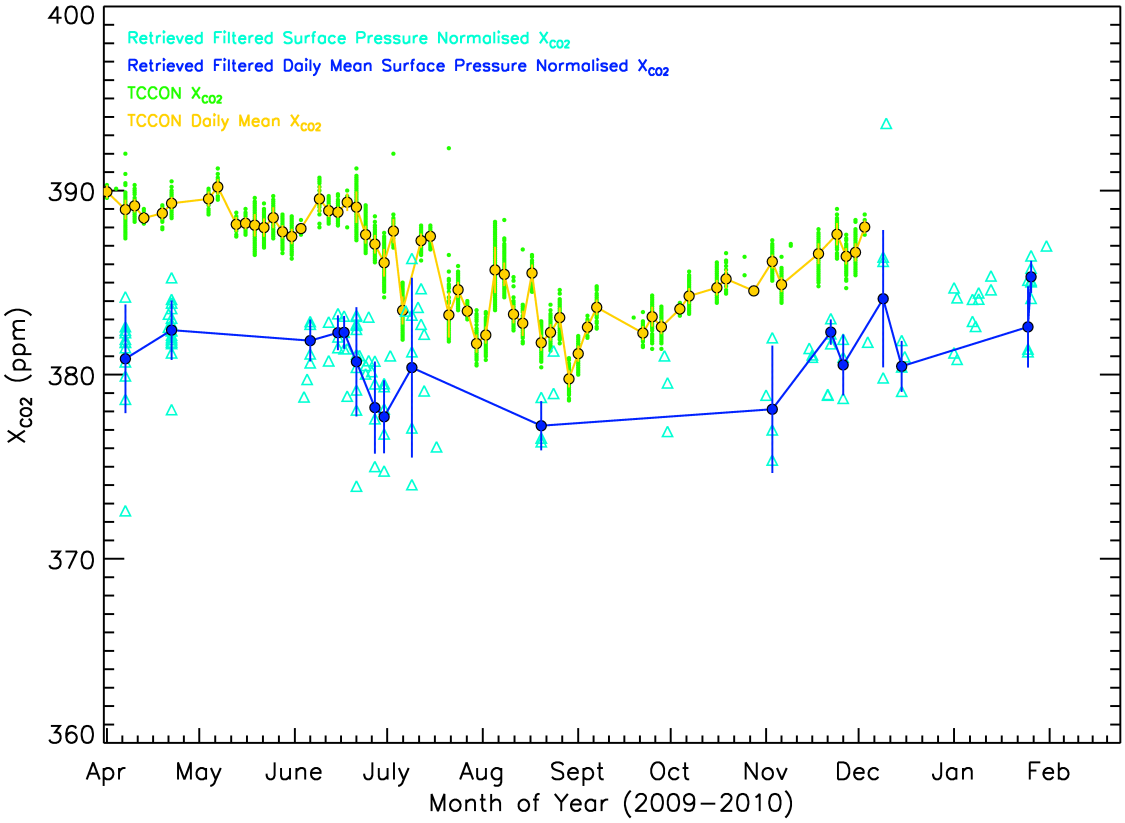

FIGURE 3.30. X_{CO2} retrieved from GOSAT using the UoL-FP retrieval algorithm with 2 aerosol profiles, both of Gaussian shape with a height and width of 2 km and optical depth of 0.05 each. The optical properties were computed using a Mie code for carbonaceous/dusty continental and carbonaceous/sooty continental aerosol mixtures described in Kahn et al. (2001). All pre-screened and cloud-screened GOSAT observations within $\pm 5^{\circ}$ of the Lamont TCCON site between April 2009 and February 2010 were retrieved and post-screened for low χ^2 values. The X_{CO2} retrieved from TCCON is given in green with the daily mean shown in orange. The retrieved GOSAT X_{CO2} is given by cyan triangles and the daily mean by blue circles, with the daily scatter given as error bars.

sibility of a cirrus cloud and is based on the height and thickness described in Eguchi et al. (2007). A Gaussian profile of 0.1 optical depth was created for each of the latitude regions described using the height and thickness given and then a look up table based on every 1 degree of latitude was created globally by interpolating between these regions with respect to latitude. Each retrieval uses the cirrus profile defined in the look up table that is closest to the specific latitude of the retrieved scene. The cirrus properties are constructed from ice cloud models based on the Baum model (Baum et al. 2005a,b). In the O_2 A Band the ratio of scattering to absorption for cirrus has very little dependence on the particle radius but a high dependence on optical depth. Conversely at the 1.61 μm

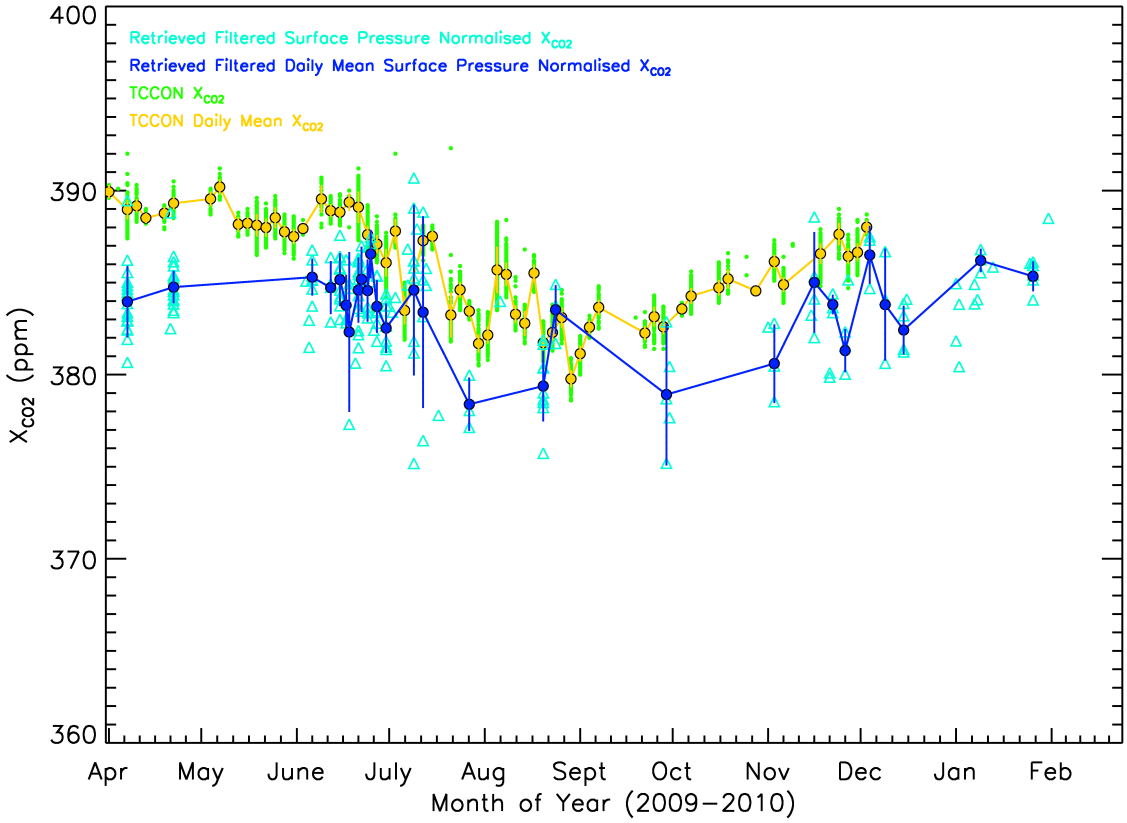

FIGURE 3.31. X_{CO2} retrieved from GOSAT using the UoL-FP retrieval algorithm with a cirrus profile and 2 aerosol profiles. The cirrus a priori profile had a Gaussian shape with a height of 10 km, width of 2 km and optical depth of 0.05. the cirrus optical properties were obtained from the Baum model (Baum et al. 2005a) and given a effective radius of 60 μm. Both aerosols had an a priori profile of Gaussian shape with a height and width of 2 km and optical depth of 0.05 each. The optical properties were computed using a Mie code for carbonaceous/dusty continental and carbonaceous/sooty continental aerosol mixtures described in Kahn et al. (2001). All pre-screened and cloud-screened GOSAT observations within $\pm 5^{\circ}$ of the Lamont TCCON site between April 2009 and February 2010 were retrieved and post-screened for low χ^2 values. The X_{CO2} retrieved from TCCON is given in green with the daily mean shown in orange. The retrieved GOSAT X_{CO2} is given by cyan triangles and the daily mean by blue circles, with the daily scatter given as error bars.

and 2.03 μm bands, there is more absorption by cirrus and therefore a higher sensitivity to the particle radius (Zhang et al. 2010). A large ice particle of an effective radius of 60 μm is assumed for all retrievals, to provide the retrieval algorithm with a high variability of the ratio of scattering to absorption between bands.

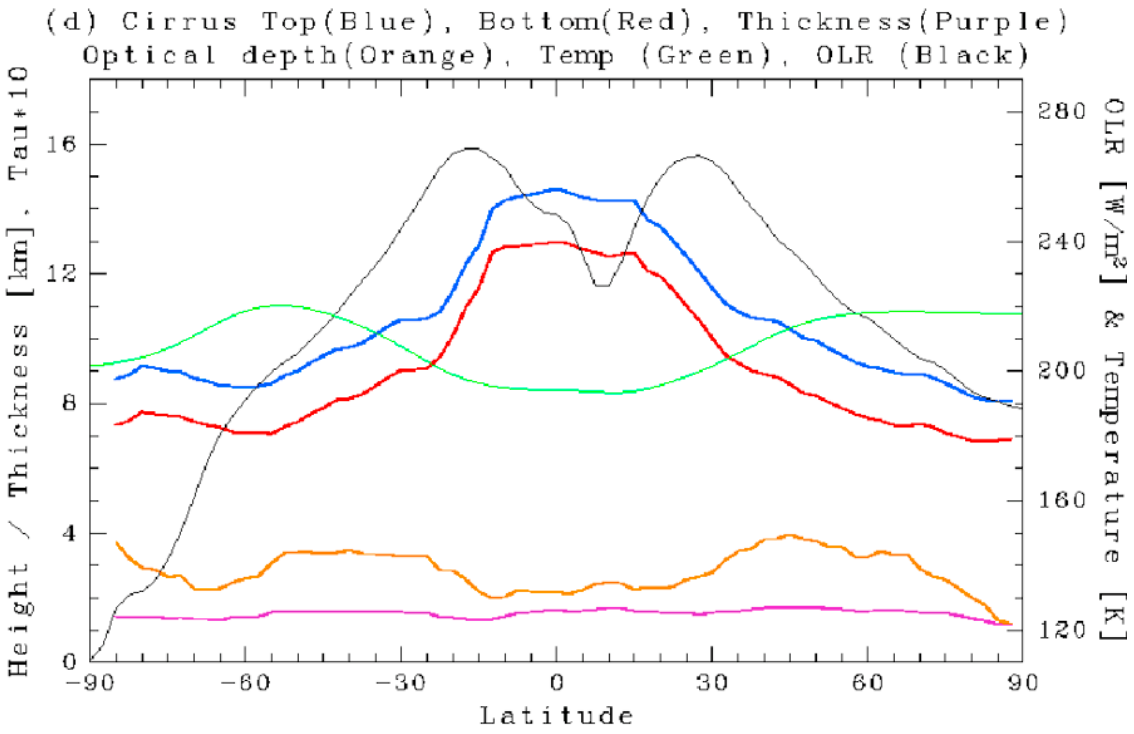

FIGURE 3.32. Cirrus cloud characteristics as a function of latitude, calculated from the Geoscience Laser Altimeter System (GLAS) and the Ice, Cloud, and land Elevation Satellite (ICESat) between 1st October and 18th November 2003. The altitude of the top of the cirrus cloud is given in blue, the altitude of the bottom of the cirrus cloud is given in red and the cirrus cloud thickness is given in purple. The cirrus cloud optical depth is given in orange and the cirrus cloud temperature is given in green. The average Outgoing Longwave Radiation (OLR) obtained from NOAA satellites during the same time period is shown in black (Eguchi et al. 2007).

Table 3.2. Mean cirrus cloud heights and widths calculated from GLAS and ICESat data for the tropics ans subtropics in both hemispheres, mid-latitudes in both hemispheres, and globally (Eguchi et al. 2007).

Latitude region	Latitude range	Height [km]	Width [km]
Tropics	15°S - 15°N	13.6	1.6
Subtropics (northern hemisphere)	15°N - 30°N	12.0	1.6
Subtropics (southern hemisphere)	15°S - 30°S	10.7	1.4
Middle latitude (northern hemisphere)	30°N - 60°N	9.2	1.6
Middle latitude (southern hemisphere)	30°S - 60°S	8.7	1.6
Globe	86°S - 86°N	10.3	1.6

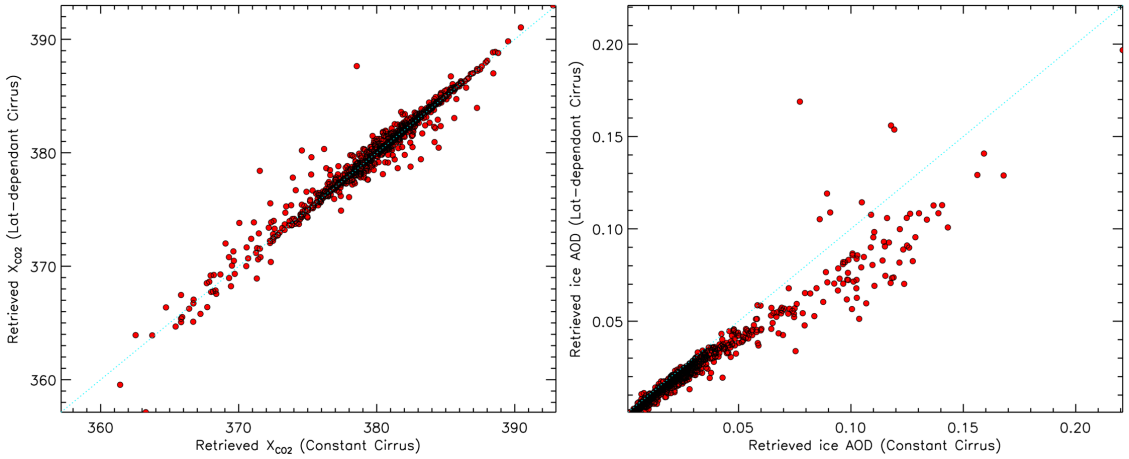

FIGURE 3.33. X_{CO2} retrieved from GOSAT between April 2009 and February 2010 within $\pm 5^{\circ}$ of the Lamont TCCON site, when a constant cirrus profile of Gaussian shape with a height of 10 km and width of 2 km was assumed for all retrievals compared to when a latitude dependent cirrus profile based on Eguchi et al. (2007) was used. Both retrievals were otherwise setup the same and both were given an a priori optical depth of 0.05 and the same optical properties. A comparison of the retrieved X_{CO2} is given by the left panel and a comparison of the retrieved cirrus optical depth is given by the right panel.

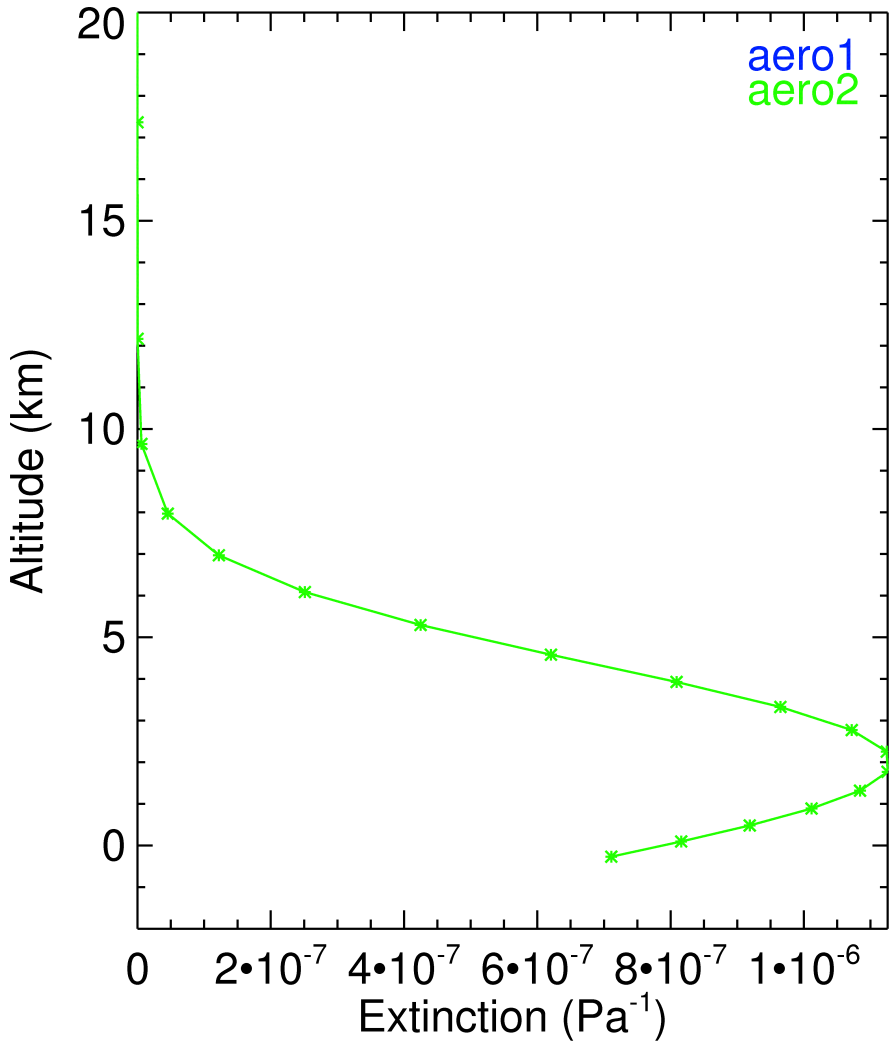

FIGURE 3.34. Gaussian aerosol profiles of 2 km height width and with 0.05 AOD.

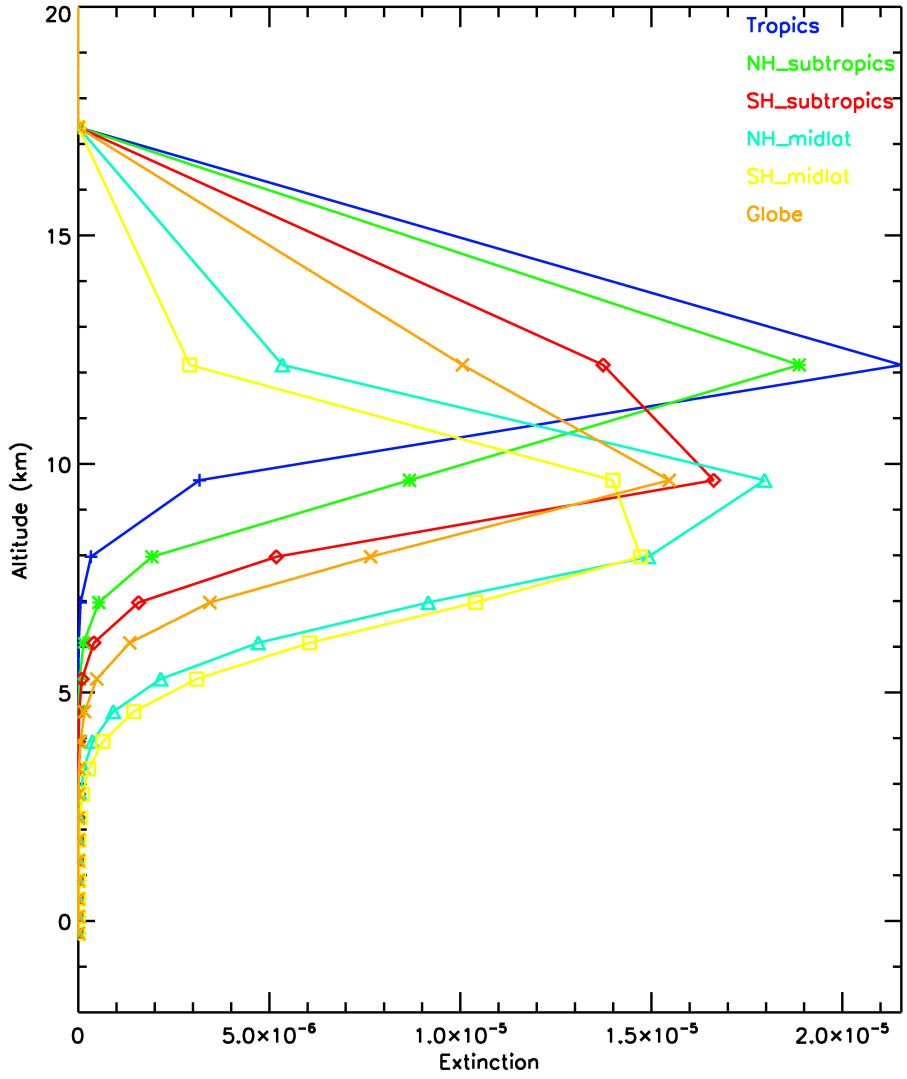

FIGURE 3.35. Gaussian profiles based on the height and thickness described for various regions by Eguchi et al, (Eguchi et al. 2007).

3.18 Surface Properties

The albedo, α, is calculated from the spectral continuum of the GOSAT L1B using the reflectivity

$$\alpha = \frac{\pi S_{GOSAT}}{S_{Solar}\cos(SZA)} \tag{3.21}$$

where SZA is the solar zenith angle, and the Solar irradiance and observed GOSAT radiance are given by S_{Solar} and S_{GOSAT} respectively. The retrieval uses two albedo parameters for each spectral band, giving the albedo for the centre wavelength of the band and the slope of the albedo. The slope of the albedo is set to zero in the a priori. The covariance for albedo is completely open (standard deviation of 1) and the slope a priori error uses a standard deviation of 0.01 cm^{-1} so that the band edges can vary by 50% to compensate for any apodization artifacts introduced during the FFT of the TANSO-FTS interferogram.

3.19 Instrument Properties

The recommended radiometric calibration and solar diffuser degradation correction (preliminary factors) were applied to the GOSAT Level 1B files (050.050C, 080.080C, 110.110C and 130.130C) which covered the years 2009 to 2011 and were acquired via the GOSAT User Interface Gateway.

The radiative transfer model produces synthetic spectra for a specified observation geometry and surface/atmospheric state. Before comparing these spectra to calibrated measured spectra they are corrected for instrument dispersion, and convolved with the instrument line shape (ILS) function and polarisation. For polarisation to be correctly used a Mueller matrix (Kuze et al. 2009) is required to combine the different Stokes vectors. However, the Mueller matrix is derived using the observation viewing angles which are known to have pointing issues due to microvibrations causing instability. Therefore, the intensity is approximated by using the mean of the polarised intensities:

$$I = \frac{P + S}{2} \tag{3.22}$$

The noise is derived from the standard deviation of the out of band radiances for each band (see Figure 3.36), which in the absence of noise would centre on zero. Similarly to

the signal, the noise from each polarisation is combined as

$$N = \frac{\sqrt{N_P^2 + N_S^2}}{2} \tag{3.23}$$

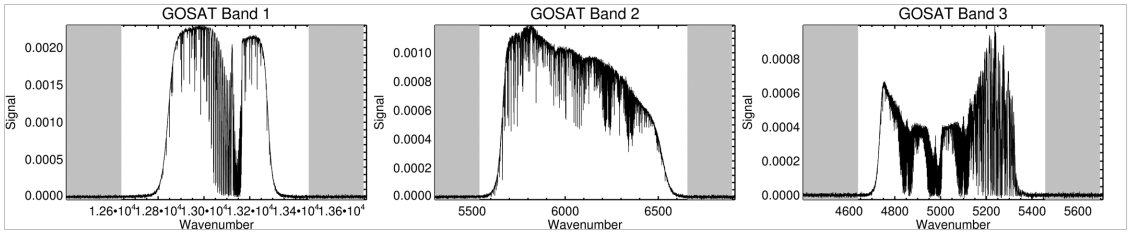

FIGURE 3.36. Example raw radiance for each GOSAT SWIR band showing out of band characteristics used to derive the noise (grey).

Systematic structures in the residual of the spectral fit were found (typically solar lines), that are most likely driven by insufficient spectroscopy. As a consequence, the reduced χ^2 of the spectral fit will increase with the theoretical SNR of the sounding. The χ^2 could become reduced by masking these spectroscopic peaks, which can be achieved by increasing the noise.

Figure 3.37 shows the real mean squared (RMS)/Signal compared to 1/SNR for each band for X_{CO2} retrieved from GOSAT for one 3-day cycle in June 2009. The noise can be inflated by using an emperical relationship between the RMS/signal and 1/SNR for each band (Crisp et al. 2012) of

$$\frac{\text{RMS}}{\text{Signal}} = A + \frac{B}{\text{SNR}} \tag{3.24}$$

where A and B are the coefficients derived (see Table 3.3). Using these coefficients the noise was then modified by

$$\text{Inflated Noise} = A * \text{Signal} + B * \text{Noise} \tag{3.25}$$

The GOSAT 3-day cycle was re-retrieved using the inflated noise and the difference of retrieved χ^2 of the fit for each band is shown in Figure 3.38. The χ^2 was found to become much lower when the noise was increased, as expected.

With the release of new TANSO-FTS L1B data versions, the noise coefficients were re-calculated for each version. Figure 3.39 shows the fit of RMS/Signal and 1/SNR for each band with each available data version shown, where September 2009 is L1B version

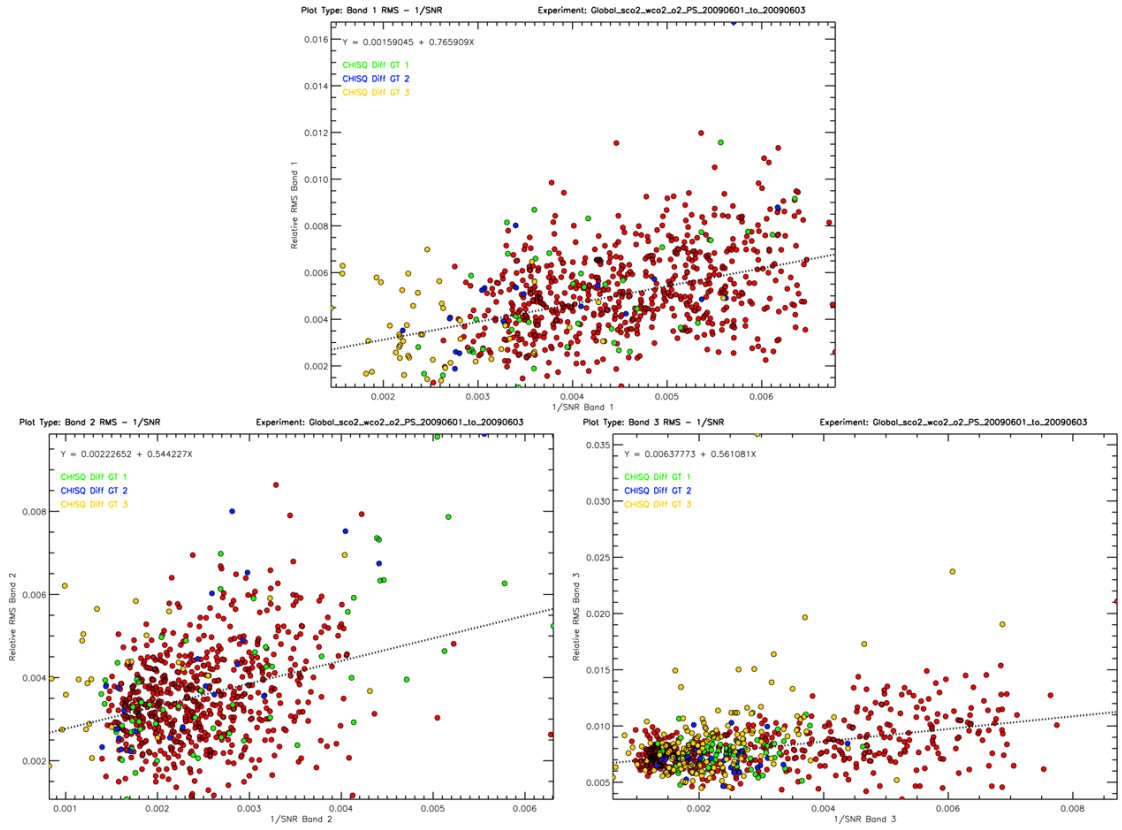

FIGURE 3.37. Fit of relative RMS (RMS/Signal) and 1/SNR for each GOSAT SWIR band retrieved by the UoL-FP algorithm for global observations of a 3-day orbital cycle between 1st-3rd June 2009. Additionally, the difference between the retrieved and expected χ^2 is highlighted for different ranges in value. A linear fit of the data is given by the dotted line for each band, with its equation provided in the top left of each panel.

v050, December 2009 is L1B version v080, and May 2010 is L1B version v100. These fits vary only slightly from the initial coefficients derived and are also similar to that reported by ACOS (Connor 2010). For simplicity, the mean of the coefficients from each L1B version was used.

Table 3.3. Derived coefficients used to inflate the noise.

Test	A (Band 1)	B (Band 1)	A (Band 2)	B (Band 2)	A (Band 3)	B (Band 3)
Initial (007.007V)	0.00159045	0.765909	0.00222652	0.544227	0.00637773	0.561081
1st-3rd September 2009 (080.080C)	0.0038452676	0.65677958	0.0021347245	0.70029702	0.0039319740	0.65454255
1st-3rd December 2009 (050.050C)	0.0045277149	0.57120579	0.0017439434	0.77762136	0.0039563910	0.63522226
1st-3rd May 2010 (100.100C)	0.0042883528	0.57437039	0.0023632774	0.51059092	0.0036055675	0.65775003
Mean	0.00422045	0.600785	0.00208065	0.662836	0.00383131	0.649172
ACOS (050.050C)	0.00234298	0.643008	0.00165767	0.634136	0.00287656	0.633723

However, recent updates in spectroscopy have reduced the systematic structures in

the residual of the spectral fit, giving the expected χ^2 values. Therefore, the original noise is now sufficient to use.

The dispersion gives the pixel-wavelength mapping and consists of two parameters for each band; the start wavenumber W and the wavenumber increment D needed to reach the next pixels wavenumber. The wavenumber, ν, for detector pixel, i, and spectrometer, k, is given by

$$\nu_i = W_k + iD_k \tag{3.26}$$

The dispersion is given in the GOSAT L1B data but requires adjusting in all SWIR bands. This adjustment can be calculated by the difference of the spectra away from a well known single strong Fraunhofer line, otherwise known as a Solar line, (12985.163 cm^{-1}) in the O_2 A band. Additionally, the O_2 A band dispersion requires shifting one spectral point lower to become approximately correct. It should be understood that although all SWIR bands dispersions are adjusted they are only approximate and require the dispersion to be retrieved.

To describe the response of the instrument to light with wavelength an instrument line shape function (ILS) is used, which was obtained from the JAXA ILSF model (Kuze et al. 2009). Band 1 has the ILS provided for both polarisations due to band 1 being sensitive to displacement of the optical axis with its shorter wavelengths, whereas bands 2 and 3 have accurate alignment. The ILS model gives the ILS for 3 different wavelengths in band 1 and 4 different wavelengths in both bands 2 and 3.

To mitigate the effect of the GOSAT band 1 non-linear response to the intensity of incident radiation on the retrieval of X_{CO2}, an additive zero level intensity offset was retrieved for the O_2 A band. To check that the inclusion of this does not cause the retrieved X_{CO2} to become worse, retrievals with and without the zero level offset applied were retrieved for GOSAT pre-screened and cloud-screened observations for September 2009 globally. Figure 3.41 shows the comparison of retrieved X_{CO2} from retrievals with and without the zero level offset retrieved in the O_2 A band. For low X_{CO2} values, slightly larger X_{CO2} values are found when a zero level offset is included in the retrieval. However, in general, the X_{CO2} remains similar. This method may also partially mitigate fluorescence observed by Frankenberg et al. (2011a).

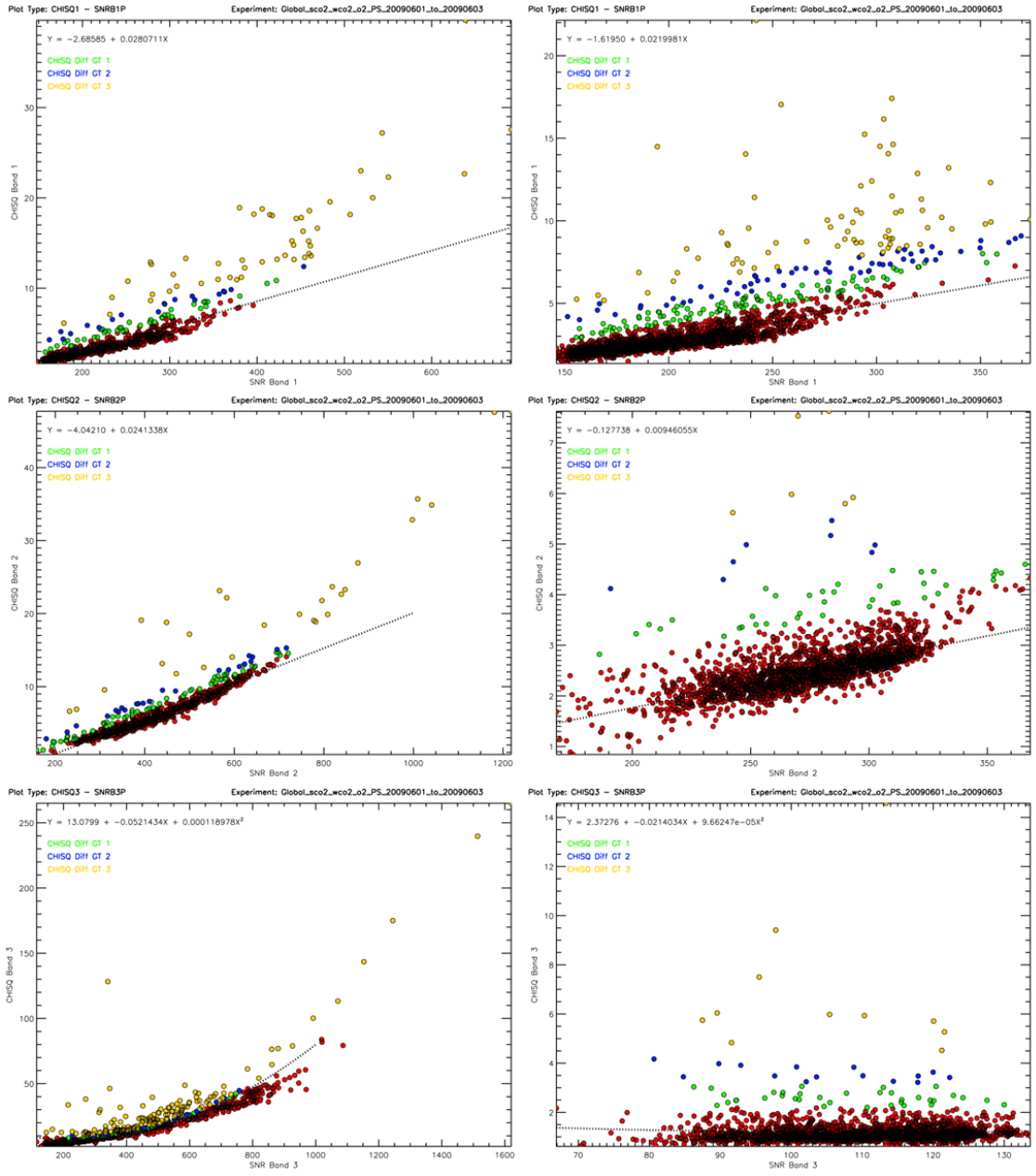

FIGURE 3.38. Comparison of retrieved χ^2 and SNR for each GOSAT SWIR band retrieved by the UoL-FP algorithm for global observations of a 3-day orbital cycle between 1st-3rd June 2009. The left column shows the data for each band when the original noise was used, and the right column shows each band when the inflated noise was used. Note that the y-axis scales are different, giving much lower χ^2 values when the inflated noise was used.

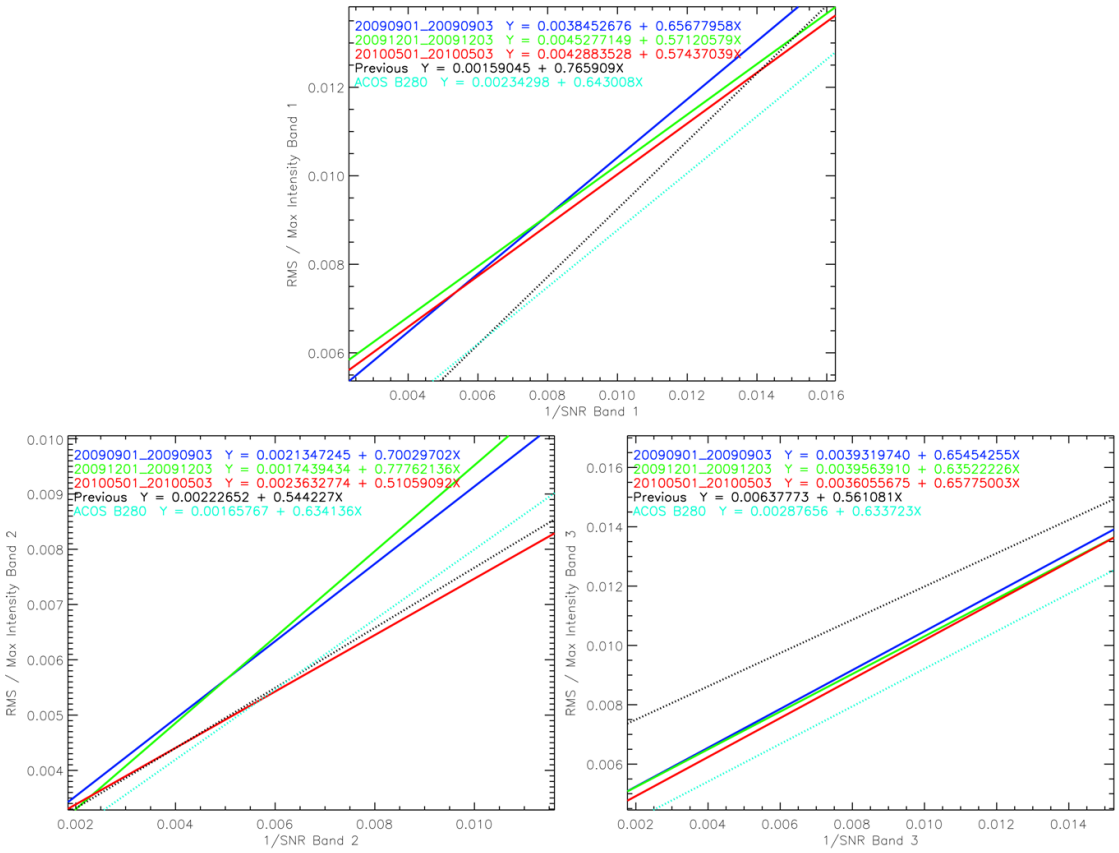

FIGURE 3.39. Linear fits of RMS/Signal and 1/SNR for each GOSAT SWIR band retrieved by the UoL-FP algorithm for global observations of a 3-day orbital cycle in 3 different time frames, covering different TANSO-FTS L1B data versions. The initial/previous fit is shown in black and that reported similarly by ACOS in cyan.

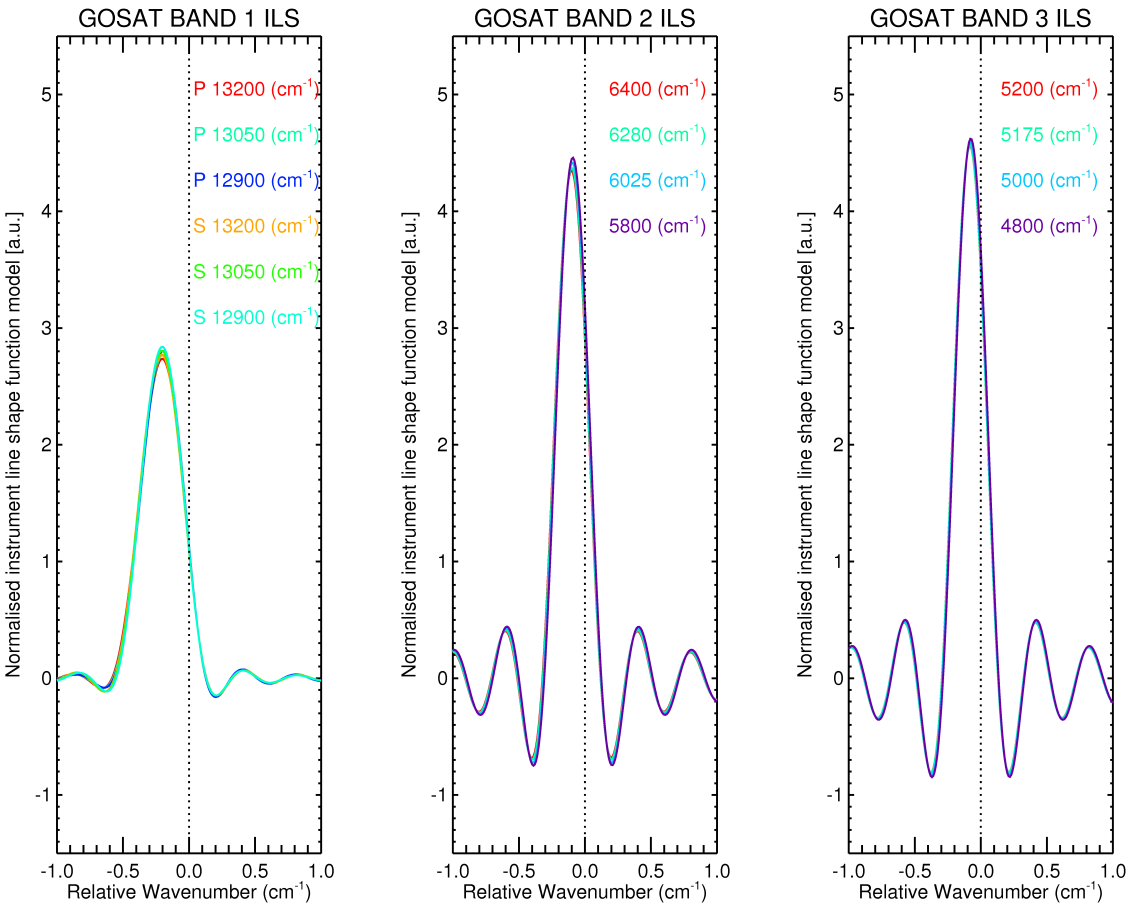

FIGURE 3.40. ILS used in the retrievals for each GOSAT SWIR spectral band with different wavenumbers given.

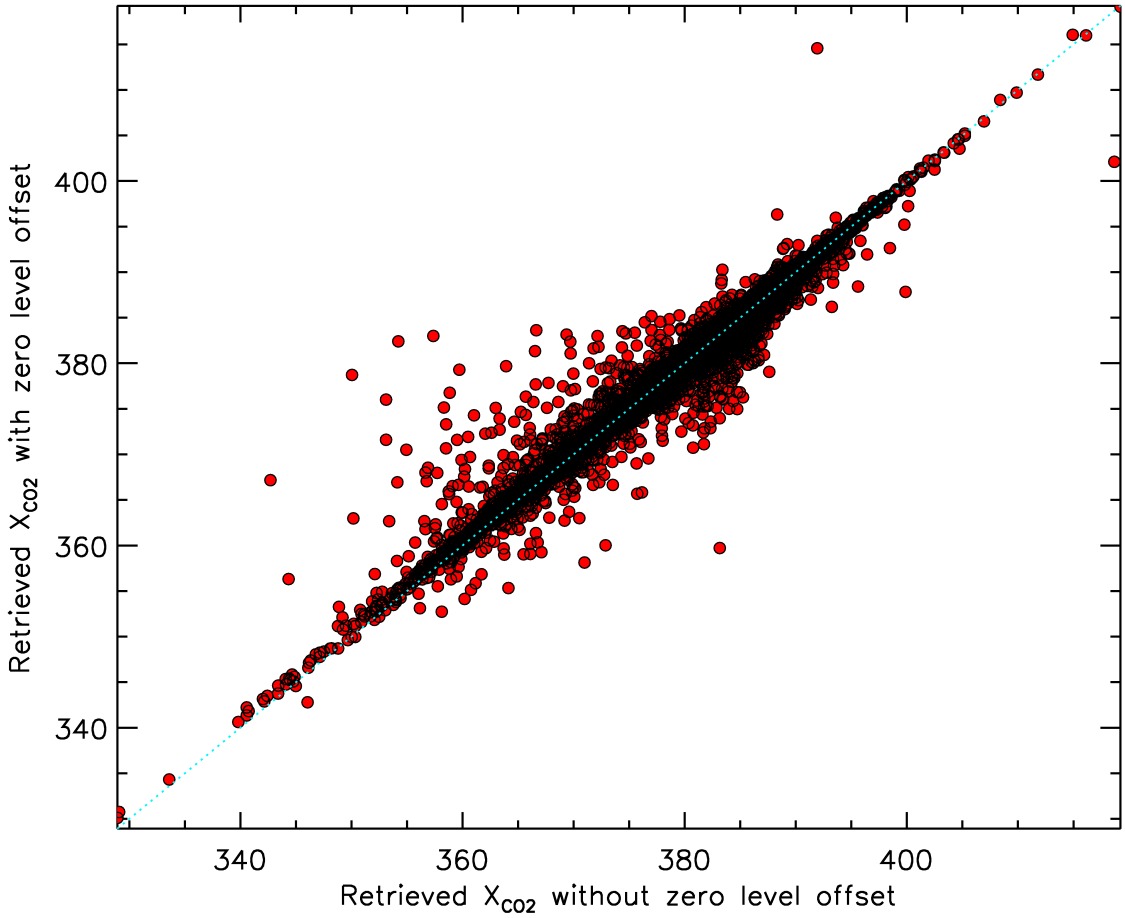

FIGURE 3.41. Comparison of retrieved X_{CO2} from GOSAT using the UoL-FP retrieval algorithm with and without an O_2 A band zero level offset retrieved. These retrievals were performed on pre-screened and cloud-screened GOSAT observations for September 2009 globally. Details of the algorithm are provided in Chapter 3.

3.20 Pre-Processing Screen

A pre-screen is applied to all GOSAT observations during the pre-processing algorithm such that only land observations with a SNR >50 in all bands are used. Although observations with a low SNR could be retrieved, it would result in a poor retrieval fit, since small changes in the signal can not be distinguished from the noise. Also, poor retrieval fits are expected over snow surfaces (see Section 3.11) so only scenes with a SZA $<70^{\circ}$ are used to reduce the computational requirement of performing retrievals globally. Additionally, the pre-screen selects non-saturated measurements with an along-track angle error <0.05, cross-track angle error <0.007, and where the IFOV surface pressure standard deviation is <10 hPa. The along-track and cross-track filters are used to keep only measurements where the pointing has not been adversely affected by microvibrations.

The IFOV of TANSO-FTS is ∼10 km in diameter and within this area the topography can change greatly. Although the pre-processing uses the mean atmospheric conditions within the IFOV, this might not provide useful a priori in extreme scenes. Also, the surface can vary significantly over such a large region, leading to variations in albedo that are unaccounted for in the retrieval. Since surfaces with a higher albedo reflect more light the observed radiance will be biased towards that surface type and therefore that location and not the entire IFOV scene. In this instance, the retrieval would require the atmospheric conditions for that location and not the mean of the IFOV. Screening to remove scenes with a high surface pressure variation helps mitigate this issue.

It is possible that during a TANSO-FTS observation the interferogram can become saturated by light. If the interferogram becomes saturated, then when the FFT is performed the spectral radiance and absorption lines will be larger everywhere leading to a poor retrieval. Therefore, a new method for detecting GOSAT saturation was created to allow these observations to be filtered out. This detection method uses the mean out-of-band radiances, since the spectra should have higher values throughout the measured spectral ranges when saturation occurs. Initially all three SWIR bands were analysed but the saturation is best detected with this method in band 2, as shown in Figure 3.44. The band 2 saturation detection was compared with the χ^2 of X_{CO2} retrievals for band 2 (see Figure 3.45) and a clear trend was found with larger χ^2 values. TANSO-FTS is capable of measuring radiances using different gain modes, such that it can cope with high intensity signals by using the medium gain so that saturation should not arise. To attempt to determine why the saturation occurs, the maximum signal of band 2 was compared with the saturation detection test for each gain mode. This is given in Figure 3.47, which distinctly shows that saturation happens when the signal intensity is highest for

observations using high gain. This highlights that the medium gain mode should be used in additional measurement locations.

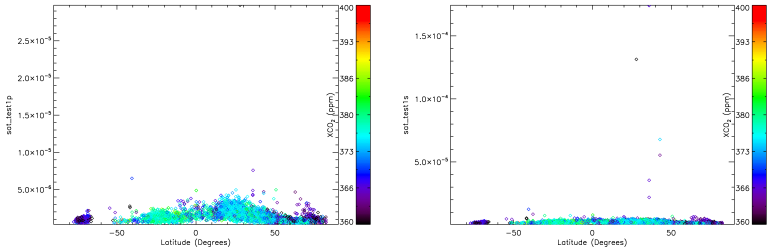

FIGURE 3.42. Mean out-of-band radiances of band 1 P (left) and S (right) compared with latitude and retrieved X_{CO2} for 1st-7th September 2009 globally.

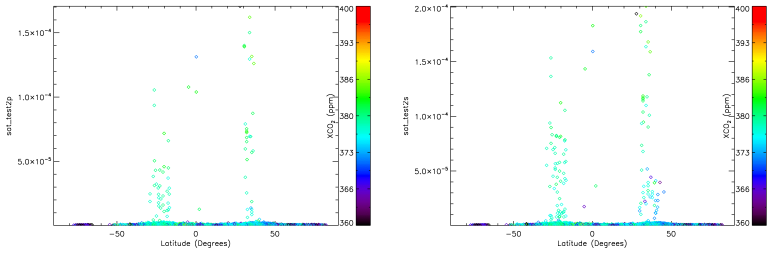

FIGURE 3.43. Mean out-of-band radiances of band 2 P (left) and S (right) compared with latitude and retrieved X_{CO2} for 1st-7th September 2009 globally.

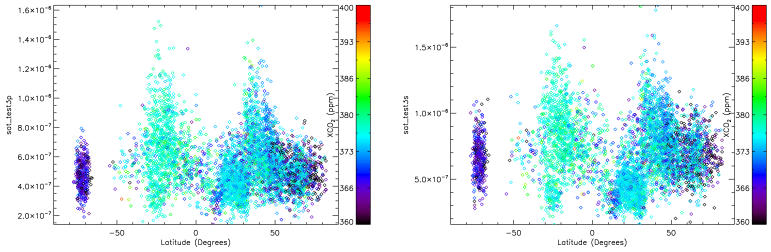

FIGURE 3.44. Mean out-of-band radiances of band 3 P (left) and S (right) compared with latitude and retrieved X_{CO2} for 1st-7th September 2009 globally.

3.21 Cloud Screen

One major disadvantage of using SWIR observations is that the IFOV must be free of thick clouds as these will cause irradiation to be reflected towards the satellite from a higher altitude, that of the cloud, rather than the Earth's surface where source/sink information can be gained. Therefore, a cloud screen is necessary to filter out exposures where thick clouds are within the IFOV. When irradiation gets reflected towards the satellite from a thick cloud the effective surface is that of the cloud rather than the Earth's surface. This results in the surface pressure being that at the cloud altitude, which typically is significantly lower than that at the Earth's surface pressure. An estimate of

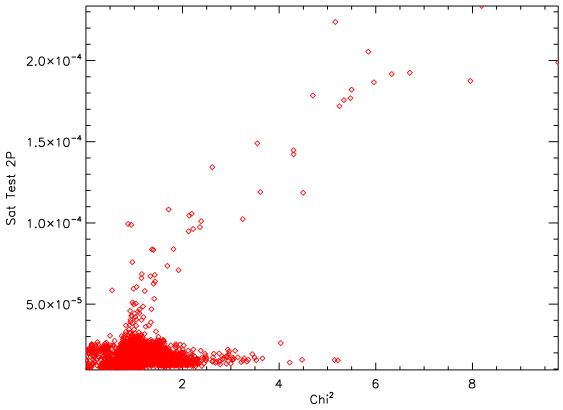

FIGURE 3.45. Saturation test for band 2 P compared with the retrieval χ^2 of band 2, for retievals of 1st-7th September 2009 globally.

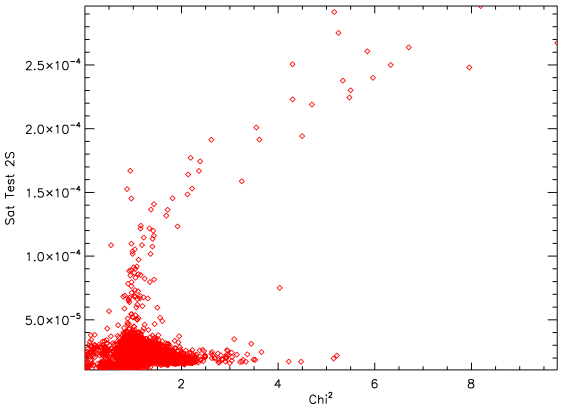

FIGURE 3.46. Saturation test for band 2 S compared with the retrieval χ^2 of band 2, for retievals of 1st-7th September 2009 globally.

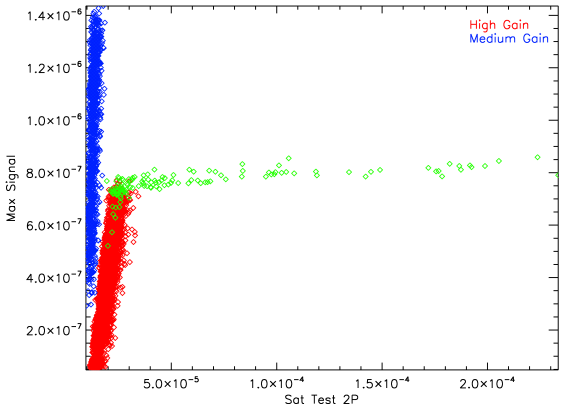

FIGURE 3.47. Saturation test compared to the maximum signal for band 2 P, with high gain mode shown in red, medium gain mode shown in blue, and exposures which fail the both polarisation saturation test thresholds shown in green. For retievals of 1st-7th September 2009 globally.

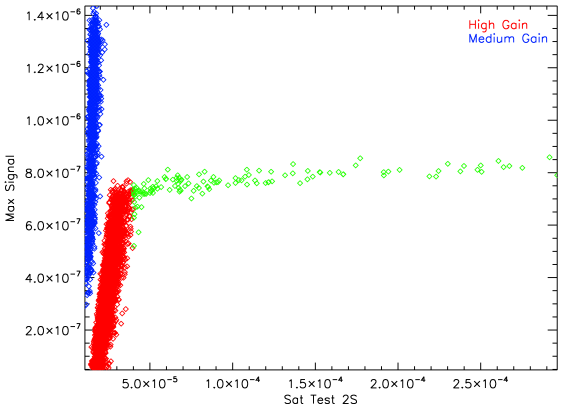

FIGURE 3.48. Saturation test compared to the maximum signal for band 2 S, with high gain mode shown in red, medium gain mode shown in blue, and exposures which fail the both polarisation saturation test thresholds shown in green. For retievals of 1st-7th September 2009 globally.

the surface pressure can be obtained by performing an O_2 A band retrievals where the surface pressure is retrieved. A fast O_2 retrieval is implemented, by using a small spectral window (13056 to 13074.8 cm-1) where the surface pressure information is obtained, to reduce the computational time as the cloud screen is performed on a large volume of data (all pre-processed exposures). If the retrieved surface pressure is compared to the a priori surface pressure then the difference in surface pressure can be determined. Since the a priori surface pressure is well constrained, a surface pressure difference of greater than 20 hPa would normally only occur if a thick cloud is present in the IFOV, thus the

exposures can be cloud screened using this method.

This cloud screen approach has been verified by using a simulator (see Chapter 5) to compare the O_2 A band retrievals with the simulated cloud optical depth. Spectral radiances for each GOSAT SWIR band were simulated using 61 level profiles of pressure, water vapour VMR, CO_2 VMR, O_2 VMR, temperature, extinction for 11 different aerosols, liquid water extinction and ice water extinction. Also included was surface pressure and for each band values for albedo shift and slope, and spectral shift and stretch. The cloud screening method was then applied to these radiances and the retrieved State Vector elements compared to the true values.

Figures 3.49 and 3.50 show histograms of the retrieved parameters for clear and cloudy scenes, where clear scenes have a total column optical depth of less than 0.3. This clearly shows how the difference in surface pressure can be used to screen for many cloudy scenes, with the statistics given in Table 3.4. The cloud screen is shown to remove $\sim$86% of cloudy scenes and keep $\sim$94% of clear scenes.

The statistics can be compared to those of alternative cloud screening methods by calculating two diagnostic quantities (Taylor et al. 2012); the accuracy of the cloud screen to correctly classify clear and cloudy scenes, and the positive predictive value that specifies the percentage of clear scenes classified as clear. The accuracy, ACC, can be given as

$$\text{ACC} = \frac{\text{True clear} + \text{True cloudy}}{\text{Total number of scenes}} = 87.90\% \tag{3.27}$$

and the positive predictive value, PPV, as

$$\text{PPV} = \frac{\text{True Clear}}{\text{True Clear} + \text{False Clear}} = 69.59\% \tag{3.28}$$

Taylor et al. (2012) compares two different cloud screening methods which have been applied to GOSAT; a full O_2 A band surface pressure retrieval method (ABO2 Cloud Screen) and the CLAUDIA-CAI cloud screen which utilises the TANSO-CAI. The ACC and PPV over land for the ABO2 cloud screen are 78.2% and 63.0%, and for the CLAUDIA-CAI cloud screen are 79.1% and 71.0% respectively. In that study the cloudiness truth of the scenes was determined by the MODIS cloud mask product (MYD35), rather than by simulated scenes. Although the values can not be directly compared to those of this simulation as the simulated scenes do not include any variation of cloudiness within the IFOV of the simulated observation, the values are in general similar.

Table 3.4. Cloud screen statistics from simulations.

Description	Number of Elements	Percentage
Total	9923	100.00
Total clear truth	2544	25.64
Total cloudy truth	7379	74.36
True clear retrieved	2387	24.06
False clear retrieved	1043	10.51
True cloudy retrieved	6336	63.85
False cloudy retrieved	157	1.58

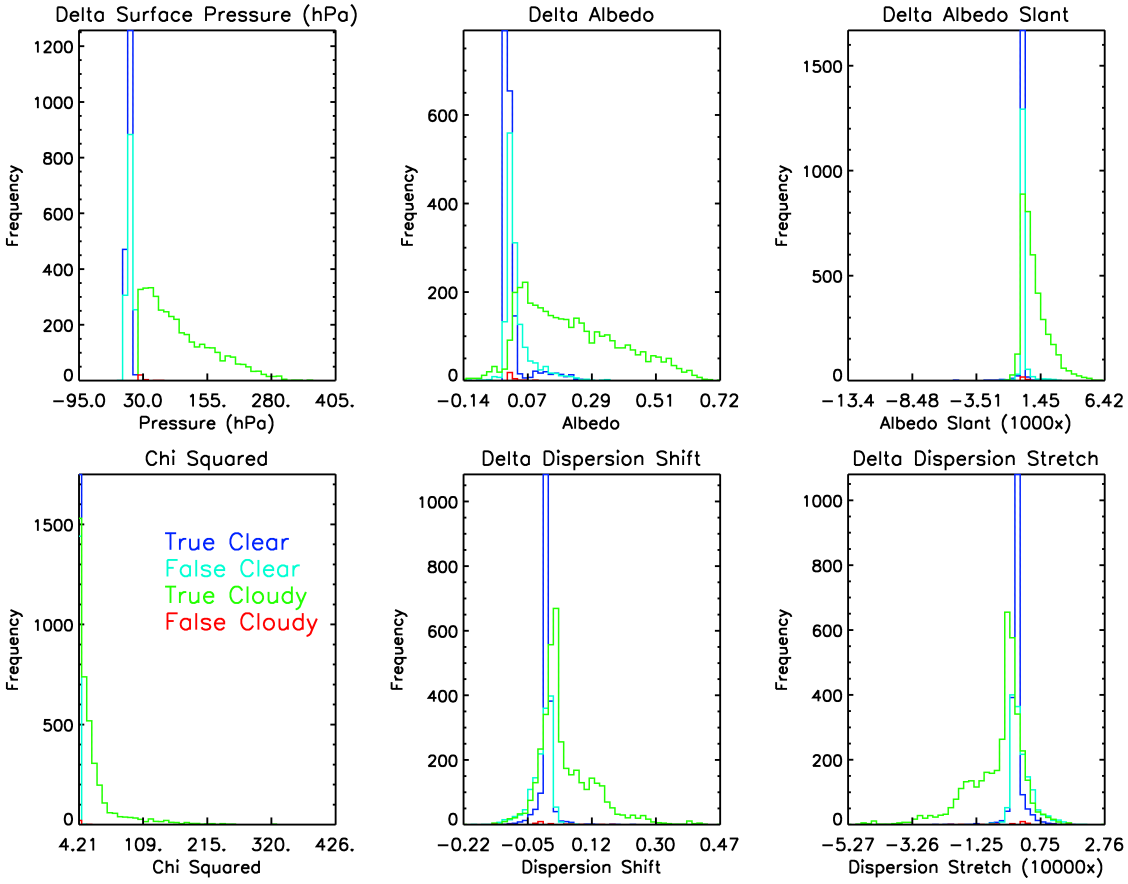

FIGURE 3.49. Histograms of χ^2, surface pressure difference, albedo and dispersion with frequencies seperated into true/false clear/cloudy, using the cloud screening method described in this section for simulated observations of GOSAT for two repeat cycles (6 days) globally.

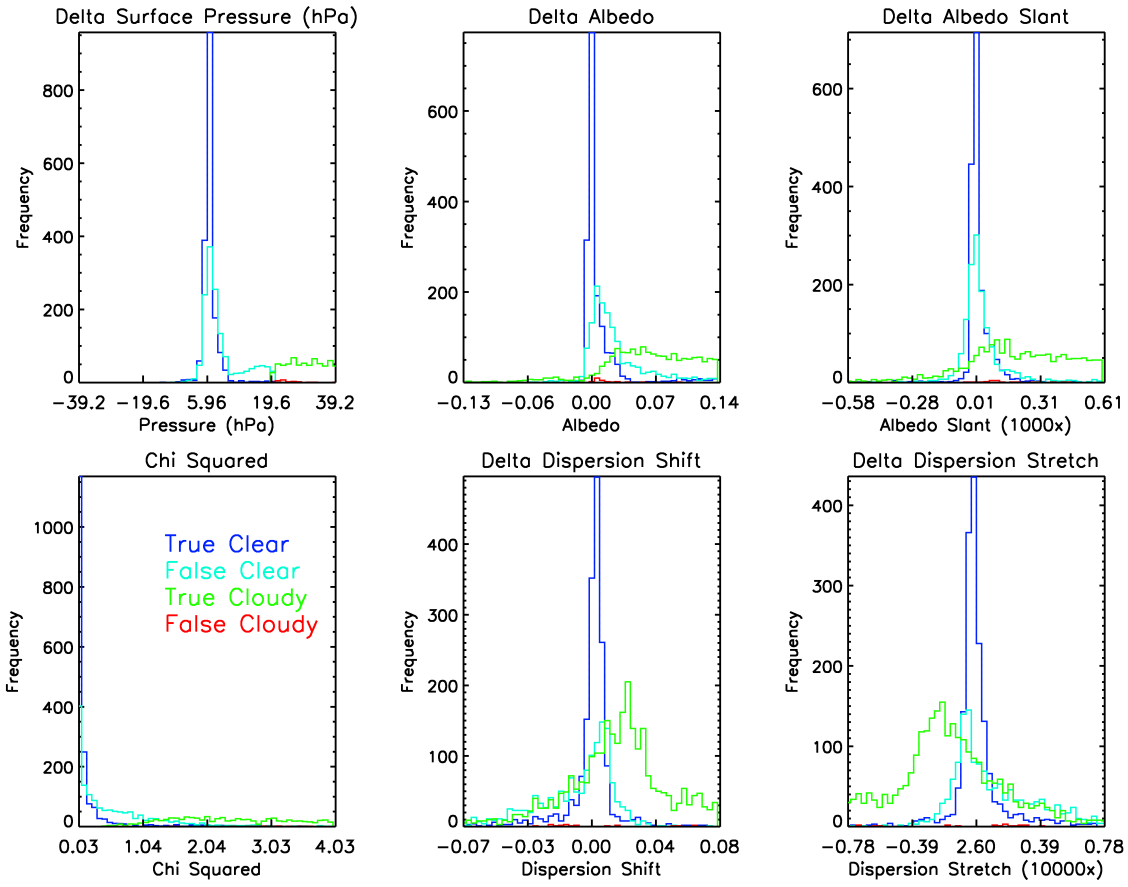

FIGURE 3.50. This shows the same as Figure 3.49 but with the x-axis scale reduced such that more detail can be viewed where clear and cloudy scenes need distinguishing.

3.22 Post-Processing Screen

Some retrievals will inherently perform poorly due to incorrect prior assumptions. Additionally, by giving the aerosols a large flexibility it can increase the chances of retrievals not coverging and obtaining the solution from a local minima, rather than the true optimal solution. Therefore some quality assurance should be used with the retrieval results. Post-screening criteria is applied to the successful retrievals to reduce the scatter and to remove problematic and potentially biased retrievals. An overview of the empirically derived post-screening criteria is shown in Table 3.5, with its application shown for a combination of seven TCCON sites (see Chapter 4) over a two year period in Figure 3.51. The post screen threshold values were inferred from correlations of various parameters with the X_{CO_2} bias between GOSAT and TCCON for coincident observations over Lamont/USA and Darwin/Australia (see Chapter 4) and by considering the distribution and scatter of global X_{CO_2} data retrieved for August 2009.

Table 3.5. UoL-FP v3G Post-Screen parameter threshold limits.

Parameter	Lower Threshold	Upper Threshold
Outcome	1	2
Band 1 χ^2	0.6	1.3
Band 2 χ^2	0.6	1.5
Band 3 χ^2	0.4	1.5
A Posterior Error		1.6
Number of Divergences		2
Retrieved - A priori Surface Pressure (hPa)	0	16
Retrieved Aerosol 1 Optical Depth		0.3
Retrieved Aerosol 2 Optical Depth		0.4
Retrieved Ice Optical Depth		0.05
Total Optical Depth		0.5
BTD 8-11		0
Cirrus Test	0.98	1.05
Retrieved Albedo Band 1 / Band 3		4
Retrieved Temperature Scale (K)	-2	
Retrieved H_2O Scale Factor	0.7	1.3
Retrieved A priori Dispersion Band 2 Shift (cm^{-1})	-0.022	0.022
Retrieved Intensity Offset	-0.002	0.0014

The post-screen selects only converged retrievals with a good spectral fit (where the

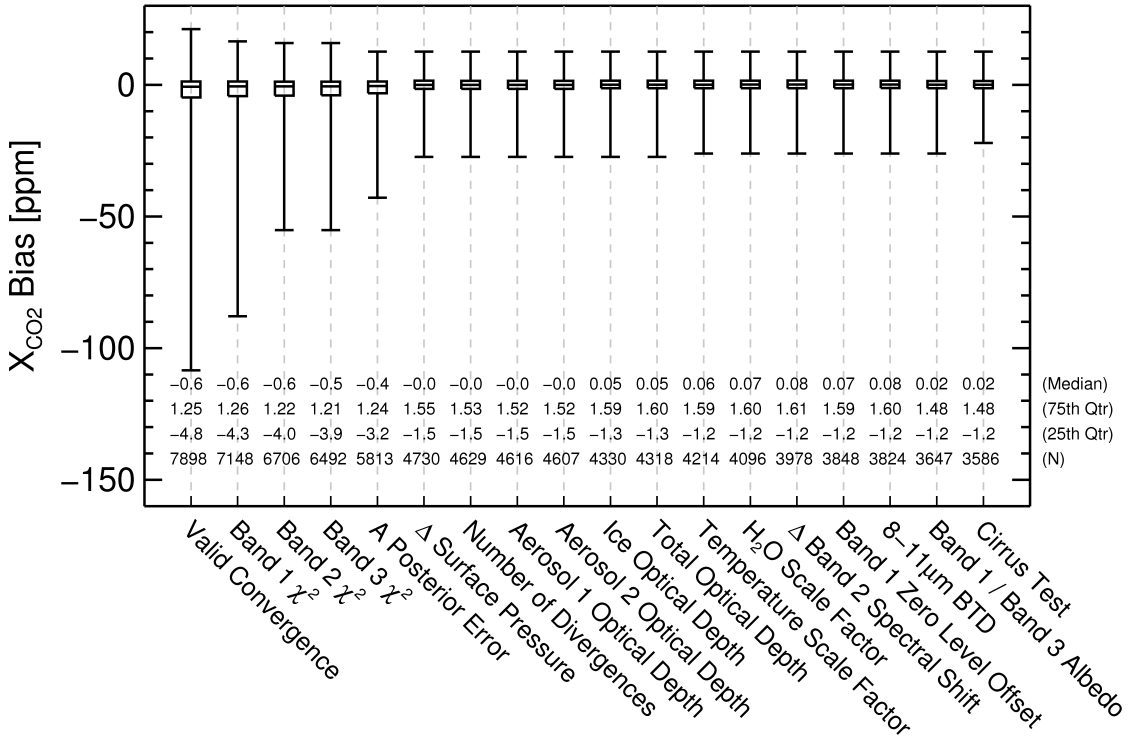

FIGURE 3.51. Box-wisker plot of X_{CO2} retrieved from GOSAT for seven TCCON sites combined between April 2009 and May 2011. The effect of each post-screen parameter is shown sequentially along the x axis.

normalized χ^2 of the fit residual is $\sim$1) and a low posterior error of X_{CO_2} ($<$1.6 ppm). In addition, we also filter for a number of parameters related to thin clouds and aerosols, which include: the difference between retrieved and ECMWF surface pressure (0-16 hPa), the retrieved cirrus optical depth ($<$0.05), the band 4 (TIR) brightness temperature difference (BTD) between 8 μm and 11 μm (where $>$0 indicates cloud/cirrus), a test for cirrus based on the radiance ratio of 2.1038 μm to 2.0906 μm (where cirrus absorption occurs below a value of 0.98), and the ratio of 0.76 μm to 2.06 μm albedo that indicates ice/snow if the value is $>$4. Scenes containing a large retrieved aerosol amount (AOD $>$0.5) are also removed. Figure 3.52 gives the correlation matrix of the state vectors used, showing many cross-correlations between statevectors. As most of the correlating state vectors are included in previously mentioned filters, water vapour and temperature which also show some correlation with X_{CO2} are used to remove cases where clear outliers exist (indicating a poor retrieval).

Thin cirrus clouds will likely not be filtered out by the cloud screen and are difficult to detect in the SWIR spectral range so three different techniques were designed to screen for cirrus clouds. The first method was to utilise the TANSO-FTS TIR band and

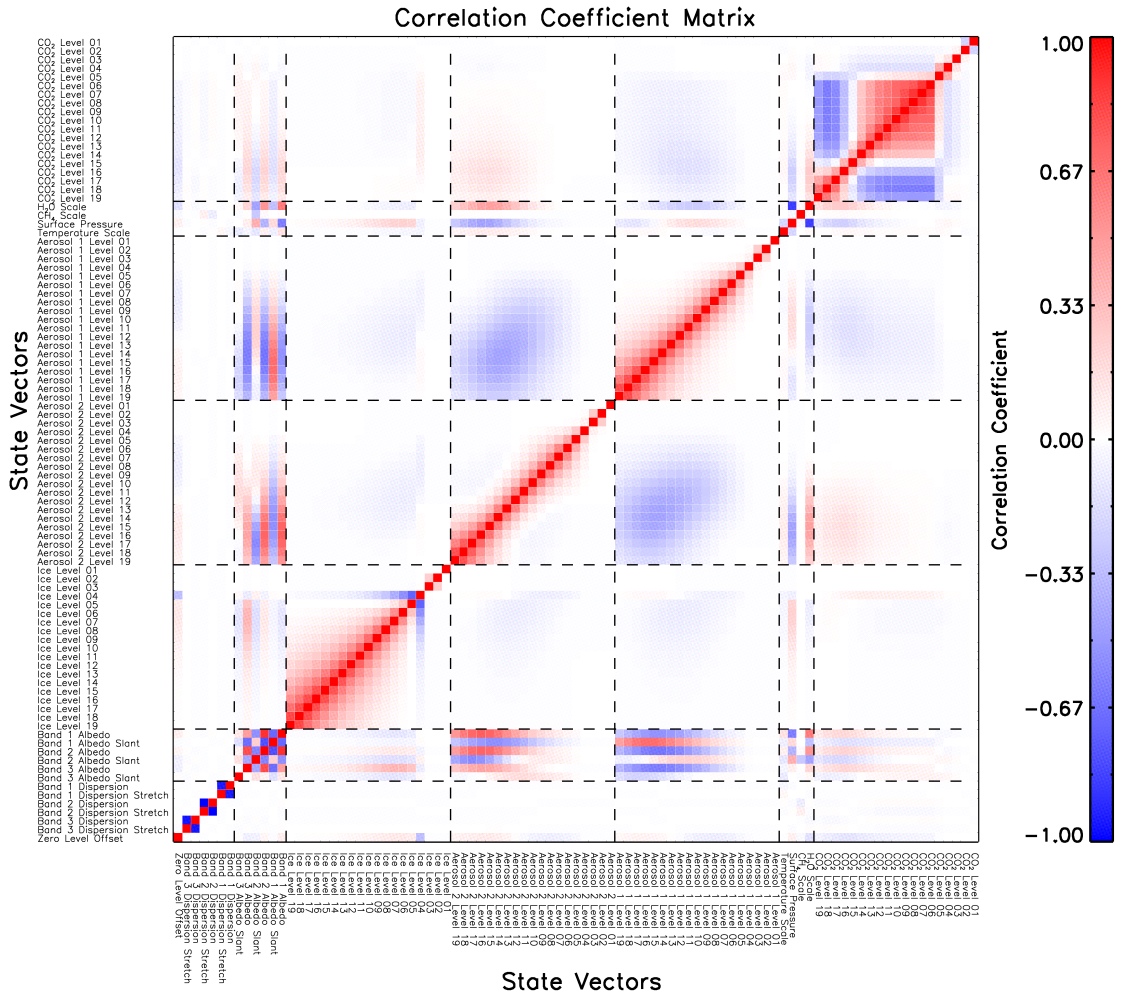

FIGURE 3.52. Example correlation matrix of the state vectors used in the UoL-FP retrieval algorithm, obtained from a X_{CO2} retrieval over Lamont/USA on April 22^{nd} 2009. For the state vector profiles (e.g. CO_2, aerosols and ice) the top of the atmosphere is given by the 1^{st} level. Note that only 19 levels are shown here due to the retrieved surface pressure being higher than the two lowest a priori pressure levels.

calculate the brightness temperature difference (BTD) between 8.3 and 11.15 μm, which has previously been used with MODIS observations to characterise scenes with clouds (Ackerman et al. 1998). This BTD can be calculated using Planck's law as

$$\text{BTD} = \left[\frac{h\nu_8}{k\ln\left(1+\frac{2h\nu_8^3}{I_8c^2}\right)}\right] - \left[\frac{h\nu_{11}}{k\ln\left(1+\frac{2h\nu_{11}^3}{I_{11}c^2}\right)}\right] \tag{3.29}$$

where ν_8 is the 8.3 μm wavenumber, ν_{11} is the 11.15 μm wavenumber, h is the Planck

constant (6.62620x10^{-34} J s), c is the speed of light (2.99792458x10^{8} m s^{-1}) and k is the Boltzmann constant (1.38062x10^{-23} J K^{-1}). This technique should indicate if cirrus clouds exist if the BTD is greater than ∼0 (Ackerman et al. 1998).

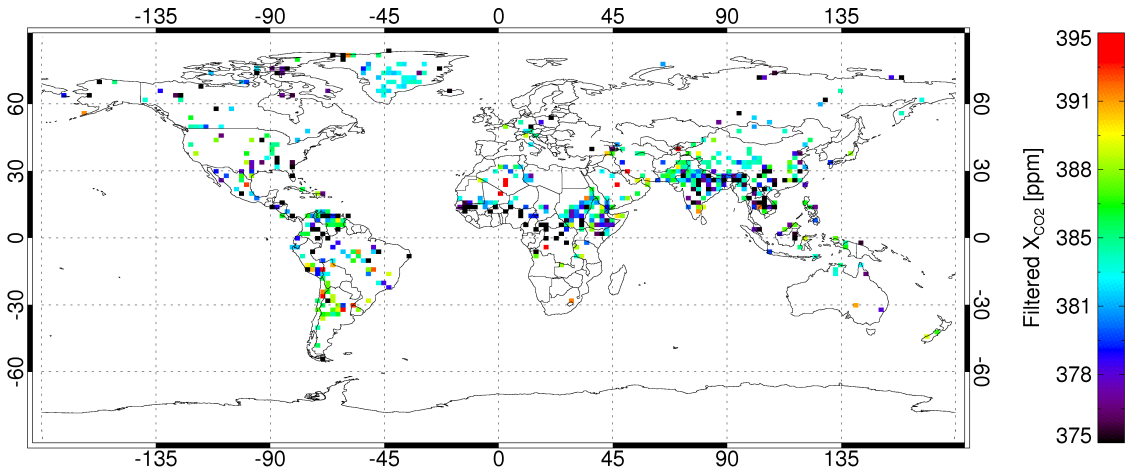

FIGURE 3.53. The retrieved X$_{CO2}$ that has been filtered out due to the 8-11 μm BTD threshold, for August 2009 globally.

The second technique uses the ratio of the retrieved albedo of band 1 to band 3. In band 1 ice/snow has a very high albedo, whilst all other surface types have a lower albedo. In band 3 ice/snow has the lowest albedo, with all other surfaces having low albedos but higher than ice/snow. By using the ratio of band 1 to band 3 albedo, if the scene contains ice/snow then the ratio will be larger. Thus this method has the potential to detect cirrus (ice cloud). Additionally, it can detect surface ice/snow which would also lead to a reduced accuracy in the X$_{CO2}$ retrieval due to a lower SNR, so would be preferable to screen out as well.

The third technique uses the fact that cirrus strongly absorbs radiances in the band 3 spectral range, with the absorption peaking towards the centre of the band. This cirrus test makes use of this absorption peak by taking the ratio of the continuum radiance at the edge of the band where the absorption is low (2.1038 μm) to the continuum radiance at the middle of the band where at the peak cirrus absorption (2.0904 μm). If no cirrus exists then the cirrus test would give a value of ∼1, but if cirrus does exist in the scene then the value ought to be slightly <1. This is clearly demonstrated in Figure 3.55, which shows the cirrus test values for the set of simulated scenes used in the cloud screen analysis, for details see Section 3.21. This indicates that a threshold of ∼0.98 would be suitable to remove scenes that contain cirrus.

Figure 3.56 shows the difference between with and without the post-screen applied

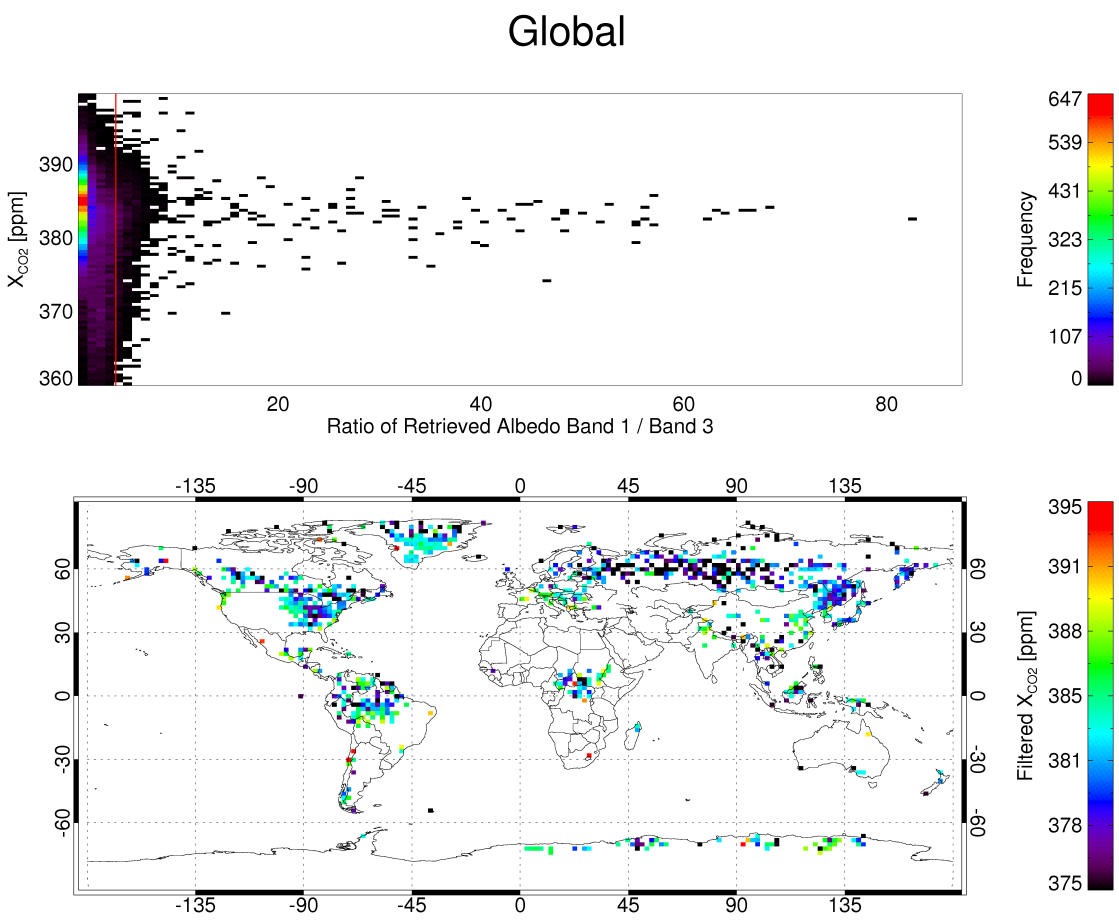

FIGURE 3.54. Ratio of band 1 retrieved albedo to band 3 retrieved albedo for August 2009 globally. The upper plot shows its correlation with retrieved X_{CO2} with the density of values given by colour and the red vertical line showing the threshold limit. The lower plot shows the retrieved X_{CO2} that has been filtered out due to this parameters threshold.

for parameters related to the quality of the retrieval performance. When no post-screen is applied, a X_{CO2} bias is found with the number of divergences and the number of iterations. There is also a large number of retrievals with poor χ^2 values. Once post-screened, the X_{CO2} biases are significantly reduced and only retrievals with a good spectral fit remain.

An example of the spectral fit and the fit residual is given in Figure 3.57, and shows that in general the retrieval fits the measured radiance well with low residuals. However, some structures remain in the residual indicating that some spectal lines are not fitted well, with the larger residual peaks relating to solar absorption lines. Future updates in spectroscopy could improve the spectral fit.

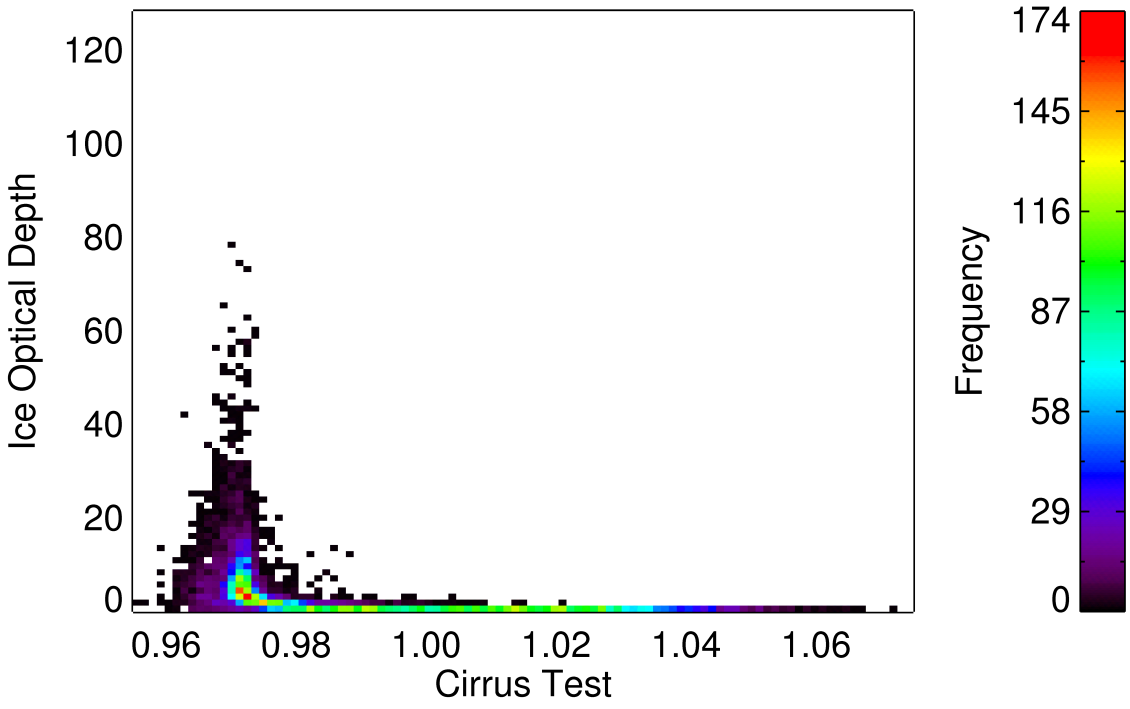

FIGURE 3.55. Cirrus test for realistic simulated scenes, as described in Section 3.21. It is compared against the simulated ice optical depth with the density of values given by the colour scale.

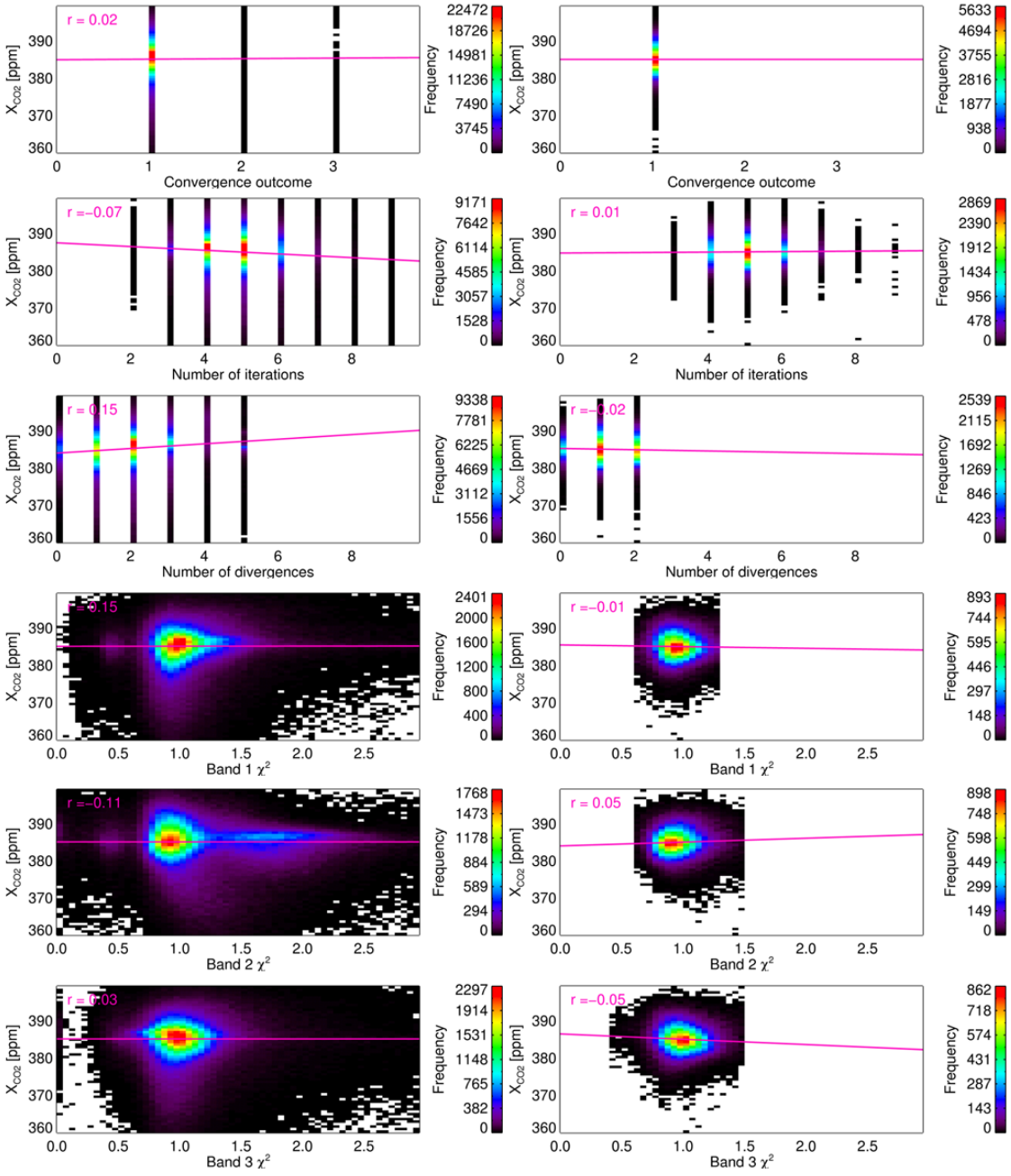

FIGURE 3.56. Example application of the post-screen on different parameters for GOSAT pre-screened and cloud screened observations September 2009. The left hand panels show the results when no post-screen is applied, and the right hand panels show the same data but filtered using the post-screen. For each panel, the colour represents the number of results within that bin with reference to the colourbar, the pink line gives a linear fit of the data, and r gives the correlation of the parameter against X_{CO2}.

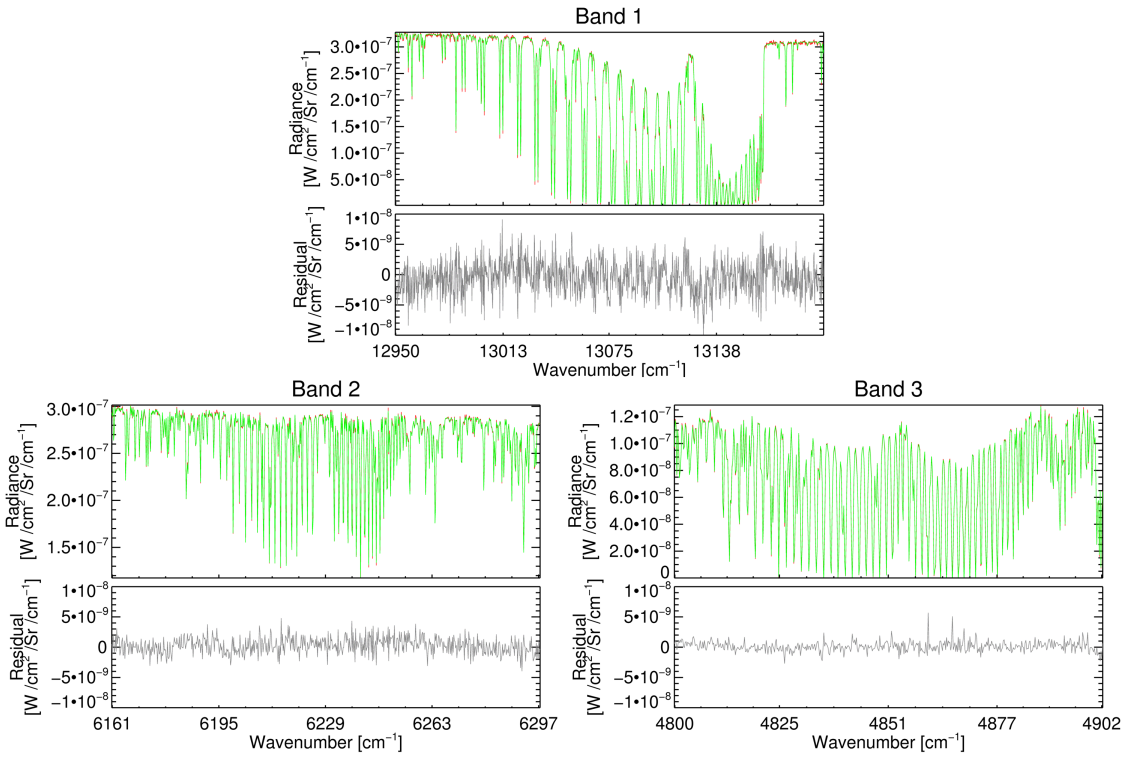

FIGURE 3.57. Example spectral fits and fit residuals for each band retrieved, where the measured radiances are given in red, the simulated radiances in green and the residual in gray. This example exposure is located over Lamont/USA where the surface is vegetation and the retrieved total optical depth was $\sim$0.1.

3.23 Summary

This chapter described the UoL-FP retrieval algorithm and how it can be used to infer X_{CO2} from cloud screened GOSAT SWIR measured radiances. The vertical sensitivity and X_{CO2} error of GOSAT was assessed using pre-flight instrument information. This shows surfaces with a low albedo in the wavelength range of the GOSAT bands (such as ocean and snow) will result in errors of about 1%, whilst brighter surfaces give much lower errors and better sensitivity to the boundary layer. The next chapter shows the X_{CO2} inferred from GOSAT using the UoL-FP retrieval algorithm and compares with ground based measurements, global chemistry transport model calculations and alternative retrieval algorithms.

Chapter 4

Atmospheric CO_2 retrieved from GOSAT: Validation, model comparison and algorithm intercomparison

4.1 Introduction

To assess the ability of the UoL-FP retrieval algorithm (version 3G) to accurately and precisely estimate X_{CO2} from GOSAT, it is essential to compare this with alternative observational data and independent model data. It is also useful to compare to alternative algorithms as this can potentially indicate retrieval algorithm dependent biases. This chapter provides an assessment of the UoL-FP retrieval algorithm through comparisons with:

1. In-situ ground based observations of X_{CO2} derived from solar absorption spectra measured by TCCON FTS instruments.

2. The GEOS-Chem global 3-D chemistry transport model atmospheric CO_2 estimations (Feng et al. 2011).

3. Alternative algorithms that retrieve X_{CO2} from GOSAT.

A total of 1,718,561 GOSAT observations globally over land between June 2009 and May 2010 have been processed using the UoL-FP retrieval algorithm (v3G), reducing to 764,290 scenes (44.47%) once pre-screened. These were then cloud-screened, leaving 372,479 scenes (21.67%) that were retrieved. Details of this are given in Table 4.1. Additionally, a total of 306,890 GOSAT observations over land for thirteen TCCON

sites between April 2009 and May 2011. Once pre-screened and cloud-screened 24,980 (8.11%) observations remained, details of which can be found in Table 4.2.

Table 4.1. UoL-FP v3G retrieval statistics for 1 year of daytime, land only global GOSAT observations.

Year Month	Total from L1B	Passed Pre-Screen	O_2 Completed	Cloudy Exposures	Clear Exposures	Retrieval Completed	Passed Post-Screen
200906	126745	55303	51768	27863	23905	22881	5724
200907	139663	61514	57799	31098	26701	25660	7474
200908	139615	60201	56234	30330	25904	24928	7306
200909	141572	62622	56988	29217	27771	27012	6761
200910	150659	70907	63121	27433	35688	34135	6197
200911	146340	72724	64645	24510	40135	37844	4563
200912	149908	74701	67443	24562	42881	39356	4358
201001	146740	65452	58947	23001	35946	33295	4213
201002	145925	62328	56048	24161	31887	30089	3492
201003	158284	64685	59158	27064	32094	30811	3691
201004	138638	55586	50783	26310	24473	23207	3484
201005	134472	58267	54104	29010	25094	23719	5015
Total	1718561	764290	697038	324559	372479	352937	62278

4.2 Comparisons with TCCON CO_2 measurements

TCCON is a network of ground-based, solar absorption, near infrared, Fourier transform spectrometers that measure atmospheric columns of the gases CO_2, CO, CH_4, H_2O and others with a precision of 0.25% for CO_2 (Wunch et al. 2010, 2011a), making it an ideal dataset for validation of retrieved X_{CO_2} from GOSAT. Since the TCCON instruments are direct solar-viewing, the effects of aerosol and high cirrus cloud are negligible. To maintain consistency between different TCCON observatories, all sites use the same instrumentation and the same software for data processing and analysis. This includes the conversion of raw interferograms into spectra, which are then spectrally fitted using the GFIT algorithm with subsequent quality controls applied to the column abundances (Wunch et al. 2011a). Wunch et al. (2010) compared the retrieved X_{CO_2} from TCCON with aircraft observations using 14 coincident profiles and found that a single, global calibration factor of 0.989 accurately matches the data within the error. Subsequently, Messerschmidt et al. (2011) found additional European TCCON sites to be consistent with this calibration factor. Additionally, an airmass dependent correction factor was applied as described in Wunch et al. (2011a).

X_{CO2} retrievals from GOSAT were performed between April 2009 and May 2011 over thirteen TCCON sites; Lamont/USA, Park Falls/USA, Orleans/France, Bialystok/ Poland, Bremen/Germany, Karlsruhe/Germany, Garmisch/Germany, Sodankyla/ Finland, Tsukuba/ Japan, Izana/Spain, Darwin/Australia, Wollongong/Australia, and Lauder/ New Zealand. Figure 4.1 shows X_{CO2} retrieved from GOSAT compared with X_{CO2} inferred from TCCON for each of these thirteen TCCON sites, where GOSAT observations within a 5° radius are used. The lower right panel of Figure 4.1 gives the mean bias, standard deviation and correlation of all daily mean coincident GOSAT X_{CO2} data compared to TCCON daily mean coincident X_{CO2} data. This gives an overall bias of -0.08 ppm, scatter of 2.52 ppm and correlation of 0.72 between GOSAT and TCCON X_{CO2}.

Although there are few daily coincidences between GOSAT and TCCON over Izana, there is a good agreement between the single soundings for Izana, with GOSAT reproducing the seasonal cycle very well but with a mean bias of approximately -3.36 ppm compared to TCCON. Although the bias is small for Lauder (-0.44 ppm), there are very few coincident points with TCCON and those that are coincident have a large standard deviation of 4.11 ppm (using daily mean data). Similarly, Tsukuba has a low bias (-0.35 ppm), a large standard deviation (3.42 ppm) and only a small number of coincident points between GOSAT and TCCON observations. Unlike most other sites, Tsukuba TCCON data was not available for the duration of the GOSAT observations. Furthermore, there was a lack of TCCON data available for the Karlsruhe and Sodankyla TCCON sites, reducing the number of GOSAT/TCCON coincidences in those locations. Since few GOSAT observations exist over Sodankyla, due to clouds, this site does not provide statistically meaningful data. The other sites all provide at least 200 coincidences between GOSAT and TCCON.

Figure 4.2 gives the locations of each TCCON site and the locations of pre-screened and cloud-screened coincident GOSAT observations. No GOSAT observations are actually observed directly at Izana, instead the coincident observations are located over the Sahara desert. Only Lamont and Parkfalls have purely land within a 5° radius of the site, all other sites include areas of ocean where observations either do not exist or are removed in the pre-screen. Furthermore, Izana, Lauder and Tsukuba are located on islands, thus reducing the number of GOSAT observations. However, many targeted observations are made (using the specific observation mode) over Japan, within the coincidence range of Tsukuba.

Bremen, Karlsruhe, and Garmisch TCCON sites are all located nearby each other, with overlapping coincidence regions. Many GOSAT observations are coincident with all three of these TCCON sites, hence making the overall GOSAT/TCCON comparison

statistics biased towards these observations. Some of the GOSAT observations coincident with these three sites are also coincident with the Orleans TCCON site. Bremen has the least number of coincident GOSAT observations that are also coincident with the Orleans site. For these reasons, Garmisch and Karlsruhe will no longer be used in this comparison.

Figure 4.3 shows the statistics of X_{CO2} retrieved from GOSAT compared to TCCON for different spatial coincidence limits. The number of coincident observations (or sample size) increases with larger spatial coincidence thresholds, simply due to GOSAT normally observing in a regular spatial pattern (such as the 5-point cross-track mode). Hence, the choice of coincidence criteria should not only be a compromise between the sample size and the spatial distance from a TCCON site, but must also take into account the statistics between GOSAT and TCCON coincident data.

In general, the X_{CO2} bias between GOSAT and TCCON observations improves with a smaller spatial coincidence (using daily mean coincident data). However, with a latitudinal coincidence less than about 2° the bias becomes worse. The bias remains almost constant below a longitudinal coincidence of 5°, whilst higher longitudinal coincidence limits produce larger biases. The bias calculated from coincident single soundings shows the same patterns but with lower values overall.

The X_{CO2} standard deviation of daily mean coincident points is almost homogeneous for all spatial coincidence thresholds considered, with a mean value of $\sim$2.45 ppm. However, the X_{CO2} standard deviation of coincident single soundings increases with bigger spatial coincidences (from $\sim$2.2 ppm to $\sim$2.7 ppm), especially with larger latitudinal coincidence limits. Similarly, the correlation coefficient of daily mean coincident GOSAT and TCCON X_{CO2} is fairly homogeneous for all spatial coincidence limits with a value of $\sim$0.76, whereas the correlation coefficient of X_{CO2} from coincident single soundings decreases with larger spatial coincidences (from $\sim$0.76 to $\sim$0.68).

Using the statistics from both daily mean and single sounding coincident data, a latitude threshold higher than 2° and a longitude threshold less than or equal to 5° would provide the best GOSAT/TCCON comparison. A spatial coincidence of 5° would therefore provide a compromise between larger spatial coincidence limits with more observations and smaller latitude limits with reduced X_{CO2} standard deviations and correlation coefficients.

Figure 4.4 shows the statistics of X_{CO2} retrieved from GOSAT compared to TCCON for different temporal coincidence limits. In general, reduced temporal coincidence gives in a small improvement in the X_{CO2} bias and standard deviation, but the number of

observations increases with higher temporal limits. There are between 1 and 3 GOSAT overpassing orbits of each TCCON site, providing all GOSAT observations within ∼70 minutes. Whereas, TCCON measurements are taken throughout daytime, observing the variability of airmass transport and source/sink processes (Butz et al. 2011). Since the diurnal cycle of CO_2 changes rapidly, a large temporal coincidence for TCCON would not reflect the same airmass as observed by GOSAT. Thus, as a compromise between the number of observations and the diurnal cycle a temporal coincidence of ± 2 hours would be suitable.

All pre-screened, cloud-screened and post-screened GOSAT measurements over land within a coincidence criteria of 5° of each TCCON site and ± 2 hours of TCCON observations were used for only the seven TCCON sites selected. Figure 4.5 shows a comparison of the retrieved X_{CO2} from GOSAT with coincident TCCON X_{CO2} data for these seven TCCON sites (without averaging kernels applied). It also shows the correlation of coincident daily mean GOSAT X_{CO2} with the average of all TCCON X_{CO2} within ± 2 hours of each coincident GOSAT data. GOSAT X_{CO2} is observed to have values consistent with TCCON retrievals for all sites for the entire time period and a very good agreement between coincident data is found. In particular, the seasonal cycle observed for northern hemispheric sites is well reproduced by GOSAT with correlation coefficients between 0.56 and 0.85, similar to that observed by (Butz et al. 2011, Oshchepkov et al. 2012a, Wunch et al. 2011b). Consistent to the TCCON measurements, the two southern hemisphere sites, Darwin and Wollongong, show weaker seasonal cycles than the northern hemisphere sites. However, the retrieved X_{CO2} from GOSAT over Wollongong is found to have a slightly enhanced seasonal cycle.

Gaps exist in the GOSAT and TCCON time-series due to clouds and instrumental issues. The number of points per site varies mainly due to seasonal cloud cover and the number of overpassing orbits. The number of soundings of each station varies from 260 for Bremen to 2445 for Lamont, with the number of coincident days with TCCON between 19 and 261, respectively. The Lamont site has the largest sample size due to multiple orbit overpasses within the coincidence criteria and less clouds than the other sites.

Using the data for all sites (lower right in Figure 4.5), the average bias of GOSAT compared to TCCON is calculated as -0.20 ppm with a standard deviation of 2.26 ppm (using daily means), which is similar to that found by Butz et al. (2011) and lower than reported by other algorithms Crisp et al. (e.g. 2012), Morino et al. (e.g. 2011), Oshchepkov et al. (e.g. 2012a). Using single soundings instead of daily means, a standard deviation of 2.46 ppm is found. The average of the bias per station is 0.10 ppm with a range of

-0.87 to 0.77 ppm and a standard deviation of 0.56 ppm (using daily mean data). The mean correlation coefficient between GOSAT and TCCON observations is found to be 0.75. The mean bias and scatter are largely influenced by the large number of soundings over the Lamont site. The highest scatter is observed for Bremen, which has the lowest number of scenes (see Table 4.3 for details).

The standard deviation of the retrieved X_{CO2} inferred from comparisons to coincident TCCON data is substantially (factor of $\sim$2 on average) larger than that predicted from the a posterior error, which is found on average to be 1.14 ppm. The additional scatter observed is likely introduced by cloud perturbations, variations of aerosols, and other geophysical parameters. A similar value is reported by O'Dell et al. (2012) from simulations.

There are some outliers between GOSAT and TCCON retrievals that have passed the screening and are likely due to scattering caused by undetected clouds or aerosols. Thus, the effect of applying a stricter post-screen was tested, where reduced upper threshold limits were applied for the retrieved ice optical depth (0.03 limit), the retrieved total optical depth (0.3 limit) and the ratio of retrieved band 1 albedo to band 3 albedo (2 limit). When applied, this caused many of the outliers to be removed, reducing the mean bias to -0.08 ppm and the scatter to 1.92 ppm (of daily means), but at the cost of the number of exposures (see Table 4.4 for details).

This comparison has not taken into account the effect of the different averaging kernels **A** and a priori, which describe the sensitivity of a retrieval algorithm to the true state throughout the atmosphere (Rodgers 2000, Rodgers & Connor 2003). The retrieved X_{CO2} for GOSAT and TCCON depends on the averaging kernel and the a priori used in the retrieval algorithm according to:

$$\mathbf{X_{CO2}} = \mathbf{h^T x_a} + \mathbf{h^T A}\left(\mathbf{x} - \mathbf{x_a}\right) \tag{4.1}$$

where $\mathbf{h}^T$ is the transpose of the pressure weighting function (O'Dell 2010), **x** is the true VMR profile, and $\mathbf{x}_a$ is the a priori VMR profile. A consequence of Equation 4.1 is that the true and the retrieved X_{CO2} will differ if **A** is different from the Unity matrix. This difference is referred to as the smoothing error and it will be different for the GOSAT and TCCON retrievals due to their different averaging kernels and a priori values.

An assessment of this effect on the comparison of X_{CO2} retrievals from GOSAT and TCCON was performed by calculating the X_{CO2} retrieved from GOSAT and TCCON using GEOS-Chem model (described in Section 4.3) calculations as the true CO_2 profile. Since the GEOS-Chem model calculations will not necessarily represent the true atmo-

spheric CO_2 profiles these values for smoothing error differences will only represent a rough estimate.

For each of the seven TCCON sites considered, GEOS-Chem was interpolated temporally to the observation time of TCCON and GOSAT using the GEOS-Chem grid cell that includes the TCCON site. The averaging kernels were applied to GEOS-Chem for the period of April 2009 to December 2010 where both model, TCCON and GOSAT data exist. Only TCCON data that was temporally closest to GOSAT data, which was coincident within ± 2 hours and 5° of each TCCON site was used.

The mean smoothing errors of TCCON and GOSAT were calculated as 0.12 ppm and 0.27 ppm respectively. The mean smoothing error difference between the model X_{CO2} with GOSAT averaging kernels applied and the model X_{CO2} with TCCON averaging kernels applied was found to be -0.14 ppm. The average of the mean smoothing error difference per station is -0.22 ppm with Lamont having the smallest mean smoothing error difference of -0.05 ppm and Orleans having the largest mean smoothing error difference of -0.50 ppm. The standard deviation of the mean smoothing error difference per site is 0.18 ppm. The mean of the scatter of the smoothing error difference per station is 0.19 ppm, with a standard deviation of 0.09 ppm. The smoothing error difference is observed to have a small seasonal cycle dependence, with northern hemispheric sites varying from approximately -1.5 ppm to 0.5 ppm and a lower amplitude for southern hemisphere stations where the seasonal cycle is reduced. Hence, for southern hemispheric sites the difference of the smoothing errors has a very small impact on the comparison of GOSAT with TCCON. However, for northern hemispheric sites there is a seasonal cycle dependence between GOSAT and TCCON X_{CO2} due to the smoothing error difference (see Figure 4.9). If the point-by-point smoothing error difference is appied to the coincident TCCON data, the mean bias of GOSAT compared to TCCON is found to increase by 0.14 ppm but the standard deviation and correlation coefficient remain the same (see Table 4.5 for further details). It cannot be expected that the estimates are necessarily representing the correct value for each individual sounding as this would require that the model reproduces the shape of the CO_2 profile at each time step and location. Indeed, it is found that including the smoothing error estimates from GEOS-Chem to the GOSAT-TCCON comparisons worsens the comparisons for some sites while it improves it for others.

Table 4.2. Statistics for the UoL-FP v3G comparison to all 13 TCCON stations.

TCCON site	Total from L1B	Passed pre-screen	Percent cloudy	Passed post-screen	Coincident days
Sodankyla (67.368° N)	35864	2858	74.25	83	19
Bialystok (53.230° N)	29376	8321	61.16	459	54
Bremen (53.100° N)	24054	5484	66.36	260	19
Karlsruhe (49.100° N)	30371	8706	65.62	383	47
Orleans (47.970° N)	24047	9511	61.32	715	47
Garmisch (47.476° N)	25505	8479	65.02	328	40
Park Falls (45.945° N)	33277	5785	55.52	421	86
Lamont (36.604° N)	30984	9888	39.44	2445	261
Tsukuba (36.051° N)	21636	3320	55.18	129	19
Izana (28.300° N)	11614	1094	11.52	230	8
Darwin (12.424° S)	17273	4511	39.64	990	54
Wollongong (34.406° S)	13182	4971	50.45	570	56
Lauder (45.038° S)	9707	1069	49.49	28	16
Total	306890	73997	56.49	7041	726

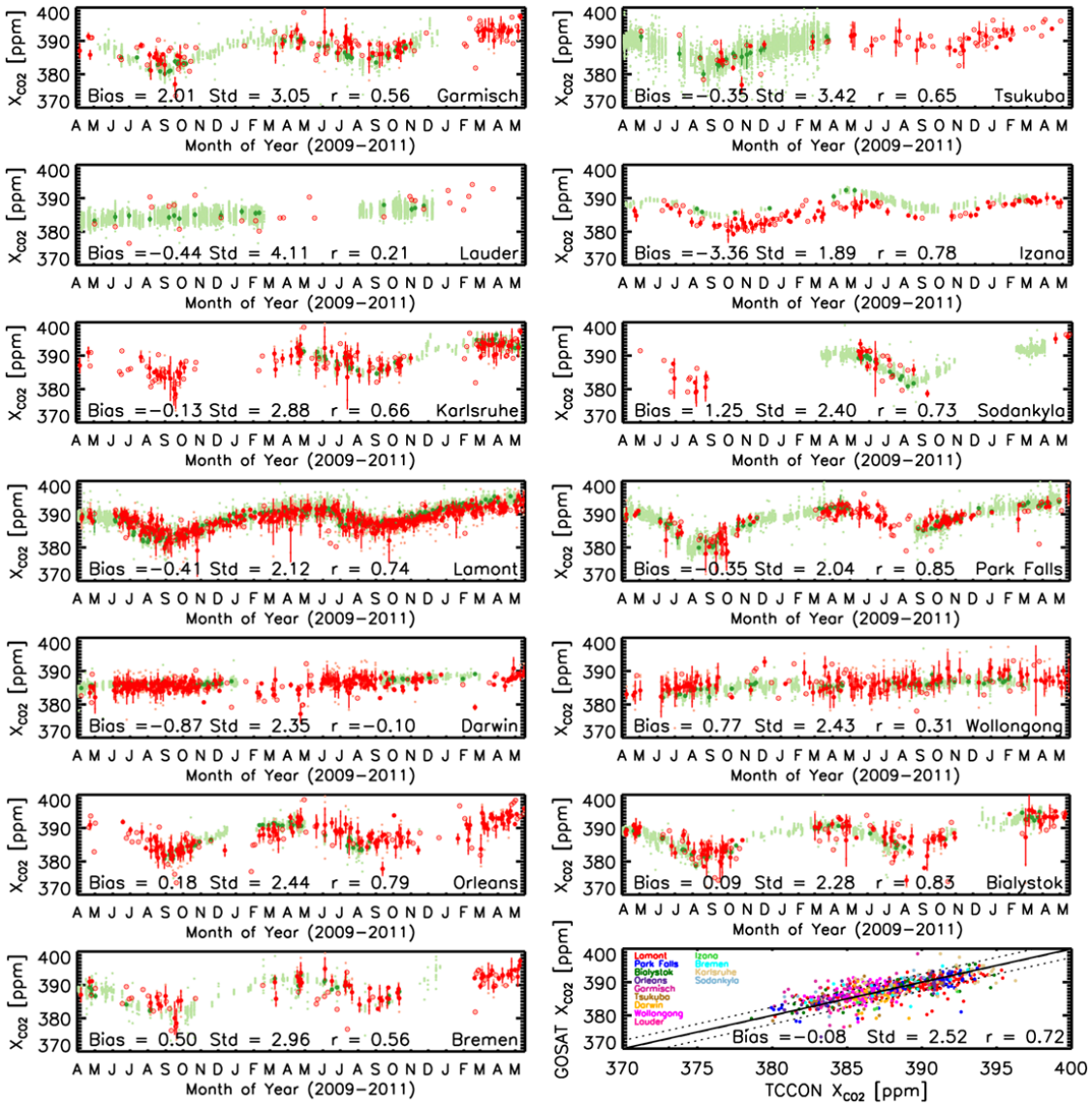

FIGURE 4.1. Comparison of retrieved X_{CO2} from GOSAT with retrieved X_{CO2} from thirteen TCCON site for coincident cloud-screened observations within 2 hours and 5° between April 2009 and May 2011. All TCCON data shown in light green, coincident daily mean TCCON shown in dark green, all GOSAT data shown in light red and daily mean GOSAT shown in dark red (with daily mean points with only one value per day are represented by open circles). The average difference between the daily means is given as the bias (ranging from -3.36 to 2.01 ppm), the standard deviation of daily means by the Std (between 1.89 and 4.11 ppm) and the correlation coefficient of daily means by r (-0.10 at Darwin to 0.85 at Park Falls). The lower right panel gives the correlation of daily mean coincident retrieved GOSAT X_{CO2} with daily mean TCCON X_{CO2} within $\pm$2 hours for the thirteen sites. This gives an overall bias of -0.08 ppm, scatter of 2.52 ppm and correlation of 0.72 between GOSAT and TCCON X_{CO2}. There are no daily mean coincident TCCON points for Izana, so no statistics exist for this location and therefore had no effect on the overall bias, standard deviation or correlation coefficient.

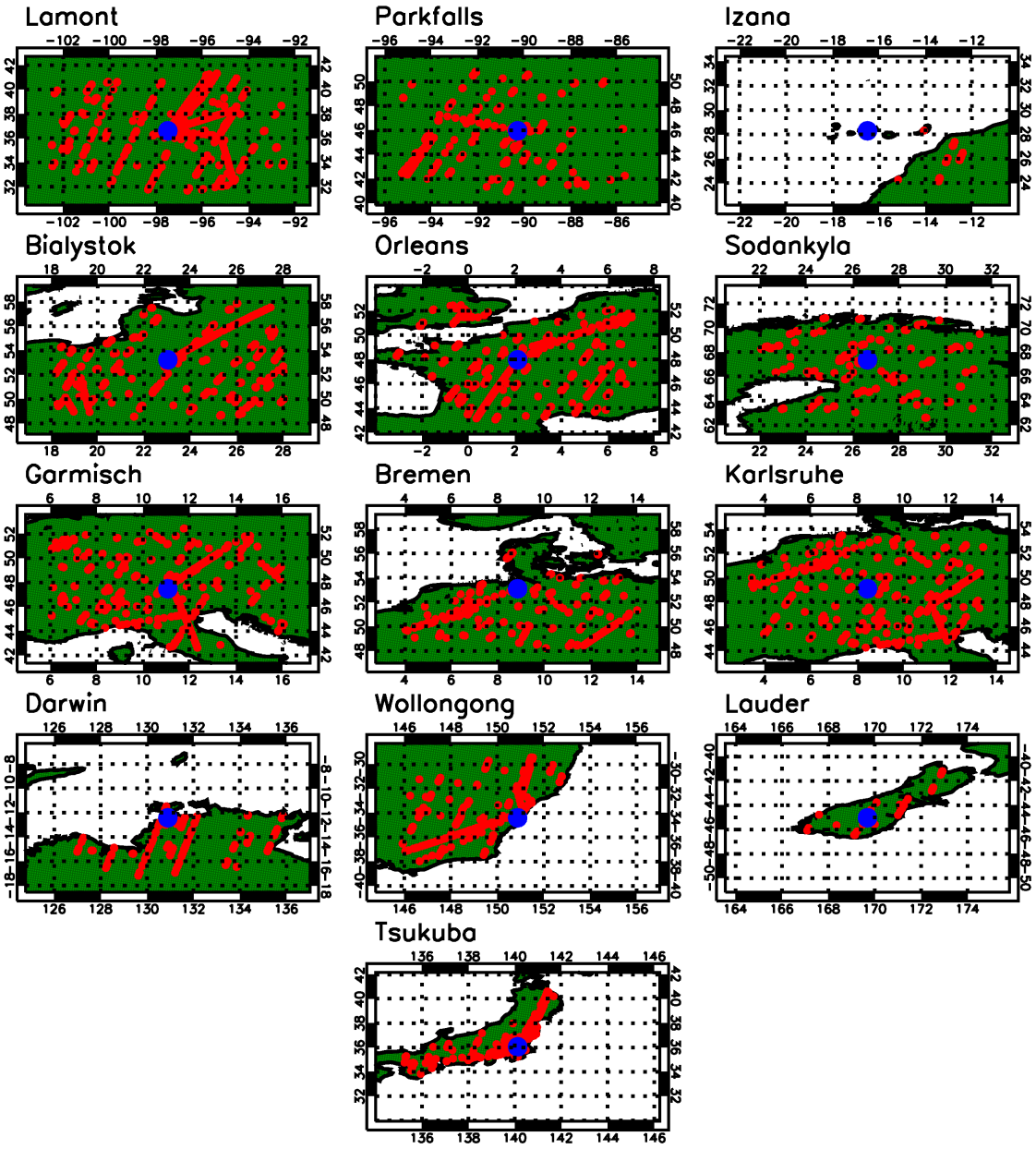

FIGURE 4.2. Locations of pre-screened and cloud-screened TANSO-FTS observations between April 2009 and May 2011 within 5° of thirteen TCCON sites. The locations of the TCCON sites are represented by a blue circle and GOSAT observation locations are given by red circles. Additionally, a green surface represents land and white shows an ocean surface. The dotted line represent a 2° grid.

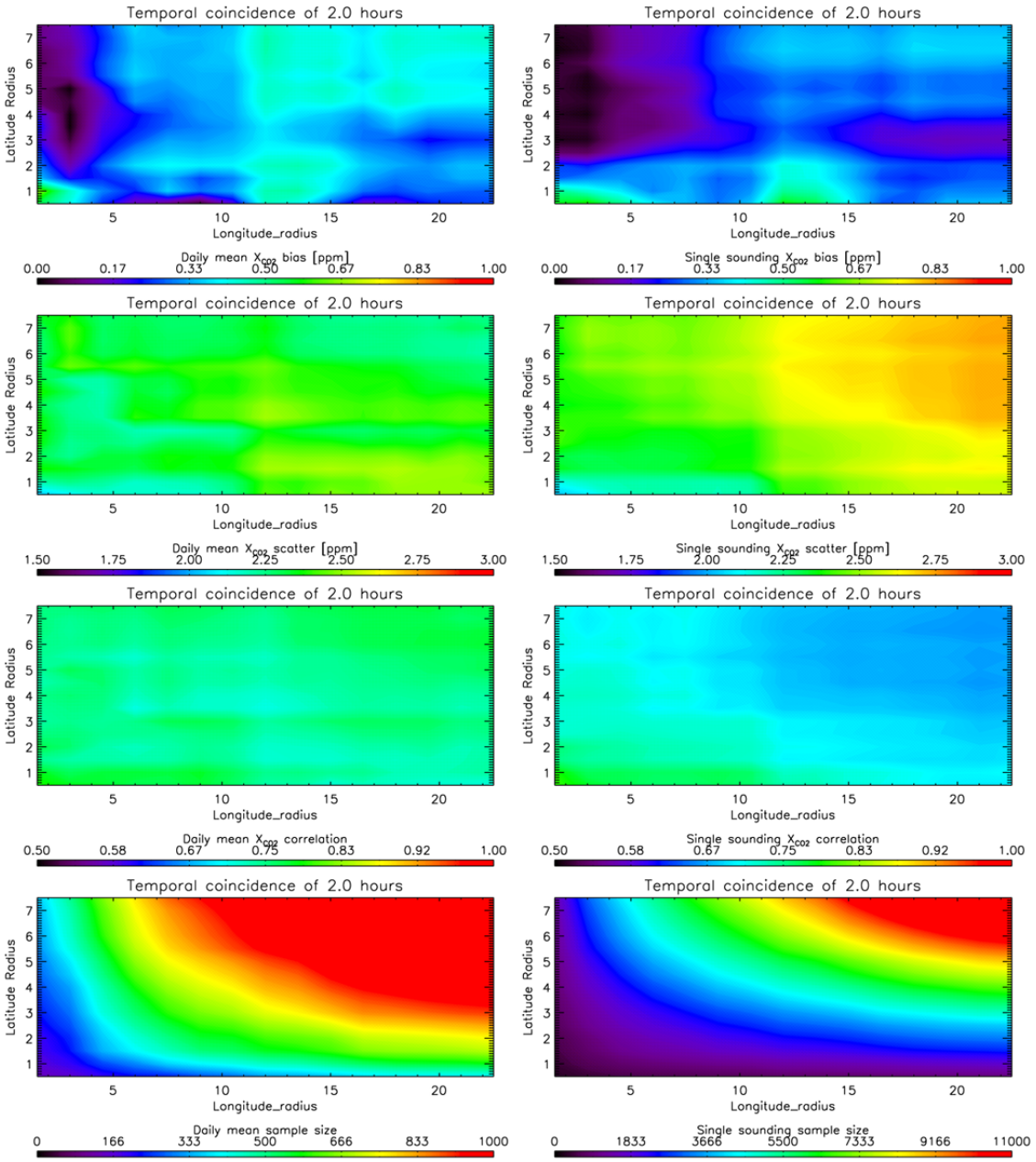

FIGURE 4.3. Statistics for a range of latitude and longitude coincidence limits for the comparison of GOSAT and TCCON X_{CO2}. The left column shows the mean bias (top left), standard deviation (left second row), correlation coefficient (left third row), and sample size of daily mean GOSAT X_{CO2} coincident with TCCON. Similar statistics are shown in the right column where GOSAT single soundings are coincident with TCCON individual observations. Additionally, a temporal coincidence of 2 hours between GOSAT and TCCON observations was used.

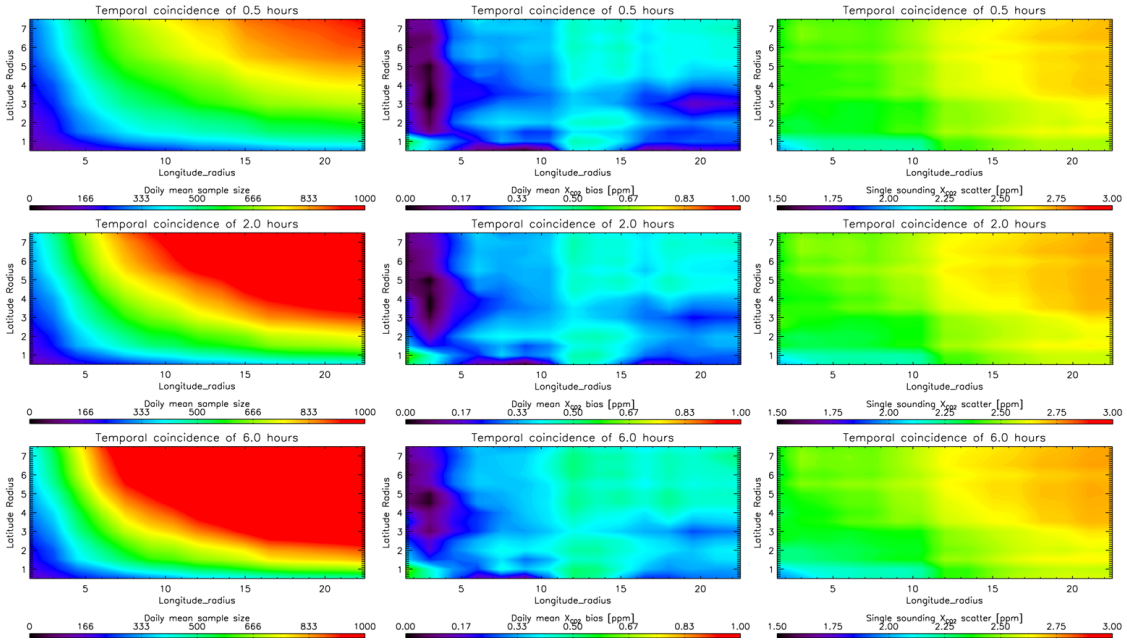

FIGURE 4.4. Statistics for a range of latitude, longitude, and temporal coincidence limits for the comparison of GOSAT and TCCON X_{CO2}. The sample size of coincident daily mean data (left column), mean bias of coincident daily mean data (middle column), and standard deviation of coincident single soundings (right column) is shown for three different temporal coincidence limits of GOSAT and TCCON X_{CO2}. The top row shows the statistics for a temporal coincidence of 30 minutes between GOSAT and TCCON observations. Similarly, the middle and bottom row shows the statistics for a temporal coincidence of 2 hours and 6 hours, respectively.

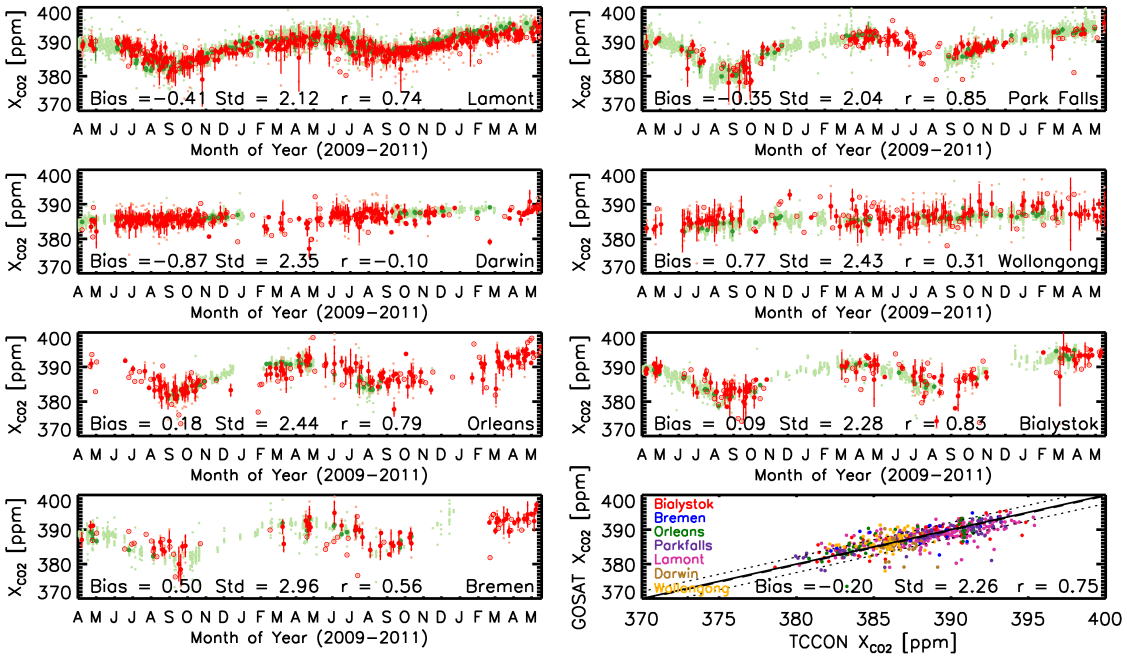

FIGURE 4.5. Comparison of retrieved X_{CO2} from GOSAT with retrieved X_{CO2} from seven TCCON site for coincident cloud-screened observations within 2 hours and 5° between April 2009 and May 2011. All TCCON data shown in light green, coincident daily mean TCCON shown in dark green, all GOSAT data shown in light red and daily mean GOSAT shown in dark red (with daily mean points with only one value per day are represented by open circles). The average difference between the daily means is given as the bias (ranging from -0.87 to 0.77 ppm), the standard deviation of daily means by the Std (between 2.04 and 2.96 ppm) and the correlation coefficient of daily means by r (-0.10 at Darwin to 0.85 at Park Falls). The lower right panel gives the correlation of daily mean coincident retrieved GOSAT X_{CO2} with daily mean TCCON X_{CO2} within ±2 hours for the seven sites. This gives an overall bias of -0.20 ppm, scatter of 2.26 ppm and correlation of 0.75 between GOSAT and TCCON X_{CO2}.

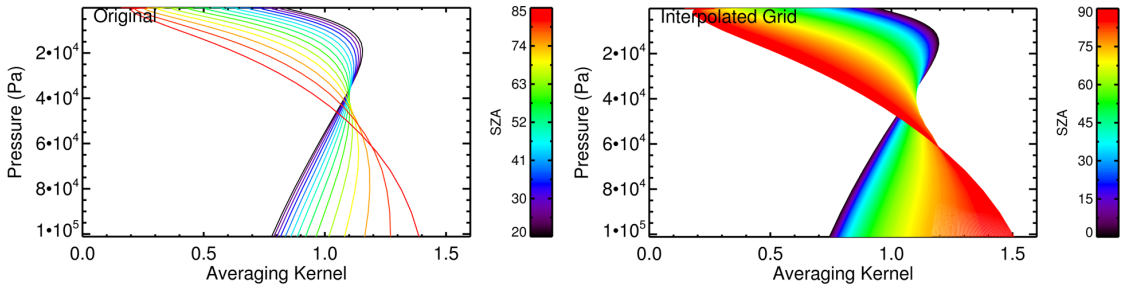

FIGURE 4.6. The Lamont/USA TCCON averaging kernel as a function of atmospheric pressure for different SZA (left). The right panel shows these averaging kernels for different SZA when interpolated onto a finer grid of 0.25°.

Table 4.3. Statistics for the UoL-FP v3G comparison to TCCON, where the bias, σ and r were calculated using coincident daily mean data and other parameters calculated from individual coincident points.

TCCON site	Total from L1B	Passed pre-screen	Percent cloudy	Passed post-screen	Coincident days	Bias (ppm)	σ (ppm)	r (Pearson)	Single sounding σ (ppm)	A Posterior error (ppm)	Mean smoothing error difference (ppm)	σ smoothing error difference (ppm)
Bialystok (53.230° N)	29376	8321	61.16	459	54	0.09	2.28	0.83	2.20	1.24	-0.21	0.32
Bremen (53.100° N)	24054	5484	66.36	260	19	0.50	2.96	0.56	2.00	1.20	-0.06	0.22
Orleans (47.970° N)	24047	9511	61.32	715	47	0.18	2.44	0.79	2.37	1.20	-0.50	0.17
Park Falls (45.945° N)	33277	5785	55.52	421	86	-0.35	2.04	0.85	3.05	1.22	-0.40	0.26
Lamont (36.604° N)	30984	9888	39.44	2445	261	0.41	2.12	0.74	2.85	1.14	-0.05	0.24
Darwin (12.424° S)	17273	4511	39.64	990	54	-0.87	2.35	-0.10	3.19	0.89	-0.08	0.07
Wollongong (34.406° S)	13182	4971	50.45	570	56	0.77	2.43	0.31	2.90	1.09	-0.26	0.10
Total	172193	48471	53.57	5860	577	-0.20	2.26	0.75	2.46	1.14	-0.14	0.26

Table 4.4. Statistics for the UoL-FP v3G comparison to TCCON with stricter post-screen, where the bias, σ and r were calculated using coincident daily mean data and other parameters calculated from individual coincident points.

TCCON site	Total from L1B	Passed pre-screen	Percent cloudy	Passed post-screen	Coincident days	Bias (ppm)	σ (ppm)	r (Pearson)	Single sounding σ (ppm)	A Posterior error (ppm)	Mean smoothing error difference (ppm)	σ smoothing error difference (ppm)
Bialystok (53.230° N)	29376	8321	61.16	179	28	0.05	1.62	0.91	1.79	1.22	-0.21	0.32
Bremen (53.100° N)	24054	5484	66.36	87	8	-0.60	1.99	0.77	1.46	1.13	-0.06	0.22
Orleans (47.970° N)	24047	9511	61.32	326	37	0.02	2.04	0.83	1.86	1.14	-0.50	0.17
Park Falls (45.945° N)	33277	5785	55.52	241	51	-0.23	1.50	0.84	2.65	1.19	-0.40	0.26
Lamont (36.604° N)	30984	9888	39.44	1448	194	-0.17	1.70	0.83	2.23	1.13	-0.05	0.24
Darwin (12.424° S)	17273	4511	39.64	711	47	-0.45	2.15	-0.06	2.04	0.85	-0.08	0.07
Wollongong (34.406° S)	13182	4971	50.45	363	48	0.70	2.14	0.48	1.96	1.04	-0.26	0.10
Total	172193	48471	53.57	3355	413	-0.08	1.84	0.81	1.92	1.11	-0.14	0.26

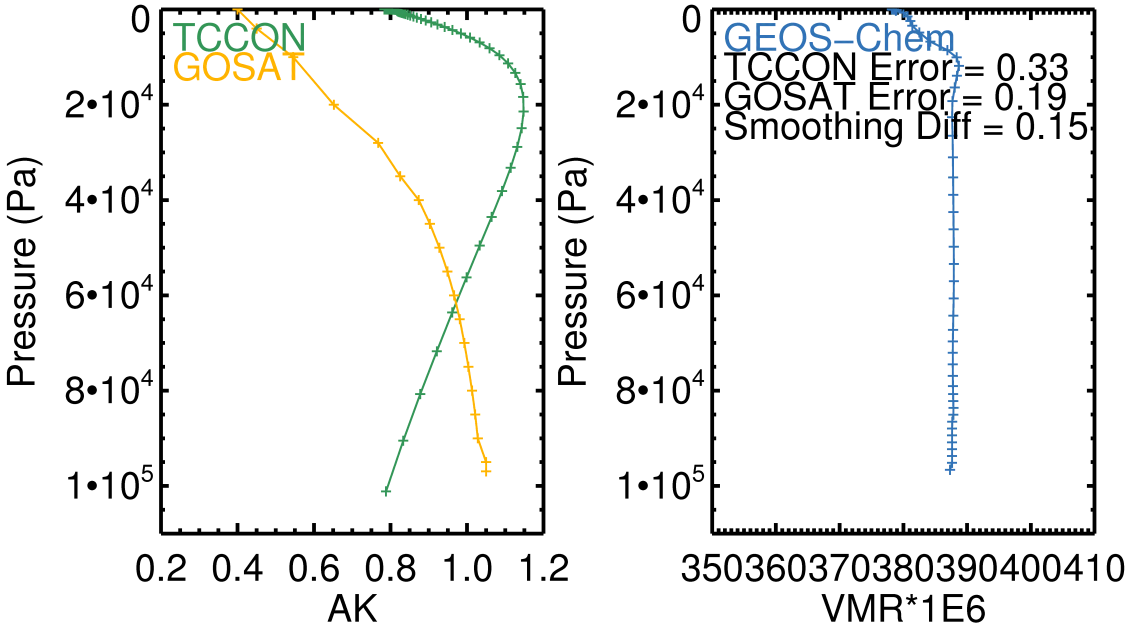

FIGURE 4.7. Example averaging kernels for TCCON and GOSAT over Lamont/USA (left) and the corresponding CO_2 VMR vertical profile (right). The estimated smoothing error for TCCON and GOSAT with respect to GEOS-Chem is given, and the smoothing error difference between TCCON and GOSAT is stated.

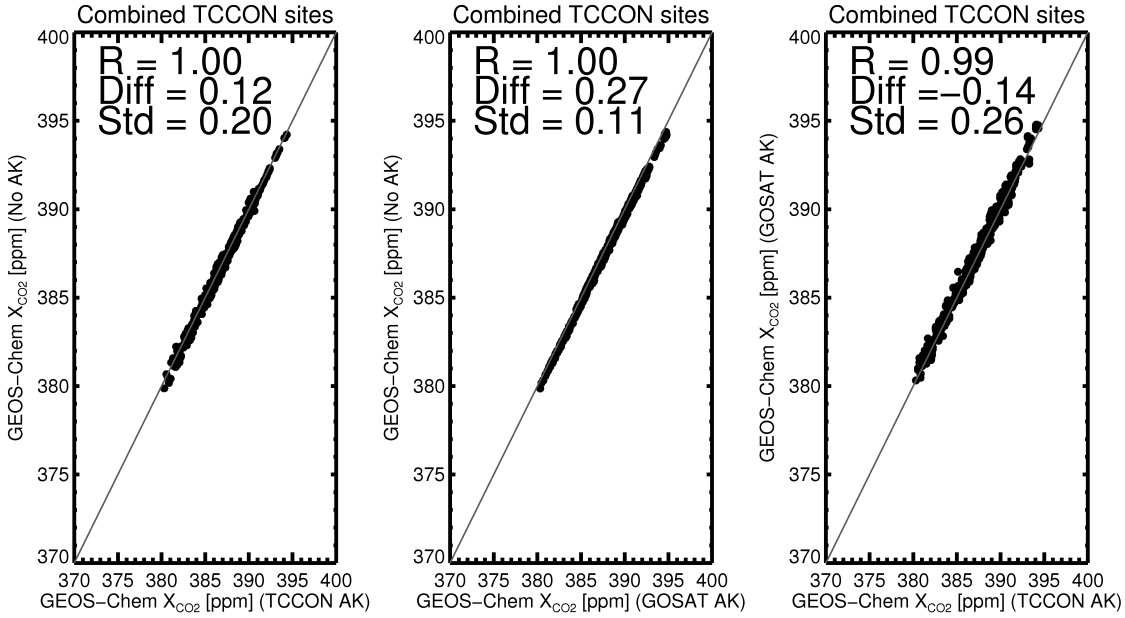

FIGURE 4.8. Correlation of GEOS-Chem with and without TCCON averaging kernels applied for data within 5° of seven TCCON sites between April 2009 and December 2010 (left). Similarly, a correlation between GEOS-Chem with and without GOSAT averaging kernels applied is shown in the centre. The mean difference (Diff) or smoothing error between with and without averaging kernels applied is given for TCCON and GOSAT. The smoothing error difference is estimated from a comparison between GEOS-Chem with TCCON and GOSAT averaging kernels applied (right).

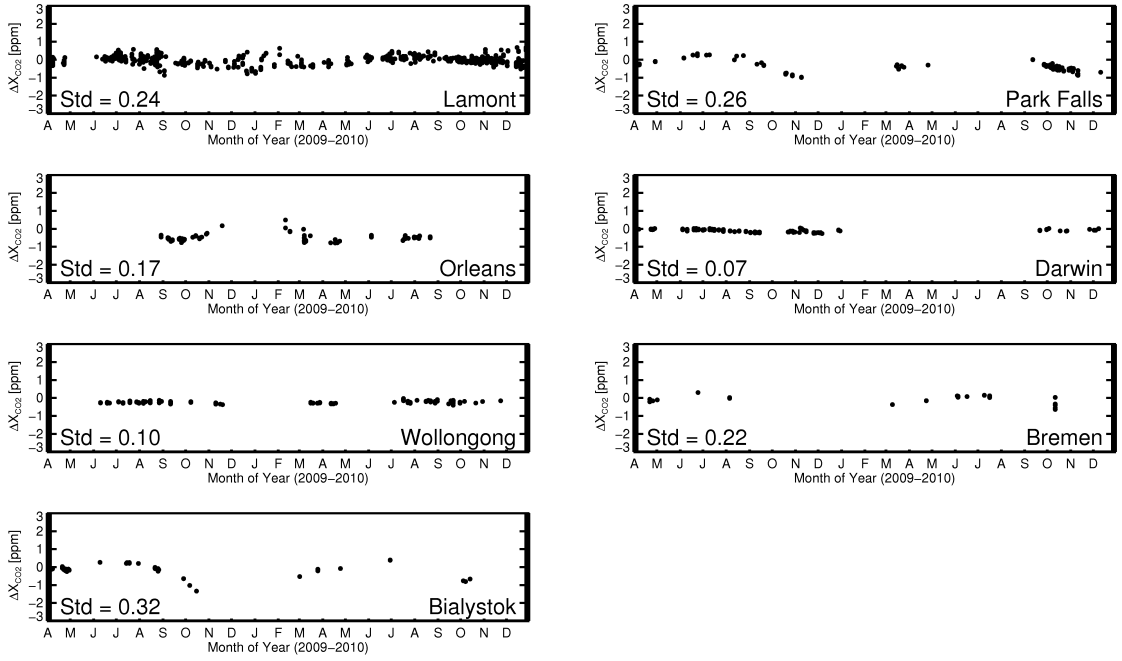

FIGURE 4.9. Calculated smoothing error differences for seven TCCON sites, for coincident cloud-screened observations within 2 hours and 5° between April 2009 and December 2010. The standard deviation of the smoothing error difference values are given by the Std (between 0.07 and 0.32 ppm).

Table 4.5. Statistics for the UoL-FP v3G comparison to TCCON with and without TCCON data being corrected by the smoothing error difference (SED) between GOSAT and TCCON. The bias, σ and r were calculated using coincident daily mean data and other parameters calculated from individual coincident points, between April 2009 and December 2010.

TCCON site	Bias without SED (ppm)	σ without SED (ppm)	r without SED (Pearson)	Bias with SED (ppm)	σ with SED (ppm)	r with SED (Pearson)	Bias difference (ppm)	σ difference (ppm)	r difference (Pearson)
Bialystok (53.230° N)	-0.13	2.34	0.73	-0.34	2.47	0.7	-0.21	0.13	-0.03
Bremen (53.100° N)	0.43	2.73	0.64	0.39	2.77	0.64	-0.04	0.04	0.00
Orleans (47.970° N)	-0.44	2.48	0.73	-0.91	2.44	0.74	-0.47	-0.04	0.00
Park Falls (45.945° N)	-0.37	2.84	0.77	-0.71	2.85	0.77	-0.34	0.01	0.00
Lamont (36.604° N)	-0.08	2.23	0.66	-0.09	2.23	0.66	-0.01	0.00	0.00
Darwin (12.424° S)	-0.96	2.36	0.09	-1.06	2.35	0.10	-0.10	-0.01	0.01
Wollongong (34.406° S)	0.91	2.47	0.24	0.67	2.47	0.24	-0.24	0.00	0.00
Total	-0.15	2.44	0.66	-0.29	2.44	0.66	-0.14	0.00	0.00

4.3 Comparisons to the GEOS-Chem model

One year of GOSAT X_{CO2} retrievals was compared with CO_2 atmospheric concentrations from the GEOS-Chem global 3-D chemistry transport model (v8-02-01) (Feng et al. 2011). The GEOS-Chem simulations use assimilated GEOS-5 meteorology from the Global Modeling and Assimilation Office based at NASA Goddard to drive the model. For the surface CO_2 fluxes, GEOS-Chem assimilates annual fossil fuel emissions estimated from CDIAC, biofuel emissions obtained from Yevich & Logan (2003) climatology, monthly biomass burning emissions extracted from the third version of the Global Fire Emission Database (GFEDv3) that uses observations of the land surface by ground-based and satellite instruments, monthly ocean fluxes that are derived from sea-surface pCO_2 observations (Takahashi et al. 2009), and biospheric fluxes that are computed using the CASA biosphere model (Randerson et al. 1997). The CASA model is three hourly and is constrained by GEOS meteorology output and Normalized Difference Vegetation Index (NDVI). The mixing depths and surface fields are updated every three hours and the GEOS-5 meteorology is updated every six hours. The 4D fields include 47 vertical levels and a horizontal grid resolution of 2° latitude by 2.5° longitude.

The GEOS-Chem simulations are forced by posterior fluxes inferred from the GLOBALVIEW CO_2 product, that includes 2009 and 2010 data (Maserie & Tans 1995). The GLOBALVIEW data from 78 surface sites are assimilated to estimate monthly surface fluxes over 144 global regions by using an ensemble Kalman Filter (EnKF) (Feng et al. 2009, 2011). Feng et al. (2011) reported that the GEOS-Chem model is within 1.5 ppm of free and upper troposphere aircraft vertical profile measurements and CO_2 retrieved from AIRS observations. Additionally, GEOS-Chem is on average within 0.5 to 1.0 ppm of observed partial CO_2 columns from the HIAPER HIPPO project (James Barlow, personal communication, 2012). The GEOS-Chem model vertical transport errors are estimated to be less than $\sim$2 ppm. This is supported by complementary model evaluation studies of CH_4, CH_3CCl_3, and SF_6 (e.g., Fraser et al. 2011, Patra et al. 2011). TCCON X_{CO2} was compared with that of GEOS-Chem (convolved with the TCCON averaging kernels) for each of the seven sites considered in the previous section and GEOS-Chem was found to have a mean bias of -0.09 ppm, standard deviation of 1.23 ppm and correlation coefficient of 0.93, comparing better than GOSAT with TCCON (see Figure 4.10). Based on the current understanding of model performance it can be concluded that the model should well reproduce large scale features of the atmospheric CO_2 distribution and that differences between GOSAT and GEOS-Chem are likely due to GOSAT retrieval biases. Although, model errors could also contribute to any observed differences.

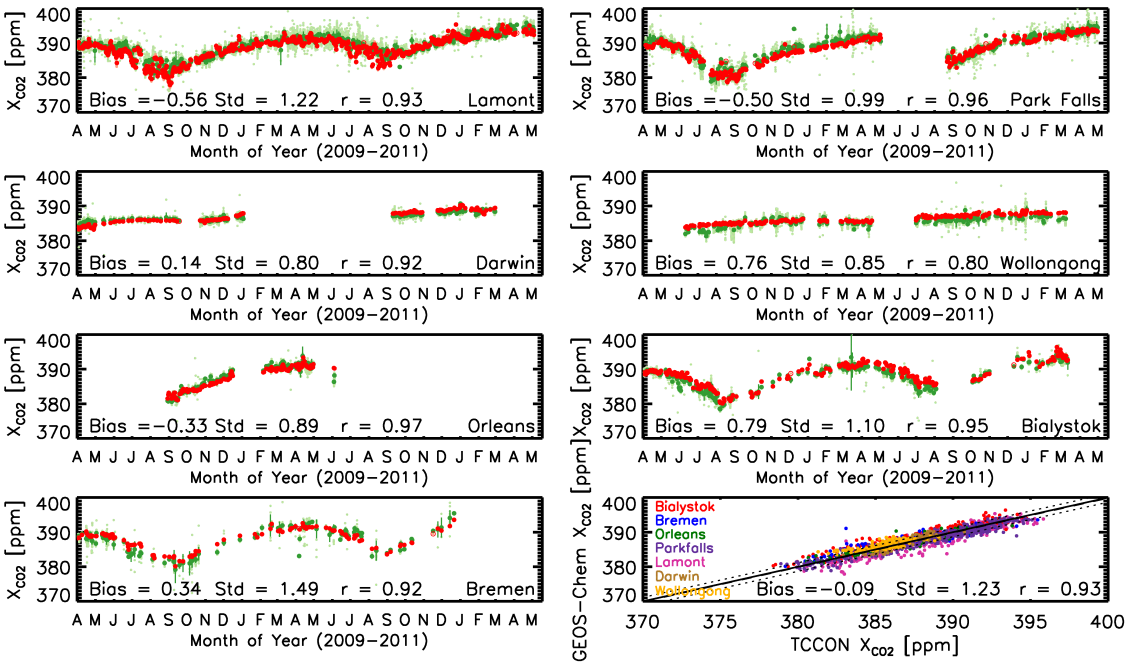

FIGURE 4.10. Comparison of X_{CO2} calculated from GEOS-Chem (with TCCON averaging kernels applied) with retrieved X_{CO2} from seven TCCON site for cloud-screened observations within 5° between April 2009 and May 2011. All TCCON data shown in light green, coincident daily mean TCCON shown in dark green, all GEOS-Chem data shown in light red and daily mean GEOS-Chem shown in dark red (with daily mean points with only one value per day are represented by open circles). The average difference between the daily means is given as the bias (ranging from -0.56 to 0.79 ppm), the standard deviation of daily means by the Std (between 0.80 and 1.49 ppm) and the correlation coefficient of daily means by r (0.80 at Darwin to 0.97 at Orleans). The lower right panel gives the correlation of daily mean retrieved GEOS-Chem X_{CO2} with daily mean TCCON X_{CO2} for the seven sites. This gives an overall bias of -0.09 ppm, scatter of 1.23 ppm and correlation of 0.93 between GEOS-Chem and TCCON X_{CO2}.

Figure 4.11 shows the comparison between X_{CO2} from GOSAT and GEOS-Chem for each season, where the GEOS-Chem CO_2 profiles were interpolated to the locations and times of the GOSAT observations, and convolved with the averaging kernel (Equation 4.1) to obtain X_{CO2} as measured by GOSAT. Overall, the spatial and temporal distribution of X_{CO2} agrees well between GOSAT and GEOS-Chem. The mean difference observed between GOSAT and GEOS-Chem X_{CO2} varies from -1.43 to -0.82 ppm seasonally, with the standard deviation ranging from 2.41 to 2.71 ppm. High correlations of the seasonal latitudinal gradient are found with correlation coefficients ranging between 0.73 and 0.96, but slightly poorer point-by-point correlation coefficients with values be-

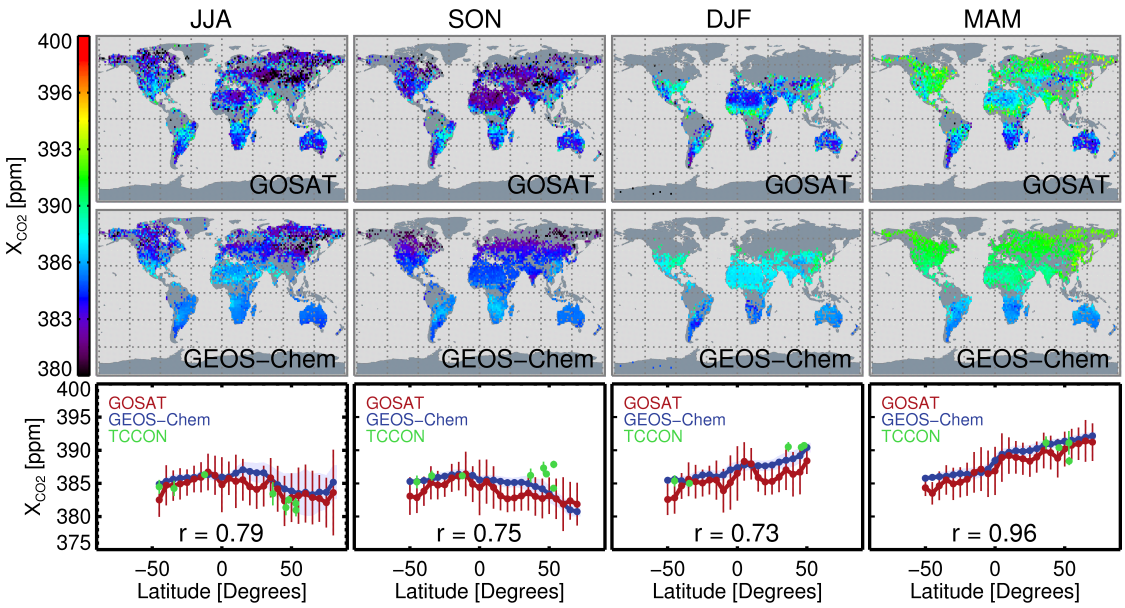

FIGURE 4.11. Comparison of X_{CO2} retrieved from GOSAT and X_{CO2} calculated from GEOS-Chem CO_2 profiles convolved with the scene-specific GOSAT averaging kernel. For each season, GOSAT is shown at the top, GEOS-Chem in the middle, and a zonal mean comparison of them at the bottom. The global maps indicate the largest differences are observed over desert regions, such as the Sahara and central Asia. The zonal mean comparison shows a very good agreement between GOSAT and GEOS-Chem. It also includes the average TCCON X_{CO2} from each site which in general agrees, with observed differences mostly due to zonal averaging of GOSAT/GEOS-Chem data.

tween 0.37 and 0.64. Between June 2009 and May 2010 the correlation between the GOSAT and GEOS-Chem annual mean latitudinal gradient is 0.76 and the annual spatial varability is found to have a global mean difference of -1.22 ppm, standard deviation of 2.59 ppm and correlation of 0.61 (not shown in Figures).

Over desert regions such as the Sahara, Saudi Arabia and Australia, differences are found between GOSAT and GEOS-Chem of up to 3 ppm. The medium gain mode is predominantly used over desert areas where surface reflectance causes the signal intensity to be high. Suto et al. (2008) found that TANSO-FTS instrument micro-vibrations produced a larger effect on medium gain observations and X_{CO2} retrievals of medium gain have been observed to be $\sim$1% higher than that of high gain (Crisp et al. 2012). However, X_{CO2} retrieved from the UoL-FP v3G algorithm for desert regions observed with the high gain mode, such as central Asia, are found to also give similar differences in X_{CO2} compared to GEOS-Chem. Since all these regions include high albedo in the

1.61 and 2.06 μm CO_2 bands and high levels dust, the X_{CO2} difference is not solely due to gain issues (as suggested by Crisp et al. (2012)) but also potentially an aerosol or other instrumental related issue.

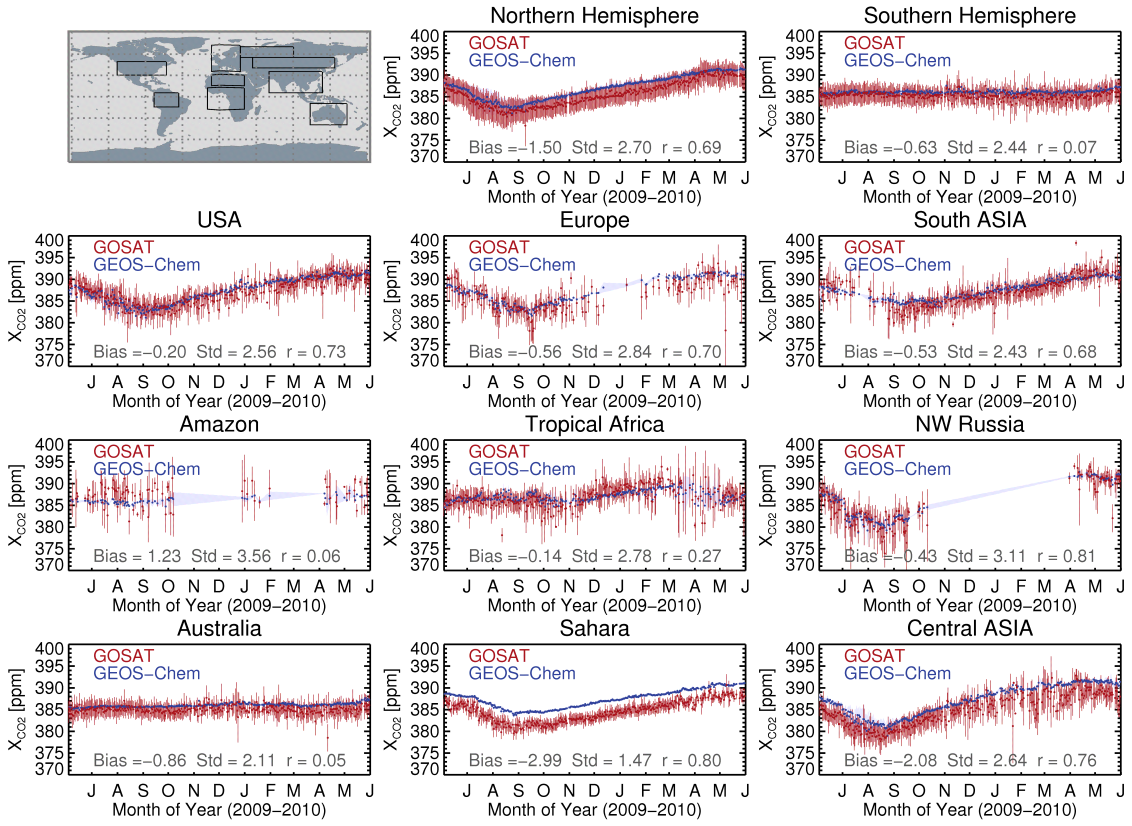

FIGURE 4.12. Comparison of X_{CO2} retrieved from GOSAT and X_{CO2} calculated from GEOS-Chem CO_2 profiles convolved with the scene-specific GOSAT averaging kernel, for a number of different regions between June 2009 and May 2010. The locations of these regions are indicated on the map by the black boxes (top left). The top centre and top right panels give the time series of GOSAT and GEOS-Chem data for the northern and southern hemispheres, showing the seasonal cycle to be well matched but with GOSAT data offset lower by -1.50 ppm in the northern hemisphere and -0.63 ppm in the southern hemisphere. The second row of plots show a very good agreement between GOSAT and GEOS-Chem both in value and seasonality for regions containing urban environments. Below these, the time series of forested regions are shown, with GOSAT reproducing the GEOS-Chem data very well but with a larger scatter and fewer data points. The bottom panels show the time series for 3 different desert regions, with GOSAT matching the seasonal cycle of GEOS-Chem very well but offset lower in value from -0.86 to -2.99 ppm.

The time series of X_{CO2} from GOSAT and GEOS-Chem for a number of different regions are shown in Figure 4.12. The seasonal cycle is found to match very well between

GOSAT and GEOS-Chem for both northern and southern hemispheres, but a difference of 1.5 ppm is observed in the northern hemisphere throughout the year and a smaller difference of 0.63 ppm in the southern hemisphere. GOSAT and GEOS-Chem X_{CO2} show a high consistency for both Europe and the USA, with a X_{CO2} difference of 0.20 ppm and 0.56 ppm and correlation coefficients of 0.73 and 0.70, respectively. On average, GOSAT and GEOS-Chem agree for South Asia with a mean difference of 0.53 ppm and correlation coefficient of 0.68, but differences are viewed in the seasonal cycle with GEOS-Chem over-estimating the X_{CO2} in autumn 2009 and under-estimating during spring 2010.

Few GOSAT soundings are observed over the Amazon due to tropical clouds, and those measurements that are retrieved have a large standard deviation (3.56 ppm) that is potentially due to partial cloud contamination. Similarly, a larger scatter is seen in tropical Africa during autumn and spring for GOSAT, whereas winter and summer have a reduced scatter and have similar values as GEOS-Chem. A very high agreement is observed for NW Russia with a correlation coefficient of 0.81 and a mean X_{CO2} difference of 0.43 ppm.

In central Asia where a desert region is observed with the high gain mode, the seasonal cycle of GOSAT and GEOS-Chem is observed to agree well (r=0.76), but consistently with a $\sim$2 ppm difference in value. Also, a $\sim$3 ppm mean difference is found over the Sahara between GOSAT and GEOS-Chem X_{CO2} where a desert region is observed with the medium gain mode, but the seasonal cycle agrees well with a correlation coefficient of 0.80. Australia, which comprises partially of desert and is oberved partially with medium and high gain modes, also shows a difference in X_{CO2} between GOSAT and GEOS-Chem with a value of 0.86 ppm.

4.4 Bias Correction Scheme

A bias correction method was developed to help identify and reduce the observed biases of retrieved X_{CO2} from GOSAT, especially over desert areas. Similar to Wunch et al. (2011b), this bias correction method is based on a multivariate linear regression of the difference between pseudo observations and retrieved X_{CO2} from GOSAT between July 2009 to June 2010 over the region south of 25°S where the variability of CO_2 is low. The pseudo-observations were generated using GEOS-Chem calculations to provide information on vertical profile and spatial variations while the temporal variations and absolute values were scaled to match Wollongong/Australia (34.406°S) and Lauder/New Zealand (45.038°S) TCCON measurements. Initially all retrieval parameters and observation related parameters were used. Similar to Wunch et al. (2011b), the four parameters with the highest correlation were identified and used to obtain the following equation:

$$\begin{aligned} X_{CO_2}^{\text{bias-corrected}}\,[\text{ppm}] = X_{CO_2}^{\text{retrieved}}\,[\text{ppm}] &+ 4.19 \\ &- 0.564 * \text{CO}_2\text{\_Signal\_Ratio} \\ &- 0.193 * (\Delta\text{P } [\text{hPa}]) \\ &+ 56.8 * \text{Ice\_Optical\_Depth} \\ &+ 0.256 * 10^{-5} * \text{O}_2\text{\_Albedo\_Slope} \end{aligned} \tag{4.2}$$

These parameters have been identified by the regression which does not provide a means of identifying the physical link. A correlation (r=0.37) of the X_{CO2} difference is observed with the ratio of the mean signal of the 1.61 μm CO_2 band to the 2.06 μm CO_2 band (CO_2_Signal_Ratio), which may be a consequence of the spectroscopic differences of the different CO_2 bands, but might also relate to aerosols or albedo. Spectroscopic errors may also result in systematic effects in the retrieved surface pressure as shown by Wunch et al. (2011b) and the X_{CO2} difference is found to correlate (r=0.30) with delta surface pressure (ΔP), even though the X_{CO_2} is already normalised with the surface pressure ratio. An anti-correlation (r=-0.22) of the X_{CO2} difference with retrieved cirrus optical depth (Ice_Optical_Depth) is observed which indicates the path length was altered. Based on the geographical location of the bias correction for this parameter it can be inferred that the ice optical depth refers to cirrus clouds. An anti-correlation (r=-0.29) of the X_{CO_2} difference is also found with the slope of the band 1 albedo (O_2_Albedo_Slope) which may be due to errors in the O_2 A band spectroscopy, zero-level offsets, or variations in signal intensity over vegetation regions that could be caused by not accounting

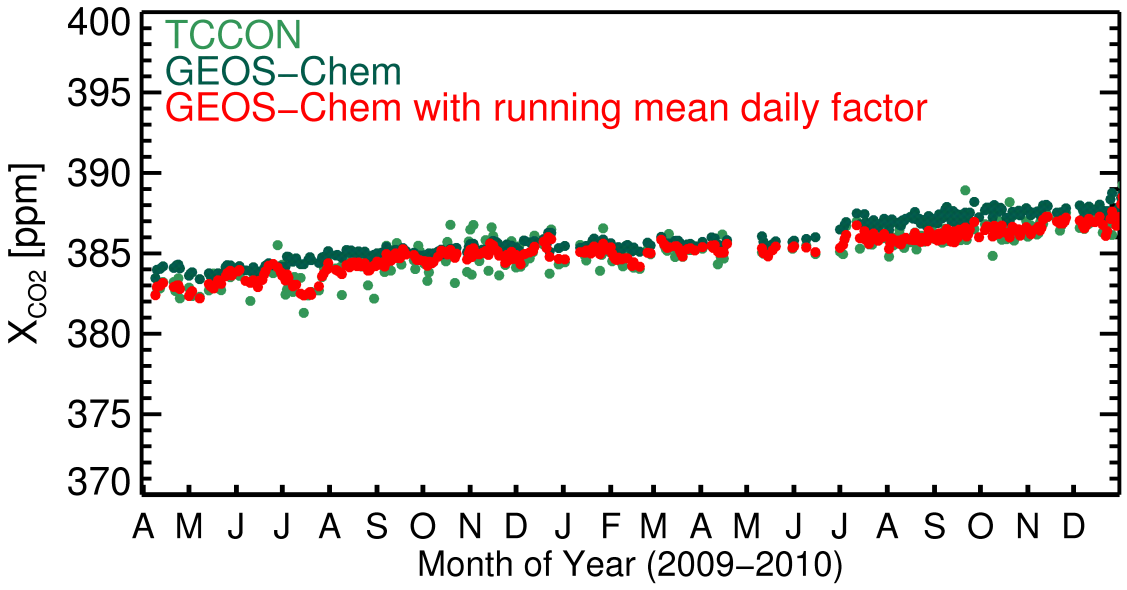

FIGURE 4.13. Illustration of X_{CO2} calculated from GEOS-Chem within 5° of Wollongong/Australia and Lauder/New Zealand combined between April 2009 and December 2010 with TCCON averaging kernels applied (dark green) compared to X_{CO2} inferred from TCCON (light green). When the daily mean difference between GEOS-Chem and TCCON is applied as a ±5 day running mean to the GEOS-Chem data, the GEOS-Chem X_{CO2} becomes closer in value to TCCON, as shown in Red.

for the known fluorescence (Frankenberg et al. 2011a).

Whilst Wunch et al. (2011b) found biases partially due to airmass and the O_2 A band signal, here no correlation is found between the airmass and the X_{CO2} difference (r = 0.01) nor the O_2 A band signal (r=0.01). Additionally, a zero level offset in the O_2 A band is already retrieved to mitigate the effects of the GOSAT Band 1 non-linearity and partially fluorescence (Butz et al. 2011, Frankenberg et al. 2011a, 2012, Suto et al. 2008).

This bias correction was applied to one year (June 2009 to May 2010) of X_{CO2} retrieved from GOSAT globally and compared to X_{CO2} calculated from the GEOS-Chem model with GOSAT averaging kernels applied. The annual mean global difference is found to be reduced from -1.22 ppm to -0.68 ppm and the correlation to increase from 0.61 to 0.74.

Figure 4.15 shows a comparison between GOSAT and GEOS-Chem X_{CO2} latitudinal gradients for each season, comparing with and without the bias correction. The seasonal latitudinal gradients show improvements with increases of the correlation between 0.01 and 0.18 depending on the season, for DJF the improvement in correlation coefficient is marginal. The majority of the improvement occurs in the northern hemisphere, especially

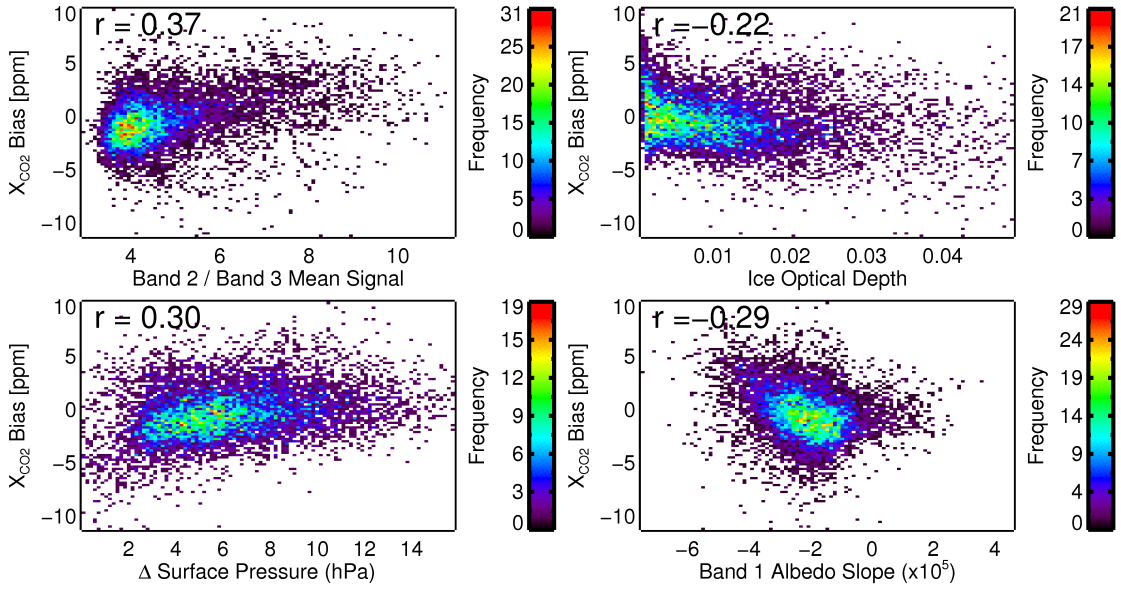

FIGURE 4.14. Correlation of the X_{CO2} bias with the ratio of band 2 to band 3 mean radiance (top left), the retrieved cirrus optical depth (top right), the ΔP (bottom left), and the retrieved band 1 albedo slope (bottom right). Where the bias is between GOSAT and the GEOS-Chem 3D chemistry transport model with GOSAT averaging kernels applied and corrected with a fit to Wollongong and Lauder TCCON measurements. The colour gives the density of values within the bin range.

over the Sahara region.

The time series of bias corrected X_{CO2} retrieved from GOSAT compared to GEOS-Chem data for different regions is shown in Figure 4.16. For most regions it is found that the bias, standard deviation and correlation coefficient have improved. In partiuclar, the bias correction has considerably reduced the larger differences previously seen over desert regions; the difference over the Sahara has reduced from -2.99 ppm to -1.20 ppm, the difference over Australia has reduced to about half, and the difference over central Asia improved from -2.08 ppm to -0.94 ppm. However, for the Sahara region, the standard deviation and correlation coefficient becomes worse. Also, for some regions (Tropical Africa and NW Russia) it is found that the bias increases when applying the bias correction.

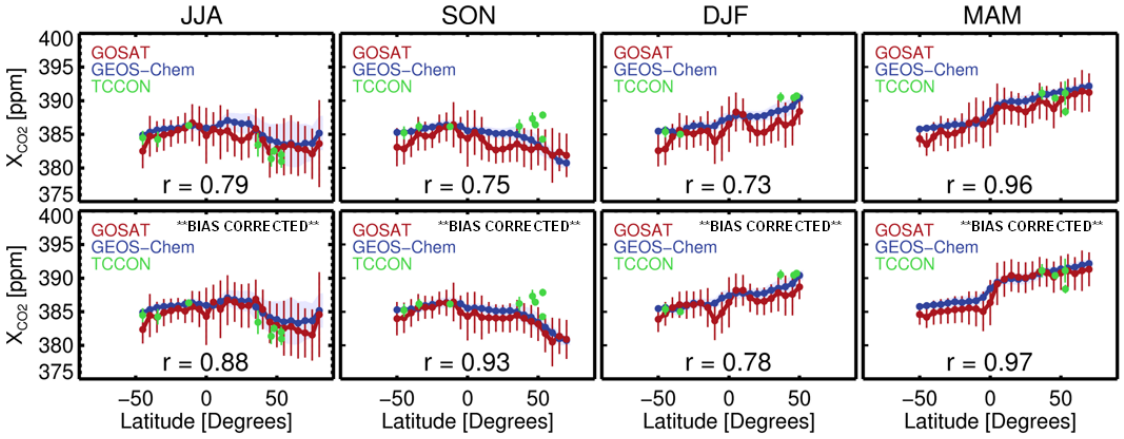

FIGURE 4.15. The top panels show zonal mean comparisons for each season of X_{CO2} retrieved from GOSAT and X_{CO2} calculated from GEOS-Chem CO_2 profiles convolved with the scene-specific GOSAT averaging kernel. The bottom panel gives revised comparisons where the GOSAT X_{CO2} was bias corrected. The latitudinal gradients of the bias corrected GOSAT X_{CO2} match very well to GEOS-Chem with correlations between 0.78 and 0.97. The bias correction leads to increases of the correlation between 0.01 and 0.18, and shows a large improvement over the latitudes that contain the Sahara.

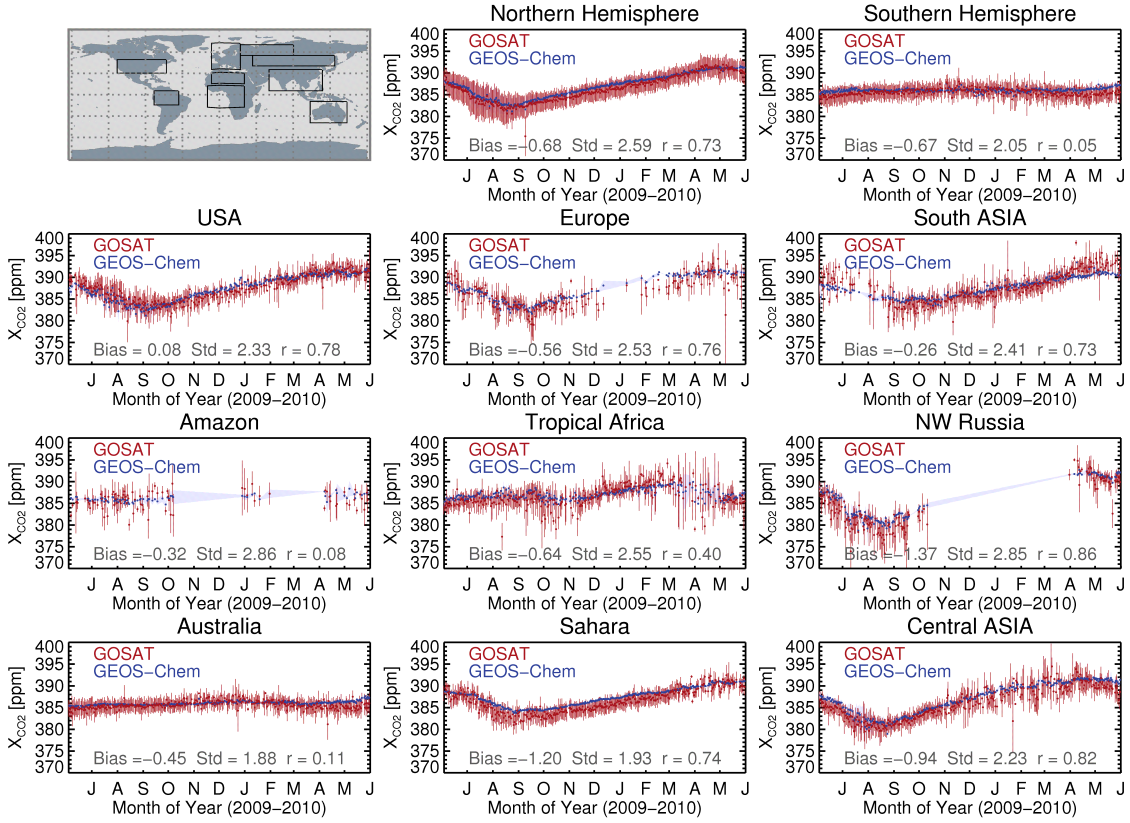

FIGURE 4.16. Comparison of bias corrected X_{CO2} retrieved from GOSAT and X_{CO2} calculated from GEOS-Chem CO_2 profiles convolved with the scene-specific GOSAT averaging kernel, for a number of different regions between June 2009 and May 2010. The locations of these regions are indicated on the map by the black boxes (top left). GOSAT agrees very well with GEOS-Chem for both hemispheres and all regions. GOSAT shows a good reproduction of the seasonal cycle of GEOS-Chem data, with the exception of south Asia where GOSAT is higher in the summer period. Minor offsets exist over the desert regions, such as Australia, the Sahara, and central Asia, which is a large improvement compared to the non-bias corrected X_{CO2} shown in Figure 4.12. Additionally, the scatter of all regions is less than that of the non-bias corrected X_{CO2}. Furthermore, the bias correction has brought the X_{CO2} over the Amazon to be of the same magnitude as GEOS-Chem.

4.5 Comparisons of GOSAT with Land Surface Types

The X_{CO2} difference between GOSAT and GEOS-Chem was compared against the land surface type for each observation. The surface type was determined by using the most common land cover type within a coincidence of $\pm 0.1^{\circ}$ of the Moderate Resolution Imaging Spectroradiometer (MODIS) Level 3 yearly 0.05° land cover type (MCD12C1) for 2007 (assuming the land cover has not significantly altered between 2007 and 2010). Figures 4.17 and 4.18 show this comparison for each of the GOSAT gain modes separately.

For retrievals of GOSAT high gain data, GOSAT and GEOS-Chem correlate well with X_{CO2} differences less than 0.23 ppm for surfaces that consist of forest, cropland, savanna, wetland, or urban environments. However, larger X_{CO2} differences (up to $\sim$3.2 ppm) are found for surfaces that consist of desert, shrubland, grassland or snow.

Where medium gain data has been retrieved, X_{CO2} differences are found to be similar to that of high gain data. The retrieved X_{CO2} from GOSAT is found on average to be $\sim$1.5 ppm lower than GEOS-Chem over both shrubland and grassland surfaces. The largest X_{CO2} difference of 2.75 ppm is observed over desert surfaces. The lowest difference (0.35 ppm) is found over savanna surfaces. No observations over other surface types exist due to the specific observation locations where medium gain was used. The X_{CO2} differences are found to be larger with certain land surface types, specifically deserts, irrespective of the gain setting used.

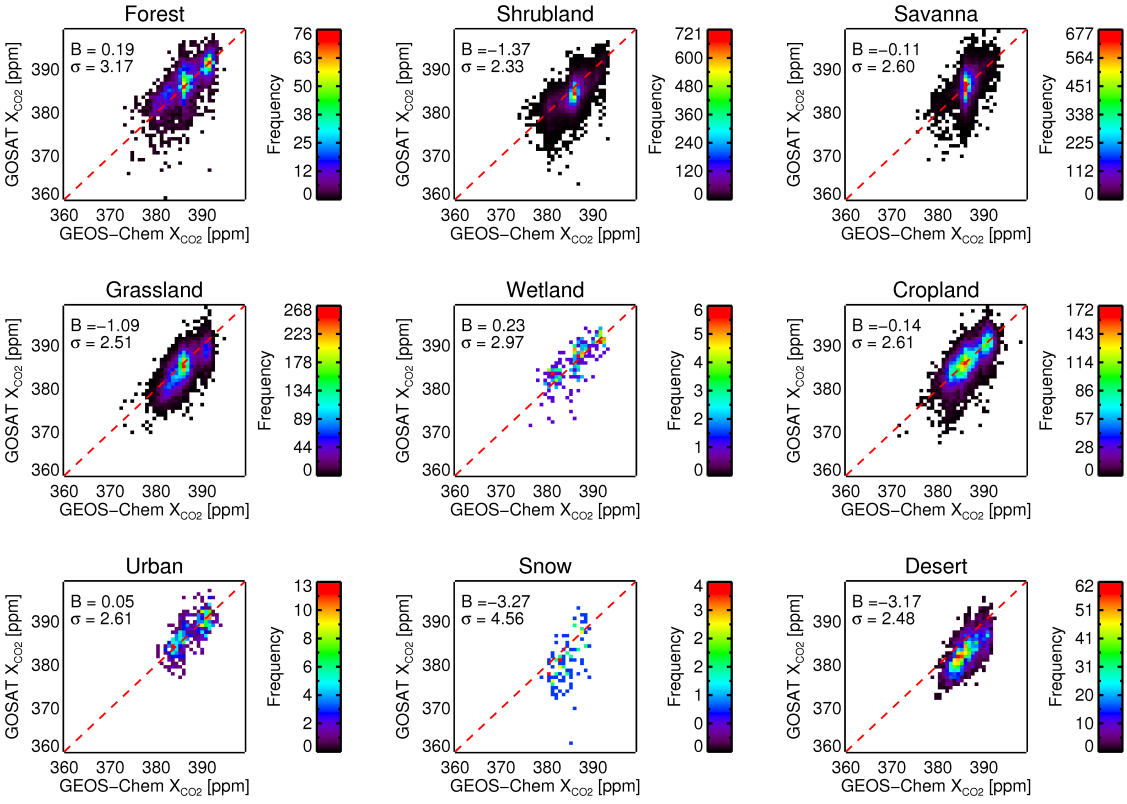

FIGURE 4.17. Comparison of X_{CO2} retrieved from high gain GOSAT data with GEOS-Chem X_{CO2} calculations for different MODIS land cover types. The red dashed line shows the one-to-one line, B represents the mean X_{CO2} difference, and σ gives the standard deviation of X_{CO2}. GOSAT and GEOS-Chem correlate well with X_{CO2} differences less than 0.23 ppm for surfaces that consist of forest, cropland, savanna, wetland, or urban environments. However, larger X_{CO2} differences (up to $\sim$3.2 ppm) are found for surfaces that consist of desert, shrubland, grassland or snow.

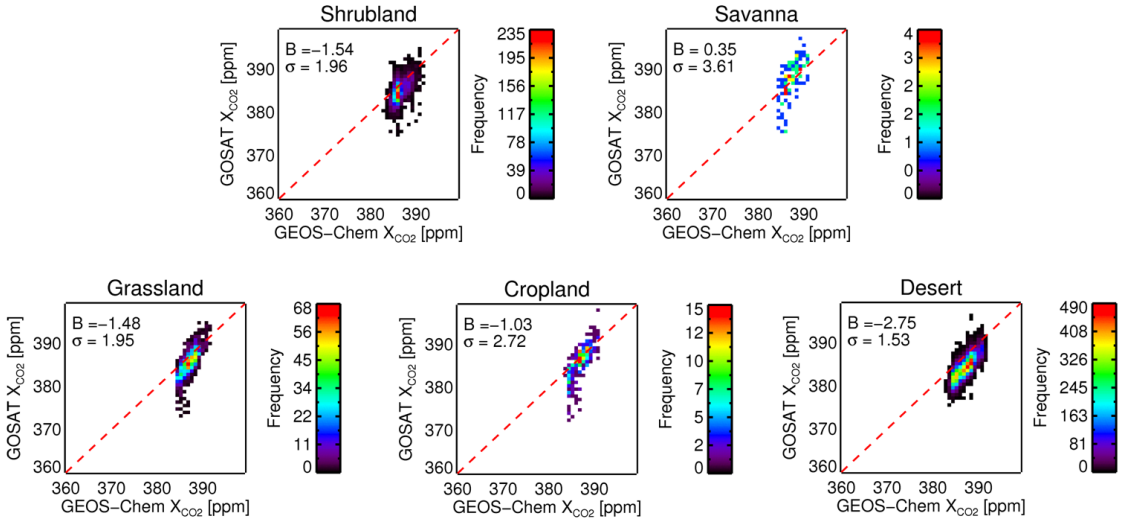

FIGURE 4.18. Comparison of X_{CO2} retrieved from medium gain GOSAT data with GEOS-Chem X_{CO2} calculations for different MODIS land cover types. The red dashed line shows the one-to-one line, B represents the mean X_{CO2} difference, and σ gives the standard deviation of X_{CO2}. The retrieved X_{CO2} from GOSAT is found on average to be $\sim$1.5 ppm lower than GEOS-Chem over both shrubland and grassland surfaces. The largest X_{CO2} difference of 2.75 ppm is observed over desert surfaces. The lowest difference (0.35 ppm) is found over savanna surfaces.

4.6 Comparisons to alternative retrieval algorithms

The retrieved X_{CO2} from GOSAT using the UoL-FP algorithm was compared with five alternative algorithms for two years of data over 11 TCCON sites; Lamont/USA, Park Falls/USA, Sodankyla/Finland, Bialystok/Poland, Bremen/Germany, Orleans/ France, Garmisch/Germany, Tsukuba/Japan, Darwin/Australia, Wollongong/Australia and Lauder/ New Zealand. The following sections give a brief description of each algorithm (futher details are given in Oshchepkov et al. (2012b)).

4.6.1 NIES PPDF D Retrieval Algorithm

The National Institute for Environmental Studies (NIES) Photon Path Length Probability Density Function (PPDF) Differential Optical Absorption Spectroscopy (DOAS) retrieval algorithm (NIES PPDF D) uses the maximum a posteriori method of optimal estimation (Rodgers 2000) with the DOAS technique (Oshchepkov et al. 2012a). It includes the HSTAR, high resolution RSTAR, radiative transfer model (Kokhanovsky et al. 2010), based on a discrete ordinate algorithm (Duan et al. 2005) and uses tabulated absorption cross-sections of HITRAN08 (Rothman et al. 2009). The solar model is based on a high resolution solar irradiance database provided by Dr. R. Kurucz (http://kurucz.harvard.edu/sun/irradiance2008/). The instrument model uses the official GOSAT ILS from JAXA (version 006) (Kuze et al. 2009). It applies a pre-screen that uses a PPDF based on the radiative transfer model (Bril et al. 2007, S. Oshchepkov & Yokota 2008, Oshchepkov et al. 2009, 2011, 2012a) and the NIES cloud-screen (Taylor et al. 2012). Only the 1.61 μm band was retrieved within the wavenumber range of 6180-6380 cm^{-1}.

The a priori CO_2 and CH_4 were obtained from daily profiles of the NIES TM global atmospheric transport model (Maksyutov et al. 2008). The a priori H_2O, temperature and surface pressure were extracted from 6 hourly model outputs from the Japan Meteorological Agency (JMA) on 0.5 degree horizontal resolution with 21 vertical levels. The albedo a priori was taken from the 16-daily MODIS land surface albedo product (MOD43B3) (Schaaf et al. 2002). The main differences between the retrieval algorithms include the; a priori, pre-screen, radiative transfer model, and solar model.

4.6.2 NIES L2 Retrieval Algorithm

The NIES L2 algorithm uses the maximum a posteriori method of optimal estimation with the Levenberg-Marquardt method (Rodgers 2000) and an accurate single scattering and approximate multiple scattering radiative transfer model of Duan et al. (2005). It uses the same absorption cross-sections, solar model, ILS and a priori as the NIES PPDF D retrieval algorithm. The polarisations were combined using a preliminary Mueller Matrix providing a single intensity to be retrieved. It pre-screens for saturated H_2O absorption lines as a test for cirrus clouds and uses the NIES cloud-screen (Taylor et al. 2012). The state vector consists of CO_2, CH_4 and H_2O 15-level VMR profiles, uniform 0-2 km AOD, surface pressure, albedo, dispersion and a temperature scaling factor. Only the 1.61 μm band was retrieved with the wavenumber ranges of 6180-6380 cm^{-1} for CO_2 and 5900-6150 cm^{-1} for CH_4. Additionally, all solar absorption lines were omitted from the retrieval.

The a priori aerosol optical properties and AOD were obtained from semi-real time daily outputs of the three-dimensional aerosol transport model, the Spectral Radiation-Transport Model for Aerosol Species (SPRINTARS) (Takemura et al. 2003), for soil dust, carbonaceous, sulfate, and sea-salt aerosols uniformly distributed within a 2-km layer from the surface (Yoshida et al. 2010). The key differences between the retrieval algorithms include the; a priori, pre-screen, radiative transfer model, and solar model, scattering approach, and the intensity used.

4.6.3 ACOS Retrieval Algorithm

The ACOS retrieval algorithm used for the NASA Atmospheric CO_2 Observations from Space (ACOS) project and the NASA OCO-2 mission is also based on the OCO algorithm (like the UoL-FP retrieval algorithm) but has been re-developed (O'Dell et al. 2012, Crisp et al. 2012). Here, it used HITRAN08 absorption cross-sections (Rothman et al. 2009) with additional line mixing in the O_2 A band. It simultaneously retrieved the O_2 A band, the 1.61 μm and 2.06 μm CO_2 bands with the average intensity of each polarisation. The state vector consisted of a 20-level CO_2 VMR profile and 20-level logarithmic extinction profiles of two aerosols, cloud and cirrus. Additionally, surface pressure was retrieved as well as a temperature offset, a scaling factor for H_2O, albedo, albedo slope and dispersion shift/stretch.

It obtained its a priori surface pressure, temperature, and water vapour from ECMWF. The a priori CO_2 VMR was extracted from latitudinal zonal land/ocean LMDZ 2004

model fields. The a priori albedo was computed from GOSAT reflectance. The a priori aerosol, cloud and cirrus profiles were constructed to provide a low altitude aerosol, a middle altitude aerosol, a middle high altitude cloud, and a high cirrus cloud. The optical properties of the aerosols used were types 2b and 3b from Kahn et al. (2001), representing a mixture of dusty maritime and coarse dust and a mixture of carbonaceous and black carbon maritime, respectively. The cloud and cirrus optical properties were taken from the Baum model (Baum et al. 2005a,b). It used a pre-screen of SNR >70, a cloud-screen based on the difference between ECMWF surface pressure and the surface pressure retrieved from a full O_2 A band retrieval (Taylor et al. 2012), and a post-screen based on χ^2 of each band, a posterior error, retrieved AOD, surface pressure and degrees of freedom.

4.6.4 RemoTeC Retrieval Algorithm

The Netherlands Institude for Space Research (SRON) retrieval algorithm (Butz et al. 2011) uses the Phillips-Tikhonov regularisation method of the CO_2 profile in addition to the least sqaures difference minimisation method with Gauss-Newton method applied (Rodgers 2000). These are balanced by a regularisation parameter. It uses a vector radiative transfer model based on the Gauss-Seidel solution of the radiative transfer equation and forward adjoint perturbation theory for the derivatives. It uses the tabulated absorption cross-sections of HITRAN08 (Rothman et al. 2009) and assumes AOD to be negligible by forcing retrievals into vanishing aerosol and cirrus optical thickness. It simultaneuously retrieves the 1.61 μm CO_2 band, CO_2 concentrations and microphysical properties of aerosol and cirrus particles. Filtered null-space components of the retrieved CO_2 profile are filled by 2005 model fields of CarbonTracker (Peters et al. 2007).

The a priori surface pressure, temperature and water vapour were obtained from ECMWF, a priori CO_2 from CarbonTracker 2005 model fields, and albedo from GOSAT reflectance. The NIES cloud-screen (Taylor et al. 2012), a pre-screen of SNR>70 and a post-screen based on χ^2 and AOD was used.

4.6.5 Intercomparison Results

Only retrieved X_{CO2} within a spatial coincidence of 5° radius of a TCCON site was used. All coincident statistics use the mean X_{CO2} within $\pm$2 hours ($\pm$1 hour for NIES 01.XX and NIES PPDF D algorithms) for temporal coincidence to TCCON data and

these values are daily averaged. These statistics are shown in Figure 4.19, which shows the correlation of each algorithm with TCCON for all sites combined.

The NIES 01.XX algorithm shows a large offset to TCCON which is known to be due to the existance of CO_2 absorption lines within the solar irradiance database used (Yoshida 2011). The NIES 01.XX results also have a large scatter which is most likely due to the assumption of a fixed aerosol profile between 0 - 2 km altitude globally. The ACOS B2.8 algorithm also has a large offset which is known to be mainly due to a surface pressure bias of 11 hPa (Crisp et al. 2012). However, the ACOS B2.9 algorithm attempts to correct for this surface pressure bias by scaling the O_2 A band absorption lines by a factor of 1.025 and also includes an O_2 A band zero level offset to help alleviate the effects of the band 1 nonlinearity. With these updates the ACOS B2.9 algorithm correlates well (r= 0.77) with TCCON. The NIES PPDF D algorithm has the highest correlation (r= 0.79) but the least amount of data. Currently it removes alot of useful data that are only partially contaminated by optical path modification. The RemoTeC_1.0 algorithm also gives a good correlation (r= 0.76) with TCCON.

The UoL-FP algorithm (no bias correction applied) has the highest amount of data and shows a good but slightly lower correlation (r= 0.72) with TCCON but has a number of outliers included which will affect this correlation. As shown in Section 4.2 if a stricter post-screen is applied then the TCCON comparison statistics improve substantially but at the cost of the amount of data. Most algorithms give a similar correlation to TCCON (UoL-FP 3G, ACOS B2.9, Remotec_1.0 and NIES PPDF D) but the small differences in the statistics should not be over-interpreted as the different screening applied to each algorithm can easily account for these differences, and the screening can easily be changed slightly to improve the statistics or allow more data.

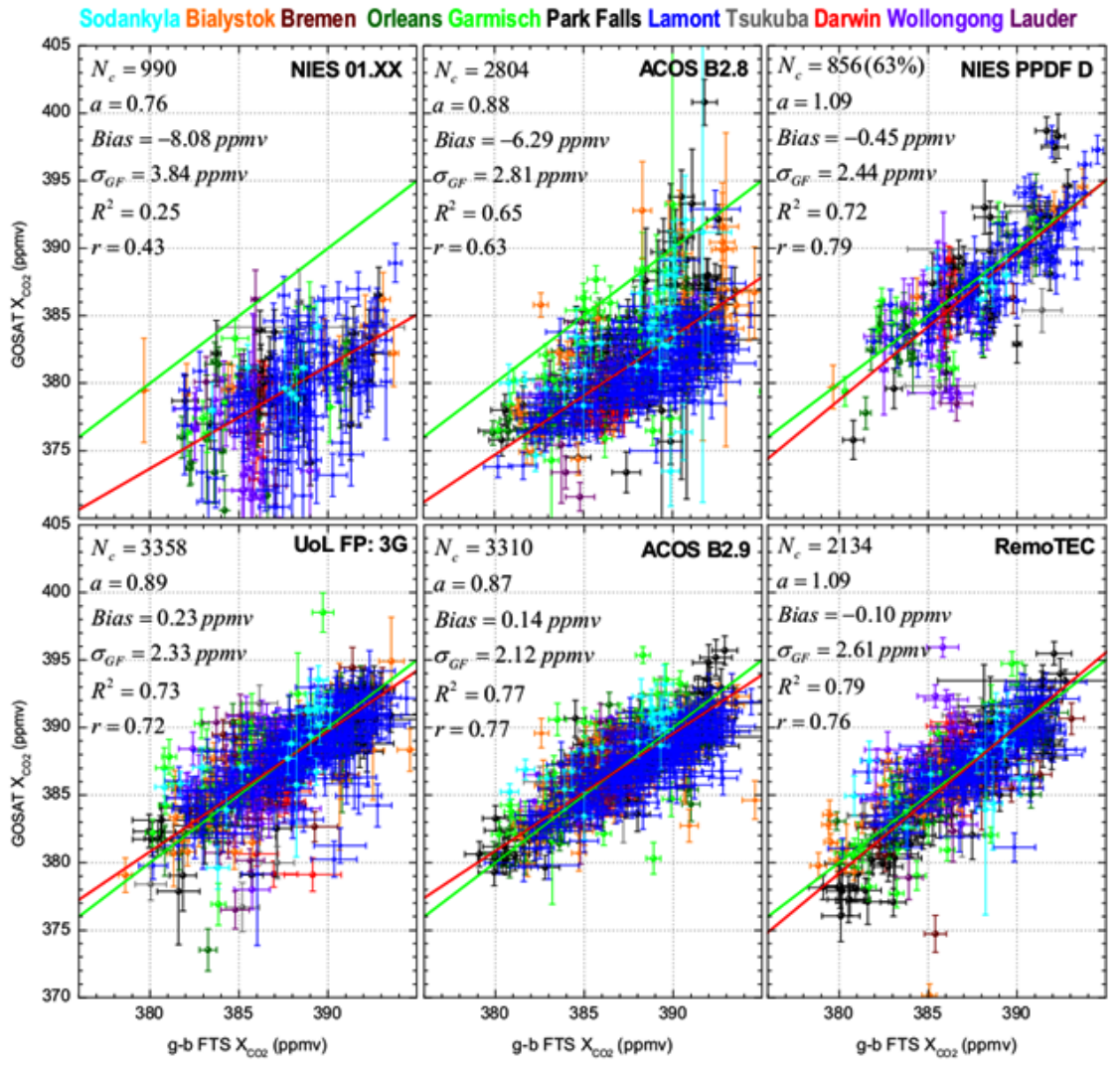

FIGURE 4.19. Correlation diagrams between GOSAT and ground based FTS measurements of X_{CO2} for six algorithms. The GOSAT data were selected within a circle of 5° latitude/longitude radius centered at each FTS station. The X_{CO2} from ground based FTS data were the mean values measured within ± 2 hours (± 1 hour for NIES 01.XX and PPDF D) of GOSAT overpass time and both GOSAT and TCCON data were daily averaged. Red lines correspond to the best fit for all sites and green line is one-to-one correspondence. The number of coincident scans and characteristics of statistical relationships between ground based FTS and GOSAT X_{CO2} are listed in the inserts of each panel.

4.7 Conclusions

X_{CO2} retrievals from GOSAT using the UoL-FP v3G algorithm were performed and show from comparison to ground-based TCCON data that the retrievals have a random error of ∼2.5 ppm, twice the a posteriori error estimate. With stricter screening this precision reduces to ∼1.9 ppm, which should be sufficient to allow improved surface flux estimates (e.g., Chevallier 2007b, Chevallier et al. 2009, Miller et al. 2007).

The mean bias inferred from TCCON comparisons is 0.2 ppm with a station-to-station variation of 0.56 ppm (standard deviation). Thus, over TCCON sites the X_{CO2} retrieval is very accurate with biases approaching only a few tenths of a ppm, which is close to typical retrieval requirements of systematic bias for X_{CO2} (e.g. Chevallier 2007b, Chevallier et al. 2009, Miller et al. 2007). The latest results from other algorithms (Bril et al. 2007, Yokota et al. 2009, Butz et al. 2011, Morino et al. 2011, Wunch et al. 2011b, Yoshida et al. 2010, Crisp et al. 2012, Oshchepkov et al. 2012a) find similar results with a variation in the number of soundings potentially due to the screening criteria applied.

However, over desert regions, which are not observed by TCCON, it is found that the retrieved X_{CO2} from GOSAT shows significant (up to ∼3 ppm) differences when compared to GEOS-Chem model calculations which are believed to be biases in the GOSAT retrieval. Similar findings have been reported in Crisp et al. (2012) who suggested that these biases are related to instrument gain. Although here, biases are observed for desert regions observed with both settings of the gain, leading to the speculation that these biases could be introduced by desert dust or related to the high surface albedo in the CO_2 bands.

This study highlights the need for further algorithm improvements, especially over the deserts, but improvements in instrument calibration or spectroscopy might also lead to reduced biases for these regions. Until sufficient algorithmic improvements have been achieved, one would suggest to either omit X_{CO2} retrievals over deserts or apply the described bias correction method which significantly reduces the biases in our X_{CO2} retrieved over deserts. However, except for the desert regions, the X_{CO2} retrievals approach the point where they should be useful for the inversion of CO_2 surface fluxes with data assimilation methods (e.g. Baker et al. 2010, Chevallier et al. 2009, Feng et al. 2009).

Chapter 5

Developing an Improved Scattering Approach

5.1 Scattering Issue

Clouds and aerosols can cause light to become scattered. This can have a number of effects on a satellite measurement; light can be scattered into and contribute to the observed radiance, light can scatter out of and reduce the observed radiance, and the photon path length of the observed light can be changed. This can lead to biases in the retrieved X_{CO2} and therefore any improvement on the current retrieval scattering approach used would be highly beneficial. This chapter describes the development of a simulator and its use to test a new scattering approach and its comparison to the X_{CO2} retrievals shown in the previous chapter.

5.2 Simulator

5.2.1 Simulator Overview

The UoL-FP Simulator was developed to allow multiple SWIR retrieval approaches to be assessed. Although the simulator has primarily been used to investigate alternative aerosol methods for use in SWIR CO_2 retrievals from GOSAT, it can be applied to many different parameter issues (such as the assessment of the cloud screen, given in Section 3.21). A flexible scheme enables parameters to be selected from various sources, allowing the simulator to be easily modified for other applications. The simulator uses

the UoL-FP retrieval algorithm to simulate spectral radiances based on a priori information of various atmospheric/surface/instrumental parameters that are described in the following sections. An overview of the simulator is given in Figure 5.1, showing the main aspects involved to get from various source data to simulated radiances.

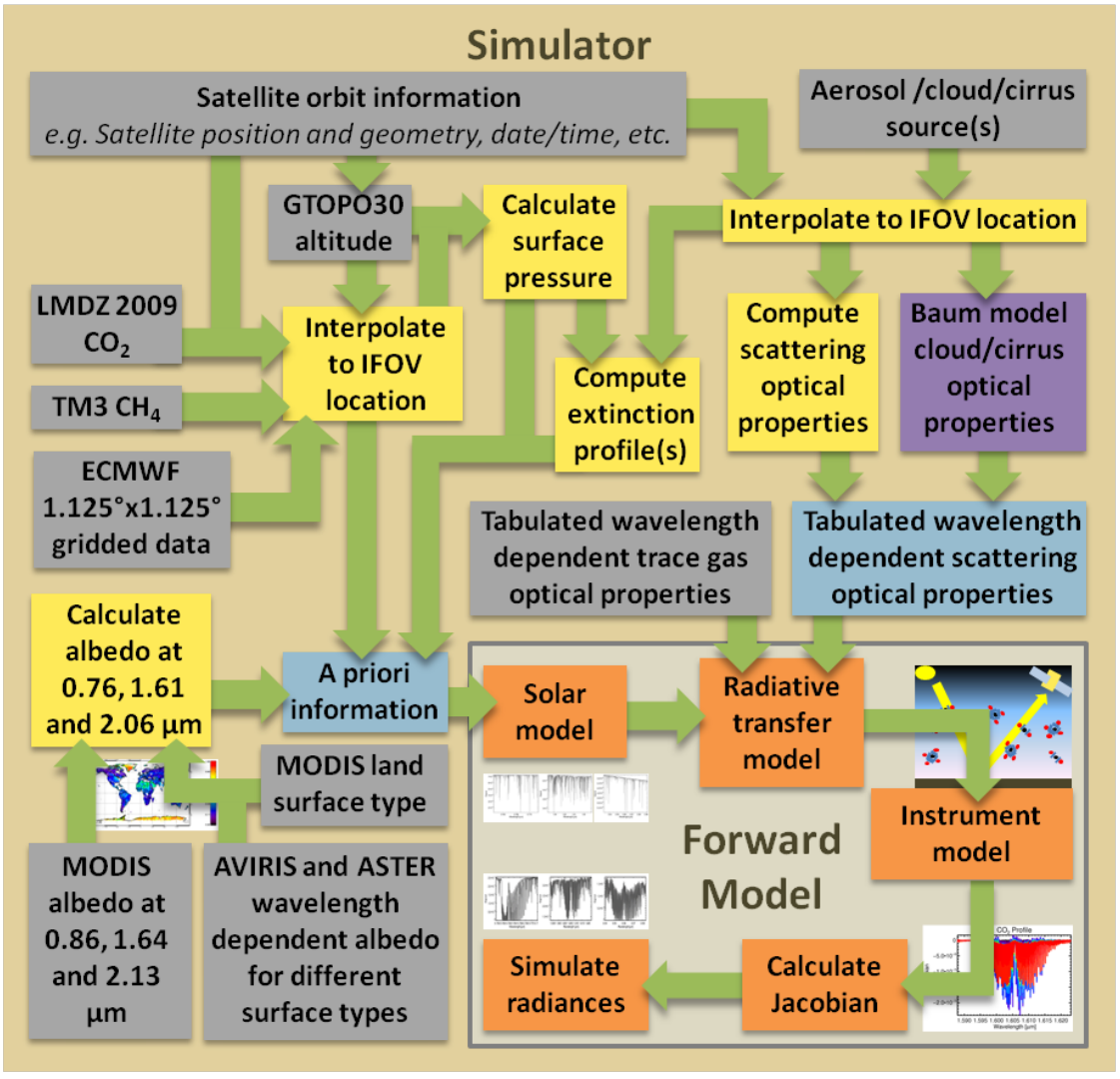

FIGURE 5.1. Diagram showing an overview of the simulator design, with arrows showing the flow of information. Grey boxes represent source data, yellow boxes indicate calculations being performed, purple boxes represent calculated selections of source data, blue boxes show input data for the Foward model, and orange boxes highlight the main computations of the Forward model.

5.2.2 Instrument Inputs

The simulator was designed to allow multiple orbit schemes to be used. This has been utilised to simulate spectral radiances for GOSAT orbits for two 3-day repeat cycles as well as Cloud-Aerosol Lidar and Infrared Pathfinder Satellite Observations (CALIPSO) orbits for a six day period, although the flexibity could allow alternative observations to be simulated. The parameters for the orbits of GOSAT are obtained from pre-processed GOSAT L1B data, see Chapter 3. This includes the satellite position, solar and observing angles, relative velocity, altitude and observed IFOV location.

To simulate a CALIPSO orbit, these parameters are obtained directly from CALIPSO Level 1 data, but the retrieval algorithm remains setup for GOSAT observations such that GOSAT observations are simulated but for a CALIPSO orbit path. Similarly, the spectral dispersion is currently designed for the GOSAT SWIR bands with the GOSAT spectral resolution of 0.2 cm^{-1}. The same dispersion for each band is used for every simulation to reduce any uncertainties this could potentially introduce.

The noise is derived as a function of the spectral signal using a modelled function derived from real GOSAT high gain measurements. Equation 5.1 defines the function and Table 5.1 gives the coefficients derived by comparing noise, N, with signal, S, from pre-processed GOSAT L1B data for August 2009, as shown in Figure 5.2.

$$N = A\mathrm{S} + B \tag{5.1}$$

Table 5.1. GOSAT noise model coefficients.

GOSAT Band	A	B
1	0.0046960347	1.1245479E-09
2	0.0025181001	6.1902212E-10
3	0.0045985506	3.8230411E-10

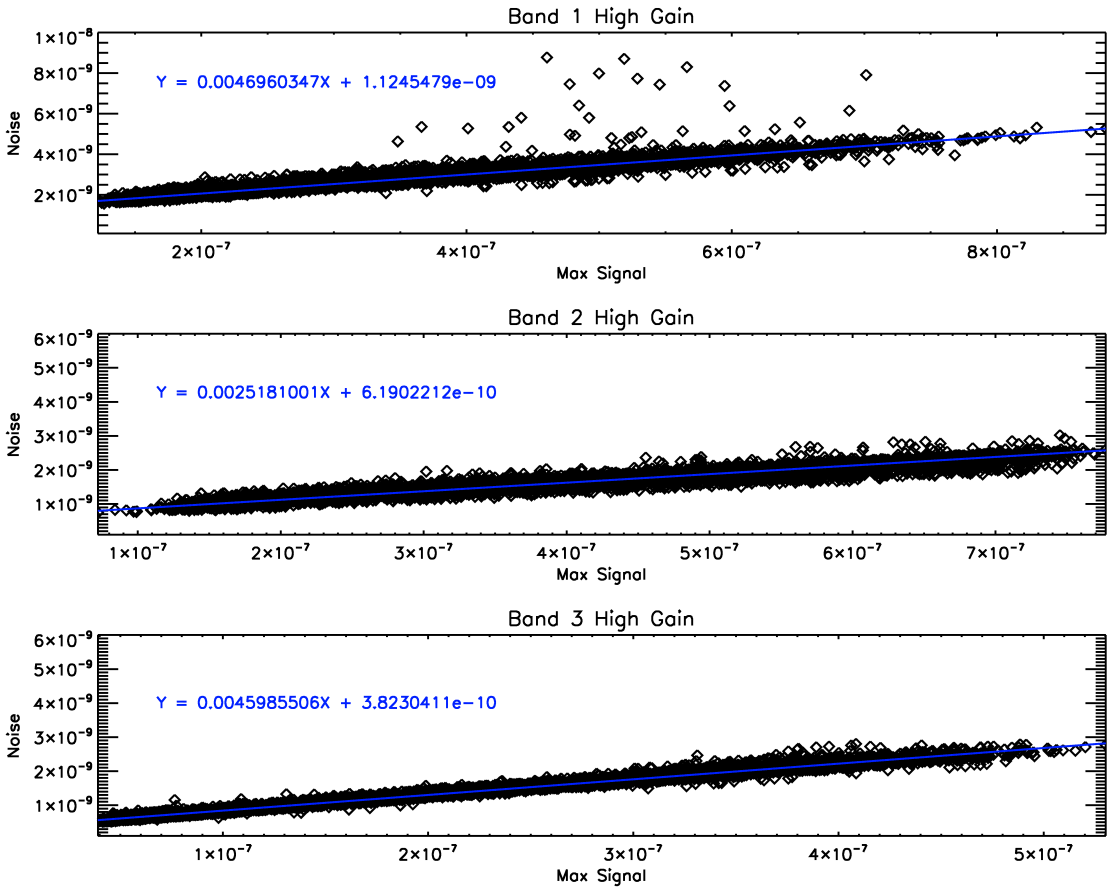

FIGURE 5.2. Correlation of real GOSAT noise and signal for August 2009 with the post-screen applied. A linear fit of the correlation is shown in blue with the equation of the fit giving the coefficients to be used in the GOSAT noise model.

5.2.3 Radiative Transfer Inputs

5.2.3.1 Atmospheric Parameters

The atmospheric temperature, pressure and water vapour are derived from ECMWF operational analysis data. The atmospheric CO_2 is obtained from LMDZ 2009 data and CH_4 from the TM3 model. All these parameters are derived using the same method as described in Chapter 3.

5.2.3.2 Surface Parameters

The albedo is generated from MODIS Level 3 16-day average global albedo data at 0.8585 μm, 1.6400 μm and 2.1300 μm. These wavelengths were selected as they are reasonably close in wavelength to the three GOSAT SWIR wavelengths; 0.765 μm, 1.61 μm and 2.06 μm. The albedo for these three GOSAT bands are derived using the corresponding wavelength MODIS albedos as well as spectral dependence data from the Airborne Visible InfraRed Imaging Spectrometer (AVIRIS) and the Advanced Spaceborne Thermal Emission and Reflection radiometer (ASTER) for different surface types, as defined in Table 5.2. MODIS Level 3 land cover data provides a global dataset of surface/biome types, allowing each MODIS grid cell (0.05° x 0.05°) to have its albedo derived using the corresponding spectral dependance from either AVIRIS or ASTER. The spectral dependence for each surface type is shown in Figure 5.3. The spectral dependence, β, is interpolated to the wavelength of MODIS and that of the desired GOSAT wavelength, λ. This provides a wavelength dependent ratio that is applied to the MODIS albedo to get the albedo at the desired wavelength, as given by Equation 5.2. For simplicity, the albedo slope was assumed flat within each band. Figures 5.4, 5.5 and 5.6 show the derived albedo globally for each GOSAT SWIR band using this method for two 3-day repeat orbit cycles of GOSAT.

$$Albedo_{\lambda} = \frac{Albedo_{MODIS}\beta_{\lambda}}{\beta_{MODIS}} \tag{5.2}$$

Table 5.2. Spectral dependence source for each MODIS surface type.

MODIS Surface Type	Spectral Dependency Source
Water	Assumed constant albedo
Evergreen needleleaf forest	AVIRIS: Evergreen needleleaf forest
Evergreen broadleaf forest	AVIRIS: Evergreen broadleaf forest
Deciduous needleleaf forest	AVIRIS: Deciduous needleleaf forest
Deciduous needleleaf forest	AVIRIS: Deciduous broadleaf forest
Mixed forests	AVIRIS: Mixed forest
Closed shrubland	AVIRIS: Closed shrubs
Open shrubland	AVIRIS: Open shrubs
Woody savannas	AVIRIS: Woody savanna
Savannas	AVIRIS: Savanna
Grasslands	AVIRIS: Grassland
Permanent wetlands	AVIRIS: Wetlands
Croplands	AVIRIS: Croplands
Urban and built-up	ASTER: Urban Scenario
Cropland/natural vegetated mosaic	AVIRIS: Croplands
Snow and ice	ASTER: Medium Snow
Barren or sparsely vegetated	AVIRIS: Bare
Unknown	Assumed constant albedo

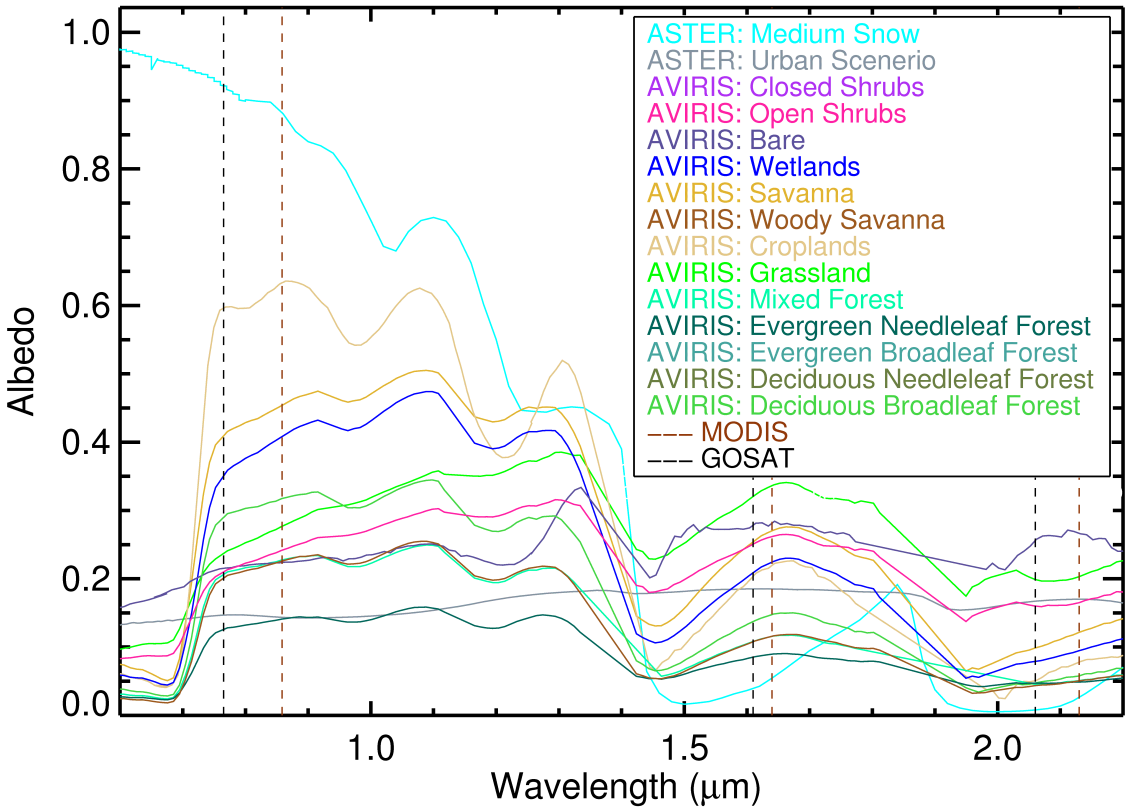

FIGURE 5.3. Spectral dependence for the different surface types used from AVIRIS and ASTER with vertical lines giving MODIS and GOSAT wavelengths used in the albedo method.

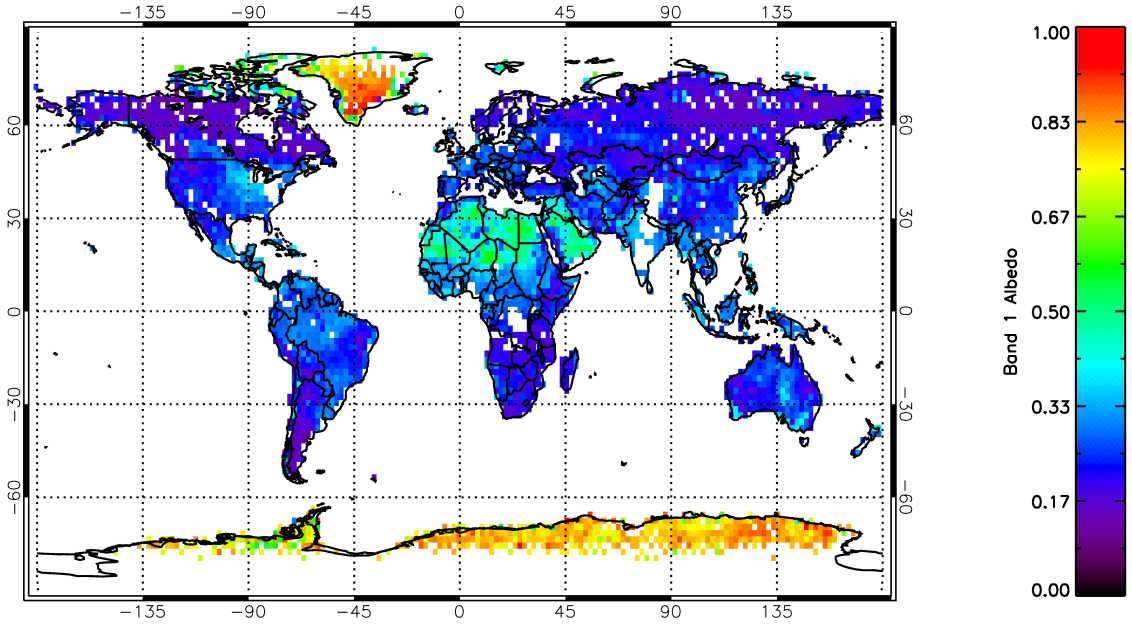

FIGURE 5.4. Derived Albedo for GOSAT band 1 for two 3-day GOSAT repeat orbit cycles averaged into 5°x5° grid cells.

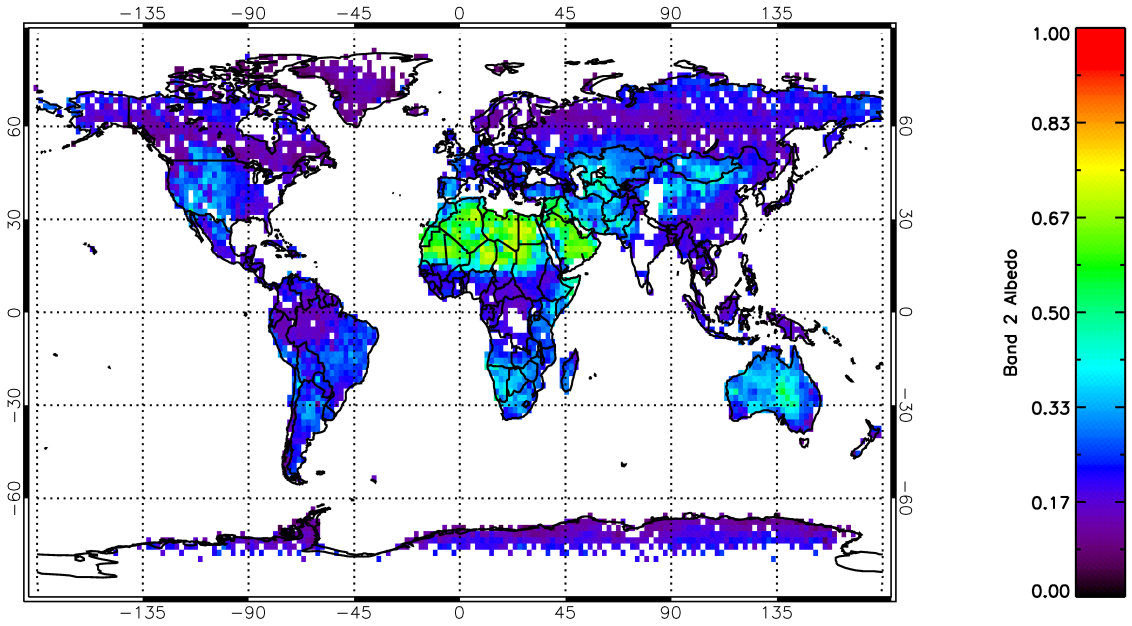

FIGURE 5.5. Derived Albedo for GOSAT band 2 for two 3-day GOSAT repeat orbit cycles averaged into 5°x5° grid cells.

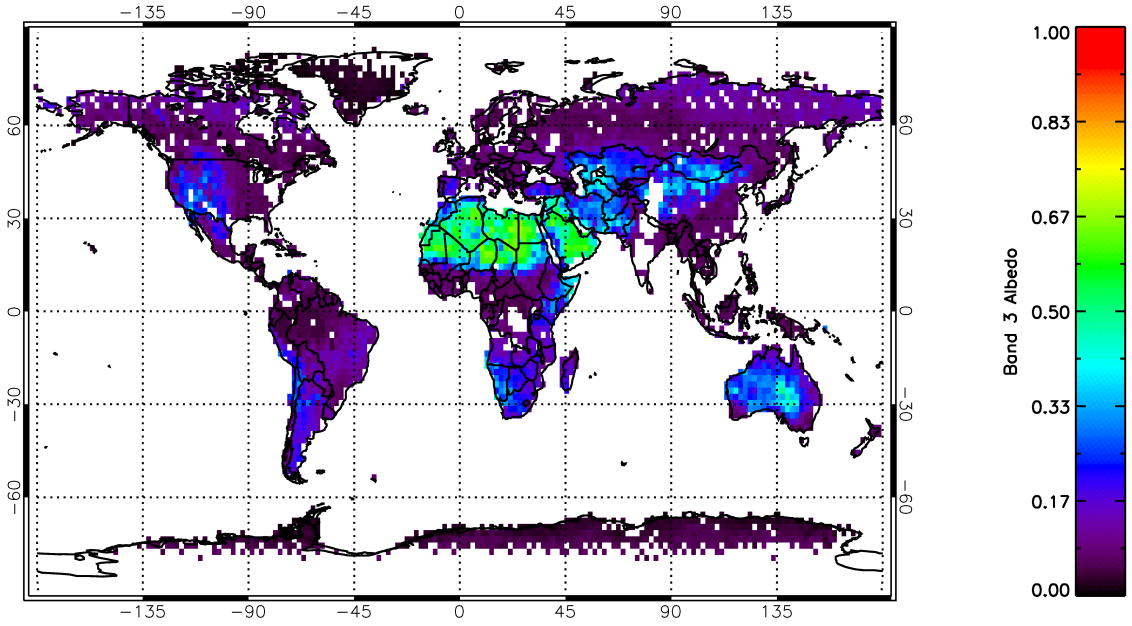

FIGURE 5.6. Derived Albedo for GOSAT band 3 for two 3-day GOSAT repeat orbit cycles averaged into 5°x5° grid cells.

5.2.3.3 GEMS Scattering Parameters

The GEMS model (experiment f1kd until October 2009 and f93i afterwards) provides mass mixing ratio profiles (MMR) for eleven different aerosol types, ice water content (IWC) MMR profiles and liquid water content (LWC) MMR profiles on 60 sigma levels every twelve hours at 00:00 and 12:00, with a model forecast every three hours proceeding an analysis. However, to reduce computational time only data for every six hours was used. These sigma levels are converted to pressure layers, P_{Layer}, using coefficients A and B (provided by GEMS) and the surface pressure, P, as

$$P_{\text{Layer}} = A_{\text{Layer}} + B_{\text{Layer}}P \tag{5.3}$$

The pressure levels are determined by taking the middle pressure between layer pressures. The MMR data are interpolated to each simulated observation location and time using the four closest grid points for the two closest six hour intervals. The extinction for each aerosol can then be derived from the MMR (Knappett 2012, Simmons 2010) by

$$E = \frac{\mu\zeta}{g} \tag{5.4}$$

where E is the extinction, ζ is the MMR, g (gravity) is defined as 9.80665 and μ is the mass extinction coefficient (MEC) for GEMS aerosols interpolated to the relative humidity and O_2 A band wavelength, see Figure 5.7. The relative humidity was derived from the ECMWF specific humidity, S, by

$$RH = \frac{p_{H2O}}{p_{Liquid}} * 100 \tag{5.5}$$

where RH is the relative humidity, p_{Liquid} is the saturated vapour pressure and p_{H2O} is the partial pressure of water vapour which can be derived to be

$$p_{H2O} = \frac{SPM_{AIR}}{M_{H2O}} \tag{5.6}$$

The molecular mass of air, M_{AIR}, and of H_2O, M_{H2O}, is assumed to be 28.97 g mol^{-1} and 18.015422 g mol^{-1} respectively. There are numerous ways to estimate the saturated vapour pressure (Murphy & Koop 2005) but the method described by Murphy & Koop (2005) currently provides the most suitable function throughout normal atmospheric tem-

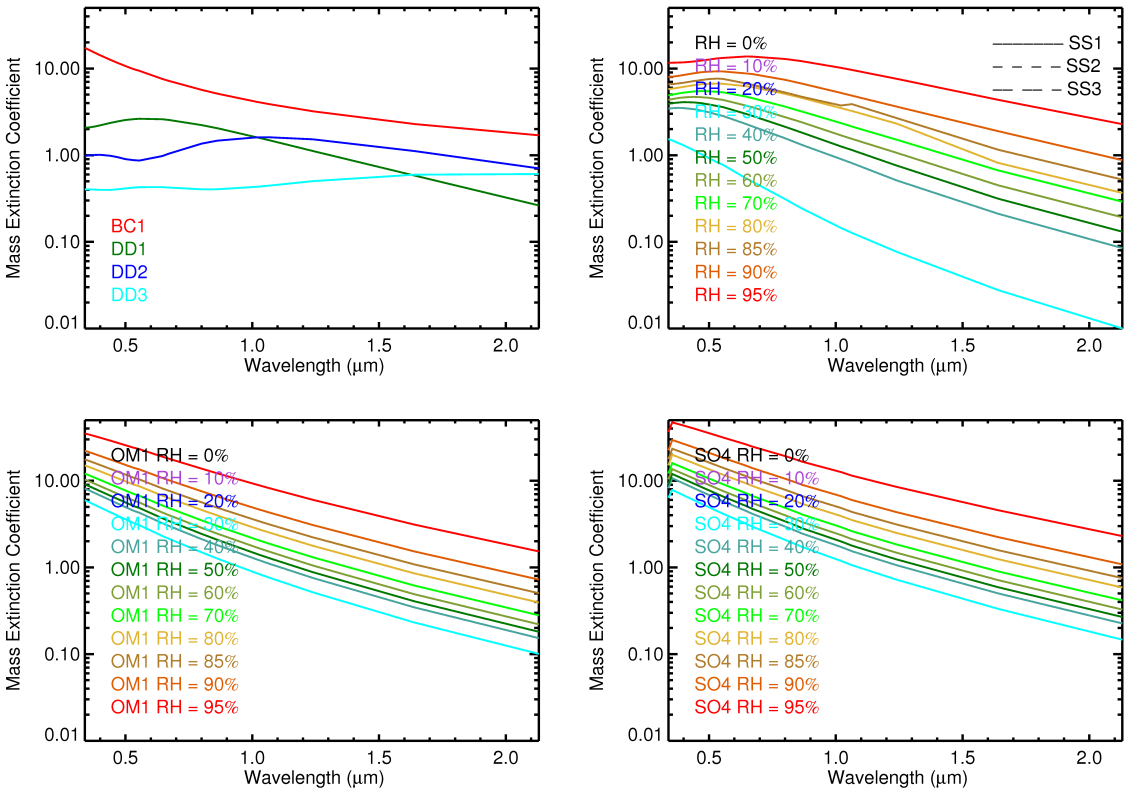

FIGURE 5.7. Mass extinction coefficients (MEC) for each of the GEMS aerosol types (Benedetti 2010). Black carbon (BC1) and desert dust aerosols (DD1, DD2 and DD3) are assumed to be independent of humidity (top left), with hydrophilic and hydrophobic black carbon having the same MEC. Organic matter (bottom left), sea salt (top right) and Sulphate (bottom right) (OM1, SS1/SS2/SS3, and SO4) are assumed to be humidity dependent.

perature ranges as well as for supercooled water.

$$\ln(p_{\text{Liquid}}) \approx 54842763 - \frac{6763.22}{T} - 4.210\ln(T) + 0.000367T + \tanh[0.0415(T - 218.8)] \left(53.878 - \frac{1331.22}{T} - 9.44523\ln(T) + 0.014025T\right) \quad (5.7)$$

The average extinction between layers is assumed as the extinction for each level with the top and bottom levels assumed to have half of the closest layers extinction. To verify that this method of calculating the extinction is approximately correct, it was computed for a wavelength of 0.55 μm and compared to the GEMS AOD product at 0.55 μm. This is shown in Figure 5.8 and proves to correlate well with some slight scatter. Note that

the AOD, τ, was calculated by

$$\tau = \frac{E_i + E_{i+1}}{2} |P_i - P_{i+1}| \tag{5.8}$$

where E is the extinction, P is the pressure and i represents the atmospheric level. The

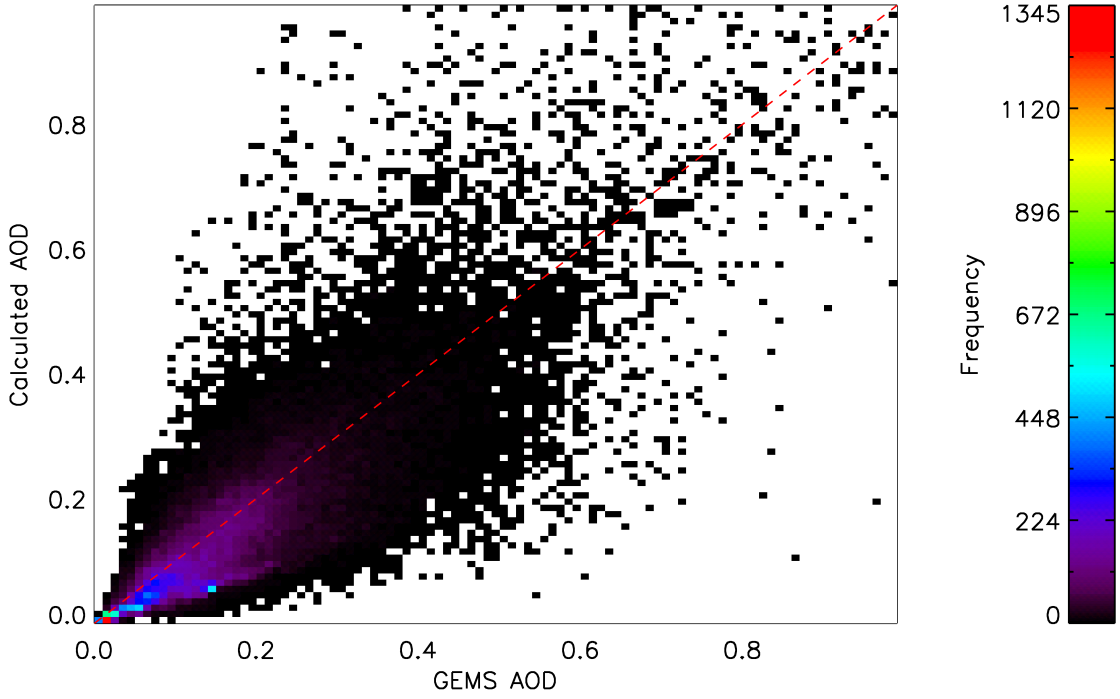

FIGURE 5.8. Comparison of the GEMS AOD 0.55 μm product with the calculated AOD, where the GEMS AOD has been interpolated with latitude, longitude and time to the simulated observations.

extinction profiles for ice and liquid clouds are calculated using the method by Slingo & Schrecker (1982),

$$E = \frac{3\zeta}{2R_{eff}\rho} \frac{RT}{MgP} \tag{5.9}$$

where the effective radius is given by R_{eff}, ρ is the density (assumed 0.92 for ice and 1 for liquid), R is the ideal gas constant, and the second term on the right hand side is added to convert from altitude layers to pressure layers. The effective radius of liquid cloud particles was calculated using the Liu & Daum (2000) method. This is given as

$$R_{eff} = 0.13 \left(\frac{3RT}{4\pi MP} \right)^{\frac{1}{3}} \left(\frac{\zeta}{N} \right)^{\frac{1}{3}-0.11} \tag{5.10}$$

where N is 600 cm^{-1} over land. The method for the ice effective radius is taken from Sun & Rikus (1999) and is given as

$$R_{eff} = \frac{1}{2}\left[\frac{3\sqrt{3}}{8}\left(45.8966\zeta^{0.2214} + \left(0.7957\zeta^{0.2535}T - 83.15\right)\right)\right.$$
$$\left.(1.2351 + (0.0105T - 273.15))\right] \tag{5.11}$$

where T is the layer temperature. Similarly, the extinction is converted from layers to levels. Not only are the effective radii used within the extinction calculation, but the effective radii at the pressure level where the maximum ice/liquid cloud extinction exists, hence cloud height, is used to define the ice/liquid cloud scattering properties within the retrieval. Ice and liquid cloud scattering properties were obtained from the Baum model (Baum et al. 2005a,b) for different effective radii; every 5 μm between 10 to 90 μm for ice cloud particles and every 1 μm between 4 and 64 μm for liquid cloud particles. For each simulation the Baum model scattering properties with the effective radii closest to that calculated from GEMS was used.

To check the simulated optical depths and effective radii provide an approximation of the real world they have been compared to the MODIS TERRA Level 3 daily product. A comparison of the AOD, given in Figure 5.9, shows that both the magnitude and spatial distribution are very similar, which was expected since GEMS assimilates MODIS AOD. Some difference are, however, expected due to the humidity being different. The calculated GEMS cloud and cirrus optical depths show a similar spatial pattern, see Figure 5.10. Although, MODIS gives much higher values over the poles, few GOSAT soundings will be observed at these latitudes and those that are will get screened out. The magnitude of the cloud/cirrus optical depths are on average lower in GEMS than MODIS. Figure 5.11 shows the effective radii of cloud/cirrus for GEMS and MODIS. The GEMS water cloud effective radii have a similar spatial distribution and magnitude as MODIS, although some differences can be seen over Siberia, the Himalayas, and the south of the Indian Ocean. The GEMS cirrus cloud effective radii have a similar magnitude on average, but are clearly lower than MODIS around the equator. Although some differences exist between GEMS and MODIS the parameters still provide a range of reasonable values. Since these differences are specific to cloud/cirrus, the effect is small as most cloudy scenes will be filtered out by a cloud screen.

Although the ice and liquid cloud properties were obtained from the Baum model, the aerosol properties were derived from refractive index (RI) values and assumptions of the GEMS aerosol sizes and modes (Benedetti 2010). However, the GEMS model is

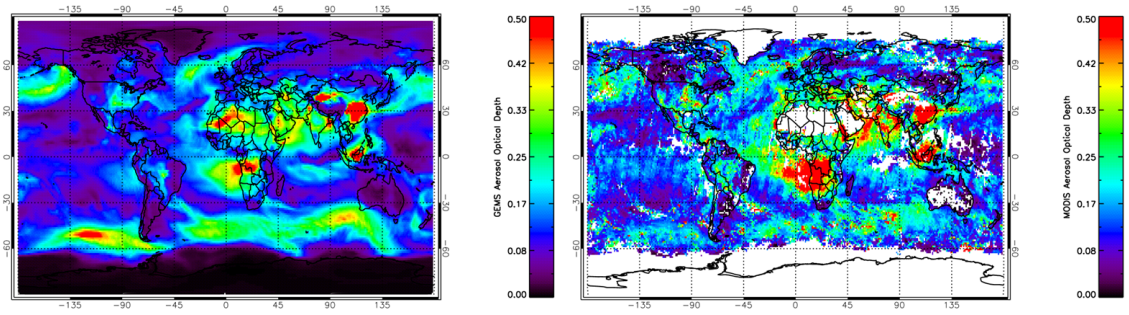

FIGURE 5.9. Comparison of calculated mean GEMS AOD (left) for all 6 hour time frames and MODIS mean daily AOD (right) between 08/09/2009 and 14/09/2009. Areas where no valid data exists is given by white.

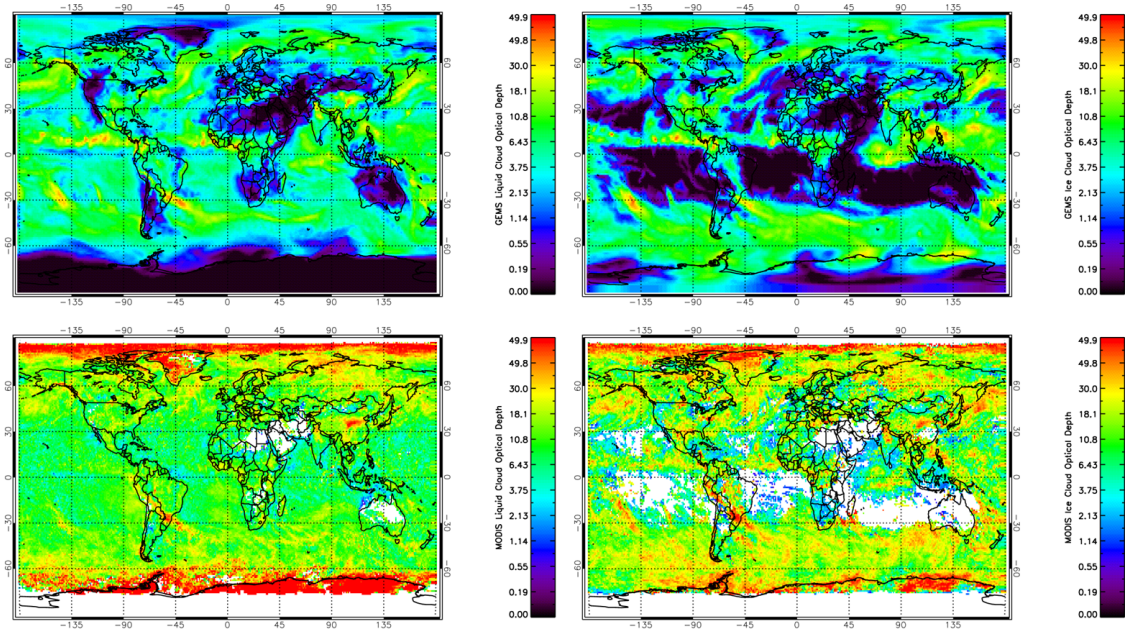

FIGURE 5.10. Comparison of calculated mean GEMS liquid cloud (top left) and ice cloud (top right) optical depth for all 6 hour time frames and MODIS mean daily liquid cloud (bottom left) and ice cloud (bottom right) optical depth between 08/09/2009 and 14/09/2009. Areas where no valid data exists is given by white.

known to include spin-down effects mainly in the dust but also in all other aerosol types (Morcrette 2012). This leads to the model overestimating the amount of small desert dust particles and underestimating the amount of large desert dust particles (Morcrette 2012). To compensate for this issue, the small and medium GEMS desert dust aerosols sizes were replaced with accumulation mode desert dust particle sizes and the large GEMS desert dust replaced by the coarse desert dust particle sizes from the climatology of

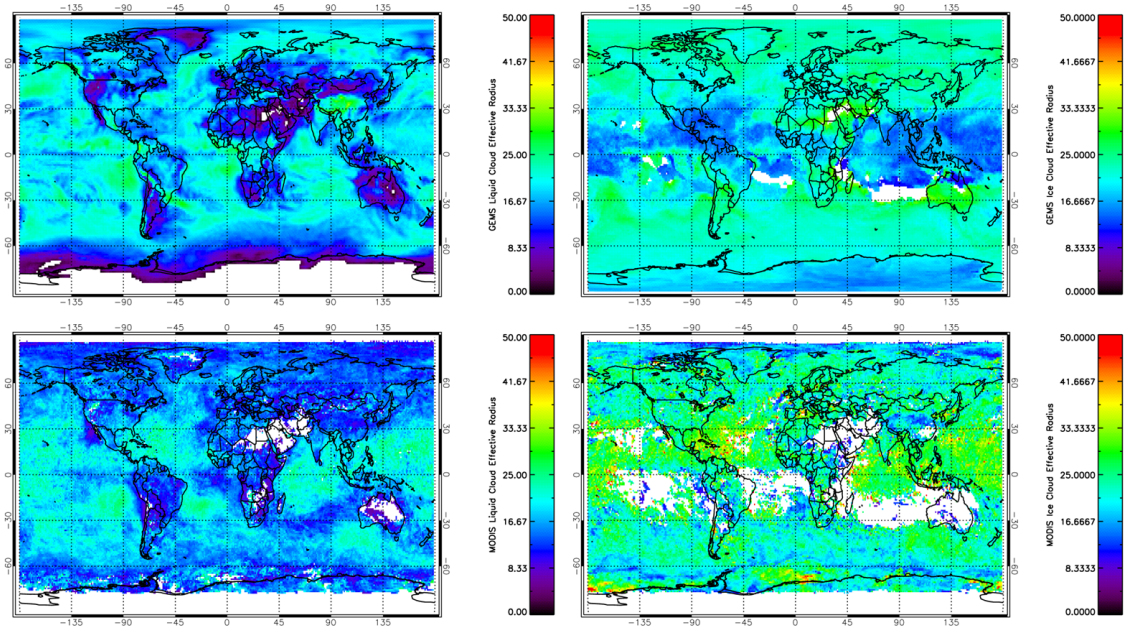

FIGURE 5.11. Comparison of calculated mean GEMS liquid cloud (top left) and ice cloud (top right) effective radius for all 6 hour time frames and MODIS mean daily liquid cloud (bottom left) and ice cloud (bottom right) effective radius between 08/09/2009 and 14/09/2009. The effective radii at the atmospheric level where the highest extinction exists is used for GEMS. Similarly, the MODIS retrieved effective radii is most sensitive within the cloud/cirrus. Areas where no valid data exists is given by white.

Kahn et al. (2001), such that the desert dust aerosols have larger sizes. The organic matter, black carbon and sulphate aerosols were replaced by the equivilent aerosol sizes from the Kahn et al. (2001) climatology which have less extreme sizes. The sea salt aerosols were kept as the GEMS sizes as the quantity of these aerosols over land is much smaller.

The RI of sulphate and sea salt were calculated by interpolating RI values from Hale & Querry (1973) between 0.2 and 0.7 mm, Palmer & Williams (1974) between 0.7 and 2.0 mm and Downing & Williams (1975) between 2.0 and 1000 mm. Additionally, Tang & Munkelwitz (1991) RI of 1.330 at 0.633 mm was used as the reference standard and Kou et al. (1993) data was used for the imaginary RI between 0.7 and 2.7 mm. These RI were computed for a humidity of 50% by spectrally interpolating between the RI of the dry aerosols and the RI of water using formulas which were derived from accurate laboratory measurements (Tang & Munkelwitz 1991, 1994, 1996) of the change in RI with relative humidity of those aerosols (Lacis 2010).

The RI for hydrophobic and hydrophilic organic matter were obtained from Dick

et al. (2007) for a humidity of $4-10\%$ and $44-76\%$, respectively. The RI for dust and soot were taken from Shettle & Fenn (1979) and are not humidity dependant. Using these RI values (shown in Figures 5.12 and 5.13) and the assumed sizes and modes given in Table 5.3, the phase function moments, geometric cross-section, extinction and scattering cross-sections and asymmetry parameter for each aerosol were computed using the Mie code of Mishchenko et al. (2002). This computes the scattering of light by polydisperse homogeneous spherical particles using Lorenz-Mie scattering (Mishchenko et al. 1999). The radius standard deviation gives a measure of the width of the size distribution around the effective radius, with the minimum and maximum radius providing the limits. All GEMS aerosols are approximated with a log normal size distribution (Benedetti 2010) that can be expressed as

$$n\left(r\right) = \text{constant} \times r^{-1}\text{exp}\left[-\frac{\left(\ln r - \ln r_g\right)^2}{2\ln^2 \sigma_g}\right] \tag{5.12}$$

where r is the radius, r_g is the geometric radius and σ_g is the standard deviation of the radius. Using a range of sizes provides a polydisperse distribution which is more realistic than a monodisperse sample since aerosols are highly variable in size (Williams et al. 2002). However, the desert dust types based on Kahn et al. (2001) are obtained (courtesy of V. Natraj) from the OCO orbit simulator (O'Brien et al. 2009) which computes these aerosols as polydisperse non-spherical homogenous particles.

The properties for the two log-normal size distribution modes (a and b) were combined for each sea salt size using the method by Abdou et al. (1997). The two modes are assumed equally weighted, such that the mean of the modes is used for the extinction cross-section, scattering cross-section, geometric cross-section and asymmetry parameter. The phase function, P, can be given by

$$P\left(\Omega,\lambda\right) = \frac{P_a\omega_a}{\omega_a+\omega_b} + \frac{P_b\omega_b}{\omega_a+\omega_b} \tag{5.13}$$

where λ is the minimum and maximum wavelengths for each GOSAT SWIR band, Ω is the scattering angle and ω is the single scattering albedo. Note that the asymmetry parameter gives an indication of the scattering direction, where a value of -1 gives a strong backwards directed peak and 1 gives a strong forward directed peak. Figure 5.14 shows the key derived properties for the eleven aerosols. It gives the asymmetry parameter for each of the eleven aerosols, showing that all aerosols scatter strongly forward at the O_2 A band wavelength and smaller aerosols have a weaker forward scattering peak with increasing wavelength. The angstrom coefficient was calculated from the extinction cross

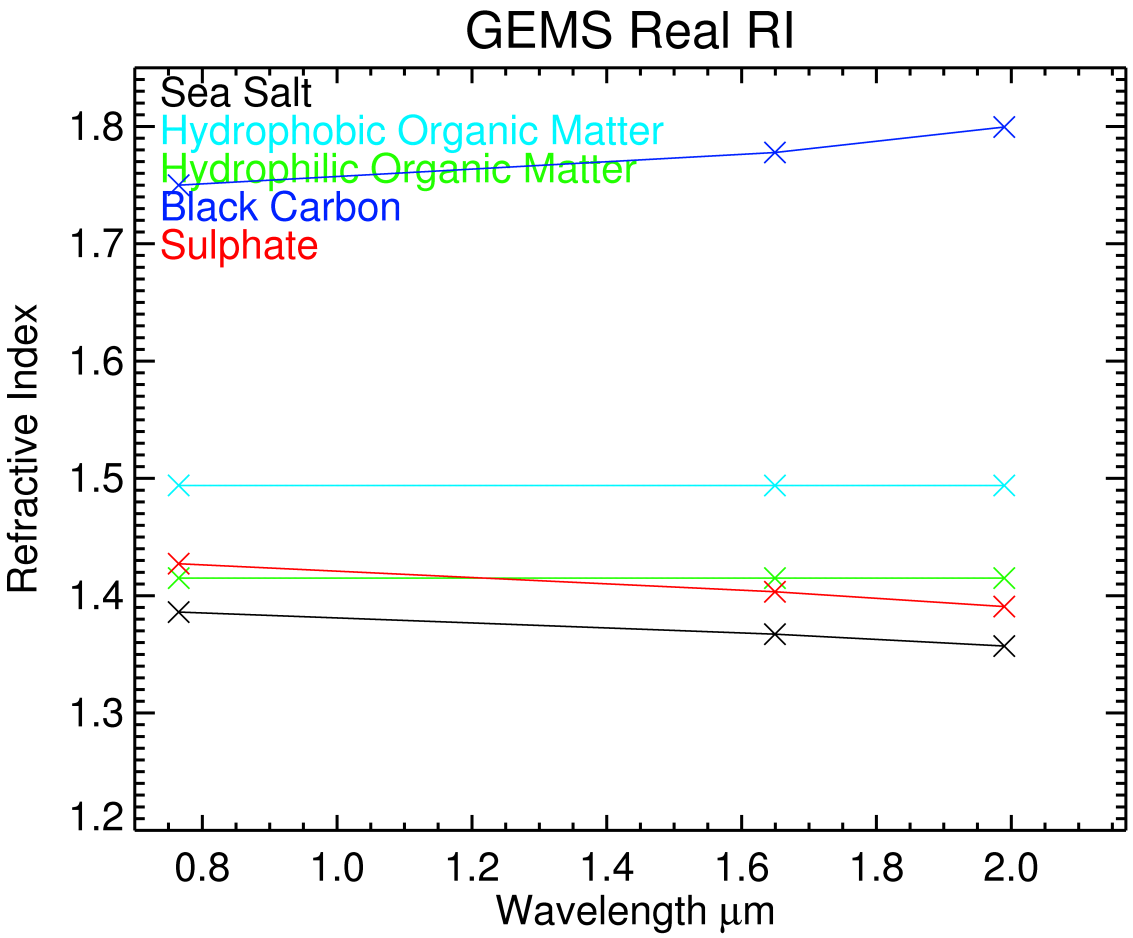

FIGURE 5.12. Assumed refractive index real values for the GEMS aerosol types.

section, C_{ext}, at different wavelengths by

$$\alpha = \frac{\ln\left(\frac{C_{ext_\lambda}}{C_{ext_{\lambda r}}}\right)}{\ln\left(\frac{\lambda_r}{\lambda}\right)} \tag{5.14}$$

where λ_r is the reference wavelength (in this case at the O_2 A band) and λ is the wavelength of the other bound that the angstrom coefficient is to be calculated between. Note that the angstrom coefficients are lower for larger particles. The ability of each aerosol to absorb or scatter light is shown by the single scattering albedo, which is simply the ratio:

$$\omega = \frac{C_{sca}}{C_{ext}} \tag{5.15}$$

where C_{sca} represents the scattering cross section. Black carbon has a low single scattering albedo, so is much more absorbing than the other aerosol types.

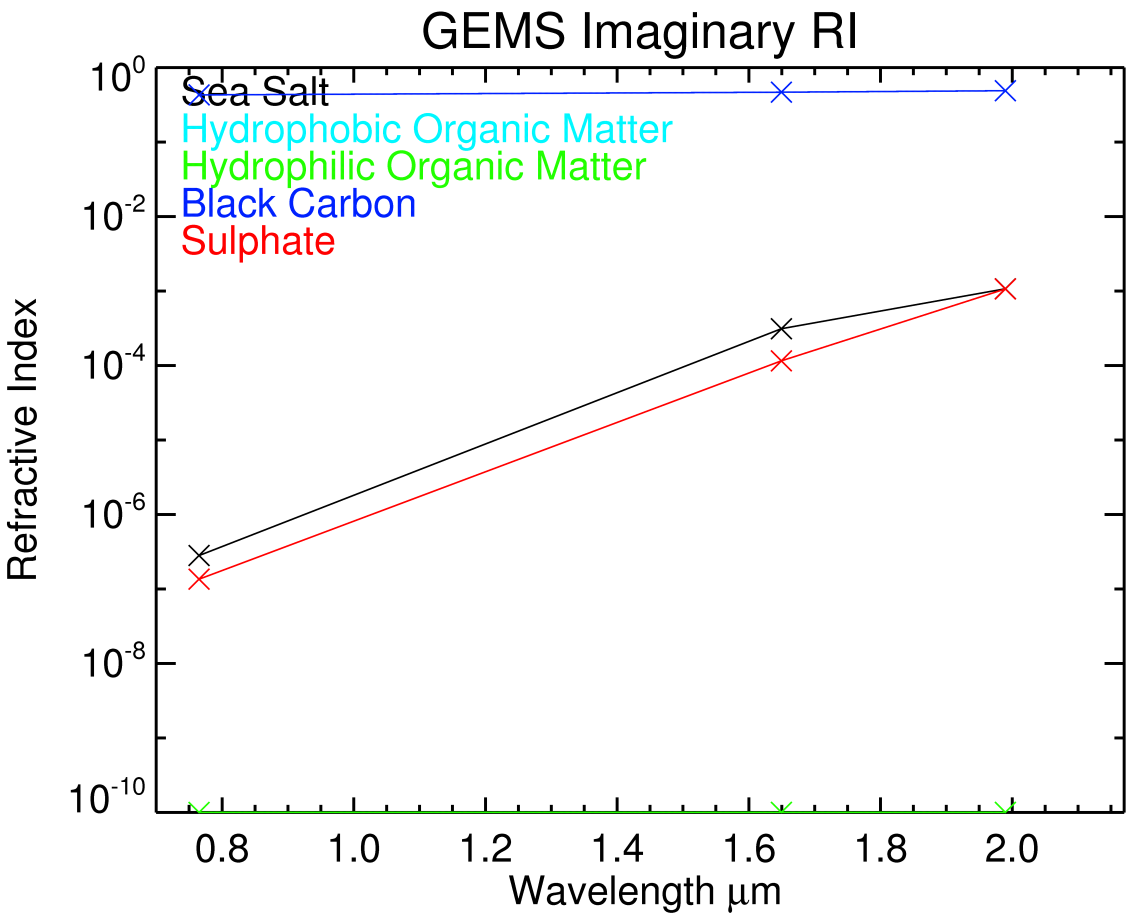

FIGURE 5.13. Assumed refractive index imaginary values for the GEMS aerosol types.

The phase function of each aerosol type is given at each GOSAT band in Figures 5.15, 5.16, and 5.17, showing the scattering amount from a forward to backward direction. Both dust types scatter strongly in the forward direction with a slight backwards peak. Accumulation dust differs from coarse dust in the CO_2 bands with a reduced backwards peak. Sea-salt mostly scatters light in a forward direction with a minor backwards peak and changes little between bands. The other aerosols all give similar scattering directions of a weaker forward peak that reduces with increasing wavelength.

Table 5.3. Aerosol sizes corresponding to the 11 GEMS aerosols (Benedetti 2010).

Aerosol	Abbreviation	Effective Radius	Radius Standard Deviation	Minimum Radius	Maximum Radius
Small Sea Salt (mode a)	SS1a	0.1992	1.90	0.0300	0.50
Medium Sea Salt (mode a)	SS2a	0.1992	1.90	0.5000	5.00
Large Sea Salt (mode a)	SS3a	0.1992	1.90	5.0000	20.00
Small Sea Salt (mode b)	SS1b	0.1992	2.00	0.0300	0.50
Medium Sea Salt (mode b)	SS2b	0.1992	2.00	0.5000	5.00
Large Sea Salt (mode b)	SS3b	0.1992	2.00	5.0000	20.00
Small Desert Dust †‡	DD1	0.47	2.60	0.0500	2.00
Medium Desert Dust †‡	DD2	0.47	2.60	0.0500	2.00
Large Desert Dust †‡	DD3	1.90	2.60	0.5000	15.00
Hydrophobic Organic Matter †§	OM1	0.13	1.80	0.0070	2.00
Hydrophilic Organic Matter †	OM2	0.124	1.80	0.0067	1.90
Hydrophobic Black Carbon †	BC1	0.1180	2.00	0.0050	0.50
Hydrophilic Black Carbon †*	BC2	0.14396	2.00	0.0061	0.61
Sulphate †	SO4	0.08	1.88	0.0070	0.81

† Kahn et al. (2001) aerosol sizes used.

‡ Non-spherical aerosol (other aerosols are spherical).

* Hydrophilic black carbon was assumed a growth factor of 1.22 (Popovicheva et al. 2008).

§ Hydrophilic organic matter was assumed a growth factor of 1.05 (Malm et al. 2005), but since the Kahn et al. (2001) organic matter is given as hydrophilic, the sizes were scaled down by one over the growth factor to get the corresponding hydrophobic organic matter sizes.

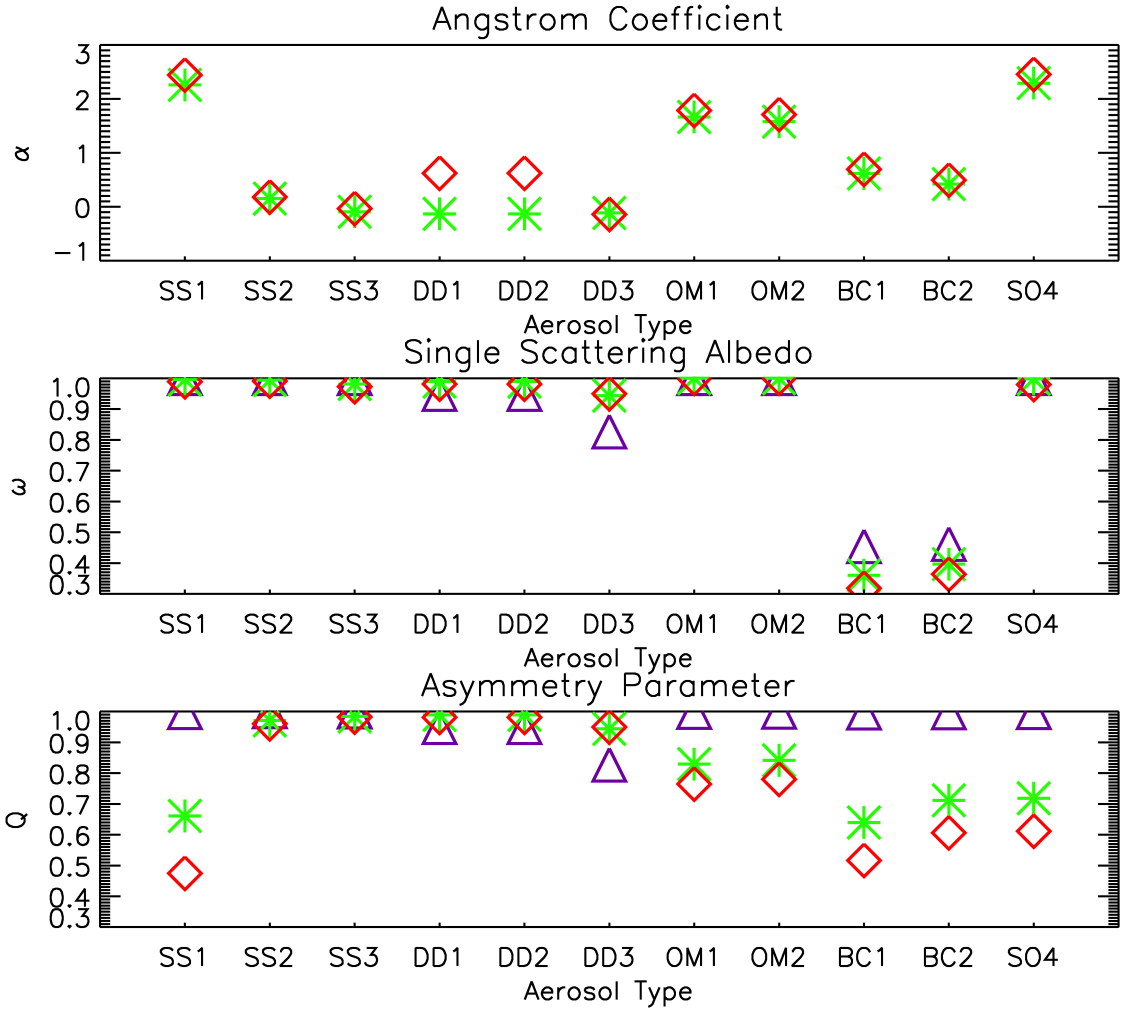

FIGURE 5.14. Derived aerosol properties for each GEMS aerosol type for the start wavelength of each GOSAT SWIR band. The angstrom coefficient between bands 1 and 2 is given by the green stars and the angstrom coefficient between bands 2 and 3 is given by the red diamonds. For both the single scattering albedo and the asymmetry parameter band 1 is given by the purple triangles, band 2 by the green stars and band 3 by the red diamonds.

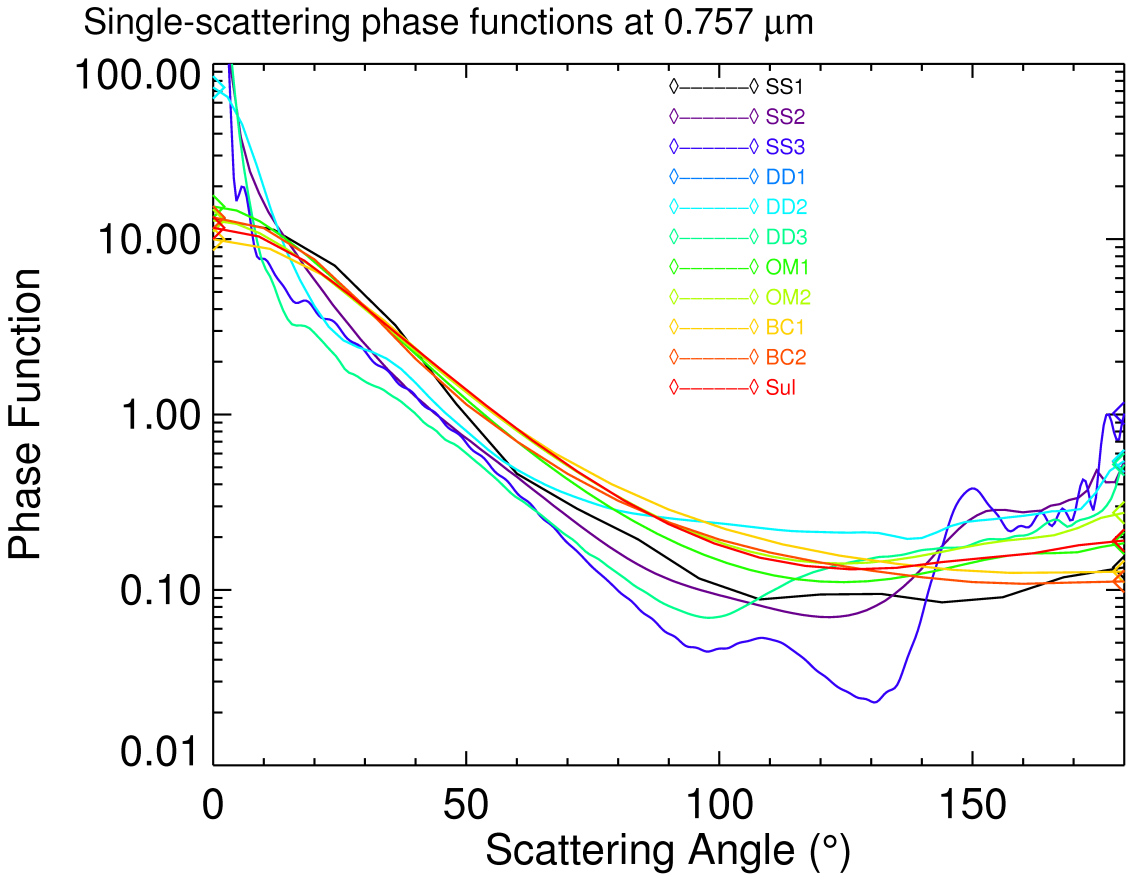

FIGURE 5.15. Derived phase function moments for the start wavelength of GOSAT band 1 as a function of scattering angle for each of the eleven GEMS aerosol types. An angle of zero points directly in the forward direction.

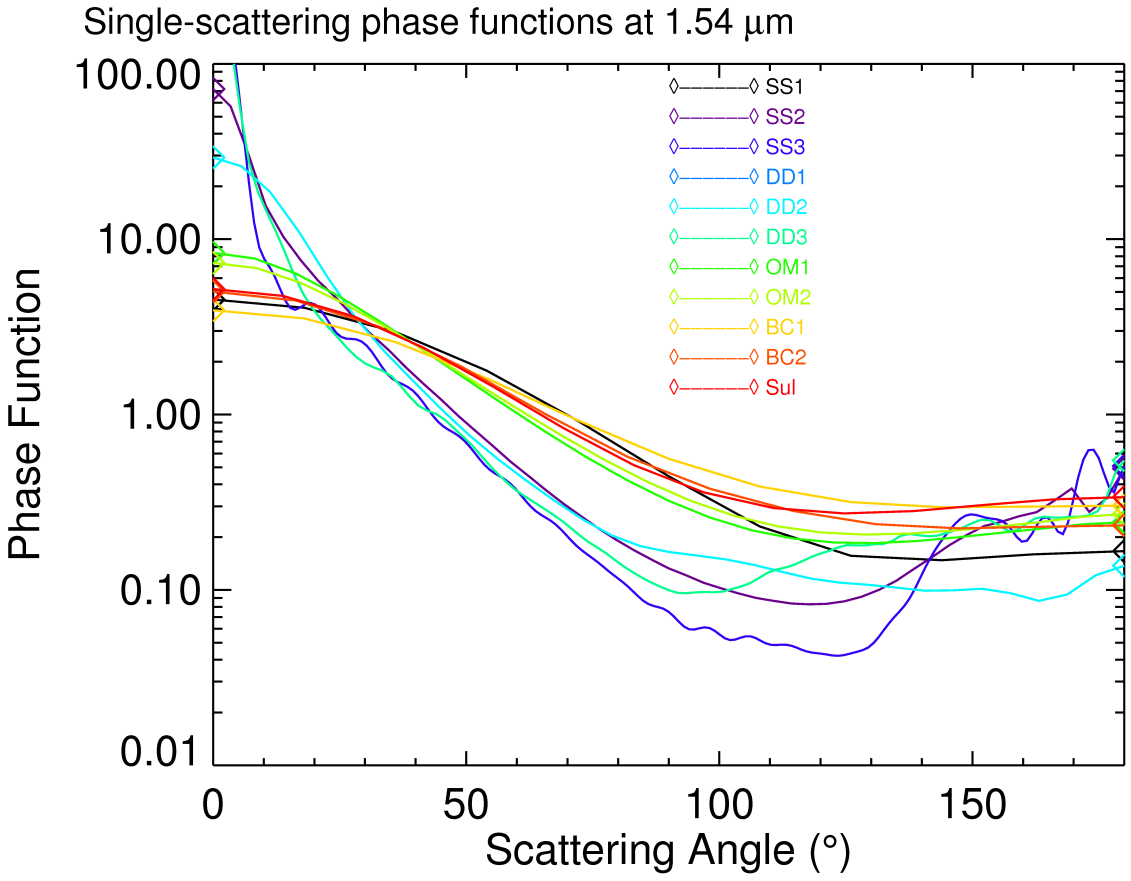

FIGURE 5.16. Derived phase function moments for the start wavelength of GOSAT band 2 as a function of scattering angle for each of the eleven GEMS aerosol types. An angle of zero points directly in the forward direction.

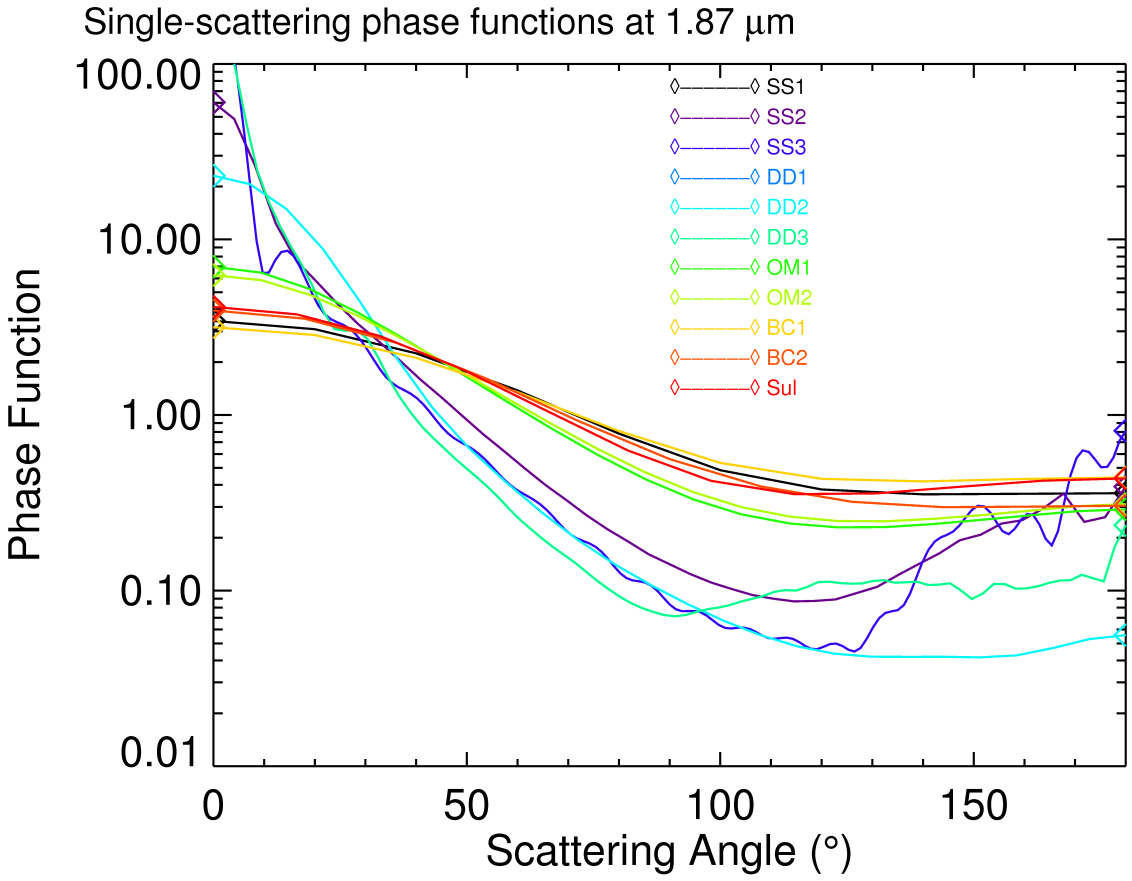

FIGURE 5.17. Derived phase function moments for the start wavelength of GOSAT band 3 as a function of scattering angle for each of the eleven GEMS aerosol types. An angle of zero points directly in the forward direction.

5.2.3.4 CALIPSO Scattering Parameters

CALIPSO was launched in April 2006 and contains three instruments; the Cloud-Aerosol LIdar with Orthogonal Polarization (CALIOP), the Imaging Infrared Radiometer (IIR), and the Wide Field Camera (WFC). Here, data products of the CALIOP instrument have been used to derive atmospheric profiles of aerosols, clouds and cirrus clouds. This can be used instead of the GEMS aerosols/clouds.

The CALIPSO Lidar Level 2 aerosol profile data provides atmospheric profiles of total extinction per 40 km ground track at a number of different wavelengths, as well as altitude, pressure, temperature and relative humidity. The extinction profiles exist on altitude levels but are needed on pressure levels for input into the UoL-FP retrieval algorithm. To convert between altitude and pressure levels the hydrostatic equation can be used

$$\frac{dP}{dz} = -\rho g \tag{5.16}$$

where P is pressure, z is altitude, g is the acceleration due to gravity (assumed constant and equal to a mean sea level value of 9.80665 m s^{-1}), and ρ is the density. The density can be substituted for as

$$\frac{dP}{dz} = -\frac{g}{1000}\left[\left(\frac{P_{dry}}{(R_{dry}T)}\right) + \left(\frac{P_{wet}}{(R_{wet}T)}\right)\right] \tag{5.17}$$

where temperature is T, the ideal gas constant for dry air is R_{dry} (which is the ideal gas constant divided by the dry air mass, 0.02897 kg mol^{-1}), the ideal gas constant for wet air is R_{wet} (which is the ideal gas constant divided by the wet air mass, 0.018015422135 kg mol^{-1}). The partial pressure of wet air P_{wet} can be derived from the relative humidity, RH, and the saturated vapour pressure, p_{Liquid}, using the method of Murphy & Koop (2005) previous described in Section 5.2.3.3 by

$$P_{wet} = RH\frac{p_{Liquid}}{100} \tag{5.18}$$

The partial pressure of dry air is then obtained by

$$P_{dry} = P - P_{wet} \tag{5.19}$$

To simulate GOSAT radiances the aerosol/cloud/cirrus extinctions need to be for the O_2 A band, therefore CALIOP extinction profiles at 532 and 1064 nm are used. The total

optical depth, τ, at each of these wavelengths can be calculated by

$$\tau = \sum \frac{\frac{dP}{dz}_i (E_i + E_{i+1})}{2} dP_{i,i+1} \tag{5.20}$$

where E is extinction and and i denotes the atmospheric level. These optical depths can be used to compute an angstrom coefficient that relates optical depth with wavelength. The angstrom coefficient can be calculated as

$$\alpha = \frac{\ln\left(\frac{\tau_{532}}{\tau_{1064}}\right)}{\ln\left(\frac{\lambda_{1064}}{\lambda_{532}}\right)} \tag{5.21}$$

The optical depth at the O_2 A band (765 nm) is then approximated as

$$\tau_{765} = \tau_{532} \left(\frac{\lambda_{765}}{\lambda_{532}}\right)^{-\alpha} \tag{5.22}$$

The extinction profile at the O_2 A band can be computed from the 532 nm extinction profile by multiplying it by the ratio τ_{765}/τ_{532}.

The CALIPSO Lidar Level 2 Vertical Feature Mask (VFM) data seperates the atmospheric profile into many altitude layers and classifies what features exists in each layer, such as clear air, cloud or aerosol. These features are also sub-catagorised for each aerosol/cloud type, as shown in Figure 5.18. Any VFM data that was catagorised as Invalid, Surface, Sub-Surface or No Signal was excluded from all computations. Stratospheric features were assumed to be cloud. Clouds were seperated into liquid and ice clouds using the cloud phase, where horizontally and randomly orientated ice was taken to be ice cloud, and unknown and water taken to be liquid cloud. Any aerosol that was sub-catagorised as Non-determined or Other was assumed as desert dust.

The VFM data is seperated into three altitude ranges with numerous discrete layers within each range; -0.5 to 8.2 km, 8.2 to 20.2 km, and 20.2 to 30.1 km. The lowest altitude range gives VFM data for 15 discrete increments for every 5 km of the ground track. However, the VFM data for the other altitude ranges are averaged over larger ground track lengths. To obtain the VFM data on a regular grid the upper altitude data is re-binned onto the same grid as the lowest altitude range.

The fractional amount of aerosol within an extinction profile layer, is calculated as the number of discrete VFM increment layers that contain aerosol divided by the total number of increment layers within the 40 km ground track. Similarly, the fractional amount of cloud and sub-catagorised clouds/aerosols are calculated in the same way.

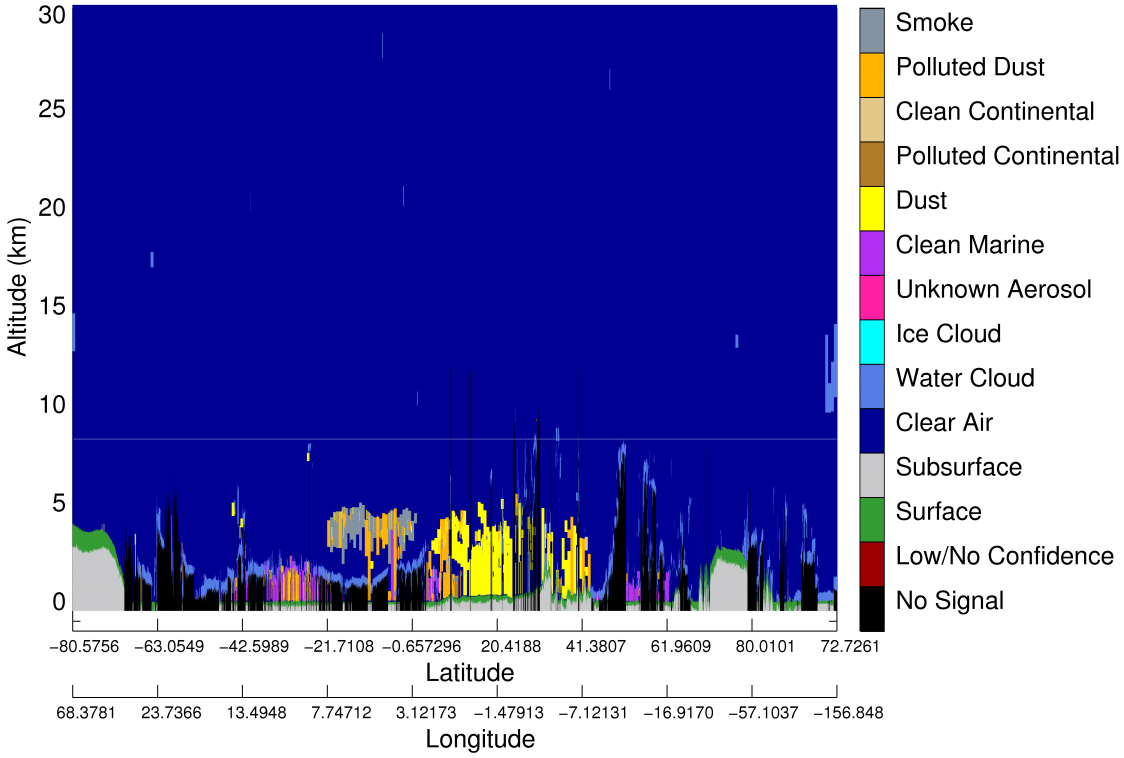

FIGURE 5.18. CALIOP VFM for one orbit track with features given by different colours. This example notably shows water clouds over the majority of the orbit track, polluted dust and smoke over Southern Africa, and a large amount of desert dust over the Sahara.

To get seperate extinction profiles for aerosol, liquid cloud and ice cloud the extinction profile is split up into those three profiles for each layer according to the ratio of their fractional amounts.

The particle properties for ice and liquid clouds are taken from the Baum model (Baum et al. 2005a,b) as described in Section 5.2.3.3, using half of the effective particle size obtained from CALIPSO IIR level 2 data as the effective radius for both liquid and ice cloud particles.

Omar et al. (2004) estimates the aerosol properties of the CALIPSO model by comparisons to observations by AERONET. Each aerosol type is assumed to be a bi-modal aerosol of fine and coarse modes (Mielonen et al. 2009, Omar et al. 2004, Simmons 2010), as shown in Table 5.4. Based on these parameters, the aerosol scattering properties for each aerosol type and mode were computed using the Mie code explained in Section 5.2.3.3, where the RIs were interpolated linearly to the wavelength of each GOSAT band. The volume fraction of each mode was used to weight the mixing of the

modes using the method by Abdou et al. (1997), which states that the combined single scattering albedo can be given as

$$\omega_{M_\lambda} = \sum_{k=1}^{k} f_{k,\lambda}\omega_{k,\lambda} \tag{5.23}$$

where M indicates the combined mixture, k represents each aerosol type/mode, and f is the fraction used to weight the aerosols contribution to the mixture. Also, Abdou et al. (1997) gives the combination of phase functions as:

$$P\left(\Omega,\lambda\right) = \sum_{k=1}^{k} \frac{f_k P_{k,\lambda}\omega_{k,\lambda}}{\omega_{M_\lambda}} \tag{5.24}$$

However, the UoL-FP retrieval algorithm was designed to calculate all scattering values relative to the O_2 A band. Therefore, Equation 5.23 and 5.24 use the relative single scattering albedo of each aerosol. The relative extinction cross section for an aerosol can be given as

$$C_{ext_{k,\lambda rel}} = \frac{C_{ext_{k,\lambda}}}{C_{ext_{k,\lambda r}}} \tag{5.25}$$

The combined relative extinction cross section is then given by:

$$C_{ext_{M,\lambda rel}} = \sum_{k=1}^{k} \frac{f_k C_{ext_{k,\lambda}}}{C_{ext_{k,\lambda r}}} \tag{5.26}$$

Similarly, the relative scattering cross section of the mixture is expressed by:

$$C_{sca_{M,\lambda rel}} = \sum_{k=1}^{k} \frac{f_k C_{sca_{k,\lambda}}}{C_{sca_{k,\lambda r}}} \tag{5.27}$$

The six aerosol types were then combined, weighted by the total column fraction of each type, for each atmospheric aerosol extinction profile. The fraction of each aerosol type that is used to create the aerosol property mixtures is shown in Figure 5.19. This, for example, shows that aerosols over the Sahara are almost completely weighted to desert dust.

The properties of each aerosol type are given in Figure 5.20, which shows a low angstrom coefficient for all aerosol types. The single scattering albedo is highest for clean marine aerosol, showing it is highly scattering and absorbs little light. For clean continental, polluted dust and smoke aerosols about half gets scattered and half absorbed. The asymmetry parameter shows all aerosol types to have a strong forward scattering

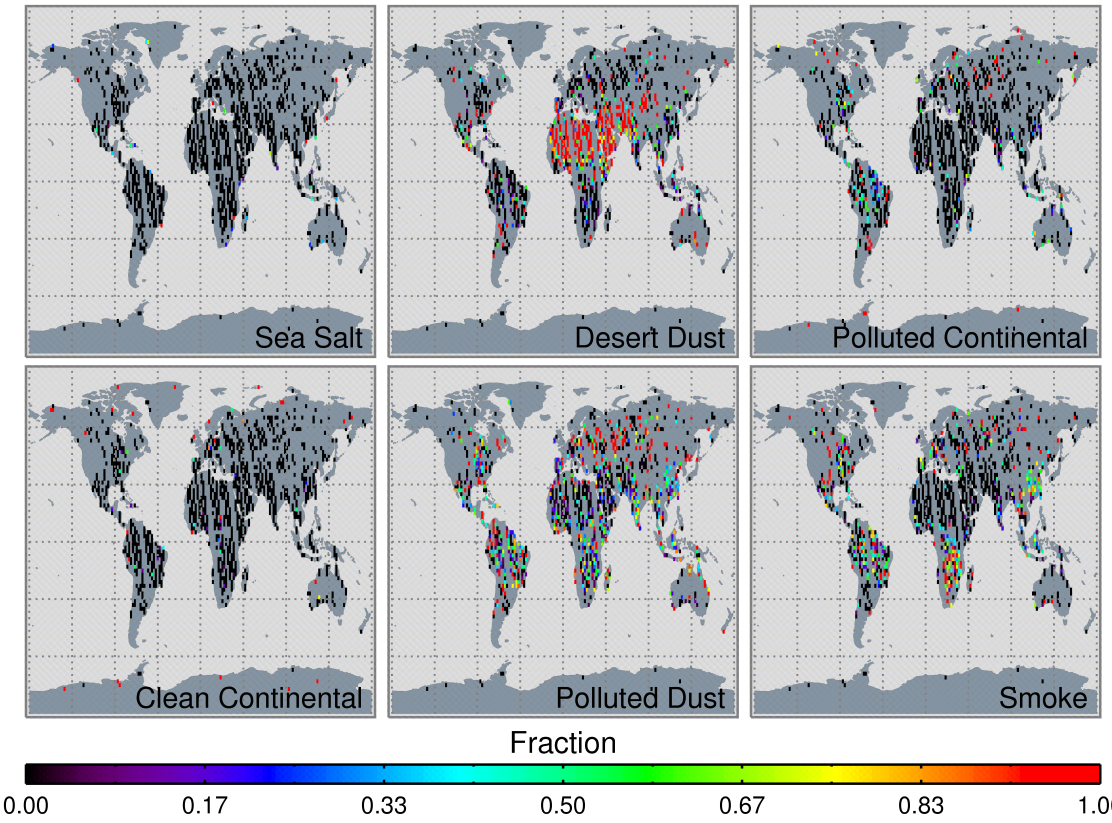

FIGURE 5.19. Optical depth fractions of each of the CALIPSO aerosol types for simulated scenes globally between 08/09/2009 to 14/09/2009.

peak at the O_2 A band, with clean marine aerosol strongly forward scattering at all SWIR bands of GOSAT. Dust, polluted dust, polluted continental and smoke aerosols all have a reduced forward scattering at the CO_2 bands compared to that of the O_2 A band. The phase functions (Figures 5.21, 5.22 and 5.23) show that the scattering directions of the coarse modes changes little with wavelength, but the fine modes become much less forward scattering, almost isotropic, at the wavelengths of the CO_2 bands. This becomes important as when the modes are combined the scattering direction at the CO_2 bands highly depends on the volume fractions used to weight the each modes contribution to the aerosol type. For example, this is demonstrated by the polluted continental aerosol that comprises approximately of half the fine mode and half the coarse mode, so the forward scattering reduces for the CO_2 bands as shown by the asymmetry parameter in Figure 5.20.

To check the simulated scenes are realistic, the calculated aerosol/cloud/cirrus parameters were compared MODIS. Although the calculated effective radii for liquid and ice clouds are designated the same for CALIPSO, the values have a reasonably large

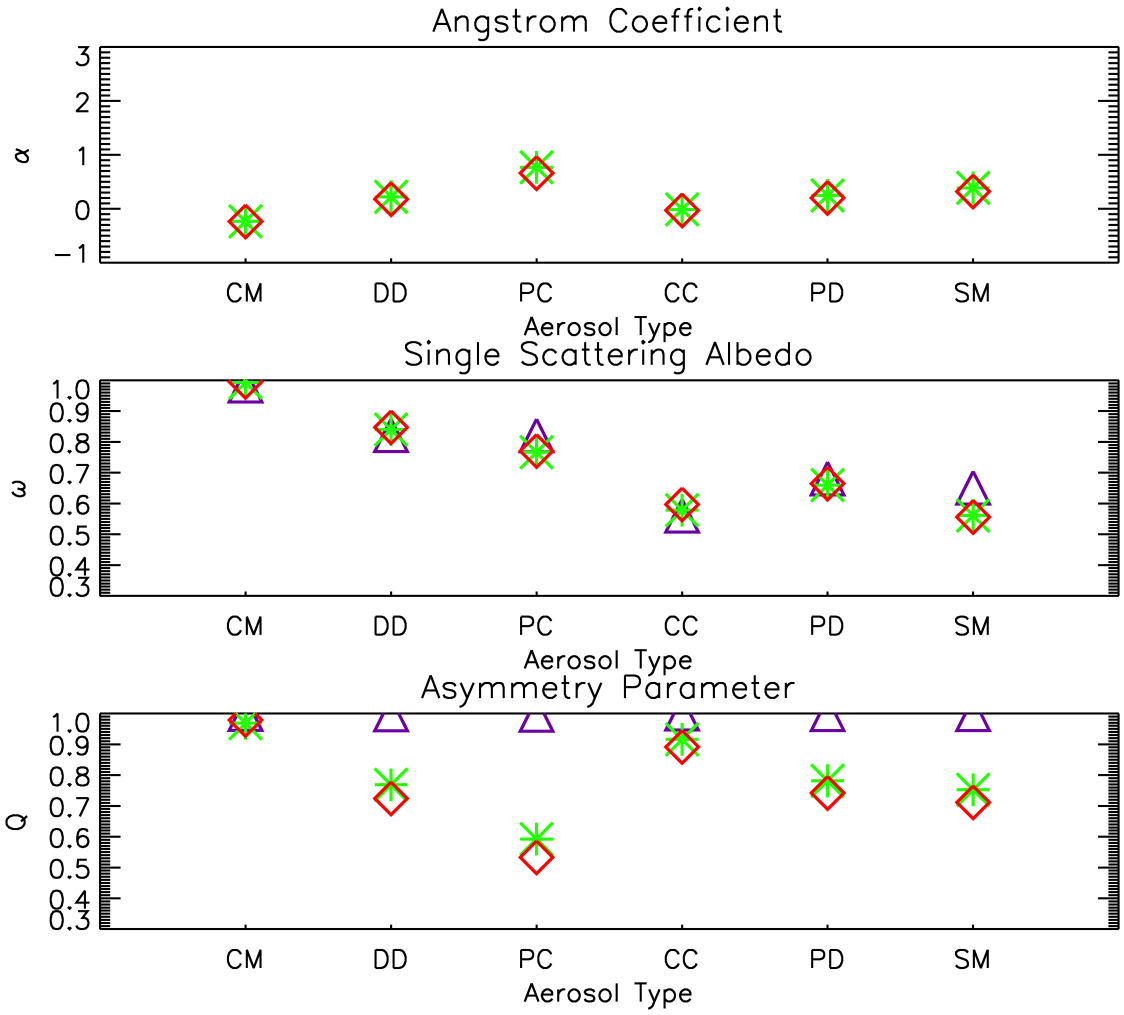

FIGURE 5.20. Derived aerosol properties for each CALIPSO aerosol type for the start wavelength of each GOSAT SWIR band. The angstrom coefficient between bands 1 and 2 is given by the green stars and the angstrom coefficient between bands 2 and 3 is given by the red diamonds. For both the single scattering albedo and the asymmetry parameter band 1 is given by the purple triangles, band 2 by the green stars and band 3 by the red diamonds. The aerosol types are represented as; CM is Clean Marine, DD is Desert Dust, PC is Polluted Continental, CC is Clean Continental, PD is Polluted Dust, and SM is smoke.

variation (between 0 and $\sim$60 μm) with the bulk of the data covering the ranges of both liquid and ice effective radii from MODIS, as shown in Figure 5.24. Thus, the calculated effective radii from CALIPSO provides a realistic basis for the cloud/cirrus properties used in the simulations. Comparing the optical depth with MODIS, Figure 5.25, reveals that both the liquid and ice cloud optical depths are highly under-estimated. However, CALIPSO measurements can not penetrate through thick clouds at these wavelengths.

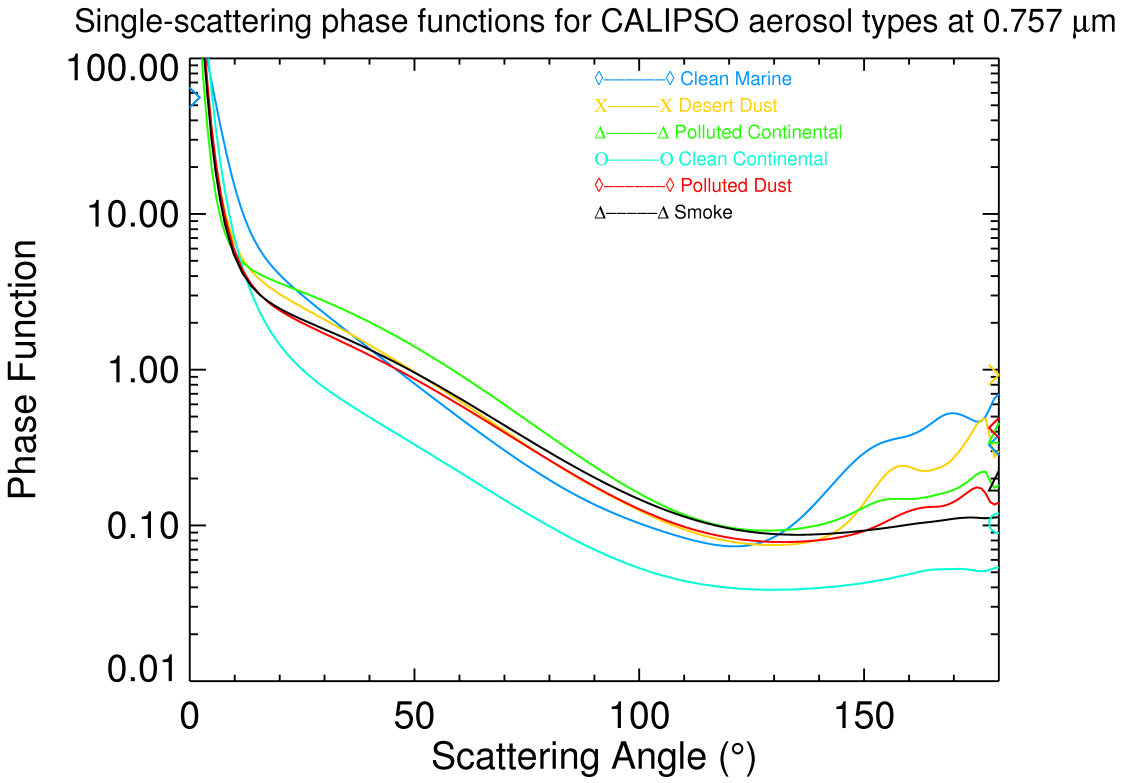

FIGURE 5.21. Derived phase function moments for the start wavelength of GOSAT band 1 as a function of scattering angle for each of the CALIPSO aerosol types and modes. An angle of zero points directly in the forward direction.

Therefore, any extinction profile that should include a thick cloud will contain invalid data and not be used. This leaves CALIPSO soundings that contain either thin or no clouds, hence biasing the optical depths to lower values compared to MODIS. Additionally, this effectively acts as an initial cloud screen, since any scene containing thick cloud would be filtered out. The optical depth calculated for aerosol has a similar range as MODIS but with the values on average to be much lower than MODIS. Figure 5.26 shows the spatial distribution of AOD which follows the same patterns as both MODIS and GEMS. Some differences in AOD are expected as both GEMS and MODIS provide AOD data for coarse grids of $\gtrsim$110 x 110 km (1° x 1°), whereas CALIPSO AOD has been calculated for a much smaller area of 0.07 x 40 km.

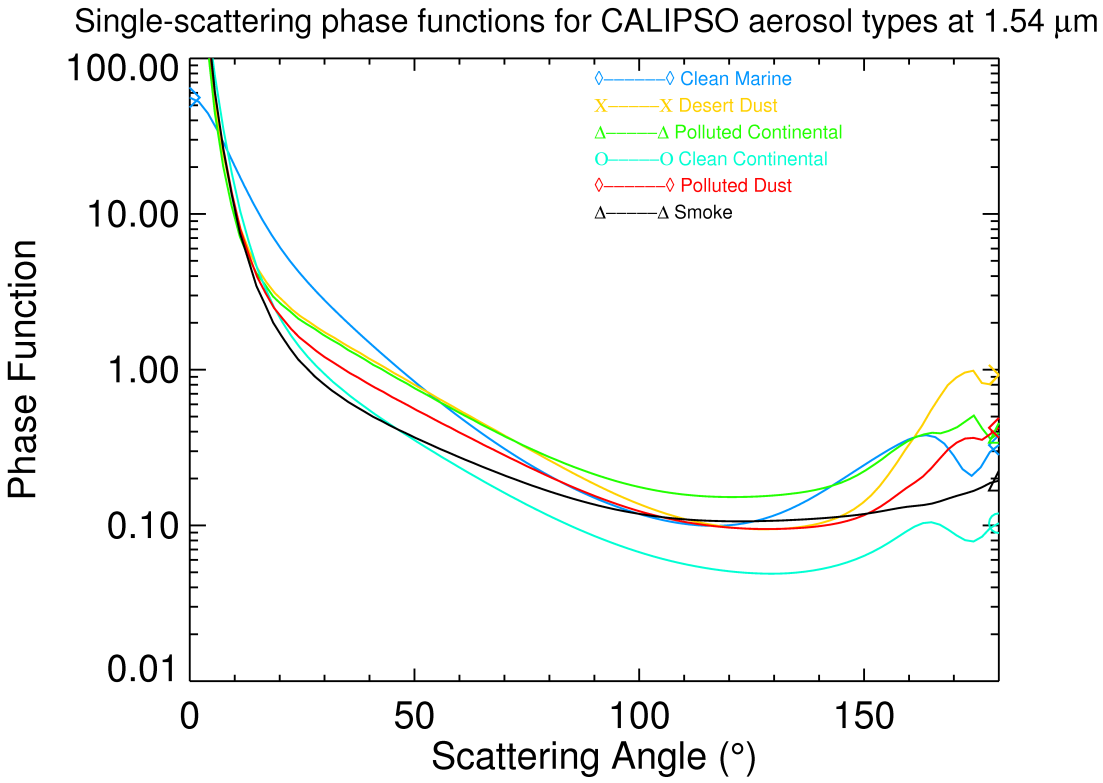

FIGURE 5.22. Derived phase function moments for the start wavelength of GOSAT band 2 as a function of scattering angle for each of the CALIPSO aerosol types and modes. An angle of zero points directly in the forward direction.

Table 5.4. CALIPSO aerosol properties (Mielonen et al. 2009, Omar et al. 2004, Simmons 2010).

Aerosol Type	Mode	Real RI at 532 nm	Imaginary RI at 532 nm	Real RI at 1064 nm	Imaginary RI at 1064 nm	Minimum Radius (μm)	Maximum Radius (μm)	Effective Radius (μm)	Radius Standard Deviation (μm)	Volume Fraction
Clean Marine	Fine	1.400	0.005	1.400	0.005	0.05	0.30	0.15	1.60	0.025
Clean Marine	Coarse	1.390	0.0005	1.390	0.0005	0.30	10.00	1.22	1.60	0.975
Desert Dust	Fine	1.414	0.0036	1.495	0.0043	0.05	0.30	0.12	1.48	0.223
Desert Dust	Coarse	1.414	0.0036	1.495	0.0043	0.30	10.00	2.84	1.91	0.777
Polluted Continental	Fine	1.404	0.0063	1.439	0.0073	0.05	0.30	0.16	1.53	0.531
Polluted Continental	Coarse	1.404	0.0063	1.439	0.0073	0.30	10.00	3.55	2.07	0.469
Clean Continental	Fine	1.380	0.0010	1.380	0.0010	0.05	0.30	0.21	1.61	0.050
Clean Continental	Coarse	1.455	0.0340	1.455	0.0340	0.30	10.00	2.63	1.90	0.950
Polluted Dust	Fine	1.452	0.0109	1.512	0.0109	0.05	0.30	0.13	1.51	0.241
Polluted Dust	Coarse	1.452	0.1370	1.512	0.1370	0.30	10.00	3.16	1.99	0.759
Smoke	Fine	1.517	0.0234	1.541	0.0234	0.05	0.30	0.14	1.56	0.329
Smoke	Coarse	1.517	0.0298	1.541	0.0298	0.30	10.00	3.73	2.14	0.671

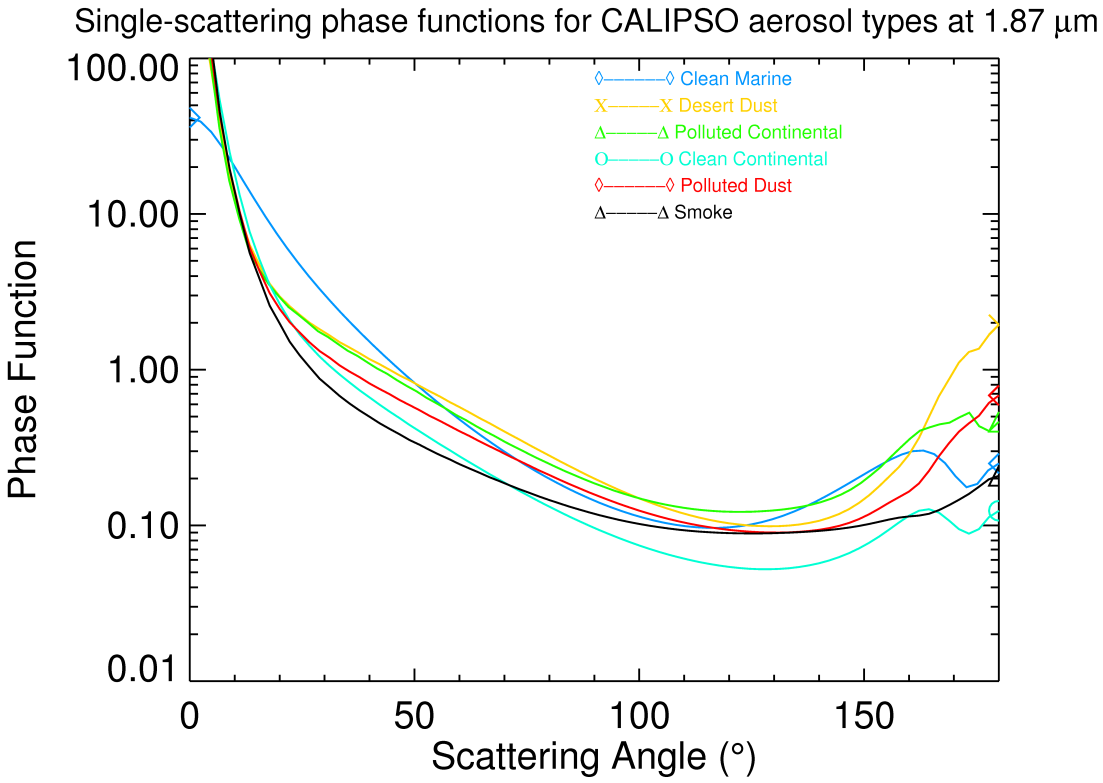

FIGURE 5.23. Derived phase function moments for the start wavelength of GOSAT band 3 as a function of scattering angle for each of the CALIPSO aerosol types and modes. An angle of zero points directly in the forward direction.

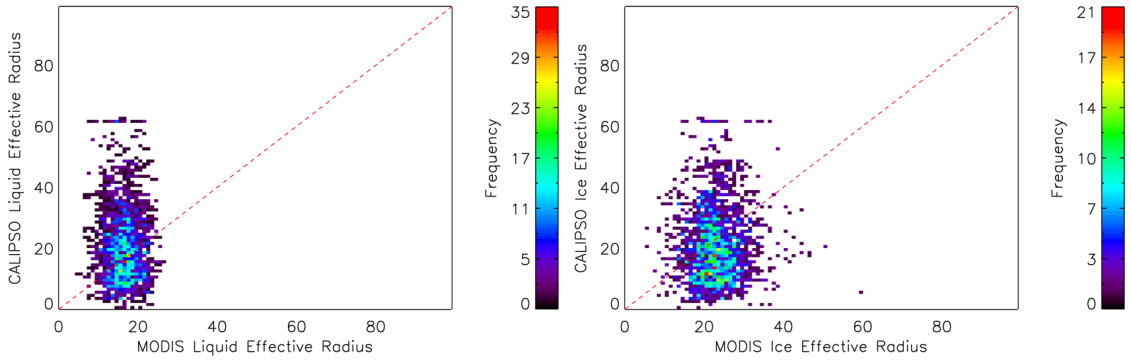

FIGURE 5.24. Correlation of the liquid (left) and ice (right) effective radius calculated from CALIPSO with that retrieved from MODIS between 08/09/2009 to 14/09/2009 for CALIPSO soundings. The calipso soundings have much lower values for cloud/cirrus optical depths since the CALIOP measured radiance will often not penetrate through clouds, leaving incomplete extinction profiles that get screened out, hence removing most cloud scenes.

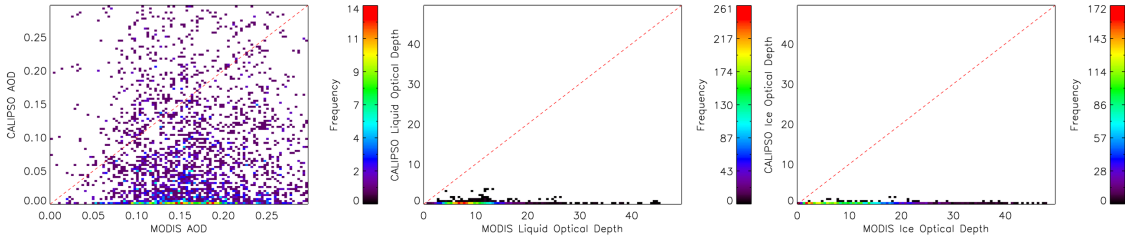

FIGURE 5.25. Correlation of the aerosol (left), liquid cloud (centre) and ice cloud (right) optical depth calculated from CALIPSO with that retrieved from MODIS between 08/09/2009 to 14/09/2009 for CALIPSO soundings.

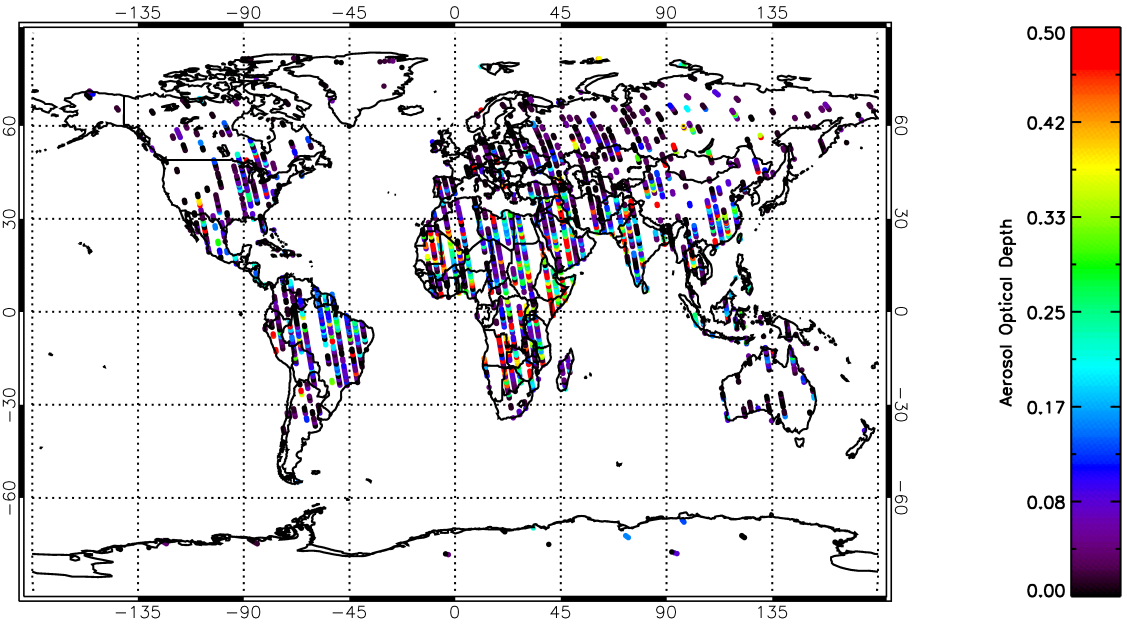

FIGURE 5.26. AOD calculated from CALIPSO between 08/09/2009 to 14/09/2009 for CALIPSO soundings.

5.3 Initial Tests

To aid the construction of a new approach to atmospheric scattering it was first neccessary to determine which aspects are important in the retrieval of X_{CO2}. Although there is a high spatial/temporal variation of aerosols and clouds, this can essentially be described by three components; the total column optical depth, the vertical distribution, and the particle properties.

The first test was to investigate how the AOD affects the retrieved X_{CO2}. Here the simulator (with GEMS aerosols/clouds) was used to simulate GOSAT spectra for different amounts of AOD, with each AOD scenario having 100 realistic scenes simulated. All of these spectra were retrieved with the same aerosol profile (Gaussian shape peaking at a height of 2 km with a width of 2 km), the same aerosol properties, the same a priori AOD of 0.2, and all other a priori and statevectors the same. Figure 5.27 shows how the results of this test demonstrate that the UoL-FP retrieval algorithm can accurately retrieve X_{CO2} within $\sim$0.1 AOD of the truth and remains within a X_{CO2} error of 0.03 ppm between a true AOD of 0.025 to 0.4 range. The performance of the retrieval to accurately retrieve X_{CO2} reduces for large differences ($>$0.2) between the a priori and true AOD, hence it is important to provide the retrieval with an a priori AOD that is not too small or too large as the retrieval will find it difficult to reach the true optimal solution.

Secondly, using the simulator in a similar fashion, the effect of the vertical distribution of aerosol on retrieved X_{CO2} was assessed. Here, spectra were simulated with a Gaussian shaped aerosol profile peaking at 2 km. The simulations used 100 realistic scenes and all were retrieved using different scenarios of the a priori aerosol profile peak height. Figure 5.28 shows that the mean resulting X_{CO2} error varies very little with the peak height of the aerosol profile. However the range of X_{CO2} values increases with the difference in height, with large differences between lower and upper altitudes.

To evaluate the impact of the aerosol properties on the retrieval of X_{CO2}, spectra were simulated for 100 realistic scenes using the Kahn aerosol mixture 4b. Retrievals of X_{CO2} were performed on these simulated spectra for 11 different scenarios, where each scenario used only the properties of a single GEMS aerosol type. The results are given in Figure 5.29 and show that there is a large variation of X_{CO2} error. There are smaller X_{CO2} errors for larger sized aerosols and larger X_{CO2} errors for smaller sized aerosols, which is likely due to the Kahn 4b mixture being a combination of medium and large sized particles. The aerosol properties cause the X_{CO2} error to be significantly higher than that of AOD or vertical distribution differences. Hence it is by far the most crucial aerosol component to get closest to truth for accurate X_{CO2} retrievals.

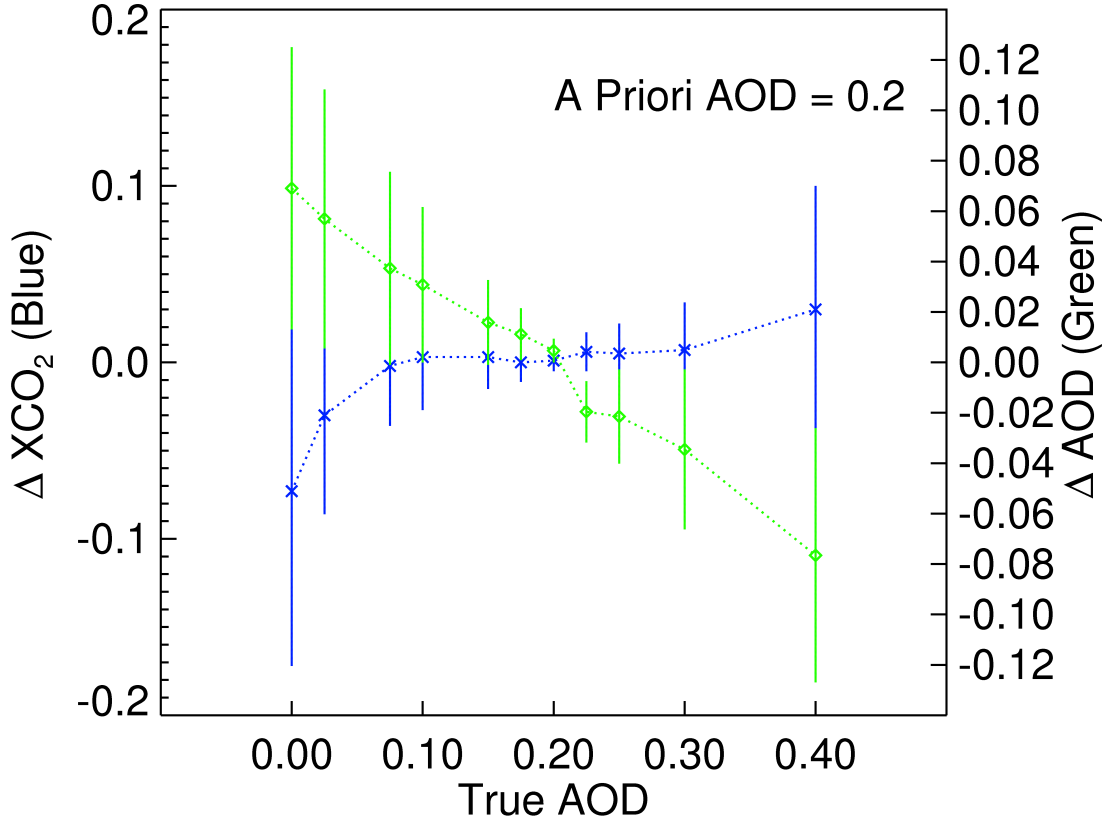

FIGURE 5.27. Mean retrieved X_{CO2} of 100 simulated GOSAT spectra for different AOD. The blue line gives the X_{CO2} error and the green line shows the AOD error, with the standard deviation of the 100 results for each AOD scenario shown by the errorbars.

Likewise, the same components were investigated for water clouds and cirrus clouds in exactly the same manner, with the components replaced with cloud/cirrus respectively. For the particle properties of both water clouds and cirrus clouds a range of effective radii obtained from the Baum model (Baum et al. 2005a,b) were used.

Figure 5.30 shows that the retrieval achieves a low X_{CO2} error when the assumed a priori cloud optical depth is within 0.15 of the truth, but increases rapidly with higher optical depth differences. For cirrus, the retrieval only performs accurately where the a priori optical depth is within 0.025 of the truth. The cirrus retrieval is extemely poor at capturing the true optical depth which clearly has an impact on the X_{CO2} error above a 0.05 difference in optical depth. Since a cloud screen is applied to real GOSAT observations, scenes with a high optical depth will already be omitted from X_{CO2} retrievals. Therefore, predominantly scenes with a low optical depth or cirrus will remain, revealing that it is more important to get the a priori cirrus optical depth close to truth than cloud

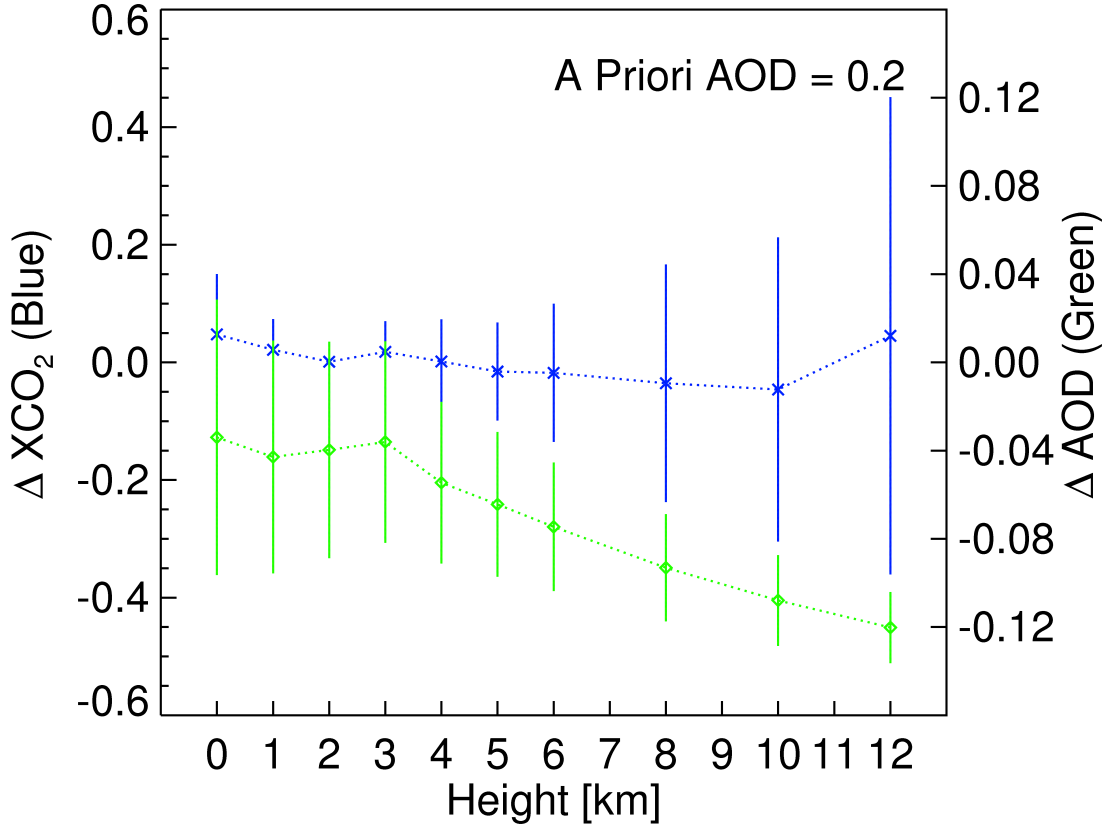

FIGURE 5.28. Mean retrieved X_{CO2} of 100 simulated GOSAT spectra for different peak heights of a Gaussian shaped aerosol profile. The blue line gives the X_{CO2} error and the green line shows the AOD error, with the standard deviation of the 100 results for each height scenario shown by the errorbars.

optical depth.

The effect of cloud height is shown in Figure 5.32 and shows a clear relationship with X_{CO2} error of $\sim$0.02 ppm/km. Figure 5.33 shows the effect of cirrus height and gives a similar trend but with a larger gradient of $\sim$0.075 ppm/km and an anti-correlation with retrieved optical depth. Again, cirrus has a far larger affect on X_{CO2} than water clouds and it is important to have an accurate a priori assumption of cirrus vertical distribution.

Similarly, there is a trend of effective radius with X_{CO2} error (see Figures 5.34 and 5.35). The gradient is higher with cirrus than cloud, with values of $\sim$0.35 ppm/10μm and $\sim$0.10 ppm/10μm respectively. The X_{CO2} error is approximately double that created by incorrect optical depth or cirrus height, making it more vital to get closer to the truth for retrievals of X_{CO2}.

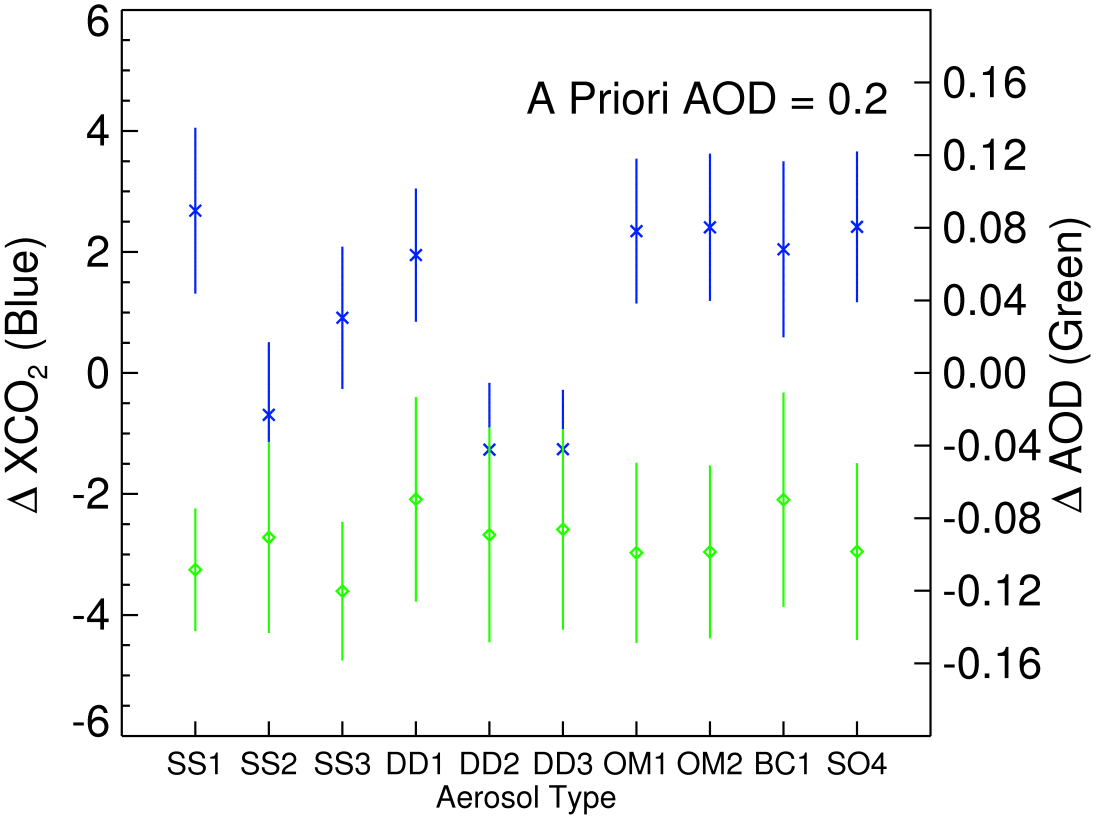

FIGURE 5.29. Mean retrieved X_{CO2} from retrievals using different aerosol types with 100 simulated GOSAT spectra. The blue line gives the X_{CO2} error and the green line shows the AOD error, with the standard deviation of the 100 results for each height scenario shown by the errorbars. The dust properties used were based purely on GEMS, giving DD1, DD2 and DD3 as small, medium and large dust particles, respectively.

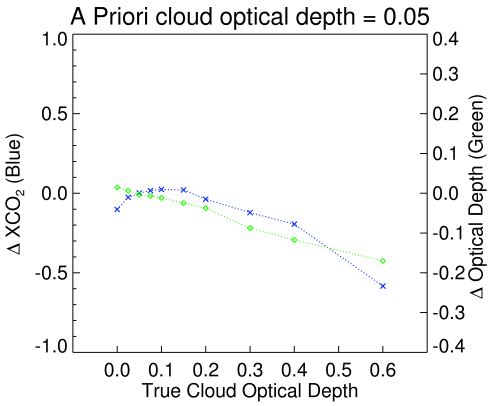

FIGURE 5.30. Mean retrieved X_{CO2} of 100 simulated GOSAT spectra for different cloud optical depths. The blue line gives the X_{CO2} error and the green line shows the optical depth error, with the standard deviation of the 100 results for each optical depth scenario shown by the errorbars.

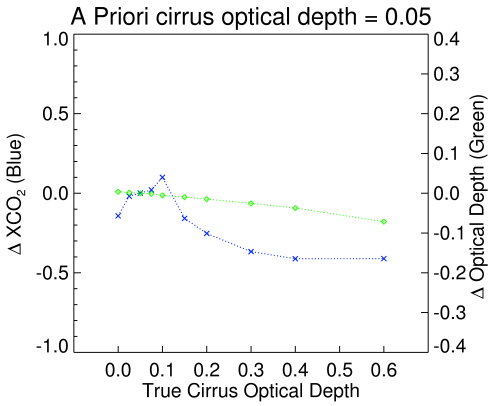

FIGURE 5.31. Mean retrieved X_{CO2} of 100 simulated GOSAT spectra for different cirrus optical depths. The blue line gives the X_{CO2} error and the green line shows the optical depth error, with the standard deviation of the 100 results for each optical depth scenario shown by the errorbars.

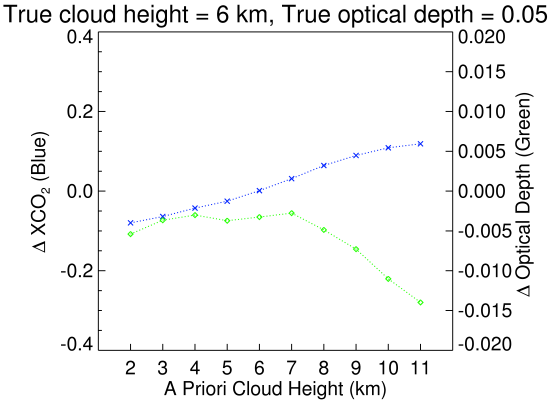

FIGURE 5.32. Mean retrieved X_{CO2} of 100 simulated GOSAT spectra for different peak heights of a Gaussian shaped cloud profile. The blue line gives the X_{CO2} error and the green line shows the optical depth error, with the standard deviation of the 100 results for each height scenario shown by the errorbars.

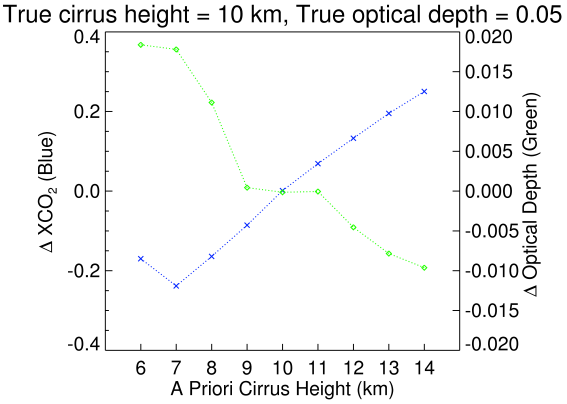

FIGURE 5.33. Mean retrieved X_{CO2} of 100 simulated GOSAT spectra for different peak heights of a Gaussian shaped cirrus profile. The blue line gives the X_{CO2} error and the green line shows the optical depth error, with the standard deviation of the 100 results for each height scenario shown by the errorbars.

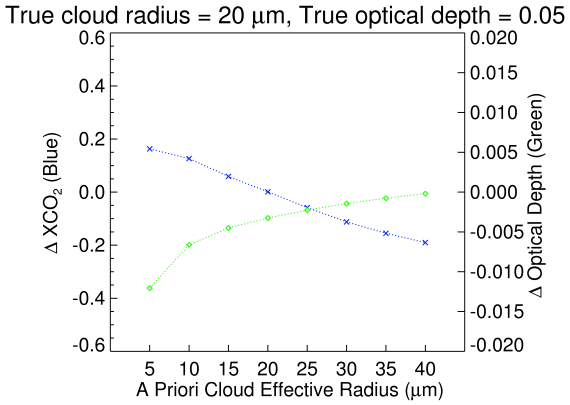

FIGURE 5.34. Mean retrieved X_{CO2} from retrievals using different cloud effective radii with 100 simulated GOSAT spectra. The blue line gives the X_{CO2} error and the green line shows the optical depth error, with the standard deviation of the 100 results for each height scenario shown by the errorbars.

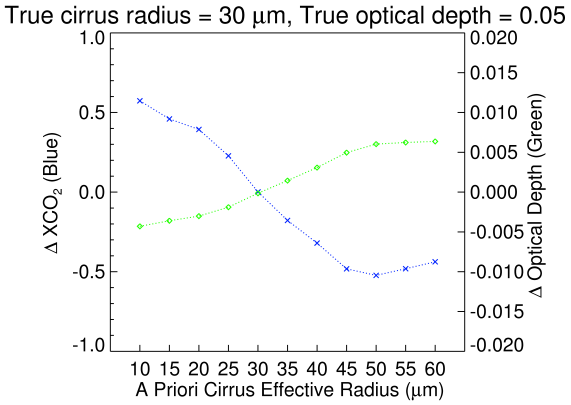

FIGURE 5.35. Mean retrieved X_{CO2} from retrievals using different cirrus effective radii with 100 simulated GOSAT spectra. The blue line gives the X_{CO2} error and the green line shows the optical depth error, with the standard deviation of the 100 results for each height scenario shown by the errorbars.

5.4 New Scattering Approach Design Basis

Whilst clouds have a large effect on the retrieval accuracy, a cloud screen could be used to remove most cloud contaminated scenes in real retrievals of X_{CO2} from GOSAT. For this reason the new scattering approach was designed to provide initially a better approach to aerosols. The current retrieval method (UoL-FP v3G) gives the retrieval a large flexibility to allow more information from the measured radiance to be used to gain aerosol information. However, this method relies upon the same two aerosol mixtures globally. One way this method could be improved is to use aerosol mixtures that are specific to the observed location and time. At present there are a number of observation methods that provide aerosol information (e.g. satellite observations, ground based measurements and aircraft observations), however due to the fact that aerosols are highly variable both spatially and temporally none of these sources can provide adequate information for this approach. Thus, the new approach was designed to use model aerosol information obtained from the GEMS model.

The aerosol extinction profiles for each of the eleven GEMS aerosol types were derived using the method explained in Section 5.2.3.3. To keep the retrieval computational time low and for direct comparison to the current retrieval method, the eleven aerosol profiles were reduced to two profiles. For each GEMS latitude/longitude grid cell the aerosol profiles are temporally interpolated to the local mid-day time, as GOSAT observes day-time SWIR radiances. Since the model only provides estimates and not the true known aerosol information, some spatial smoothing is applied by taking the eight closest surrounding grid cells. The mean profiles of each aerosol type are calculated for this enlarged region and the two aerosol types which have the largest AOD are seperated into two profile groups. The profile shape of all other aerosol profiles are correlated with both of these two profiles and then added to the group of which each aerosol correlates highest with. The aerosol profiles within each group are then added together to maintain the total AOD. This selection method of grouping the aerosols ideally contains at least one aerosol which will significantly contribute to the scene, allowing the retrieval to utilise both profiles for flexibility. Clearly the case can exist where only one aerosol type significantly contributes to a scene, in which case the retrieval would likely be forced to only use that groups profile. To overcome this possibility and allow more adaptability to the retrieval a lower AOD limit of 0.025 per group profile was enforced. There are cases, such as desert dust over the Sahara, where the AOD can be too large for the retrieval algorithm to accurately perform retrievals for (Kuang et al. 2002). To compensate for this, where the combined total AOD is greater than 0.275 in value, both group profiles

are reduced such that their ratio remains the same (with exception to the lower limit) and their combined total AOD equals this upper limit. The aerosol properties of each group were also designed to be specific to the scene by combining the individual aerosol types of each group, using the method described in Section 5.2.3.3 where the AOD fractions as the weighting of aerosol types contributing to the combination.

5.5 Comparison of Scattering Approach Tests

Although the new scattering approach design includes all three main aerosol components, it is possible that certain aspects might not provide any benefit over the flexibility of the current retrieval method. Therefore, in addition to the current retrieval method and the new scattering design being compared though retrievals of simulated scenes, each aerosol component of the new design is tested individually too. The next section explains each of these tests and makes a comparison between them.

5.5.1 Model Based Simulations: Aerosols Only

Spectral radiances of two 3-day cycles of GOSAT were simulated with scenes containing aerosols but not cirrus/clouds, using the GEMS model in the simulator. This provided a total of 9858 simulated exposures that were distributed globally using the GOSAT 5-point observation mode. The simulated spectra were retrieved using the same instrument, surface and atmospheric variables with the exception of the aerosol components which were different for each test;

- Use the current retrieval method (UoL-FP v3G) aerosol approach for reference to compare new tests against. Here the cirrus profile is omitted leaving only two aerosol profiles with a total AOD of 0.1.
- Use the current retrieval method but replace the AOD with that of the new scattering approach design.
- Use the current retrieval method but replace the aerosol profiles with that of the new scattering approach design, where the profile shape is retained but its total AOD is reduced to 0.1 for all scenes.
- Use the current retrieval method but replace the aerosol optical properties with that of the new scattering approach design.

- Use all three aspects of the new scattering approach design.

The retrievals of each test were quality filtered to remove any poor retrievals, similar to the post-screening applied to the real GOSAT retrievals. However, many of the post-screen filter parameters do not exist in the simulations, so a more basic screen was applied that filters for only converged retrievals with $<$3 divergences, a total retrieved AOD of $<$0.3 and a difference between true and retrieved surface pressure of $>$-1 hPa. Not only are these parameters included in the post-screen, the parameters and filter thresholds were obtained empirically from comparisons with the X_{CO2} bias of the current retrieval approach that was used to retrieve the simulated scenes. Figure 5.36 shows the X_{CO2} bias and number of exposures for each of the filter parameters, as well as the threshold values that provide an appropriate compromise between the number of exposures and maintaining a low X_{CO2} bias and scatter. Although stricter screening could be applied, it would reduce the number of exposures and bias the screening to this retrieval approach setup.

The statistics on the number of exposures passing the quality filter, the resulting X_{CO2} bias and standard deviation of each test is given by Table 5.5. In addition to the five retrieval tests stated above, the simulated scenes were retrieved using exactly the same a priori values as used in the simulations, but one aerosol was used instead of all 11 aerosols. The one aerosol profile was the sum of all 11 aerosol profiles, so as to the keep the profile shape and AOD the same, and the optical properties of the 11 aerosols were mixed together (weighted with the total column AOD). The only difference between the simulations and retrievals in this test was that the simulations mixed the aerosol optical properties at each atmospheric layer, whereas the retrievals used the aerosol optical properties mixed for the total atmospheric column. This test results in a X_{CO2} bias of -0.02 ppm with standard deviation of 0.63 ppm, showing some small differences between the retrieval and simulation that are due to the difference in mixing of optical properties and other retrieval related artefacts.

The current retrieval method (UoL-FP v3G) has a X_{CO2} bias of 0.06 ppm and a standard deviation of 0.82 ppm. The new scattering approach method shows an improvement upon this, with a lower X_{CO2} bias of 0.03 ppm and a reduced standard deviation of 0.69 ppm, such that it almost approaches the precision and accuracy of the retrievals using the simulation a priori. Looking at each new scattering approach aspect seperately, using the AOD produces a slightly higher bias of 0.07 ppm and a worse standard deviation of 0.92 ppm. Using the new profiles results in a slightly lower bias of 0.05 ppm but higher standard deviation of 0.87 ppm (compared to the current retrieval method). When the

new aerosol properties are used the standard deviation improves (0.76 ppm) but the bias becomes slightly larger (0.07 ppm). In general, the difference in bias and standard deviation between the retrieval tests is small and all tests perform well on average (biases $<$0.07 ppm). Furthermore, the number of exposures left once quality screened is similar between retrieval tests, ranging between 50.3% and 54.1%.

Table 5.5. Retrieval statistics for each of the aerosol retrieval tests of aerosol only loaded simulated scenes.

Aerosol test	Number of screened retrievals	Δ X_{CO2} mean (ppm)	Δ X_{CO2} σ (ppm)
Retrieval using simulation a priori	5249	-0.02	0.63
Current retrieval method (UoL-FP v3G)	4962	0.06	0.82
Current retrieval method with the new scattering approach AOD	4988	0.07	0.92
Current retrieval method with the new scattering approach aerosol profiles	5002	0.05	0.87
Current retrieval method with the new scattering approach aerosol properties	5332	0.07	0.76
New scattering approach method AOD, aerosol profiles and aerosol properties	5297	0.03	0.69

Figure 5.37 shows the difference between true and retrieved X_{CO2} of each retrieval test to assess potential geographical biases. Large X_{CO2} differences are found over desert regions in the current retrieval method (UoL-FP v3G), as already observed in comparisons between real GOSAT observations and GEOS-Chem model estimations (see Section 4.3. Additionally, other biases can be seen in Europe, North East Asia, central and southern Africa, and East USA. The retrieval using simulation a priori provides a basis for what could best be achieved and shows no desert biases and much lower biases elsewhere in the world. Some small biases are found though, mainly located over East

USA.

Similarly, the new scattering approach method also shows low biases throughout the world, but the aerosol is quite similar to the aerosol used in the simulations so is expected to perform well. Using each aspect of the new scattering approach method with the current retrieval method provides tests that are quite different to the simulations. When either the new AOD or new profiles are used the geographical biases remain similar to that of the current retrieval method. However, when the new optical properties are used the biases over the desert regions significantly reduce, as well as biases in other areas such as Europe and central/southern Africa. This leaves only small geographical biases similar to that produced by the new scattering approach method. Thus, changing the aerosol optical depth and profile shape has little or no benefit to the retrieval of X_{CO2} but using aerosol optical properties that are scene dependent and closer to the truth provides a large improvement in X_{CO2}. These results agree with the conclusion of the initial aerosol tests. Hence, if scene dependent aerosol optical properties were used in retrievals of X_{CO2} from real GOSAT measurements then better results would be expected.

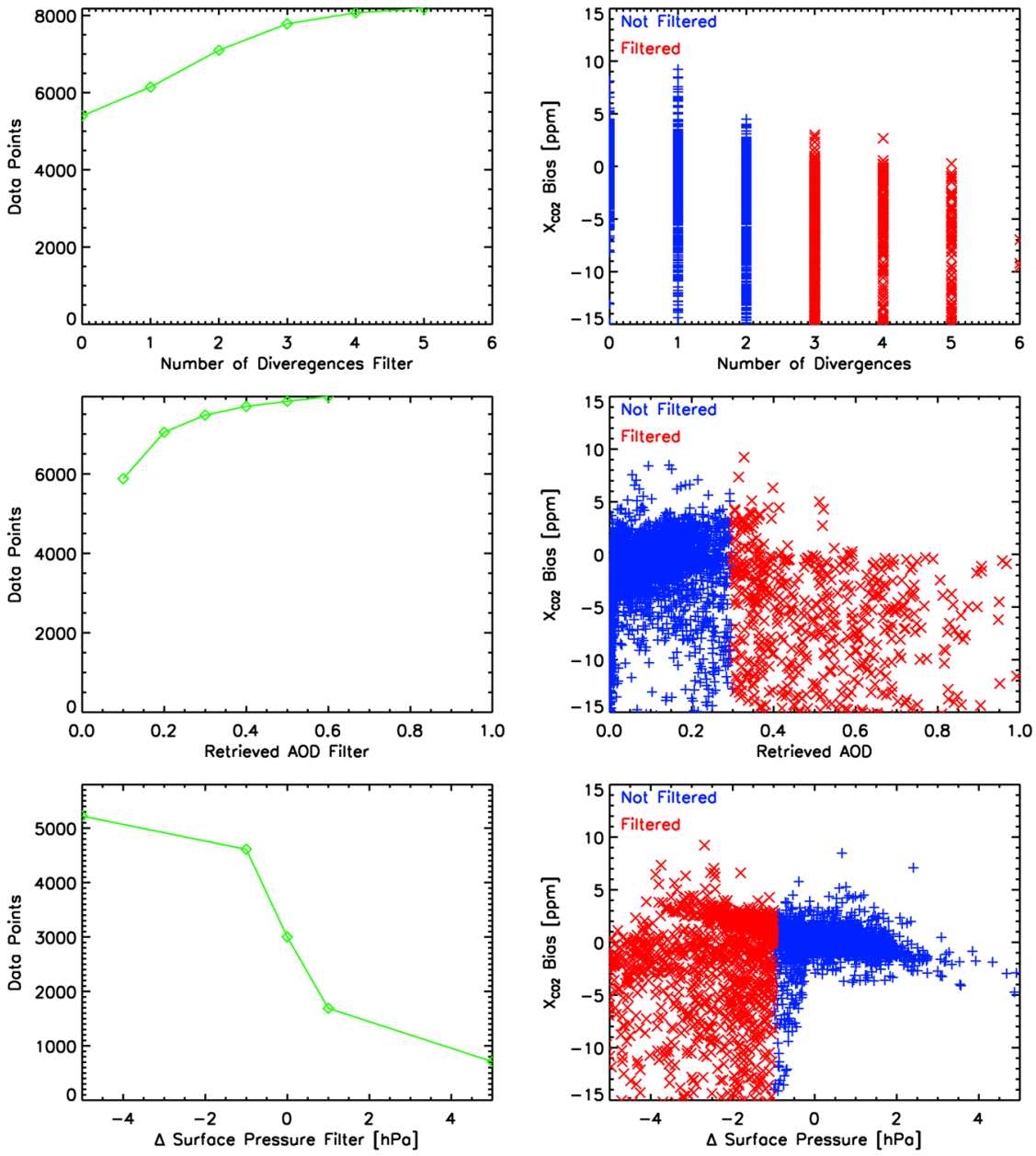

FIGURE 5.36. Comparison of X_{CO2} bias with each quality filter parameter for retrievals of aerosol only simulations using the current retrieval algorithm (right column). The screened data is given in blue and the data filtered out is shown in red. The left column shows the corresponding number of exposures when different filter thresholds are applied to each parameter.

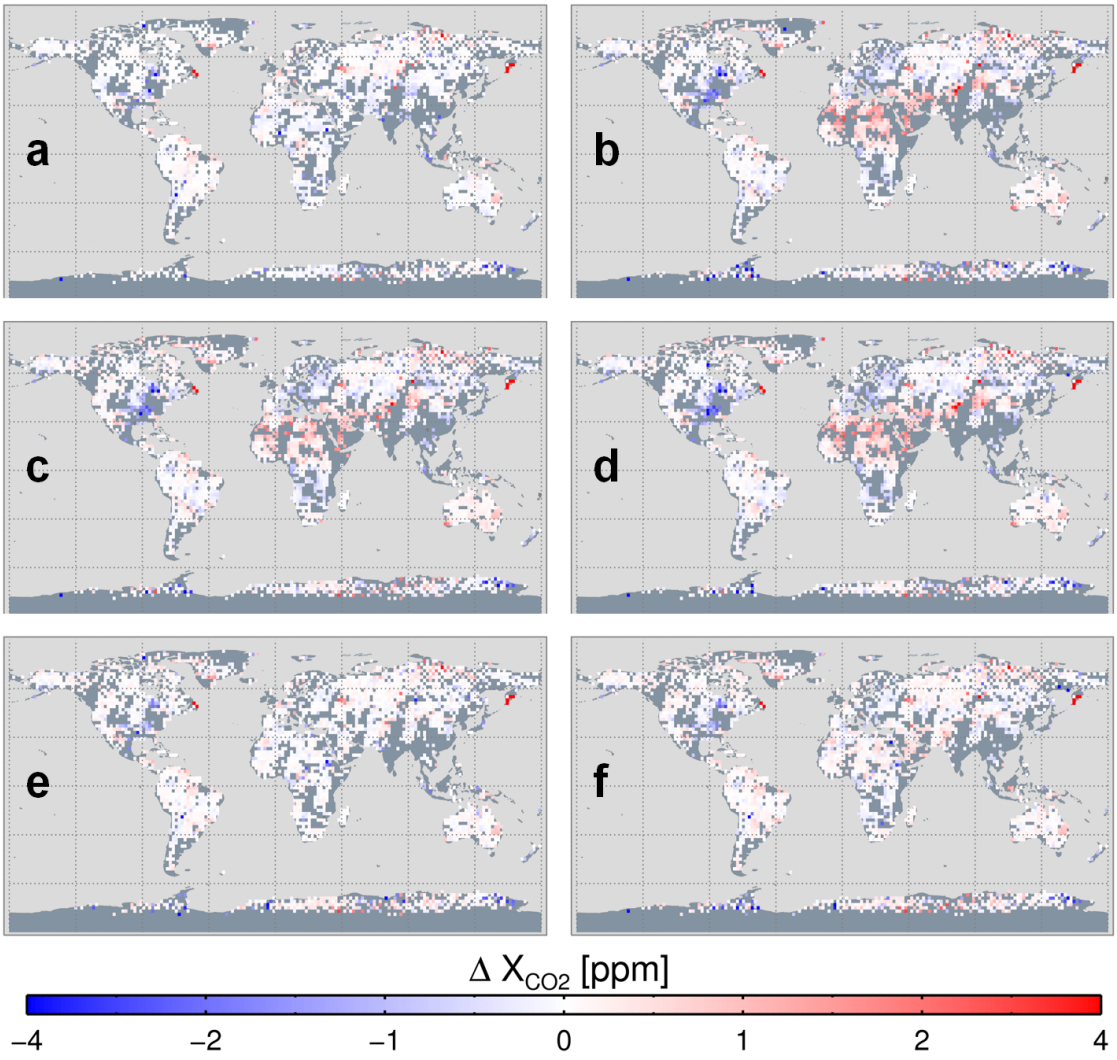

FIGURE 5.37. Difference between true and retrieved X_{CO2} of each retrieval test, where a is the retrieval using the simulation a priori, b is the current retrieval method with the new AOD, c is the current retrieval method, d is the current retrieval method with the new aerosol profile shapes, e is the new scattering approach method, and f is the current retrieval method with the new aerosol optical properties. Grey areas show where no data exists.

5.5.2 Model Based Simulations: Aerosols, Clouds and Cirrus

In real GOSAT observations the scenes would not just contain aerosols but also possibly cirrus and water clouds, therefore it is neccessary to test how these would interact with the aerosol methods. Here, the simulations are setup in exactly the same way as in the previous section, but cirrus and water clouds are included in the scenes according to what the GEMS model estimates. Before any retrievals were performed the simulated scenes were cloud screened, where scenes were determined as clear if the O_2 A band retrieved surface pressure was within <20 hPa of the truth. The five different retrieval tests were performed on 3281 cloud screen exposures and quality filtered. The resulting statistics are given in Table 5.6. The new AOD method shows the lowest X_{CO2} bias and standard deviation, but the smallest number of exposures. The differences between the statistics of each test are quite small and all tests perform well on average (X_{CO2} bias <0.56 ppm).

Table 5.6. Retrieval statistics for each of the retrieval tests of aerosol/cirrus/cloud loaded simulated scenes.

Aerosol test	Number of screened retrievals	Δ X_{CO2} mean (ppm)	Δ X_{CO2} σ (ppm)
Current retrieval method (UoL-FP v3G)	1362	-0.49	2.02
Current retrieval method with the new scattering approach AOD	1331	-0.43	1.89
Current retrieval method with the new scattering approach aerosol profiles	1331	-0.55	2.09
Current retrieval method with the new scattering approach aerosol properties	1403	-0.51	2.01
New scattering approach method AOD, aerosol profiles and aerosol properties	1393	-0.56	1.97

Figure 5.38 shows the difference between true and retrieved X_{CO2} of each retrieval test to assess potential geographical biases. Some negative biases are found in all test results, suggesting there to be a small issue with the simulations. Large regional biases

are found over desert regions, such as the Sahara, in the current retrieval method (UoL-FP v3G), the new AOD method, and the new aerosol profile shapes method. This bias is significantly reduced when the new aerosol optical properties method is used or the new scattering approach method is used. Changing the aerosol optical depth and profile shape has little benefit to the simulated retrieval of X_{CO2} but using scene dependent aerosol optical properties provides a large improvement in X_{CO2}, as found in the previous section. However, this may not be true for real retrievals due to GOSAT instrument calibrations coupling with spectroscopy and aerosols.

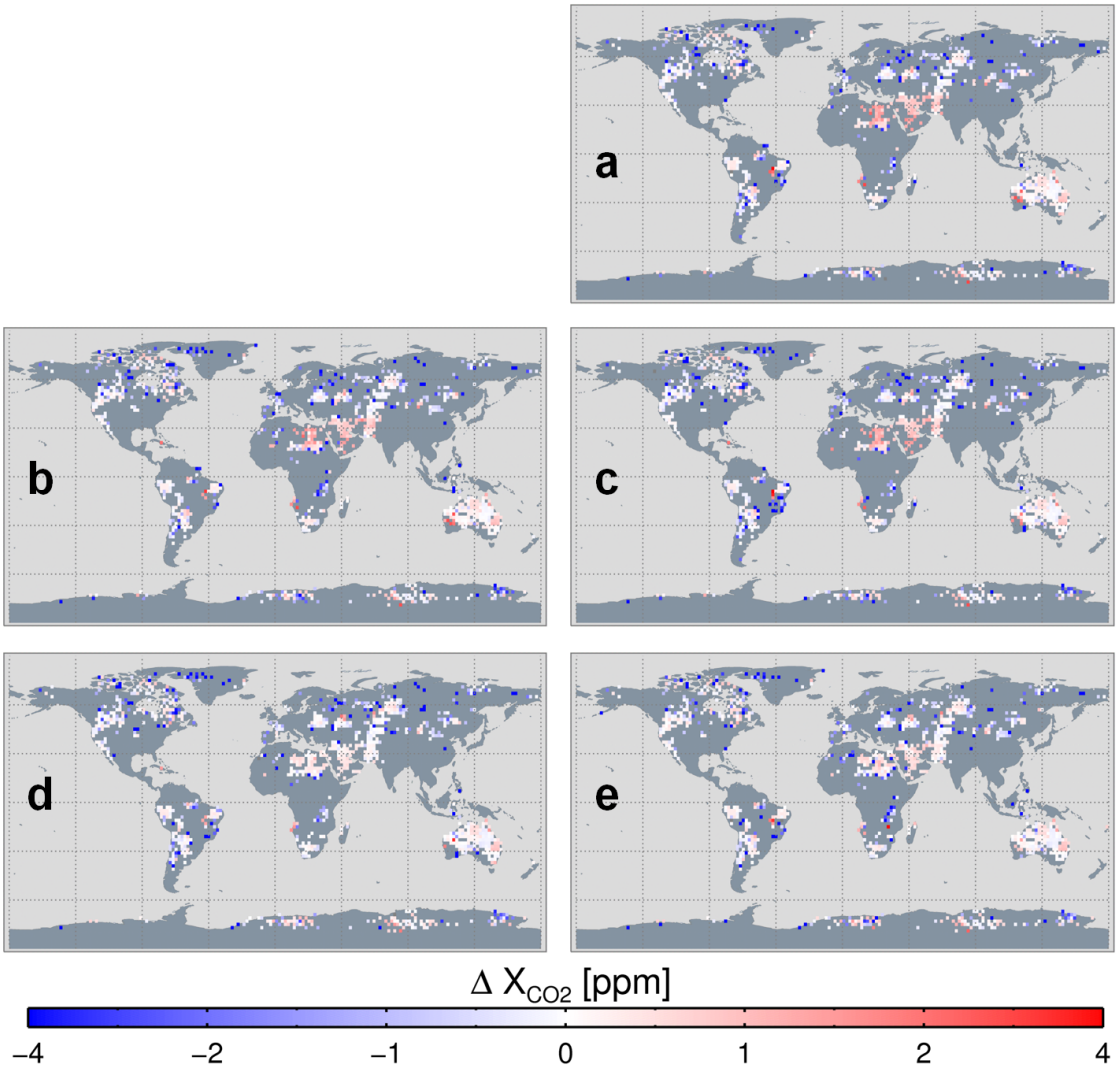

FIGURE 5.38. Difference between true and retrieved X_{CO2} of each retrieval test, where a is the current retrieval method with the new AOD, b is the current retrieval method, c is the current retrieval method with the new aerosol profile shapes, d is the new scattering approach method, and e is the current retrieval method with the new aerosol optical properties.

5.5.3 Verification with Satellite Based Simulations

Since GEMS data is used in both the simulations and the new scattering approach design it is a partially circular test, such that one would expect the new scattering approach to give high correlations. To break this circularity, completely independent aerosol information from CALIPSO was used in the simulations instead of GEMS. The calipso based simulations were cloud screened and then retrieved with each of the five tests.

A total of 4505 cloud screened exposures were retrieved and quality filtered (see Section for details) with the statistics given in Table 5.7. There is very little difference between the statistics of each test; X_{CO2} biases range between -0.08 to -0.01 ppm, the standard deviation of X_{CO2} ranges from 1.24 to 1.39 ppm, and the number of exposures range between 2997 and 3221. The current retrieval method (UoL-FP v3G) has the lowest X_{CO2} bias but the largest standard deviation. The new aerosol optical properties provide the largest number of exposures and the new scattering approach method gives the smallest standard deviation. However, the differences between tests are so small that a single test can not be justified as the best.

Table 5.7. Retrieval statistics for each of the retrieval tests of CALIPSO based aerosol/cloud/cirrus loaded simulated scenes.

Aerosol test	Number of screened retrievals	Δ X_{CO2} mean (ppm)	Δ X_{CO2} σ (ppm)
Current retrieval method (UoL-FP v3G)	3193	-0.01	1.39
Current retrieval method with the new scattering approach AOD	2998	-0.03	1.29
Current retrieval method with the new scattering approach aerosol profiles	2997	-0.08	1.30
Current retrieval method with the new scattering approach aerosol properties	3221	-0.03	1.29
New scattering approach method AOD, aerosol profiles and aerosol properties	3116	-0.05	1.24

Figure 5.39 shows the difference between the true and retrieved X_{CO2} of each retrieval test to assess potential geographical biases. The current retrieval method (UoL-FP v3G) retrieves lower X_{CO2} values over most of the world, except for over desert regions, such as the Sahara, where much higher values than the truth are retrieved. Similar biases are found in retrievals using the new AOD or new profiles. However, when the new aerosol optical properties are used the biases over the desert regions reduce, as well as the negative biases in other areas. Similarly, the new scattering approach method also gives reduced biases, suggesting that it is influenced mostly by the aerosol optical properties and less so by the profile shape and AOD. Hence, using scene dependent aerosol optical properties reduces geographical biases and thus gives an improvement in X_{CO2}. This concurs with the findings from the GEMS based simulations discussed in Sections 5.5.1 and 5.5.2.

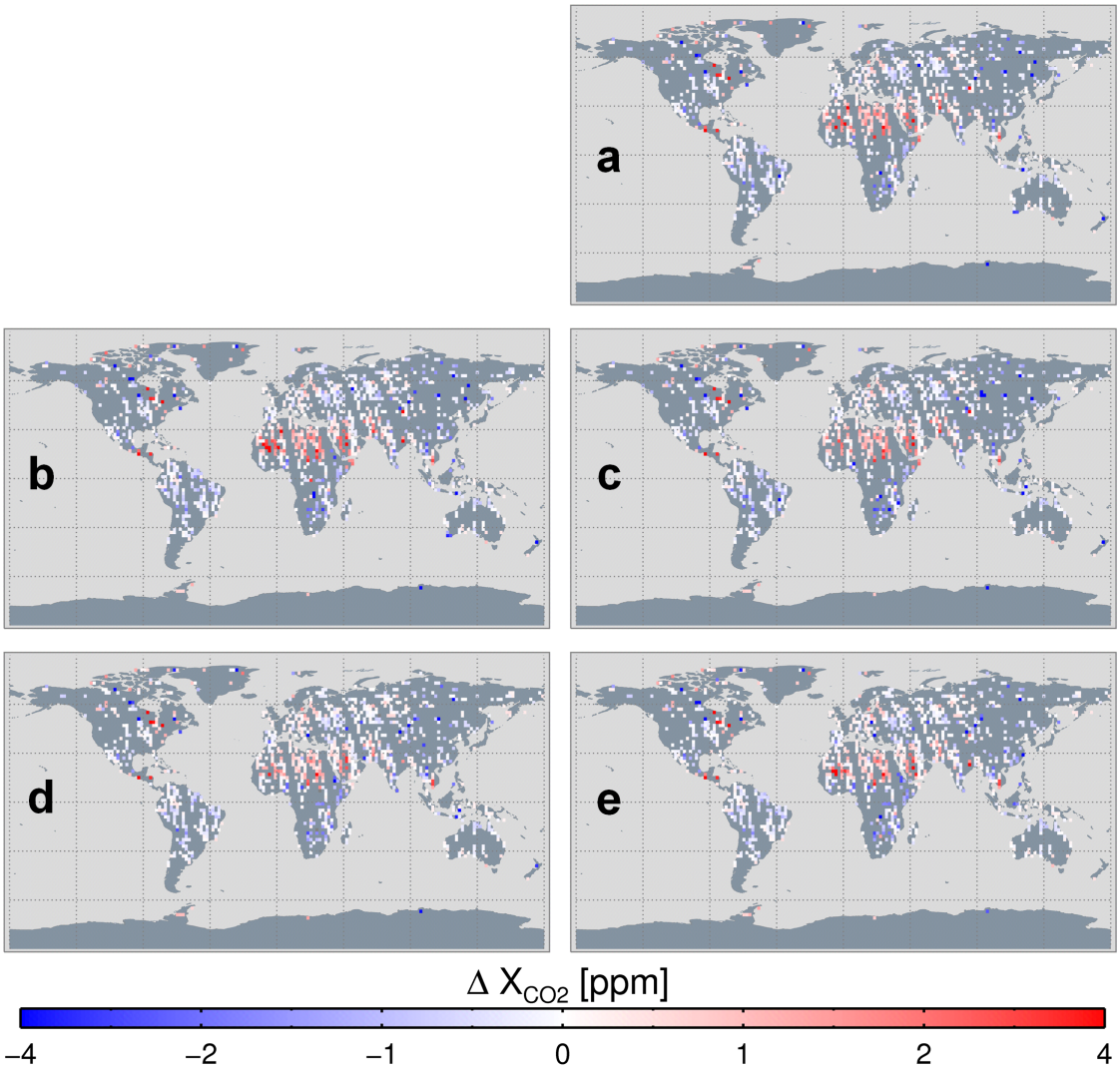

FIGURE 5.39. Difference between true and retrieved X_{CO2} of each retrieval test, where a is the current retrieval method with the new AOD, b is the current retrieval method, c is the current retrieval method with the new aerosol profile shapes, d is the new scattering approach method, and e is the current retrieval method with the new aerosol optical properties.

5.6 Application to GOSAT

Although the simulations show that using spatially dependent aerosol optical properties improves the current retrieval approach, the true outcome can only be found by testing it with real measurements. X_{CO2} was retrieved using the spatially dependent aerosol optical properties method (to be further known as UoL-FP v3.4G) for the same GOSAT data that was used in the UoL-FP v3G retrievals so that a direct comparison of the retrieved results was possible. This includes X_{CO2} retrieved over 7 different TCCON sites for a 2 year period and one year globally with a comparison to the GEOS-Chem model, as described in Chapter 4.

Figure 5.40 shows a comparison of X_{CO2} retrieved from GOSAT using the UoL-FP v3.4G method with X_{CO2} retrieved by the TCCON. The same TCCON sites and data have been used as that shown in Chapter 4. The mean GOSAT-TCCON bias of the UoL-FP v3.4G retrieval algorithm is found to be -0.18 ppm with a standard deviation of 2.45 ppm and correlation coefficient of 0.70. Compared to the results of UoL-FP v3G (see Chapter 4), this method shows a slightly lower bias but a slightly larger standard deviation and slightly worse correlation coefficient. Table 5.8 gives the statistics for the UoL-FP v3.4G retrieval method, showing that the number of retrieved exposures passing the post-screen is 4494, which is lower than that found for UoL-FP v3G. Similarly, the number of coincident exposures with TCCON is slightly less than that found for UoL-FP v3G. However, it should be noted that the post-screen was optimised for UoL-FP v3G and not for UoL-FP v3.4G, and could result in good retrievals being incorrectly filtered out. To avoid this potential issue, the GOSAT-TCCON bias retrieved for UoL-FP v3G and UoL-FP v3.4G were compared for only exposures that exist after post-screening in both datasets. This is shown in Figure 5.41, and it is found that the UoL-FP v3.4G method reduces the bias by -0.05 ppm. However, the bias is less important than geographical biases which can be assessed with a comparison to the GEOS-Chem 3-D chemistry transport model.

One year of global GOSAT data was retrieved using the UoL-FP v3.4G method. Figure 5.42 shows a comparison of each season between GOSAT and GEOS-Chem, with large scale features consistent with that previously found using UoL-FP v3G (see Chapter 4). However, in general, there are slightly more geographical biases than that found with UoL-FP v3G. Additionally, the zonal mean comparisons show slightly worse correlation coefficients, ranging between 0.62 and 0.94, with the majority of the differences being towards the poles.

The time series of UoL-FP v3.4G X_{CO2} from GOSAT and GEOS-Chem for a number

Table 5.8. Statistics for the UoL-FP v3.4G comparison to TCCON, where the bias, σ and r were calculated using coincident daily mean data.

TCCON site	Total from L1B	Passed pre-screen	Percent cloudy	Passed post-screen	Coincident days	Bias (ppm)	σ (ppm)	r (Pearson)
Bialystok (53.230° N)	29376	8321	61.16	295	46	-0.25	2.81	0.76
Bremen (53.100° N)	24054	5484	66.36	150	19	0.57	2.87	0.56
Orleans (47.970° N)	24047	9511	61.32	508	46	0.28	2.44	0.83
Park Falls (45.945° N)	33277	5785	55.52	315	69	-0.30	1.84	0.84
Lamont (36.604° N)	30984	9888	39.44	1837	235	-0.32	2.37	0.66
Darwin (12.424° S)	17273	4511	39.64	916	53	-1.21	2.42	-0.11
Wollongong (34.406° S)	13182	4971	50.45	473	57	0.94	2.58	0.31
Total	172193	48471	53.57	4494	525	-0.18	2.45	0.70

of different regions are shown in Figure 5.43. The seasonal cycle is found to match very well between GOSAT and GEOS-Chem for both northern and southern hemispheres, but a difference of 1.59 ppm is observed in the northern hemisphere throughout the year and a smaller difference of 0.79 ppm in the southern hemisphere, which are both larger than that found with UoL-FP v3G. GOSAT and GEOS-Chem X_{CO2} show a high consistency for both Europe and the USA, with a X_{CO2} difference of -0.43 ppm and -0.16 ppm and correlation coefficients of 0.69 and 0.72, respectively. These values are similar to that observed with UoL-FP v3G, as is that of South Asia, which on average, GOSAT and GEOS-Chem agree with a mean difference of -0.27 ppm and correlation coefficient of 0.70, but differences are viewed in the seasonal cycle with GEOS-Chem over-estimating the X_{CO2} in autumn 2009 and under-estimating during spring 2010.

The retrieved X_{CO2} over the Amazon shows a small improvement (compared to UoL-FP v3G) with the bias reducing to 1.17 ppm and standard deviation reducing to 3.31 ppm. Similarly, the bias and standard deviation over NW Russia is improved with values of -0.38 ppm and 3.58 ppm, respectively. Tropical Africa remains very similar to that of UoL-FP v3G.

In central Asia where a desert region is observed with the high gain mode, the seasonal cycle of GOSAT and GEOS-Chem is observed to agree well (r=0.73), but consistently with a $\sim$2 ppm difference in value, similar to that of UoL-FP v3G. Also, a $\sim$3 ppm mean difference is found over the Sahara between GOSAT and GEOS-Chem

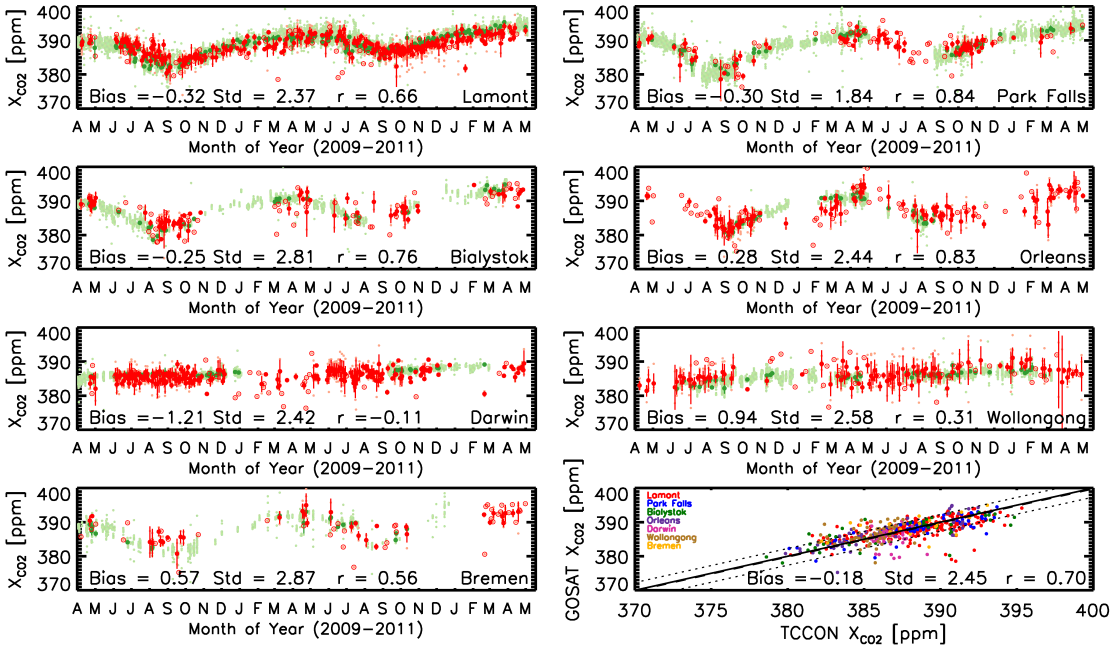

FIGURE 5.40. Comparison of UoL-FP v3.4G retrieved X_{CO2} from GOSAT with retrieved X_{CO2} from seven TCCON site for coincident cloud-screened observations within 2 hours and 5° between April 2009 and May 2011. All TCCON data shown in light green, coincident daily mean TCCON shown in dark green, all GOSAT data shown in light red and daily mean GOSAT shown in dark red (with daily mean points with only one value per day are represented by open circles). The average difference between the daily means is given as the bias (ranging from -1.21 to 0.94 ppm), the standard deviation of daily means by the Std (between 1.84 and 2.87 ppm) and the correlation coefficient of daily means by r (-0.11 at Darwin to 0.84 at Park Falls). The lower right panel gives the correlation of daily mean coincident retrieved GOSAT X_{CO2} with daily mean TCCON X_{CO2} within ±2 hours for the seven sites. This gives an overall bias of -0.18 ppm, scatter of 2.45 ppm and correlation of 0.70 between GOSAT and TCCON X_{CO2}.

X_{CO2} where a desert region is observed with the medium gain mode, but the seasonal cycle agrees well with a correlation coefficient of 0.76. Australia, which comprises partially of desert and is observed partially with medium and high gain modes, also shows a difference in X_{CO2} between GOSAT and GEOS-Chem with a value of -1.14 ppm. No improvement is observed in any of these desert regions, compared to UoL-FP v3G.

In the UoL-FP v3G retrievals, X_{CO2} biases were found with most parameters (see Chapter 4). Figure 5.44 shows a comparison of UoL-FP v3G and UoL-FP v3.4G results for correlations of X_{CO2} with various retrieval parameters. The UoL-FP v3.4G method significantly reduces all of these parameter biases, indicating that the retrieval performs

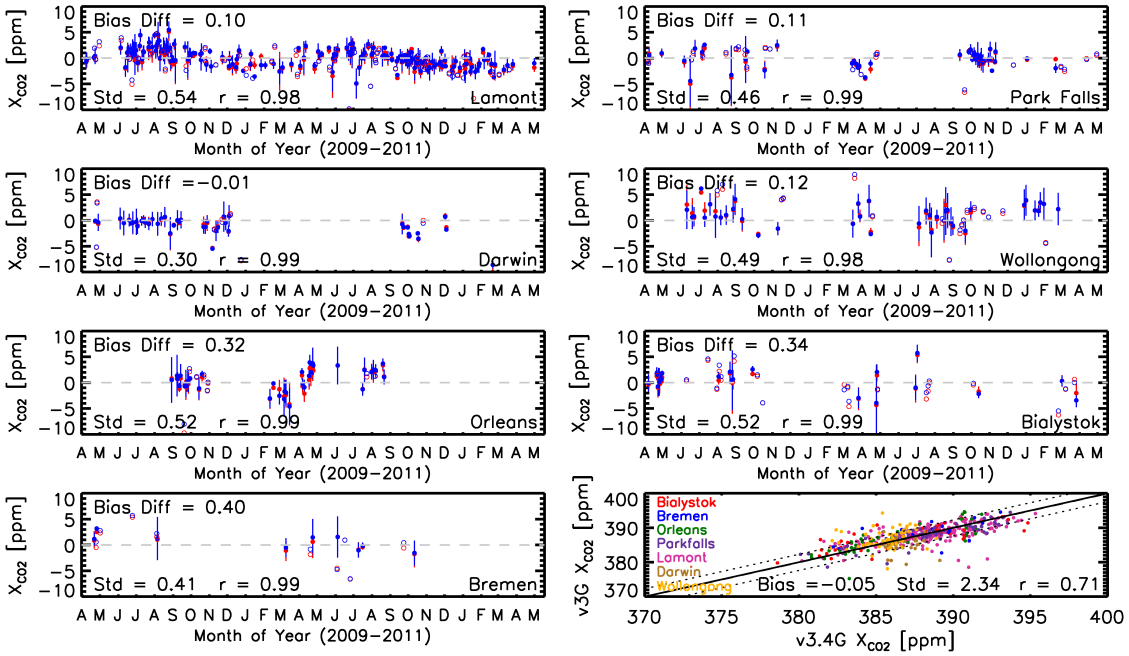

FIGURE 5.41. Comparison of the point-by-point biases of UoL-FP v3G and UoL-FP v3.4G retrieved X_{CO2} from GOSAT with retrieved X_{CO2} from seven TCCON site for coincident cloud-screened observations within 2 hours and 5° between April 2009 and May 2011. UoL-FP v3G daily mean GOSAT-TCCON bias is shown in red (with daily mean points with only one value per day are represented by open circles). Similarly, the UoL-FP v3.4G daily mean GOSAT-TCCON bias is shown in blue. The average bias difference ranges from -0.01 to 0.40 ppm, the standard deviation (Std) ranges between 0.30 and 0.54 ppm, and the correlation coefficient (r) has a station-to-station range of 0.98 to 0.99. The lower right panel gives the correlation of the daily mean biases and shows an overall bias difference of -0.05 ppm, scatter of 2.34 ppm and correlation of 0.71 between UoL-FP v3G and UoL-FP v3.4G. Hence, this shows UoL-FP v3.4G improves the X_{CO2} slightly.

much better. In Chapter 4, a bias correction scheme was introduced that attempts to correct the retrieved X_{CO2} using four parameters that correlate most with the X_{CO2} bias. Figure 5.44 shows the correlation of these parameters with X_{CO2} for the UoL-FP v3G method and the UoL-FP v3.4G method. This shows that the UoL-FP v3.4G method virtually removes the band 1 albedo slope bias and the band 2 / band 3 mean signal bias, suggesting that these biases were not spectroscopy/signal related but actually aerosol related biases and are corrected using this method. The biases with ice optical depth and surface pressure difference still exist, indicating that these may not be related to aerosols. The ice optical depth bias may potentially be due to the retrieval algorithm not accounting sufficiently for cirrus/clouds, which has been shown to create X_{CO2} biases

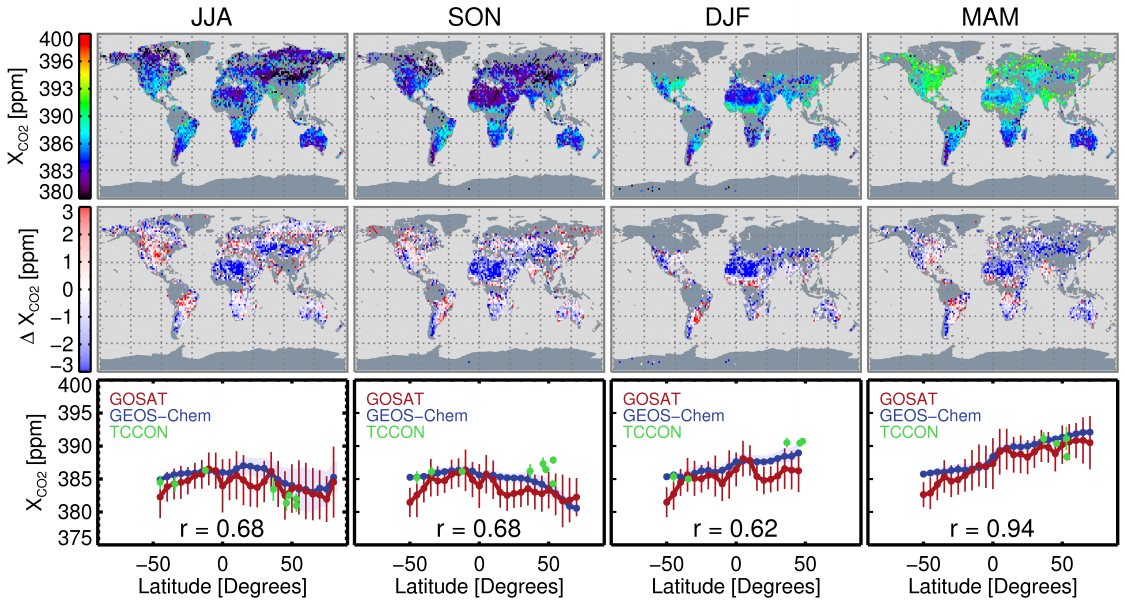

FIGURE 5.42. Comparison of UoL-FP v3.4G X_{CO2} retrieved from GOSAT and X_{CO2} calculated from GEOS-Chem CO_2 profiles convolved with the scene-specific GOSAT averaging kernel. For each season, GOSAT is shown at the top, the difference between GOSAT and GEOS-Chem in the middle, and a zonal mean comparison of them at the bottom. The global maps indicate the largest differences are observed over desert regions, such as the Sahara and central Asia. The zonal mean comparison shows a good agreement between GOSAT and GEOS-Chem, but worse than that observed with UoL-FP v3G (see Figure 4.11. It also includes the average TCCON X_{CO2} from each site which in general agrees, with observed differences mostly due to zonal averaging of GOSAT/GEOS-Chem data.

(see Section 5.3).

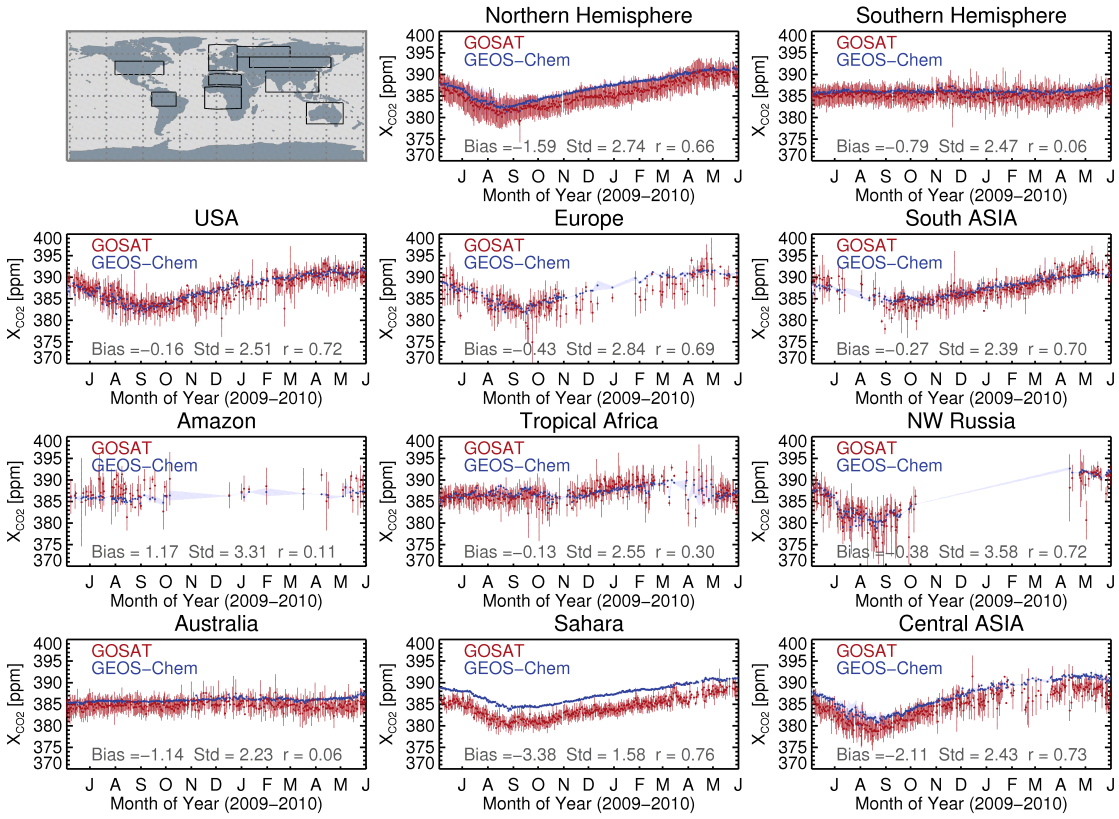

FIGURE 5.43. Comparison of UoL-FP v3.4G X_{CO2} retrieved from GOSAT and X_{CO2} calculated from GEOS-Chem CO_2 profiles convolved with the scene-specific GOSAT averaging kernel, for a number of different regions between June 2009 and May 2010. The locations of these regions are indicated on the map by the black boxes (top left). The top centre and top right panels give the time series of GOSAT and GEOS-Chem data for the northern and southern hemispheres, showing the seasonal cycle to be well matched but with GOSAT data offset lower by -1.59 ppm in the northern hemisphere and -0.79 ppm in the southern hemisphere. The second row of plots show a very good agreement between GOSAT and GEOS-Chem both in value and seasonality for regions containing urban environments. Below these, the time series of forested regions are shown, with GOSAT reproducing the GEOS-Chem data very well but with a larger scatter and fewer data points. The bottom panels show the time series for 3 different desert regions, with GOSAT matching the seasonal cycle of GEOS-Chem very well but offset lower in value from -1.14 to -3.38 ppm.

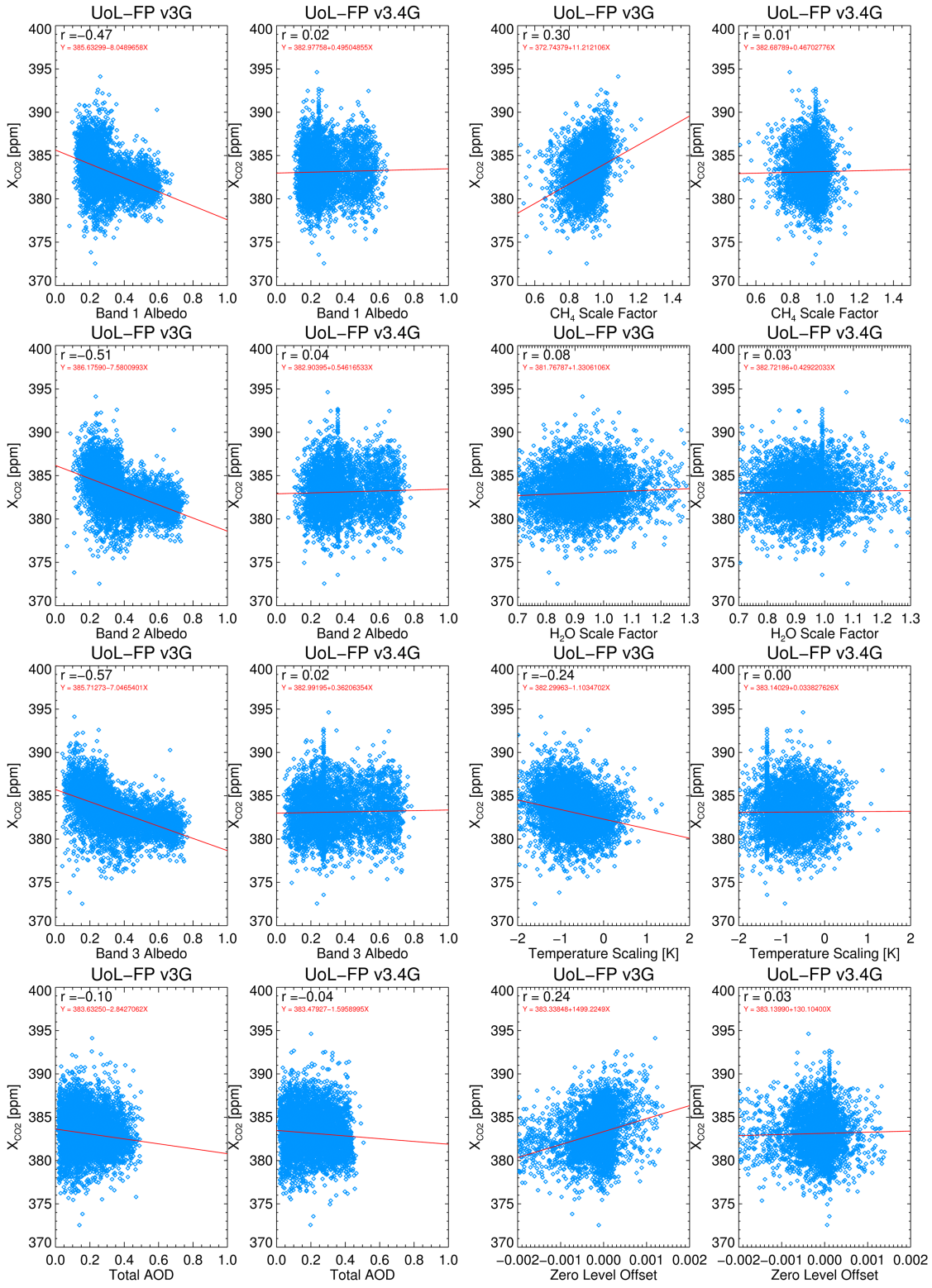

FIGURE 5.44. Comparison of UoL-FP v3G and UoL-FP v3.4G results for correlations of X_{CO2} with various retrieval parameters. The blue diamonds represent the data, the red line gives a linear fit of the data with the equation of the fit given in red, and the correlation coefficient is given by r.

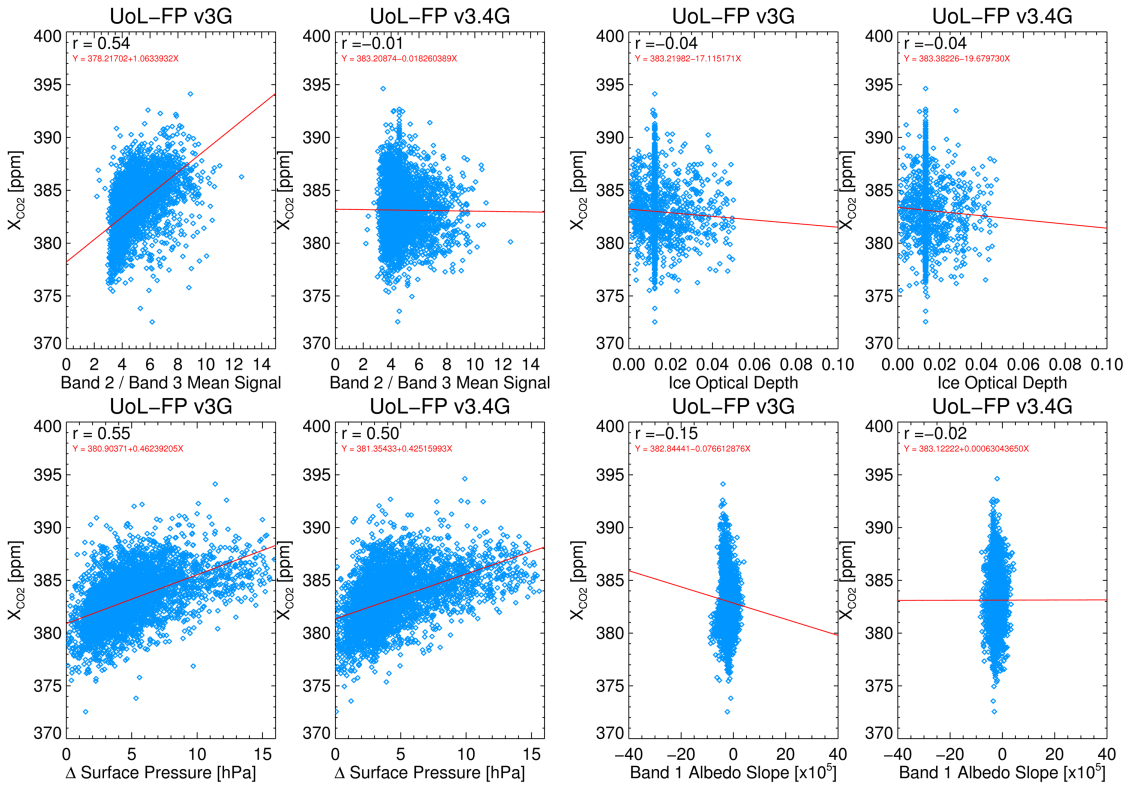

FIGURE 5.45. Comparison of UoL-FP v3G and UoL-FP v3.4G results for correlations of X_{CO2} with each of the parameters previously used for the bias correction. The blue diamonds represent the data, the red line gives a linear fit of the data with the equation of the fit given in red, and the correlation coefficient is given by r.

5.7 Scattering Conclusion

A flexible simulation algorithm was designed and used to test how various aerosol and cloud components effect retrievals of X_{CO2}. The aerosol properties were found to have the largest effect on X_{CO2}. The simulator was also used to test different aerosol setups in the retrieval of X_{CO2}, finding that spatially dependent AOD and profile shapes do not reduce the X_{CO2} bias. However, spatially dependent aerosol optical properties show an improvement in the X_{CO2} retrieved, with the bias and scatter reduced. Therefore, a new approach was applied to real retrievals of X_{CO2} from GOSAT where the aerosol optical properties were replaced with spatially dependent aerosol optical properties. A comparison with seven different TCCON sites showed that the new approach reduces the bias slightly. A comparison with GEOS-Chem showed that the geographical biases are not improved. This may be due to potential problems with instrument calibration and spectroscopy that are coupled with aerosols in the retrieval of X_{CO2}. However, the biases observed in different retrieval parameters, such as the band 1 albedo slope and the ratio of band 2 to band 3 mean signal, have been significantly reduced and thus suggests the new method removes some of the biases, but not all.

Chapter 6

Conclusions

6.1 Assessment of GOSAT retrievals

CO_2 retrievals with high accuracy and precision from satellites is a major challenge but can be of great benefit for the understanding of the carbon cycle. Here, an existing optimal estimation retrieval algorithm developed for the OCO mission was modified and applied to retrieved CO_2 from SWIR radiances observed by the Japanese GOSAT satellite. The main developments of the algorithm included the setup of the instrument and retrieval strategy as well as creation of the pre-processing, cloud screen and post-processing aspects. These advancements set the algorithm apart from the original and was therefore named as the UoL-FP retrieval algorithm.

The algorithm has successfully retrieved X_{CO2} from GOSAT observations for over two years. Comparisons were performed to observations by the TCCON ground based network with a mean smoothing error difference of -0.14 ppm. The single sounding precision was found to be between 2.04 and 2.96 ppm and the bias between -0.87 and 0.77 ppm for seven TCCON sites distributed in the USA, Europe and Australia. Using a stricter post-screen improves the comparison by reducing the single sounding precison to 1.50 to 2.15 ppm and the bias to -0.6 to 0.7 ppm, but at the cost of the number of exposures. The mean bias inferred from TCCON comparisons is very accurate with mean biases approaching only a few tenths of a ppm, which is close to typical retrieval requirements of systematic bias for X_{CO2} (e.g. Chevallier 2007b, Chevallier et al. 2009, Miller et al. 2007). Future improvements in spectroscopy, instrument calibration and atmospheric scattering are expected to provide improved results.

Global seasonal comparisons of retrieved X_{CO2} from GOSAT to model calculations of the GEOS-Chem 3D chemistry transport model are demonstrated. A correlation of

0.61 was determined between GOSAT and GEOS-Chem, with a correlation of 0.76 for the latitudinal gradient. A high level of consistency between GOSAT and GEOS-Chem was observed over expected source regions for both the seasonal cycles and amplitudes of X_{CO2}. Large biases were found over central Asia and the Sahara, but with the development of a bias correction scheme these were significantly reduced.

To further improve and test the retrieval algorithm, a simulator was built to allow multiple retrieval approaches to be tested and was initially used to analyse the effects of aerosols and clouds on the retrieval of X_{CO2}. It was further used to develop a new scattering method for use in the X_{CO2} retrievals based on aerosol information from the GEMS model. This new method was applied to real GOSAT X_{CO2} retrievals and a comparison to TCCON gave an improvement of 0.02 ppm for the bias. Although a global comparison with the GEOS-Chem model showed the geographical biases to become slightly worse towards the poles, the biases of some retrieval parameters largely improved. This simulator has provided a framework for future retrieval algorithm developments.

6.2 Outlook

6.2.1 Future Implications

The X_{CO2} retrievals approach the point where they should be useful for the inversion of CO_2 surface fluxes with data assimilation methods (e.g. Baker et al. 2010, Chevallier et al. 2009, Feng et al. 2009). If assimilated into chemistry transport models, the high density of globally inferred X_{CO2} from GOSAT has the potential to reduce model uncertainties of surface fluxes, especially over regions poorly sampled by ground-based measurements. This could lead to an improved quantification of terrestrial CO_2 sources and sinks, and therefore a better understanding of the carbon cycle. This would allow more accurate predictions of future climate change and improved methods of adaptation. Furthermore, as government legislations, both national and international, aim to reduce future emissions of CO_2, accurate predictions of global CO_2 fluxes using satellite data could allow improved policies and global monitoring.

6.2.2 Retrieval algorithm development

Improving the retrieval algorithm is an ongoing task and there are many ways that it could be done. Any enhancement upon the existing spectroscopy would clearly be beneficial.

The a priori could also be improved, for example having the CO_2 profiles for years surpassing 2009 would provide better spatial estimates as it would include the biomass burning for the actual years.

Although the aerosol approach has already been further developed, there is still other options that could be explored that might prove to be superior. Such options might include; deriving aerosol information from TANSO-CAI as this would provide it exactly for the TANSO-FTS observation location and time, using an alternative aerosol model (e.g. SPRINTARS (Takemura et al. 2003)), or using generic small, medium and large sized aerosol particles for the scattering properties as this could give a more flexible scheme. The use of TANSO-CAI observations has been limited so far by data storage constraints. However, with increased storage capabilities this data could potentially provide information including; aerosol optical depth, aerosol type, cloud optical depth, cloud type, and aerosol/cloud distribution within the IFOV. TANSO-CAI could then also be used as an alternative cloud screening method as demonstrated by Taylor et al. (2012), allowing the possibility of comparing cloud fraction with X_{CO2}.

The simulator could be used to test many different retrieval designs, including new approaches of aerosols, cirrus clouds and water clouds as well as retrieval algorithm variations, such as using alternative spectral bands or different state vector parameters. For this reason, the simulator could also be further developed to provide more realistic simulations of scenes. This could involve albedo, topographic, aerosol, cirrus, and cloud variations across the IFOV.

Possible ways to improve the present X_{CO2} could be to apply a new bias correction method or to advance the pre/cloud/post-screens. Finally, performing more detailed inter-comparisons with alternative retrieval algorithms could indicate possible retrieval algorithm dependent issues that could be improved.

6.2.3 Future missions

Whilst GOSAT was the first greenhouse gas dedicated satellite, there are many more future missions currently planned. The next satellite that will allow CO_2 to be retrieved will be the Orbiting Carbon Observatory 2 (OCO-2) satellite through the NASA Earth System Science (ESSP) program, for launch in 2014. OCO-2 will include one instrument consisting of three high resolution grating spectrometers that will observe O_2 and CO_2 absorption bands with a spatial resolution of 1 x 1.5 km^2 and swath width of 10 km. This high spatial resolution instrument has the potential to make observations in the small gaps between clouds, thus providing more measurements globally.

It is proposed that in 2015/2016 the Tropical Carbon Mission (TCM) may launch, which is a bilateral Earth Observation mission between the UK and US space agencies. It will contain a NASA Orbiting Carbon Observatory 3 (OCO) instrument and a UK Carbon Monoxide and Methane Spectrometer (CMS). It will measure between $\pm$ 35° latitude and will reduce sampling biases from clouds and the diurnal CO_2 cycle by using a precessing orbit at 430 km altitude and 35° inclination. This is proposed to complement the OCO-2 mission by providing more measurements over the tropical regions.

There will be a GOSAT-2 satellite launching in 2016. Its design specifications will be finalised this year, but it will likely be of similar design to GOSAT. This would have the benefit of globally repeating measurements over the same locations, but with the disadvantage of limited coverage.

The Carbon Monitoring Satellite (CarbonSat) is planned to be launched in 2018 as part of the ESA Earth Explorer Opportunity Missions (EE-8). CarbonSat will comprise of two instruments; a Cloud and Aerosol Imager (CAI) and an Imaging Spectrometer (IS) that will observe radiances in the O_2, CH_4 and CO_2 absorption bands. It will have a spatial resolution of 2 x 2 km^2 and swath of 500 km, providing a very large coverage and highly dense dataset of observations globally.

For possible launch in 2018 is the MicroCarb satellite being developed as part of the CNES microsatellite series. The instrument design will either be a scattering grating spectrometer or a static Fourier Transform interferometer and will measure radiances in the O_2 and CO_2 absorption bands. If this mission proves beneficial it could lead to a constellation of microsatellites providing increased sampling.

The last mission currently planned is the Active Sensing of CO_2 Emissions over Night, Days and Seasons (ASCENDS) satellite for launch in 2021 or later as a NASA Earth science decadal survey study. ASCENDS is currently planned to use laser-based differential absorption of O_2 and CO_2. This active method would allow observations to be made at night time, at high latitudes and through all seasons irrespective of how much cloud exists. For improved flux interpretation, it is planned to also contain a passive CO sensor.

The present retrieval algorithm and simulator were designed with a flexible scheme to allow alternative instruments to be used. Therefore, these could potentially be used with any of the future missions, allowing the development of a long-term dataset of X_{CO2}.

6.2.4 Final comments

This thesis describes a new retrieval algorithm capable of inferring X_{CO2} from remotely sensed SWIR satellite observations. A comparison with coincident ground-based TCCON measurements shows that with strict filtering the retrieval algorithm should be sufficient to allow improved surface flux estimates (e.g., Chevallier 2007b, Chevallier et al. 2009, Miller et al. 2007). Furthermore, over TCCON sites the X_{CO2} retrieval is very accurate with biases approaching only a few tenth ppm, which is close to typical retrieval requirements of systematic bias for X_{CO2} (e.g. Chevallier 2007b, Chevallier et al. 2009, Miller et al. 2007).

The latest results from other algorithms (Bril et al. 2007, Yokota et al. 2009, Butz et al. 2011, Morino et al. 2011, Wunch et al. 2011b, Yoshida et al. 2010, Crisp et al. 2012, Oshchepkov et al. 2012a) find similar results with a variation in the number of soundings potentially due to the screening criteria applied. However, over desert regions, which are not observed by TCCON, it is found that the retrieved X_{CO2} from GOSAT shows significant (up to $\sim$3 ppm) differences when compared to GEOS-Chem model calculations which are believed to be biases in the GOSAT retrieval. Similar findings have been reported in Crisp et al. (2012) who suggested that these biases are related to instrument gain. Although here, biases are observed for desert regions observed with both settings of the instrument gain, showing that these biases are only partially due to gain and this leads to the speculation that these biases could be introduced by desert dust or related to the high surface albedo in the CO_2 bands. This study highlights the need for further algorithm improvements, especially over the deserts. However, except for the desert regions, the X_{CO2} retrievals approach the point where they should be useful for the inversion of CO_2 surface fluxes with data assimilation methods (e.g. Baker et al. 2010, Chevallier et al. 2009, Feng et al. 2009), which could then lead to a better understanding of the carbon cycle and improvements in future climate predictions.

Finally, this thesis also describes new simulator that can be used for the development of SWIR retrieval algorithms. Its use has been demonstrated for testing new scattering methods for retrievals of X_{CO2} from GOSAT, but the flexibility of the simulator design is such that it could be applied to future missions.

Bibliography

Abdou, W. A., Martonchik, J. V., Kahn, R. A., West, R. A. & Diner, D. J. (1997), 'A modified linear-mixing method for caculating atmospheric path radiances of aerosol mixtures', *Journal of Geophysical Research* **102**(D14), 16883–16888.

Ackerman, S. A., Strabala, K. I., Menzel, W. P., Frey, R. A., Moeller, C. C. & Gumley, L. E. (1998), 'Discriminating clear-sky from clouds with modis', *Journal of Geosphysical Research* **103**(D24), 32141–32157.

Ackerman, T. P. & Stokes, G. M. (2003), 'The atmospheric radiation measurement program', *Physics Today* **56**(1), doi:10.1063/1.1554135.

Ahmadav, R., Gerbig, C., Kretschmer, R., Korner, S., Rodenbeck, C., Bousquet, P. & Ramonet, M. (2009), 'Comparing high resolution wrf-vprm simulations and two global co_2 transport models with coastal tower measurements of co_2', *Biogeosciences* **6**, 807–817.

ARM (2011a), *Temperature, Humidity, Wind, and Pressure System Handbook, ARM Climate Research, Facility*.

ARM (2011b), *TWP MET Instrument Details, ARM Surface Meteorology Systems, ARM Climate Research, Facility*.

Baines, S. J. & Worden, R. H. (2004), 'Geological storage of carbon dioxide', *Geological Society, Special Publication* **233**.

Baker, D. F., Boesch, H., Doney, D. C., O'Brien, D. & Schimel, D. S. (2010), 'Carbon source/sink information provided by column co_2 measurements from the orbiting carbon observatory', *Journal of Atmospheric Chemisty and Physics* **10**, 4145–4165.

Baker, D. F., Doney, A. S., & Schimel, D. S. (2006b), 'Variational data assimilation for atmospheric co_2', *Tellus* **58B**, 359–365.

Barkley, M. P., Friesz, U. & Monks, P. S. (2006a), 'Measuring atmospheric co_2 from space using full spectral initiation (fsi) wfm-doas', *Journal of Atmospheric Chemisty and Physics* **6**, 3517–3534.

Barkley, M. P., Monks, P. S. & Engelen, R. J. (2006), 'Comparison of sciamachy and airs co_2 measurements over north america during the summer and autumn of 2003', *Geophysical Research Letters* **33**(L20805), doi:10.1029/2006GL026807.

Barkley, M. P., Monks, P. S., Friesz, U., Mittermeier, R. L., Fast, H., Korner, S. & Heimann, M. (2006b), 'Comparisons between sciamachy atmospheric co_2 retrieved using (fsi) wfm-doas to ground based ftir data and the tm3 chemistry transport model', *Journal of Atmospheric Chemistry and Physics* **6**, 4483–4498.

Baum, B. A., Heymsfield, A. J., Yang, P. & Bedka, S. T. (2005a), 'Bulk scattering properties for the remote sensing of ice clouds. part i: Microphysical data and models', *Journal of Applied Meteorology* **44**, 1885–1895.

Baum, B. A., Yang, P., Heymsfield, A. J., Platnick, S., King, M. D., Hu, Y. X. & Bedka, S. T. (2005b), 'Bulk scattering properties for the remote sensing of ice clouds. part ii: Narrowband models', *Journal of Applied Meteorology* **44**, 1896–1911.

Benedetti, A. (2010), 'Gems aerosol property information', *Personal Communication* .

Boesch, H., Baker, D., Connor, B., Crisp, D. & Miller, C. (2011), 'Global characterization of co_2 column retrievals from shortwave-infrared satellite observations of the orbiting carbon observatory-2 mission', *Journal of Remote Sensing* **3**(2), 270–304.

Boesch, H., Toon, G. C., Sen, B., Washenfelder, R. A., Wennberg, P. O., Buchwitz, M., de Beek, R., Burrows, J. P., Crisp, D., Christi, M., Connor, B. J., Natraj, V., & Yung, Y. L. (2006), 'Space-based near-infrared co_2 measurements: Testing the orbiting carbon observatory retrieval algorithm and validation concept using sciamachy observations over park falls, wisconsin', *Journal of Geophysical Research* **111**(D23302), doi:10.1029/2006JD007080.

Bopp, L., Qu*é*r*é*, C. L., Heimann, M., Manning, A. C. & Monfray, P. (2002), 'Climate-induced oceanic oxygen fluxes: Implications for the contemporary carbon budget', *Global Biogeochemical Cycles* **16**(1022), doi:10.1029/2001GB001445.

Bousquet, P., Ciais, P., Peylin, P., Ramonet, M. & Monfray, P. (1999), 'Inverse modeling of annual atmospheric co_2 sources and sinks 1. method and control inversion', *Journal of Geophysical Research* **104**(D21), 26161–26178.

Bovensmann, H., Burrows, J. P., Buchwitz, M., Frerick, J., Noel, S., Rozanov, V. V., Chance, K. V. & Goede, A. (1999), 'Sciamachymission objectives and measurement modes', *Journal of Atmospheric Science* **56**, 127–150.

Bril, A., Oshchepkov, S., Yokota, T. & Inoue, G. (2007), 'Parameterization of aerosol and cirrus cloud effects on reflected sunlight spectra measured from space: application of the equivalence theorem', *Journal of Applied Optics* **46**(13), 2460–2470.

Buchwitz, M., Chevallier, F., Bergamaschi, P., Aben, I., Boesch, H., Hasekamp, O., Notholt, J., Reuter, M. & et al. (2011), *User Requirements Document for the GHG-CCI project of ESAs Climate Change Initiative, pp. 45, version 1, 3. February 2011.*

Buchwitz, M., de Beek, R., Noel, S., Burrows, J. P., Bovensmann, H., Bremer, H., Bergamaschi, P., Korner, S. & Heimann, M. (2005), 'Carbon monoxide, methane and carbon dioxide columns retrieved from sciamachy by wfm-doas: Year 2003 initial data set', *Journal of Atmospheric Chemistry and Physics* **5**, 3313–3329.

Burton, M. R., Oppenheimer, C., Horrocks, L. A. & Francis, P. W. (2000), 'Remote sensing of co_2 and h_2o emission rates from masaya volcano, nicaragua', *Geology* **28**(10), 915–918.

Butz, A., Guerlet, S., Hasekamp, O., Schepers, D., Galli, A., Aben, I., Frankenberg, C., Hartmann, J. M., Tran, H., Kuze, A., Aleks, G. K., Toon, G., Wunch, D., Wennberg, P., Deutscher, N., Griffith, D., Macatangay, R., Messerschmidt, J., Notholt, J. & Warneke, T. (2011), 'Toward accurate co_2 and ch_4 observations from gosat', *Journal of Geophysical Research Letters* (L14812), doi:10.1029/2011GL047888.

Canadell, J. G., Qu$\acute{e}$r$\acute{e}$, C. L., Raupach, M. R., Field, C. B., Buitenhuis, E., Ciais, P., Conway, T. J., Gillett, N. P., Houghton, R. A. & Marland, G. (2007), 'Contributions to accelerating atmospheric co_2 growth from economic activity, carbon intensity, and efficiency of natural sinks', *Proceedings of the National Academy of Sciences USA* **104**, 18870–18886.

Chadwick, A., Holloway, S. & Riley, N. (2000), 'Deep co_2 sequestion offshore, a provable greenhouse mitigation strategy', *Offshore Magazine* pp. 134–135.

Chahine, M. T., L.Chen, Dimotakis, P., Jiang, X., Li, Q., Olsen, E. T., Pagano, T., Randerson, J. & Yung, Y. L. (2008), 'Satellite remote sounding of mid-tropospheric co_2', *Journal of Geosphysical Research Letters* **35**(L17807), doi:10.1029/2008GL035022.

Chedin, A., Serrar, S., Scott, N. A., Crevoisier, C. & Armante, R. (2003), 'First global measurement of midtropospheric co_2 from noaa polar satellites: Tropical zone', *Journal of Geophysical Research* **108**(D18, 4581), doi:10.1029/2003JD003439.

Chevallier, F. (2007b), 'Impact of correlated observation errors on inverted co_2 surface fluxes from oco measurements', *Journal of Geophysical Research Letters* **34**(L24804), doi:10.1029/2007GL030463.

Chevallier, F., Bréon, F. M. & Rayner, P. J. (2007a), 'Contribution of the orbiting carbon observatory to the estimation of co_2 sources and sinks: Theoretical study in a variational data assimilation framework', *Journal of Geophysical Research* **112**(D09307), doi:10.1029/2006JD007375.

Chevallier, F., Engelen, R. J. & Peylin, P. (2005a), 'The contribution of airs data to the estimation of co_2 sources and sinks', *Journal of Geophysical Research Letters* **32**(L23801), doi:10.1029/2005GL024229.

Chevallier, F., Fisher, M., Peylin, P., Serrar, S., Bousquet, P., Breon, F. M., Chedin, A. & Ciais, P. (2005b), 'Inferring co_2 sources and sinks from satellite observations: Method and application to tovs data', *Journal of Geophysical Research* **110**(D24309), doi:10.1029/2005JD006390.

Chevallier, F., Maksyutov, S., Bousquet, P., Bréon, F. M., Saito, R., Yoshida, Y. & Yokota, T. (2009), 'On the accuracy of the co_2 surface fluxes to be estimated from the gosat observations', *Journal of Geophysical Research Letters* **36**(L19807), doi:10.1029/2009GL040108.

Christi, M. J. & Stephens, G. L. (2004), 'Retrieving profiles of atmospheric co_2 in clear sky and in the presence of thin cloud using spectroscopy from the near and thermal infrared: A preliminary case study', *Journal of Geophysical Research* **109**(D04316), doi:10.1029/2003JD004058.

Connor, B. (2010), 'Acos noise coefficients', *Personal Communication* .

Connor, B. J., Boesch, H., Toon, G., Sen, B., Miller, C. & Crisp, D. (2008), 'Orbiting carbon observatory: Inverse method and prospective error analysis', *Journal of Geophysical Research* **113**(D05305), doi:10.1029/2006JD008336.

Crevoisier, C., Chedin, A., Matsueda, H., Machida, T., Armante, R. & Scott, N. A. (2009), 'First year of upper tropospheric integrated content of co_2 from iasi hyperspectral infrared observations', *Journal of Atmospheric Chemistry and Physics* **9**, 4797–4810.

Crisp, D., Fisher, B. M., O'Dell, C., Frankenberg, C., Basilio, R., Boesch, H., Brown, L. R., Castano, R., Connor, B., Deutscher, N. M., Eldering, D., Griffith, D., Gunson, M., Kuze, A., Mandrake, L., McDuffie, J., Messerschmidt, J., Miller, C. E., Morino, I., Natraj, V., Notholt, J., O'Brien, D., Oyafuso, F., Polonsky, I., Robinson, J., Salawitch, R., Sherlock, V., Smyth, M., Suto, H., Taylor, T., Thompson, D. R., Wennberg, P. O., Wunch, D. & Yung, Y. L. (2012), 'The acos x_{CO2} retrieval algorithm, part 2: Global x_{CO2} data characterization', *Atmospheric Measurement Techniques Discussions* **5**, 1–60.

den Elzen, M. G. J. & Lucas, P. L. (2005), 'The fair model: A tool to analyse environmental and costs implications of regimes of future commitments', *Environmental Modeling & Assessment* **10**(2), 115–134.

Desai, A. R., Helliker, B. R., Moorcroft, P. R., Andrews, A. E. & Berry, J. A. (2010), 'Climatic controls of interannual variability in regional carbon fluxes from top-down and bottom-up perspectives', *Biogeosciences* **115**(G02011), doi:10.1029/2009JG001122.

Desai, A. R., Noormets, A., Bolstad, P. V., Chen, J., Cook, B. D., Davis, K. J., Euskirchen, E. S., Gough, C., Martin, J. G., Ricciuto, D. M., Schmid, H. P., Tang, J. & Wang, W. (2008), 'Influence of vegetation and seasonal forcing on carbon dioxide fluxes across the upper midwest, usa: Implications for regional scaling', *Agricultural and Forest Meteorology* **148**(2), 288–308, doi:10.1016/j.agrformet.2007.08.001.

Dick, W. D., Ziemann, P. J. & McMurry, P. H. (2007), 'Multiangle light-scattering measurements of refractive index of submicron atmospheric particles', *Journal of Aerosol Science and Technology* **41**, 549–569.

Dolman, A. J., Gerbig, C., Noilhan, J., Sarrat, C. & Miglietta, F. (2009), 'Detecting regional variability in sources and sinks of carbon dioxide: A synthesis', *Biogeosciences* **6**(2), 1015–1026.

Downing, H. D. & Williams, D. (1975), 'Optical constants of ware in the infrared', *Journal of Geophysical Research* **80**, 1656–1661.

Duan, M., Min, Q. & Li, J. (2005), 'A fast radiative transfer model for simulating high-resolution absorption bands', *Journal of Geophysical Research* **110**(D15201), doi:10.1029/2004JD005590.

Dufour, E. & Breon, F. M. (2003), 'Spaceborne estimate of atmospheric co_2 column by use of the differential absorption method: Error analysis', *Journal of Applied Optics* **42**, 3595–3609.

ECMWF (2007), 'Ecmwf 91 model level definitions'.

ECMWF (2008), *ECMWF TECHNICAL NOTES, ECaccess User Guide, User Support, Operations Department*.

Eguchi, N., Yokota, T. & Inoue, G. (2007), 'Characteristics of cirrus clouds from icesat/glas observations', *Geophysical Research Letters* **34**(L09810), doi:10.1029/2007GL029529.

Engelen, R. J., Andersson, E., Chevallier, F., Hollingsworth, A., Matricardi, M., McNally, A. P., Thepaut, J. N. & Watts, P. D. (2004), 'Estimating atmospheric co_2 from advanced infrared satellite radiances within an operational 4d-var data assimilation system: Methodology and first results', *Journal of Geophysical Research* **109**(D19309), doi:10.1029/2004JD004777.

Engelen, R. J. & Stephens, G. L. (2004), 'Information content of infrared satellite sounding measurements with respect to co_2', *Journal of Applied Meteorology and Climatology* **43**(373-378), doi: 10.1175/1520–0450(2004)043.

Fan, S., Gloor, M., Mahlman, J., Pacala, S., Sarmiento, J., Takahashi, T. & Tans, P. (1998), 'A large terrestrial carbon sink in north america implied by atmospheric and oceanic carbon dioxide data and models', *Science* **282**(5388), 442–446.

Fang, C. & Moncrieff, J. B. (2001), 'The dependence of soil co_2 efflux on temperature', *Soil Boilogy & Biochemistry* **33**, 155–165.

Feng, L., Palmer, P. I., Boesch, H. & Dance, S. (2009), 'Estimating surface co_2 fluxes from space-borne co_2 dry air mole fraction observations using an ensemble kalman filter', *Journal of Atmospheric Chemistry and Physics* **9**, 2619–2633, doi:10.5194/acp–9–2619–2009.

Feng, L., Palmer, P. I., Yang, Y., Yantosca, R. M., Kawa, S. R., Paris, J. D., Matsueda, H. & Machida, T. (2011), 'Evaluating a 3-d transport model of atmospheric co_2 using ground-based, aircraft, and space-borne data', *Journal of Atmospheric Chemistry and Physics* **11**, 2789–2803.

Follows, M. J., Dutkiewicz, S., Grant, S. & Chisholm, S. W. (2007), 'Emergent biogeography of microbial communities in a model ocean', *Science* **315**(1843), doi:10.1126/science.1138544.

Frankenberg, C., Fisher, J. B., Worden, J., Badgley, G., Saatchi, S. S., Lee, J. E., Toon, G. C., Butz, A., Jung, M., Kuze, A. & Yokota, T. (2011a),

'New global observations of the terrestrial carbon cycle from gosat: Patterns of plant fluorescence with gross primary productivity', *Geophysical Research Letters* **38**(L17706), doi:10.1029/2011GL048738.

Frankenberg, C., O'Dell, C., Guanter, L. & McDuffie, J. (2012), 'Chlorophyll fluorescence remote sensing from space in scattering atmospheres: implications for its retrieval and interferences with atmospheric co_2 retrievals', *Atmospheric Measurement Techniques Discussions* **5**, 2487–2527, doi:10.5194/amtd–5–2487–2012.

Frankenberg, C., Warneke, T., Butz, A., Aben, I., Hase, F., Spietz, P. & Brown, L. (2011b), 'Pressure broadening in the 2n3 band of methane and its implication on atmospheric retrievals', *Journal of Atmospheric Chemistry and Physics* **8**, 5061–5075.

Fraser, A., Miller, C. C., Palmer, P. I., Deutscher, N. M., Jones, N. B. & Griffith, D. W. T. (2011), 'The australian methane budget: Interpreting surface and train-borne measurements using a chemistry transport model', *Journal of Geophysical Research* **116**(D20306), doi:10.1029/2011JD015964.

Freund, P. (2003), 'Making deep reductions in co_2 emissions from coal-red power plant using capture and storage of co_2', *Proceedings Institution of Mechanical Engineers, Part A: Journal of Power and Energy* **217**, doi:10.1243/095765003321148628.

Friedlingstein, P., Cox, P., Betts, R., Bopp, L., Bloh, W. V., Brovkin, V., Cadule, P., Doney, S., Eby, M., Fung, I., Bala, G., John, J., Jones, C., Joos, F., Kato, T., Kawamiya, M., Knorr, W., Lindsay, K., Matthews, H. D., Raddatz, T., Rayner, P., Reick, C., Roeckner, E., Schnitzler, K. G., Schnur, R., Strassmann, K., Weaver, A. J., Yoshikawa, C. & Zeng, N. (2006), 'Climatecarbon cycle feedback analysis: Results from the c4mip model intercomparison', *Journal of Climate* **19**, 3337–3353.

Frondini, F., Chiodini, G., Caliro, S., Cardellini, C., Granieri, D. & Ventura, G. (2004), 'Diffuse co_2 degassing at vesuvio, italy', *Bulletin of Volcanology* **66**, 642–651.

Fung, I., Doney, S. C., Lindsay, K. & John, J. (2005), 'Evolution of carbon sinks in a changing climate', *Proceedings of the National Academy of Sciences USA* **102**, 11201–11206.

GLOBALVIEW-CO_2 (2011), 'Globalview-co_2: Cooperative atmospheric data integration project - carbon dioxide, cd-rom, noaa esrl, boulder, colorado'.

Gregory, L. (2011), *Cimel Sunphotometer (CSPHOT) Handbook, DOE/SC-ARM/TR-056*.

Griffiths, P. R. & de Haseth, J. A., eds (2007), *Fourier Transform Infrared Spectrometry, Second Edition*, WILEY.

Gurney, K. R., Law, R., Denning, A. S., Rayner, P., Baker, D., Bousquet, P., Bruhwiler, L., Chen, Y., Ciais, P., Fan, S., Fung, I. Y., Gloor, M., Heimann, M., Higuchi, K., John, J., Kowalczyki, E., Maki, T., Maksyutov, S., Peylin, P., Prather, M., Pak, B. C., Sarmiento, J., Taguchi, S., Takahashi, T. & Yuen, C. W. (2002b), 'Transcom 3 co_2 inversion intercomparison: 1. annual mean control results and sensitivity to transport and prior flux information', *Tellus* **107**(D22), 4635.

Gurney, K. R., Law, R. M., Denning, A. S., Rayner, P. J., Baker, D., Bousquet, P., Bruhwiler, L., Chen, Y. H., Ciais, P., Fan, S., Fung, I. Y., Gloor, M., Heimann, M., Higuchi, K., John, J., Maki, T., Maksyutov, S., Masarie, K., Peylin, P., Prather, M., Pak, B. C., Randerson, J., Sarmiento, J., Taguchi, S., Takahashi, T. & Yuen, C. W. (2002a), 'Towards robust regional estimates of co_2 sources and sinks using atmospheric transport models', *Nature* **415**, 626–630.

Hale, G. M. & Querry, M. R. (1973), 'Optical constants of water in the 200-nm to 200-mm wavelength region', *Journal of Applied Optics* **12**, 555–563.

Hammitt, J. K. & Adams, J. L. (1996), 'The value of international cooperation for abating global climate change', *Resource and energy economics* **18**(3), 219.

Hartmann, J. M., Tran, H. & Toon, G. C. (2009), 'Influence of line mixing on the retrievals of atmospheric co_2 from spectra in the 1.6 and 2.1 μm regions', *Journal of Atmospheric Chemistry and Physics* **9**(7303-7312), doi:10.5194/acp–9–7303–2009.

Haywood, A. M., Chandler, M. A., Valdes, P. J., Salzmann, U., Lunt, D. J. & Dowsett, H. J. (2008), 'Comparison of mid-pliocene climate predictions produced by the hadam3 and gcmam3 general circulation models', *Global and Planetary Change* **66**(208-224), doi:10.1016/j.gloplacha.2008.12.014.

Hoscilo, A., Page, S. E., Tansey, K. J. & Rieley, J. O. (2011), 'Effect of repeated fires on land-cover change on peatland in southern central kalimantan, indonesia, from 1973 to 2005', *International Journal of Wildland Fire* **20**, 578–588.

Houghton, J., ed. (2004), *Global Warming, The Complete Briefing, Third Edition*, Cambridge University Press.

Houghton, R. A. (2002), 'Magnitude, distribution and causes of terrestrial carbon sinks and some implications for policy', *Climate Policy* **2**, 71–88.

Houweling, S. (2009), 'Methane from tm3 model run', *Personal Communication* .

Houweling, S., Breon, F. M., Aben, I., Rodenbeck, C., Gloor, M., Heimann, M. & Ciais, P. (2004), 'Inverse modeling of co_2 sources and sinks using satellite data: A synthetic inter-comparison of measurement techniques and their performance as a function of space and time', *Journal of Atmospheric Chemistry and Physics* **4**, 523–538.

Houweling, S., Hartmann, W., Aben, I., Schrijver, H., Skidmore, J., Roelofs, G. J. & Breon, F. M. (2005), 'Evidence of systematic errors in sciamachy-observed co_2 due to aerosols', *Journal of Atmospheric Chemistry and Physics* **5**, 3003–3013.

Hungershoefer, K., Breon, F. M., Peylin, P., Chevallier, F., Rayner, P., Klonecki, A., Houweling, S. & Marshall, J. (2010), 'Evaluation of various observing systems for the global monitoring of co_2 surface fluxes', *Atmospheric Chemistry and Physics* **10**, 10503–10520.

IPCC (1990), 'Climate change: The ipcc scientific assessment (1990) [j.t. houghton, g.j. jenkins and j.j. ephraums (eds)]', *Cambridge University Press, Cambridge, Great Britain, New York, NY, USA and Melbourne, Australia.* .

IPCC (1996), 'Climate change 1995: Working group i: The science of climate change. contribution of working group i to the second assessment report of the intergovernmental panel on climate change, 1995 [j. t. houghton, l. g. meira filho, b. a. callander, n. harris, a. kattenberg and k. maskell (eds)]', *Cambridge University Press, Cambridge, Great Britain.* .

IPCC (2001), 'Climate change 2001: Working group i: The scientific basis. contribution of working group i to the third assessment report of the intergovernmental panel on climate change, 2001 [j.t. houghton, y. ding, d. j. griggs, m. noguer, p.j. van der linden, x. dai, k. maskell, and c.a. johnson (eds)]', *Cambridge University Press, Cambridge, United Kingdom and New York, NY, USA.* .

IPCC (2007), 'Climate change 2007: Working group i: The physical science basis. contribution of working group i to the fourth assessment report of the intergovernmental panel on climate change, 2007 [s. solomon, d. qin, m. manning, z. chen, m. marquis, k. b. averyt, m. tignor, and h. l. miller (eds)]', *Cambridge University Press, Cambridge, United Kingdom and New York, NY, USA.* .

Jacobson, M. Z., ed. (2005), *Fundamentals of Atmospheric Modelling, Second Edition*, Cambridge University Press.

JAXA (2009), 'Greenhouse gases observing satellite ibuki (gosat) first light acquired by onboard sensors'.

JAXA, NIES & MOE (2008), Thermal and near infrared sensor for carbon observation (tanso) on board the greenhouse gases observing satellite (gosat) research announcement, Technical report, GOSAT Project Office, Center for Global Environmental Research, National Institute for Environmental Studies.

Jenouvrier, A., Daumont, L., Jarlot, L. R., Tyuterev, V. G., Carleer, M., Vandaele, A. C., Mikhailenko, S. & Fally, S. (2007), 'Fourier transform measurements of water vapor line parameters in the 4200-6600 cm-1 region', *Journal of Quantitative Spectroscopy and Radiative Transfer* **105**(2), 326–355.

Jourdan, O., Oshchepkov, S. & Gayet, J. F. (2003), 'Statistical analysis of cloud light scattering and microphysical properties obtained from airborne measurements', *Journal of Geophysical Research* **108**(D5), 4155, doi:10.1029/2002JD002723.

Jr., N. L. S., Lopes, A., Panosso, A. R., Camara, F. T. & Pereira, G. T. (2005), 'Soil co_2 efflux following rotary tillage of a tropical soil', *Soil & Tillage Research* **84**, 222–225.

Kadygrov, N., Maksyutov, S., Eguchi, N., Aoki, T., Nakazawa, T., Yokota, T. & Inoue, G. (2009), 'Role of simulated gosat total column co_2 observations in surface co_2 flux uncertainty reduction', *Journal of Geophysical Research* **114**(D21208), doi:10.1029/2008JD011597.

Kahn, R., Banerjee, P. & McDonald, D. (2001), 'Sensitivity of multiangle imaging to natural mixtures of aerosols over oceans', *Journal of Geophysical Research* **106**(D16), doi:10.1029/2000JD900497.

Kandlikar, M. (1996), 'Indices for comparing greenhouse gas emissions: integrating science and economics', *Energy economics* **18**(4), 265.

Keller, K., McInerney, D. & Bradford, D. F. (2008), 'Carbon dioxide sequestration: how much and when?', *Climate Change* **88**, 267–291.

Knappett, D. (2012), 'Observing the distribution of atmospheric methane from space', *PhD Thesis, University of Leicester, UK* .

Kokhanovsky, A. A., Budak, V. P., Cornet, C., Duan, M., Emde, C., Katsev, I. L., Klyukov, D. A., Korkin, S. V., Labonnote, L. C., Mayer, B., Min, Q., Nakajima, T., Ota, Y., Prikhach, A. S., Rozanov, V. V., Yokota, T. & Zege, E. P. (2010), 'Benchmark

results in vector atmospheric radiative transfer', *Journal of Quantitative Spectroscopy and Radiative Transfer* **111**, 1931–1946.

Kou, L., Labrie, D. & Chylek, P. (1993), 'Refractive indices of water and ice in the 0.65 2.5-mm spectral range', *Journal of Applied Optics* **32**, 3531–3540.

Kuang, Z., Margolis, J., Toon, G., Crisp, D. & Yung, Y. (2002), 'Spaceborne measurements of atmospheric co_2 by high-resolution nir spectrometry of reflected sunlight: An introductory study', *Journal of Geophysical Research Letters* **29**(15, 1716), doi:10.1029/2001GL014298.

Kuze, A., O'Brien, D. M., Taylor, T. E., Day, J. O., O'Dell, C. W., Kataoka, F., Yoshida, M., Mitomi, Y., Bruegge, C. J., Pollock, H., Basilio, R., Helmlinger, M., Matsunaga, T., Kawakami, S., Shiomi, K., Urabe, T. & Suto, H. (2011), 'Vicarious calibration of the gosat sensors using the railroad valley desert playa', *IEEE Transactions on Geoscience and Remote Sensing* **49**(5), 1781–1795.

Kuze, A., Suto, H., Nakajima, M. & Hamazaki, T. (2009), 'Thermal and near infrared sensor for carbon observation fourier-transform spectrometer on the greenhouse gases observing satellite for greenhouse gases monitoring', *Applied Optics* **48**(35), 6716–6733.

Lacis, A. A. (2010), 'Refractive indices of three hygroscopic aerosols and their dependence on relative humidity, http://gacp.giss.nasa.gov/data_sets/'.

Lackner, K. S. (2003), 'A guide to co_2 sequestration', *Science* **300**, 1677–1678.

Lamouroux, J., Tran, H., Laraia, A. L., Garmache, R. R., Rothman, L. S., Gordon, I. E. & Hartmann, J. M. (2010), 'Updated database plus software for line-mixing in co_2 infrared spectra and their test using laboratory spectra in the 1.5-2.3 μm region', *Journal of Quantitative Spectroscopy and Radiative Transfer* **111**, 2321–2331.

Lawson, R. P., Baker, B. A., Schmitt, C. G. & Jensen, T. L. (2001), 'An overview of microphysical properties of arctic clouds observed in may and july 1998 during fire ace', *Journal of Geophysical Research* **106**(D14), 14989–15014.

Lee, H., Schuur, E. A. G. & Vogel, J. G. (2010), 'Soil co_2 production in upland tundra where permafrost is thawing', *Journal of Geophysical Research* **115**(G01009), doi:10.1029/2008JG000906.

Liou, K. N., ed. (1992), *Radiation and Cloud Processes in the Atmosphere; Theory, Observation, and Modeling*, Vol. Oxford Monographs on Geology and Geophysics No. 20, Oxford University Press.

Liou, K. N., ed. (2002), *An Introduction to Atmospheric Radiation, Second Edition*, Vol. Volume 84 in the INTERNATIONAL GEOPHYSICS SERIES, ACADEMIC PRESS.

Liu, Y. & Daum, P. H. (2000), 'Spectral dispersion of cloud droplet size distributions and the parameterization of cloud droplet effective radius', *Journal of Geophysical Research Letters* **27**(13), 1903–1906.

Lorentz, H. A. (1906), 'the absorption and emission of lines of gaseous bodies', *In "H.A. Lorentz Collected Papers" (The Hague 1934-1939)* **3**, 215–238.

Maksyutov, S., Patra, P. K., Onishi, R., Saeki, T. & Nakazawa, T. (2008), 'Nies/frcgc global atmospheric tracer transport model: Description, validation, and surface sources and sinks inversion', *Journal of the Earth Simulator* **9**, 3–18.

Malm, W. C., Day, D. E., Kreidenweis, S. M., Jr., J. L. C., Carrico, C., McMeeking, G. & Lee, T. (2005), 'Hydroscopic properties of an organic-laden aerosol', *Atmospheric Environment* **39**, 4969–4982.

Masarie, K. A. & Tans, P. P. (1995), 'Extension and integration of atmospheric carbon dioxide data into a globally consistent measurement record', *Journal of Geosphysical Research* **100**, 11593–11610.

Maserie, K. A. & Tans, P. P. (1995), 'Extension and integration of atmospheric carbon dioxide data into a globally consistent measurement record', *Journal of Geophysical Research* **100**(D6), 11593–11610.

McLeman, R. & Smit, B. (2006), 'Migration as an adaption to climate change', *Climate change* **76**, 31–53.

McNeil, B. I., Matear, R. J., Key, R. M., Bullister, J. L. & Sarmiento, J. L. (2003), 'Antropogenic co_2 uptake by the ocean based on the global chlorofluorocarbon data set', *Science* **299**(5604), 235–239.

Messerschmidt, J., Geibel, M. C., Blumenstock, T., Chen, H., Deutscher, N. M., Engel, A., Feist, D. G., Gerbig, C., Gisi, M., Hase, F., Katrynski, K., Kolle, O., Lavrič, J. V., Notholt, J., Palm, M., Ramonet, M., Rettinger, M., Schmidt, M., Sussmann, R., Toon, G. C., Truong, F., Warneke, T., Wennberg, P. O., Wunch, D. & Xueref-Remy, I. (2011),

'Calibration of tccon column-averaged co_2: the first aircraft campaign over european tccon sites', *Journal of Atmospheric Chemistry and Physics* **11**, 10765–10777.

Michelson, A. A. & Morley, E. W. (1887), 'On the relative motion of the earth and the luminiferous ether', *American Journal of Science - Third Series* **XXXIV**(203), 333–345.

Mielonen, T., Arola, A., Komppula, M., Kukkonen, J., Koskinen, J., de Leeuw, G. & Lehtinen, K. E. J. (2009), 'Comparison of caliop level 2 aerosol subtypes to aerosol types derived from aeronet inversion data', *Journal of Geophysical Research Letters* **36**(L18804), doi:10.1029/2009GL039609.

Miller, C. E., Crisp, D., DeCola, P. L., Olsen, S. C., Randerson, J. T., Michalak, A. M., Alkhaled, A., Rayner, P., Jacob, D. J., Suntharalingam, P., Jones, D. B. A., Denning, A. S., Nicholls, M. E., Doney, S. C., Pawson, S., Boesch, H., Connor, B. J., Fung, I. Y., OBrien, D., Salawitch, R. J., Sander, S. P., Sen, B., Tans, P., Toon, G. C., Wennberg, P. O., Wofsy, S. C., Yung, Y. L. & Law, R. M. (2007), 'Precision requirements for space-based xco_2 data', *Journal of Geophysical Research* **112**(D10314), doi:10.1029/2006JD007659.

Mishchenko, M. I., Dlugach, J. M., Yanovitskij, E. G. & Zakharova, N. T. (1999), 'Bidirectional reflectance of flat, optically thick particulate laters: an efficient radiative transfer solution and applications to snow and soil surfaces', *Journal of Quantitative Spectroscopy and Radiative Transfer* **63**, 409–432.

Mishchenko, M. I., Travis, L. D. & Lacis, A. A., eds (2002), *Scattering, Absorption, and Emission of Light by Small Particles*, Cambridge University Press.

Moa, J. P. & Kawa, S. R. (2004), 'Sensitivity studies for space-based measurement of atmospheric total column carbon dioxide by reflected sunlight', *Journal of Applied Optics* **43**, 914–927.

Morcrette, J. J. (2012), 'Gems aerosol information', *Personal Communication* .

Morino, I., Uchino, O., Inoue, M., Yoshida, Y., Yokota, T., Wennberg, P., Toon, G., Wunch, D., Roehl, C. M., Notholt, J., Warneke, T., Messerschmidt, J., Griffith, D. W., Deutscher, N. M., Sherlock, V., Connor, B., Robinson, J., Sussmann, R. & Rettinger, M. (2011), 'Preliminary validation of column-averaged volume mixing ratios of carbon dioxide and methane retrieved from gosat short-wavelength infrared spectra', *Journal of Atmospheric Chemistry and Physics* **4**(6), 1061–1076, doi:10.5194/amt–4–1061–2011.

Muller-Karger, F. E., Varela, R., Thunell, R., Luerssen, R., Hu, C. & Walsh, J. (2005), 'the importance of continental margins in the global carbon cycle', *Journal of Geophysical Research Letters* **32**(L01602), doi:10.1029/2004GL021346.

Murphy, D. M. & Koop, T. (2005), 'Review of the vapour pressures of ice and supercooled water for atmospheric applications', *Quarterly Journal of the Royal Meteorological Society* **131**, 1539–1565.

NATIONS, U. (1998), 'Kyoto protocol to the united nations framework convention on climate change'.

NATIONS, U. (2009), 'Copenhagen accord'.

Natraj, V. & Spurr, R. (2007), 'A fast linearized pseudo-spherical two orders of scattering model to account for polarization in vertically inhomogeneous scattering-absorbing media', *Journal of Quantitative Spectroscopy and Radiative Transfer* **107**, 263–293.

O'Brien, D. M., Mitchell, R. M., English, S. A. & Costa, G. A. D. (1998), 'Airborne measurements of air mass from o_2 a-band absorption spectra', *Journal of Atmospheric Oceanic Technology* **15**, 1271–1286.

O'Brien, D. M. & Rayner, P. J. (2002), 'Global observations of the carbon budget: 2. co_2 column from differential absorption of reflected sunlight in the 1.61 um band of co_2', *Journal of Geosphysical Research* **107(D18)**(4354), doi:10.1029/2001JD000617.

O'Brien, D., Polonsky, I. & O'Dell, C. W. (2009), 'Orbiting carbon observatory algorithm theoretical basis document: the oco simulator'.

O'Dell, C. W. (2010), 'Acceleration of multiple-scattering, hyperspectral radiative transfer calculations via low-streams interpolation', *Journal of Geophysical Research* **115**(D10206), doi:10.1029/2009JD012803.

O'Dell, C. W., Connor, B., Boesch, H., O'Brien, D., Frankenberg, C., Castano, R., Christi, M., Eldering, D., Fisher, B., Gunson, M., McDuffie, J., Miller, C. E., Natraj, V., Oyafuso, F., Polonsky, I., Smyth, M., Taylor, T., Toon, G. C., Wennberg, P. O. & Wunch, D. (2012), 'The acos co_2 retrieval algorithm part 1: Description and validation against synthetic observations', *Journal of Atmospheric Measurement Techniques* **5**, 99–121.

Ohlson, M., Dahlberg, B., Okland, T., Brown, K. J. & Halvorsen, R. (2009), 'The charcoal carbon pool in boreal forest soils', *Nature Geoscience* **2**, 692–695,doi:10.1038/NGEO617.

Omar, A. H., Winker, D. & Won, J. G. (2004), 'Aerosol models for the calipso lidar inversion algorithms', *Laser Radar Technology for Remote Sensing* **5240**(1), 153–164.

Oshchepkov, S., Bril, A., Maksyutov, S. & Yokota, T. (2011), 'Detection of optical path in spectroscopic space-based observations of greenhouse gases: Application to gosat data processing', *Journal of Geophysical Research* **116**(D14304), doi:10.1029/2010JD015352.

Oshchepkov, S., Bril, A. & Yokota, T. (2009), 'An improved photon path length probability density function-based radiative transfer model for space based observation of greenhouse gases', *Journal of Geophysical Research* **114**(D19207), doi:10.1029/2009JD012116.

Oshchepkov, S., Bril, A., Yokota, T., Morino, I., Yoshida, Y., Matsunaga, T., Belikov, D., Wunch, D., Wennberg, P., Toon, G., O'Dell, C., Butz, A., Guerlet, S., Cogan, A. & et al. (2012a), 'Effects of atmospheric light scattering on spectroscopic observations of greenhouse gases from space: Validation of ppdf-based co_2 retrievals from gosat', *Journal of Geophysical Research* **117**(D12305), doi:10.1029/2012JD017505.

Oshchepkov, S., Bril, A., Yokota, T., Wennberg, P., Deutscher, N. M., Wunch, D., Toon, G., Yoshida, Y., O'Dell, C. W., Crisp, D., Miller, C. E., Frankenberg, C., Butz, A., Aben, I., Guerlet, S., Hasekamp, O., Boesch, H., Cogan, A., Parker, R., Griffith, D., Macatangay, R., Notholt, J., Sussmann, R., Rettinger, M., Sherlock, V., Robinson, J., Kyro, E., Heikkinen, P., Feist, D. G., Morino, I., Kadygrov, N., Belikov, D., Maksyutov, S., Matsunaga, T., Uchino, O. & Watanabe, H. (2012b), 'Effects of atmospheric light scattering on spectroscopic observations of greenhouse gases from space. part 2: Algorithm intercomparison in the gosat data processing for co2 retrievals over tccon sites', *Journal of Geophysical Research* p. In Submission.

Pacala, S. W., Hurtt, G. C., Baker, D., Peylin, P., Houghton, R. A., Birdsey, R. A., Heath, L., Sundquist, E. T., Stallard, R. F., Ciais, P., Moorcroft, P., Caspersen, J. P., Shevliakova, E., Moore, B., Kohlmaier, G., Holland, E., Gloor, M., Harmon, M. E., Fan, S. M., Sarmiento, J. L., Goodale, C. L., Schimel, D. & Field, C. B. (2001), 'Consistent land- and atmosphere-based us carbon sink estimates', *Science* **292**, 2316–2320.

Pade, C. & Guimaraes, M. (2007), 'The co_2 uptake of concrete in a 100 year perspective', *Cement and Concrete Research* **37**, 1348–1356.

Pagano, T. S. (2011), 'Seven years of years of observations of mid-tropospheric co_2 from the atmospheric infrared sounder', *Acta Astronautica* **69**, 355–359.

Palmer, K. P. & Williams, D. (1974), 'Optical properties of water in the near infrared', *Journal of the Optical Society of America* **64**, 1107–1110.

Palmer, P. I., Feng, L. & Boesch, H. (2011), 'Spatial resolution of tropical terrestrial co_2 fluxes inferred using space-borne co_2 sampled in different earth orbits: the role of spatial error correlations', *Journal of Atmospheric Measurement Techniques* **4**, 1995–2006,doi:10.5194/amtd–4–3251–2011.

Parker, R., Boesch, H., Cogan, A., Fraser, A., Feng, L., Palmer, P. I., Messerschmidt, J., Deutscher, N., Griffith, D. W. T., Notholt, J., Wennberg, P. O. & Wunch, D. (2011), 'Methane observations from the greenhouse gases observing satellite: Comparison to ground-based tccon data and model calculations', *Geophysical Research Letters* **38**(L15807), doi:10.1029/2011GL047871.

Patra, P. K., Houweling, S., Krol, M., Bousquet, P., Belikov, D., Bergmann, D., Bian, H., Smith, P. C., Chipperfield, M. P., Corbin, K., Cheiney, A. F., Fraser, A., Gloor, E., Hess, P., Ito, A., Kawa, S. R., Law, R. M., Loh, Z., Maksyutov, S., Meng, L., Palmer, P. I., Prinn, R. G., Rigby, M., Saito, R. & Wilson, C. (2011), 'Transcom model simulations of ch_4 and related species: linking transport, surface flux and chemical loss with ch_4 variability in the troposphere and lower stratosphere', *Jounral of Atmospheric Chemistry and Physics* **11**, 12813–12837.

Paustian, K., Six, J., Elliott, E. T. & Hunt, H. W. (2000), 'Management options for reducing co_2 emissions from agricultural soils', *Biogeochemistry* **48**, 147–163.

Peppler, R. A., Kehoe, K. E., Sonntag, K. L., Bahrmann, C. P., Richardson, S. J., Christensen, S. W., McCord, R. A., Doty, K. J., Wagener, R., Eagen, R. C., Liljegren, J. C., Orr, B. W., Sisterson, D. L., Halter, T. D., Keck, N. N., Long, C. N., Macduff, M. C., Mather, J. H., Perez, R. C., Voyles, J. W., Ivey, M. D., Moore, S. T., Nitschke, K. L., Perkins, B. D. & Turner, D. D. (2008), *Quality Assurance of ARM Program Climate Research Facility Data*.

Peters, W., Jacobson, A. R., Sweeney, C., Andrews, A. E., Conway, T. J., Masarie, K., Miller, J. B., Bruhwiler, L. M. P., Petron, G., Hirsch, A. I., Worthy, D. E., van der Werf, G. R., Randerson, J. T., Wennberg, P. O., Krol, M. C. & Tans, P. P. (2007), 'An atmospheric perspective on north american carbon dioxide exchange: Carbontracker', *Proceedings of the National Academy of Sciences* **104**(48), 18925–18930.

Pickett-Heaps, C. A., Rayner, P. J., Law, R. M., Ciais, P., Patra, P. K., Bousquet, P., Peylin, P., Maksyutov, S., Marhshall, J., Rodenbeck, C., Langenfelds, R. L., Steele,

L. P., Francey, R. J., Tans, P. & Sweeney, C. (2011), 'Atmospheric co_2 inversion validation using vertical profile measurements: Analysis of four independent inversion models', *Journal of Geosphysical Research* **116**(D12305), doi:10.1029/2010JD014887.

Popovicheva, O., Persiantseva, N. M., Shonija, N. K., DeMott, P., Koehler, K., Petters, M., Kreidenweis, S., Tishkova, V., Demirdjian, B. & Suzanne, J. (2008), 'Water interaction with hydrophobic and hydrophilic soot particles', *Physical Chemistry Chemical Physics* **10**, 2332–2344.

Randerson, J. T., Thompson, M. V., Conway, T. J., Fung, I. Y. & Field, C. B. (1997), 'The contribution of terrestrial sources and sinks to trends in the seasonal cycle of atmospheric carbon dioxide', *Global Biogeochemical Cycles* **11**, 535–560.

Rayner, P. J., Law, R. M., OBrien, D. M., Butler, T. M. & Dilley, A. C. (2002), 'Global observations of the carbon budget, 3, initial assessment of the impact of satellite orbit, scan geometry, and cloud on measuring co_2 from space', *Journal of Geophysical Research* **107(D21)**(4557), doi:10.1029/2001JD000618.

Rayner, P. J. & O'Brien, D. M. (2001), 'The utility of remotely sensed co_2 concentration data in surface source inversions', *Geophysical Research Letters* **28**(1), 175–178.

Riley, W. J., Biraud, S. C., Torn, M. S., Fischer, M. L., Billesbach, D. P. & Berry, J. A. (2009), 'Regional co_2 and latent heat surface fluxes in the southern great plains: Measurements, modeling, and scaling', *Journal of Geophysical Research* **114**(G04009), doi:10.1029/2009JG001003.

Robinson, M. M., Dowsett, H. J. & Chandler, M. A. (2008), 'Pliocene role in assessing future climate impacts', *EOS, Transactions, American Geophysical Union* **89**(49).

Robuck, A., MacCracken, M. C., Perry, J. S. & Munn, T., eds (2002), *Volcanic Eruptions, The Earth system: physical and chemical dimensions of global environmental change,Encyclopedia of Global Environmental Change*, Vol. Volume 1, pp 738-744, John Wiley and Sons.

Rodgers, C. D. & Connor, B. J. (2003), 'Intercomparison of remote sounding instruments', *Journal of Geophysical Research* **108(D3)**(4116), doi:10.1029/2002JD002299.

Rodgers, C. D., ed. (2000), *INVERSE METHODS FOR ATMOSPHERIC SOUNDING: Theory and Practice*, Vol. Vol. 2, World Scientific.

Rothman, L. S., Gordon, I. E., Barbe, A., Benner, D. C., Bernath, P. F., Birk, M., Boudon, V., Brown, L. R., Campargue, A., Champion, J. P., Chance, K., Coudert, L. H., Dana, V., Devi, V. M., Fally, S., Flaud, J. M., Gamache, R. R., Goldman, A., Jacquemart, D., Kleiner, I., Lacome, N., Lafferty, W. J., Mandin, J. Y., Massie, S. T., Mikhailenko, S. N., Miller, C. E., Ahmadi, N. M., Naumenko, O. V., Nikitin, A. V., Orphal, J., Perevalov, V. I., Perrin, A., Cross, A. P., Rinsland, C. P., Rotger, M., Šimečková, M., Smith, M. A. H., Sung, K., Tashkun, S. A., Tennyson, J., Toth, R. A., Vandaele, A. C. & Auwera, J. V. (2009), 'The hitran 2008 molecular spectroscopic database', *Journal of Quantitative Spectroscopy and Radiative Transfer* **110**(9-10), 533–572.

Roy, D., Boschetti, L., Justice, C. & Ju, J. (2008), 'The collection 5 modis burned area product global evaluation by comparison with the modis active fire product', *Remote Sensing of Environment* **112**, 3690–3707.

Ryan, S. (2001), 'Estimating volcanic co_2 emission rates from atmospheric measurements on the slope of mauna loa', *Chemical Geology* **177**, 201–211.

S. Oshchepkov, A. B. & Yokota, T. (2008), 'Ppdf-based method to account for atmospheric light scattering in observations of carbon dioxide from spcae', *Journal of Geophysical Research* **113**(D23210), doi:10.1029/2008JD010061.

Sabine, C. L., Feely, R. A., Gruber, N., Key, R. M., Lee, K., Bullister, J. L., Wanninkhof, R., Wong, C. S., Wallace, D. W. R., Tilbrook, B., Millero, F. J., Peng, T. H., Kozyr, A., Ono, T. & Rios, A. F. (2004), 'The oceanic sink for anthropogenic co_2', *Science* **305**, 367–371.

Schaaf, C. B., Gao, F., Strahler, A. H., Lucht, W., Li, X., Tsang, T., Strugnell, N. C., Zhang, X., Jin, Y., Muller, J. P., Lewis, P., Barnsley, M., Hobson, P., Disney, M., Roberts, G., Dunderdale, M., Doll, C., d Entremont, R. P., Hu, B., Liang, S., Privette, J. L. & Roy, D. (2002), 'First operational brdf, albedo nadir reflectance products from modis', *Journal of Remote Sensing and Environment* **83**(15), 135–148.

Scheising, O. (2009), 'Analysis and interpretation of satellite measurements in the near-infrared spectral region: Atmospheric carbon dioxide and methane', *PhD thesis, Germany, University of Bremen FB1, Institute of Environmental Physics (IUP)* .

Schneising, O., Buchwitz, M., Burrows, J. P., Bovensmann, H., Reuter, M., Notholt, J., Macatangay, R. & Warneke, T. (2008), 'Three years of greenhouse gas column-averaged dry air mole fractions retrieved from satellite part 1: Carbon dioxide', *Journal of Atmospheric Chemisty and Physics Discussions* **8**, 5477–5536.

Sheese, P. E., Llewllyn, E. J., Gattinger, R. L., Bourassa, A. E., Degenstein, D. A., Lloyd, N. D. & McDade, I. C. (2010), 'Temperatures in the upper mesosphere and lower thermosphere from osiris observations of o_2 a band emission spectra', *Canadian Journal of Physics* **88**, 919–925, doi:10.1139/P10–093.

Shettle, E. P. & Fenn, R. W. (1979), 'Models for the aerosols of the lower atmosphere and the effects of humidity on their optical properties', *Environmental Research Papers* **M6**, AFOL–TR–79–0214.

Shinohara, H., Hirabayashi, J., Nogami, K. & Iguchi, M. (2011), 'Evolution of volcanic gas composition during repeated culmination of volcanic activity at kuchinoerabujima volcano, japan', *Journal of Volcanology and Geothermal Research* **202**, 107–116.

Simmons, A. (2010), *A Monitoring and Forecasting System for Atmospheric Compositions, Final report of the GEMS project*.

Slingo, A. & Schrecker, H. M. (1982), 'On the shortwave radiative properties of stratiform water clouds', *Quarterly Journal of the Royal Meteorological Society* **108**, 407–426.

Smith, W. L., Woolf, H. M., Hayden, C. M., Wark, D. Q. & McMillin, L. M. (1979), 'Smith, w. l., , the tiros-n operational vertical sounder', *Bulletin of the American Meteorological Society* **60**, 1177–1187.

Spinetti, C., Carrere, V., Buongiorno, M. F., Sutton, A. J. & Elias, T. (2008), 'Carbon dioxide of pu'u'o'o volcanic plume at kilauea retrieved by aviris hyperspectral data', *Remote Sensing of Environment* **112**, 3192–3199.

Spurr, R. J. D., Kurosu, T. P. & Chance, K. V. (2001), 'A linearized discrete ordinate radiative transfer model for atmospheric remote sensing retrieval', *Journal of Quantitative Spectroscopy and Radiative Transfer* **68**, 689–735.

Steinacker, J., Henning, T. H., Bacmann, A. & Semenov, D. (2003), '3d continuum radiative transfer in complex dust configurations around stellar objects and active galactic nuclei, 1. computational methods and capabilities', *Astronomy & Astrophysics* **401**, 405–418.

Stige, L. C., Ottersen, G., Hjermann, D. O., Dalpadado, P., Jensen, L. K. & Stenseth, N. C. (2011), 'Environmental toxicology: Population modeling of cod larvae shows high sensitivity to loss of zooplankton prey', *Marine Pollution Bulletin* **62**, 395–398.

Sun, Z. & Rikus, L. (1999), 'Parametrization of effective sizes of cirrus-cloud particles and its verification against observations', *Quarterly Journal of the Royal Meteorological Society* **125**, 3037–3055.

Suto, H., Kawashima, T., Yoshida, J., Ishida, J., Kuze, A., Nakajima, M. & Hamazaki, T. (2008), 'The pre-launch performance test and calibration results of thermal and near infrared sensor for carbon observation (tanso) on gosat', *Journal of Sensors, Systems, and Next-Generation Satellites XII, Proc. of SPIE* **7106**(71060L), doi:10.1117/12.799961.

Suto, H., Kuze, A., Shiomi, K., Nakajima, M. & Hamazaki, T. (2011), 'Updated level-1 processing after two-years operation of tanso-fts', *Proc. SPIE* **8154**(81541A), doi:10.1117/12.893405.

Takahashi, T., Sutherland, S. C., Sweeney, C., Poisson, A., Metzl, N., Tillbrook, B., Bates, N., Wanninkhof, R., Feely, R. A., Sabine, C., Olafsson, J. & Nojiri, Y. (2002), 'Global sea-air co_2 flux based on climatological surface ocean pco_2, and seasonal biological and temperature effects', *Deep-Sea Research Part II* **49**, 1601–1622.

Takahashi, T., Sutherland, S. C., Wanninkhof, R., Sweeney, C., Feely, R. A., Chipman, D. W., Hales, B., Friederich, G., Chavez, F., Sabine, C., Watson, A., Bakker, D. C. E., Schuster, U., Metzl, N., Inoue, H. Y., Ishii, M., Midorikawa, T., Nojiri, Y., Krtzinger, A., Steinhoff, T., Hoppema, M., Olafsson, J., Arnarson, T. S., Tilbrook, B., Johannessen, T., Olsen, A., Bellerby, R., Wong, C. S., Delille, B., Bates, N. R. & de Baar, H. A. W. (2009), 'Climatological mean and decadal change in surface ocean pco_2, and net seaair co_2 flux over the global oceans', *Deep Sea Research Part II: Topical Studies in Oceanography* **56**(8-10), 554–577.

Takemura, T., Nakajima, T., Higurashi, A., Ohta, S. & Sugimoto, N. (2003), 'Aerosol distributions and radiative forcing over the asian pacific region simulated by spectral radiation-transport model for aerosol species (sprintars)', *Journal of Geophysical Research* **108**(D23), 8659.

Tang, I. N. & Munkelwitz, H. R. (1991), 'Simultaneous determination of refractive index and density of an evaporating aqueous solution droplet', *Journal of Aerospace Science and Technologies* **15**, 201–207.

Tang, I. N. & Munkelwitz, H. R. (1994), 'Water activities, densities, and refractive indices of aqueous sulfates and sodium nitrate droplets of atmospheric importance', *Journal of Geophysical Research* **99**, 18801–18808.

Tang, I. N. & Munkelwitz, H. R. (1996), 'Chemical and size effects of hygroscopic aerosols on light scattering coefficients', *Journal of Geophysical Research* **101**, 19245–19250.

Tans, P. & Keeling, R. (2012), 'Noaa/esrl'.

Taylor, T. E., O'Dell, C. W., O'Brien, D. M., Kikuchi, N., Yokota, T., Nakajima, T. Y., Ishida, H., Crisp, D. & Nakajima, T. (2012), 'Comparison of cloud-screening methods applied to gosat near-infrared spectra', *IEEE Transactions on Geoscience and Remote Sensing* **50**(1), 295–309.

Thuillier, G., Herse, M., Simon, P. C., Labs, D., Mandel, H., Gillotay, D. & Foujols, T. (2003), 'The solar spectral irradiance from 200 to 2400 nm as measured by the solspec spectrometer from the atlas 1-2-3 and eureca missions', *Solar Physics* **214**(1), 1–22.

Tol, R. S. J. (2002), 'Estimates of the damage costs of climate change, part ii. dynamic estimates', *Environmental and Resource Economics* **21**(2), 135–160.

Toth, R. A. (2005), 'Measurements of positions, strengths and self-broadened widths of h_2o from 2900 to 8000 cm1: Line strength analysis of the 2nd triad bands', *Journal of Quantitative Spectroscopy and Radiative Transfer* **94**(1), 51–107.

Toth, R. A., Brown, L. R., Miller, C. E., Devi, V. M. & Benner, D. C. (2008), 'Spectroscopic database of co_2 line parameters: 43007000cm^{-1}', *Journal of Quantitative Spectroscopy and Radiative Transfer* **109**, 906–921.

Trenberth, K. E. (1998), 'Atmospheric moisture residence times and cycling: Implications for rainfall rates and climate change', *Climate Change* **39**(4), 667–694.

Tsunogai, U., Yoshida, N. & Gamo, T. (1999), 'Carbon isotopic compositions of c_2-c_5 hydrocarbons and methyl chloride in urban, coastal, and maritime atmospheres over the western north pacific', *Journal of Geosphysical Research* **104**(D13), 16033–16039.

USGS (1996), 'Gtopo30'.

van der Werf, G. R., Randerson, J. T., Giglio, L., Collatz, G. J., Mu, M., Kasibhatia, P. S., Morton, D. C., DeFries, R. S., Jin, Y. & van Leeuwen, T. T. (2010), 'Global fire emissions and the contribution of deforestation, savanna, forest, agricultural, and peat fires (1997-2009)', *Journal of Atmospheric Chemistry and Physics* **10**, 11707–11735, doi:10.5194/acp–10–11707–2010.

Vangwichith, M., Tran, H. & Hartmann, J. M. (2009), 'Line-mixing and collision induced absorption for o_2-co_2 mixtures in the oxygen a-band region', *Journal of Quantitative Spectroscopy and Radiative Transfer* **110**, 2212–2216.

Warren, S. G. (1984), 'Optical constants of ice from the ultraviolet to the microwave', *Journal of Applied Optics* **23**(8), 1206–1225.

Weaver, A. J. (2011), 'Toward the second commitment period of the kyoto protocol', *Science* **332**, 795–796.

Wigley, T. M. L. & Schimel, D. S., eds (2000), *The Carbon Cycle*, Cambridge University Press.

Williams, J., de Reus, M., Krejci, R., Fischer, H. & Stroem, J. (2002), 'Application of the variability-size relationship to atmospheric aerosol studies: estimating aerosol lifetimes and ages', *Journal of Atmospheric Chemistry and Physics* **2**, 133–145.

Wofsy, S. C. & Harriss, R. C. (2002), 'The north american carbon program (ncap)', *report of the NACP Committee of the U.S. Interagency Carbon Cycle Science Program, U.S. Global Change Res. Program, Washington, D. C.* .

Wofsy, S. C., Team, T. H. S., Modellers, C. & Teams, S. (2010), 'Hiaper pole-to-pole observations (hippo): fine-grained, global-scale measurements of climatically important atmospheric gases and aerosols', *Philosophical Transactions of The Royal Society* **369**, 2073–2086.

Wooster, M. J., Freeborn, P. H., Archibald, S., Oppenheimer, C., Roberts, G. J., Smith, T. E. L., Govender, N., Burton, M. & Palumbo, I. (2011), 'Field determination of biomass burning emission ratios and factors via open-path ftir spectroscopy and fire radiative power assessment: headfire, backfire and residual smouldering combustion in african savannahs', *Journal of Atmospheric Chemistry and Physics* **11**, 11591–11615, doi:10.5194/acp–11–11591–2011.

Wunch, D., Toon, G. C., Blavier, J. F. L., Washenfelder, R. A., Notholt, J., Connor, B. J., Griffith, D. W. T., Sherlock, V. & Wennberg, P. O. (2011a), 'Total carbon column observing network', *Philosophical Transactions of The Royal Society* **369**, 2087–2112.

Wunch, D., Toon, G. C., Wennberg, P. O., Wofsy, S. C., Stephens, B. B., Fischer, M. L., Uchino, O., Abshire, J. B., Bernath, P., Biraud, S. C., Blavier, J. F. L., Boone, C., Bowman, K. P., Browell, E. V., Campos, T., Connor, B. J., Daube, B. C., Deutscher, N. M., Diao, M., Elkins, J. W., Gerbig, C., Gottlieb, E., Griffith, D. W. T., Hurst,

D. F., Jiménez, R., Aleks, G. K., Kort, E. A., Macatangay, R., Machida, T., Matsueda, H. & Moore, F. (2010), 'Calibration of the total carbon column observing network using aircraft profile data', *Journal of Atmospheric Measurement Techniques* **3**(1351-1362), doi:10.5194/amt–3–1351–2010.

Wunch, D., Wennberg, P. O., Toon, G. C., Connor, B. J., Fisher, B., Osterman, G. B., Frankenberg, C., Mandrake, L., O'Dell, C., Ahonen, P., Biraud, S. C. & et al. (2011b), 'A method for evaluating bias in global measurements of co_2 total columns from space', *Journal of Atmospheric Chemistry and Physics* **11**(12317-12337), doi:10.5194/acp–11–12317–2011.

Yevich, R. & Logan, J. A. (2003), 'An assessment of biofuel use and burning of agricultural waste in the developing world', *Global Biogeochem. Cycles* **17(4)**(1095), doi:10.1029/2002GB001952.

Yokota, T., Yoshida, Y., Eguchi, N., Ota, Y., Tanaka, T., Watanabe, H. & Maksyutov, S. (2009), 'Global concentrations of co_2 and ch_4 retrieved from gosat: First preliminary results', *Scientific Online Letters on the Atmosphere* **5**, 160–163, doi:10.2151/sola.2009041.

Yoshida, Y. (2011), 'Nies retrieval algorithm issues', *Personal Communication* .

Yoshida, Y., Kikuchi, N. & Yokota, T. (2012), 'On-orbit radiometric calibration of swir bands of tanso-fts onboard gosat', *Atmospheric Measurement Techniques Discussions* **5**, 5,doi:10.5194/amtd–5–4711–2012.

Yoshida, Y., Ota, Y., Eguchi, N., Kikuchi, N., Nobuta, K., Tran, H., Morino, I. & Yokota, T. (2010), 'Retrieval algorithm for co_2 and ch_4 column abundances from short-wavelength infrared spectral observations by the greenhouse gases observing satellite', *Atmospheric Measurement Techniques Discussions* **3**, 4791–4833.

Zhang, Z., Platnick, S., Yang, P., Heidinger, A. K. & Comstock, J. M. (2010), 'Effects of ice particle size vertical inhomogeneity on the passive remote sensing of ice clouds', *Journal of Geosphysical Research* **115**(D17203), doi:10.1029/2010JD013835.